Model for Deposition Build-up in Biomass Boilers

Hansen, Stine Broholm

Publication date:
2015

Document Version
Peer reviewed version

Model for Deposition Build-up in Biomass Boilers

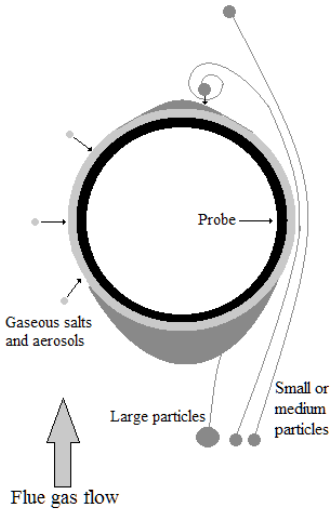

Stine Broholm Hansen

PhD Thesis

November 2015

DTU Chemical Engineering
Department of Chemical and Biochemical Engineering

Model for Deposition Build-up in Biomass Boilers

PhD Thesis

Stine Broholm Hansen

November 2015

CHEC Research Centre
Department of Chemical and Biochemical Engineering
Technical University of Denmark

Preface and Acknowledgement

The present dissertation is written to fulfill the partial requirements of obtaining a Ph.D. degree at the Technical University of Denmark. The work has been carried out between January 2010 and September 2015 in the CHEC (Combustion and Harmful Emission Control) research centre at the Department of Chemical and Biochemical Engineering, Technical University of Denmark. The work has been funded by the Technical University of Denmark, the Danish Strategic Research Council (GREEN) and DONG Energy A/S. The supervisors were Professor Peter Glarborg, Senior Researcher Peter Arendt Jensen, Dr. Techn. Flemming J. Frandsen and Senior Engineer, Lich.Tech Bo Sander (DONG Energy Thermal Power).

I wish to thank all my supervisors for their invaluable support and guidance throughout the project and for continuously challenging my ideas and results in order to improve the project. Peter Glarborg always believed in me and encouraged me. Peter Arendt Jensen always participated in fruitful discussions and my work benefited from his great insight into the experimental work conducted and from his experiences with modeling. Flemming Frandsen is an open book of knowledge on ash transformations, which has definitely helped my understanding of the complicated processes. My work also benefited greatly from Bo Sander and his great knowledge on the practical aspects of combustion.

My 'colleagues' at DONG Energy also deserve my gratitude for housing me the past years and for pleasant times over lunch and coffee breaks. In particular Maja Bøg Toftegaard Andersen and Alice Jochumsen have supported me and my work. My gratitude also goes out to Anne Juul Damø for fruitful talks and pleasant company at conferences and lunches.

Finally, I would like to thank my husband, Flemming, and my two darling girls, Sofie and Johanne, for their support and for for bearing with me and giving me space, when work on this thesis required all my time and energy.

Stine Broholm Hansen
November 2015

Summary

In order to reduce CO_2 emissions and the dependency on fossil fuels, complete substitution of coal with biomass it aimed at year 2050 in Denmark. However, the implementation of biomass as fuel in pulverized fuel combustion plants is a challenging process, due to the ash formation from biomass being different than that of coal.

This PhD presents increased knowledge on the ash transformations and deposit formation occurring in suspension firing of biomass. As part of the study, a model describing these processes has been developed.

Initially, a number of full-scale deposit probe measuring campaigns conducted in grate-fired and suspension-fired boilers, fired with biomass, have been reviewed and compared. The influence of operational parameters on the chemistry of ash and deposits, on deposit build-up rates and on shedding behavior has been examined.

The firing technology and the fuel utilized influence the fly ash and deposit chemical composition. In grate-firing, K, Cl and S are enriched in the fly ash compared to the fuel ash, while the fly ash in suspension-firing is relatively similar to the fuel ash. The chemical composition of the deposits formed is determined by the fly ash composition and the flue gas temperature; increases in the local flue gas temperature lead to higher contents of Si and Ca and lower contents of Cl in the deposits.

The net deposit build-up rates in grate-fired and suspension-fired boilers are at similar levels; 0-100 $g/m^2/h$, while the ash deposit propensity (%) is an order of magnitude larger in grate fired boilers than in suspension-fired boilers. Deposit build-up rates were found to increase at flue gas temperatures close to the melting temperatures of the fly ash. Thus, the build-up rates are also influenced by fuel ash composition.

Shedding of deposits occurs by melting during straw-firing on a grate at high flue gas temperatures (>900 °C). At lower flue gas temperatures, the deposits can be removed by soot blowing. During straw/wood-firing in suspension-fired boilers, shedding occurred by debonding with incomplete removal at flue gas temperatures of 600-1000 °C, and by debonding with complete removal during wood-firing in suspension-fired boilers at high flue gas temperatures (1300 °C). Shedding events were not observed during wood suspension-firing at low flue gas temperatures (<900 °C). Here, a steady-state mass of deposits on the probe was observed.

For grate-firing of straw and for straw/wood firing in suspension-fired boilers

was observed that increased exposure times and probe temperatures lead to deposits which are difficult to remove.

A model for deposit formation in suspension firing of biomass has been developed. The model consist of two parts; First, a model for the ash formation is proposed, and secondly, a model for deposit build-up has been formulated.

In the ash formation model, the release of K, Cl and S was assumed, simple description of the gas phase reactions was proposed along with quantification of aerosol formation. The coarse ash fraction was described by a new model for particle size distribution. The model is similar to fragmentation models suggested for coal combustion, but takes vaporization of K, Cl and S into account.

The deposit formation model describes deposit build-up by diffusion and condensation of vapors, thermophoresis of aerosols, convective diffusion of small particles, impaction of large particles and reaction. Two models have been proposed. The models differ in the description of sticking probability of impacted particles. Model #1 employs a reference viscosity in the description of sticking probability and all particles with a given viscosity is assumed to have the same sticking probability. Model #2 combines impaction of (visco)elastic particles on a solid surface with particle capture by a viscous surface. A critical velocity is calculated by considering the particle size, velocity and angle of the impact along with physical properties of the particle in terms of Young's Modulus and of the surface in terms of viscosity.

Both models were used to describe deposit formation observed in entrained flow reactor (EFR) experiments with straw and wood as fuels. During the EFR experiments, the concentration of ash particles was measured by sampling of the flue gas. It was found that this concentration varied significantly and can be regarded as uncertain. This complicated the model validation. However, it was found that Model #1, using a reference viscosity, was not able to describe the observed influence of temperature on deposit build-up rates, but predicted a much stronger influence of this parameter. This conclusion can be drawn regardless of the uncertainties in the concentrations.

Model #2 was able to describe the influence of temperatures on deposit build-up rates observed in the EFR experiments. A parametric study and a sensitivity analysis was conducted, but the uncertainties in the ash concentration inhibited a complete model validation. Model #2 was also applied to full scale tests where deposit build-up was quantified on probes during suspension firing of straw and/or wood. Also in this scenario was Model #2 able to describe the tendencies observed in the tests, though overestimations of some of the observed rates occurred.

Based on these examinations, where a wide range of temperatures (700-1000 °C) and fuel mixes (straw/wood) has been applied, Model #2 can be regarded as a promising tool for description of deposit formation both in small scale and in full scale combustion. However, some physical parameters need further examinations.

Resumé (Danish Summary)

Denne ph.d. præsenterer øget viden om de aske transformationer og den belægningsdannelse, der forekommer i suspensionsfyring af biomasse. Som en del af studiet, er en model der beskriver disse processer blevet udviklet.

En række fuldskala målekampagner med belægningssonder er i første omgang blevet gennemgået og sammenlignet. Disse målekampagner er gennemført i ristefyrede og suspensionsfyrede kedler, hvor der er fyret med biomasse. Indflydelsen af driftsparametre på kemien i aske og belægninger, på hastigheder af belægningsdannelse og på afkast af belægninger er blevet undersøgt.

Brændingsteknologien og typen af biomasse påvirker den kemiske sammensætning af flyveaske og belægninger. I ristefyrede anlæg, er K, Cl og S beriget i flyveasken i forhold til i brændselsasken, mens flyveasken i suspensionsfyring har en sammensætning der ligner brændselsaskens. Den kemiske sammensætning af de dannede belægninger bestemmes af flyveaskens sammensætning og af røggastemperaturen; stigninger i den lokale røggas temperatur fører til højere indhold af Si og Ca og lavere indhold af Cl i belægningerne.

I ristefyrede og suspensionsfyrede kedler er nettohastigheden af belægningsdannelse på nogenlunde samme niveau; 0-100 $g/m^2/t$, mens askens tendens til belægningsdannelse (%) er en størrelsesorden større i ristefyrede kedler end i suspensionsfyrede kedler. Det blev observeret at hastigheden af belægningsdannelse stiger betydeligt ved røggastemperaturer tæt på smeltetemperaturerne af flyveasken. Således er hastigheden af belægningsdannelse også påvirket af brændslets aske sammensætning.

Afkast af belægninger sker ved ristefyring af halm via smeltedannelse når røggastemperaturer er over 900 °C. Ved lavere røggastemperatur, kan belægningerne fjernes ved sodblæsning. Når biomasse anvendes i suspensionsfyring sker der afkast af belægninger ved et afbræk nær probens overflade. Når der fyres med blandinger af halm og træ opnås der kun en ufuldstændig fjernelse. Dette er obeserveret ved røggas temperaturer på 600-1000 °C. Når der fyres med træpiller, der sker fuldstændig fjernelse ved høje røggastemperaturer (1300 °C). Der blev ikke observeret afkast af belægninger ved lave røggastemperaturer (<900 °C) ved suspension-fyring af træpiller. Her blev en stabil masse af belægninger på belægningssonden observet.

Ved ristefyring af halm og ved suspensionsfyring af halm/træ blandinger blev det observeret, at øget eksponeringstid og øget temperatur af belægningssondens

overflade fører til dannelse af belægninger, der er vanskelige at fjerne.

En model for dannelse af belægninger ved suspensionsfyring af biomasse er blevet udviklet. Modellen består af to dele; Først en model for askedannelse, efterfulgt af en model for askens belægningsdannelse.

I modellen for askedannelse, er der lavet antagelser omkring frigivelse af K, Cl og S, der er foreslået en simpel beskrivelse af gasfase reaktioner og en simpel kvantificering af aerosoldannelse. Den grove aske fraktion blev beskrevet med en ny model for partikelstørrelsesfordeling. Modellen ligner fragmenterings modeller foreslået for kul forbrænding, men tager fordampning af K, Cl og S i betragtning.

Modellen for belægningsdannelse inkluderer diffusion og kondensation af gasformige komponenter, termoforese af aerosoler, diffusion af små partikler, anslag af større partikler og reaktion i beskrivelsen af belægningsopbygning. To modeller, der adskiller sig i beskrivelsen af partiklernes vedhæftning er blevet beskrevet. Model #1 anvender en kritisk viskositet i beskrivelsen af vedhæftning og alle partikler med en given viskositet antages at have samme sandsynlighed for at danne belægning, når de rammer overfladen. Model #2 kombinerer anslag af (visko)elastiske partikler på en fast overflade med at partikler kan opfanges af en overflade med allerede dannet, blød belægning. En kritisk hastighed for anslaget beregnes ved partiklens størrelse, hastighed og anslagsvinkel sammen med fysiske egenskaber af partiklen i form af Young modulet og af overfladen i form af viskositet.

Begge modeller blev brugt til at beskrive belægningsdannelse observeret i Entrained Flow Reactor (EFR) eksperimenter med halm og træ som brændsel. Under EFR eksperimenterne blev koncentrationen af askepartikler målt ved prøvetagning af røggassen. Det blev konstateret, at denne koncentration varierede betydeligt, og målingerne kan betragtes som usikre. Dette komplicerede valideringen af modellen. Det blev imidlertid konstateret, at Model # 1 der anvender en reference viskositet, ikke var i stand til at beskrive den observerede indflydelse af røggastemperaturen, men forudsagde en meget stærkere indflydelse af denne parameter. Denne konklusion kan drages uanset usikkerheden i koncentrationerne.

Model #2 var i stand til at beskrive den indflydelse af røggastemperaturen der blev observeret i EFR forsøgene. Et parameter studie og en følsomhedsanalyse blev gennemført, men usikkerheden i askekoncentrationen forhindrer en komplet validering af modellen. Model # 2 blev også anvendt til at beskrive belægningsdannelse i fuld skala. Her blev der valideret imod forsøg, hvor var blevet målt belægningshastigheder på sonder under suspensionsfyring af halm og/eller træ i kraftværker. Også i dette scenario kunne model #2 beskrive de tendenser der var observeret i forsøgene, dog med overestimering af nogle af de observerede belægningshastigheder.

Baseret på disse undersøgelser, hvor der er anvendt en bred variation af temperaturer (700-1000 °C) og brændsels blandinger (halm/træ), kan Model # 2 betragtes som et lovende redskab til beskrivelse af belægningsdannelse, både i lille og i fuldskala forbrænding. Der er dog brug for yderligere undersøgelser af nogle fysiske parametre.

Contents

Chapter 1

Introduction

In order to reduce CO_2 emissions and the dependency on fossil fuels, Danish and international energy policy have increasingly supported the use of biomass for heat and power production during the last 20 years. In Denmark, complete substitution of coal with biomass is aimed at year 2050 [1].

Combustion is the main process in the thermochemical treatment of biomass for heat and power production in Denmark [2]. The first combined heat and power plants (CHP plants) using pure biomass were commissioned in Denmark in 1989 in Haslev and Rudkøbing. In these plants, straw was fired as cigar-firing or on a grate. Later, more grate-fired CHP plants for straw or wood combustion have been commissioned [3].

Combustion in grate-fired systems often have an electrical efficiency of 25-30%, whereas combustion in suspension-firing often have a higher electrical efficiency 46-48%. Thus, suspension-firing is an attractive option [4]. However, the implementation of biomass as fuel in pulverized fuel combustion plants is a challenging process, which require retrofitting of existing plants and/or commissioning of new plants [5]. One of the challenges arising from this implementation can be related to the ash formation from biomass being different than that of coal.

In 2001, a multi-fuel combustion unit was commissioned at the Danish Avedøre Power Plant. In this plant, wood pellets are combusted in suspension-firing, currently with coal ash addition to control deposit formation [6]. In 2003 and 2008, two combustion units at the Amager Power Plant in Denmark was retrofitted for substitution of coal with biomass. At Amager power station straw and/or wood pellets are used as fuel [5].

1.1 Deposit Formation

Ash from bituminous coal is often dominated by Si and Al, which form compounds with relatively high melting temperatures during combustion. Ash from biomass, such as straw and wood, has a high content of K as compared to coal ash. K-rich ash

often has a low melting temperature and thereby forms particles which may stick to heat transfer surfaces [7]. Utilization of biomass for power production thereby increases the rate of formation of deposits which are difficult to remove, especially in the boiler chamber and on superheater coil surfaces, compared to those formed during coal-firing [7].

The deposit behavior occurring in utility boilers is controlled by a number of consecutive steps [8];

1. Release of critical elements (K, Na, Cl, S etc.) from the fuel
2. Formation of gaseous species, aerosols and ash particles (collectively denoted as fly ash)
3. Transport and adhesion of fly ash (including gaseous species) to heat transfer surfaces
4. Deposit build-up and consolidation
5. Shedding of deposits

The occurrence of these steps are controlled by both fuel choice and type of utility boiler. Thus, experiences from a scenario with one fuel and/or boiler may not be easily transfered to or even relevant for another scenario.

1.1.1 Release of Elements and Formation of Fly Ash

The release of critical elements and formation of fly ash have been studied extensively for grate-firing conditions and is quite well understood [9–13]. In suspension-firing, the conditions in the combustion zones differ markedly from those in the combustion zone of grate-fired boilers. This leads to altered conditions for the ash formation, and experience from grate-firing cannot always be applied to suspension-firing or other combustion technologies. Only a few studies on the ash transformation processes have been conducted at lab-scale [14–16] and pilot scale [17] for conditions resembling suspension-firing. Description of the ash characteristics is important for the prediction of deposit formation and subsequently for deposit shedding.

1.1.2 Transport and Adhesion of Fly Ash

Deposits are formed in biomass-fired boilers by at least three different mechanisms, which apply to different parts of the fly ash [18]. Inertial impaction apply to large fly ash particles (>10 μm). The impact velocity and angle, along with the stickiness of the ash particles, determines if the particles are deposited on the heat transfer surface upon impaction [18, 19]. Thermophoresis, where a temperature gradient is the driving force for the transport of the particles toward the cold heat transfer surface, apply to aerosol particles (< 1 μm). Condensation on heat transfer surfaces apply

to gas phase species such as KCl and K_2SO_4. In this case, a concentration gradient is the driving force for the diffusion of gaseous species to the surface, where they deposit by condensation [18].

As stated by Baxter [18], the mechanisms of deposit formation are universal and apply to all types of fuels and combustion systems. However, due to different compositions and morphologies of ashes, the relative impact of the mechanisms varies among the different scenarios. Furthermore, the models also differs in the prediction of the stickiness of the impacting ash particles, as this parameter is sensitive to material and temperature. Thus, great differences are observed for deposition of e.g. droplets of molten ash and dry, solid ash particles.

Numerous models have been developed for coal ash deposition, both considering slagging deposits in the radiative zone [20, 21] of a boiler and considering fouling in the convective pass [22]. Coal models developed before 1997 has been reviewed by Wang and Harb [23].

For biomass, deposit formation models have been developed for deposit formation in grate-fired boilers [19, 24–27] and CFB boilers [28, 29]. Deposit formation during suspension-firing with biomass present has to the authors knowledge only been modeled for co-combustion of biomass and coal by e.g. Plaza et al. [30], Garba et al. [31] and Losurdo et al. [32, 33]. No models for pure biomass combustion in suspension has been proposed, at this time. However, various work has been conducted with the aim of describing how the type of biomass as fuel and possibly use of additives influence deposition rates in laboratory or pilot scale experiments, mainly resembling suspension-firing [17, 34–43].

Deposit formation models are found in three levels according to their complexity; (*i*) empirical indices models, (*ii*) mechanistic models and (*iii*) complicated CFD (Computational Fluid Dynamics) models [19]. Most models proposed during the past decade(s) are primarily CFD models. These have been reviewed by Weber et al. [44] and are concluded to be indicative, at best, due to tuning of key parameters to obtain a model fit [44]. In mechanistic models, calculations of the complicated combustion process and fluid dynamics are simplified. These models have been used for assessing the ash deposition tendency and prediction of ash behavior. Thus, the mechanistic models can provide a basement for developing comprehensive models that can simulate ash deposition and the overall impact of this in a boiler [19]. Mechanistic models of deposit formation are mainly found in relatively old models of coal ash deposition (e.g by Baxter [18]). A mechanistic model has also been developed for grate-firing of straw by Zhou et al. [19].

The models mentioned above has primarily been applied to a (few) single scenario(s) and have thus not been validated against a broader range of e.g. temperatures and fuel compositions.

1.1.3 Shedding of Deposits

The amount of deposits present on boiler surfaces is influenced by both deposit formation and deposit removal (shedding) processes. Shedding of deposits depends on deposit characteristics and may be caused by natural boiler events, such as tube fluctuations, or artificially by e.g. soot blowing in the boiler chamber. Soot blowers operate by injecting jets of steam, water or high-pressure air into the boiler, thereby inducing thermal and mechanical stresses.

Various types of shedding mechanisms have been observed and are described by Zbogar et al. [45]. In Figure 1.1 different shedding mechanisms are shown. Erosion,

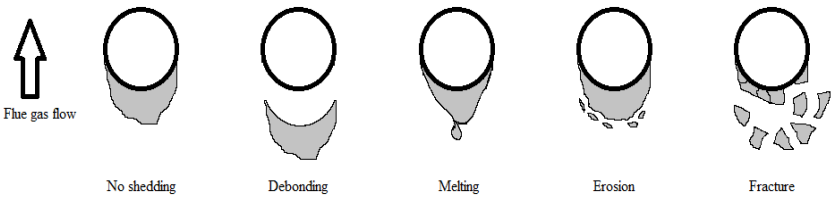

Figure 1.1: Illustration of shedding mechanisms.

debonding and melting can be termed natural shedding mechanisms, while artificial shedding induced by soot blowing can cause deposit fracture and debonding.

Shedding is influenced by the strength development of the deposits. The strength can mainly be achieved by either solidification of molten or partially molten material or by sintering (fusion) of solid particles [45]. These processes depend on local temperatures, time and the physical and chemical structure of the deposits.

The strength development and shedding of deposits have been examined to some extent for deposits formed during coal-firing [46] and for kraft recovery boilers [47]. Only limited studies have been conducted in biomass-fired boilers [45, 48].

1.2 Project Objectives

This PhD is aimed at improve the understanding of the deposit formation process occurring in suspension-firing of biomass. Furthermore, the aim to develop a mechanistic model for deposit build-up on a cylinder during in biomass suspension-firing. The subjects specifically investigated cover:

- Provide insight to the deposit formation occurring in biomass suspension-firing in terms of (*i*) ash formation, (*ii*) deposit formation and (*iii*) shedding.

- Examine and highlight similarities and differences to relatively well-known combustion systems; suspension-firing of coal and grate-firing of biomass (primarily straw).

- Formulate a model describing the ash formation in biomass suspension-firing.
- Formulate a mechanistic model for deposit formation during suspension-firing of biomass and validate the model in both small scale (EFR) and full scale combustion.

The experimental work used as basis of this work has been conducted previously within the CHEC research group at the Department of Chemical and Biochemical Engineering at Technical University of Denmark (DTU). The experiments include published [16, 39, 49] and unpublished [37, 50] entrained flow reactor (EFR) experiments and experiments conducted in full scale boilers, both grate [51–58] and suspension-fired [5, 6, 59–63].

1.2.1 Thesis Structure

Besides this introduction, the thesis consist of the following chapters;

Chapter 2: Ash Formation in Biomass Suspension-Firing

Chapter 2 provides a comparison of the major combustion characteristics in coal and biomass combustion. Furthermore a literature review on the combustion of biomass particles and ash formation processes is conducted.

Chapter 3: Deposit Probe Measurements in Full Scale Boilers

A review and comparison of the full scale experiments conducted with deposit probes in full scale grate- and suspension-fired boilers during combustion of biomass is presented. Fly ash and deposit chemistry, deposit formation rates and observations on shedding are included.

Chapter 4: Model for Fly Ash Formation

A model describing the formation of ash in suspension-firing of biomass. The model contains two parts; (*i*) description of the release of gases, the gas phase reactions and the aerosol formation (*ii*) description of the coarse ash particle size distribution and bulk chemistry.

Chapter 5: Deposit Build-up

This chapter describes a mechanistic model relevant for combustion of straw and/or wood in suspension. The description of sticking probability has been given special attention, and two model proposals are suggested. Also, models for description of the physical properties of straw and wood ashes are suggested.

Chapter 6: Model Evaluation in Small Scale Combustion

In chapter 6, the models formulated in chapters 4 and 5 are validated against deposit formation observed in an EFR reactor in previously conducted experiments. The two models for description of sticking probability are evaluated and the best model is chosen. A parametric study and a sensitivity analysis of the model is provided.

Chapter 7: Model Evaluation with Full Scale Experiments

The model is used to describe deposit formation rates in a full scale suspension boiler. The results are compared to rates measured during full scale measuring campaigns with deposit probes.

Chapter 8: Conclusions

Chapter 9: Suggestions for Further Work

Chapter 2

Ash Formation in Biomass Suspension Firing

The main focus of this literature survey is to gain an understanding of the formation of fly ash in suspension-firing of biomass as this serve as precursor for deposit formation. Ash and deposit formation during suspension-firing of coal and to some extent also during grate-firing of biomass are reasonably well understood processes [8, 19, 24]. Initially, the major characteristics of biomass combustion in suspension is compared to coal combustion in suspension. Subsequently, the characteristics of biomass in combustion is examined more detailed, where experiences from grate-firing are included for the purpose of comparison. Finally, characteristics of aerosols and fly ash particles observed in biomass suspension-firing are reviewed.

2.1 Coal vs. Biomass

When coal and biomass are utilized as fuels, there are several differences which are important for the characteristics of the ash and thus the deposits formed. First of all, there are differences in the composition of the fuels. The differences in the proximate analysis of a bituminous coal and two biofuels used in suspension-firing are shown in Table 2.1.

It is seen that the biomasses contain considerably more volatiles than coal, whereas the coal exceeds the biomasses in ash-content and carbon content. The large volatile content of biomass will naturally influence the behavior of the fuel particles during devolatilization, as a large fraction of the particles is released from biomass. Furthermore, the bonding structure within the fuel also influences the devolatilization behavior. Basically, biomasses are composite materials constructed of oxygen-containing organic polymers [65]. The major organic components are thus cellulose, hemicellulose and lignin [65–67]. Biomass is thereby primarily constructed with aliphatic bonds [68] along with ether and acetate bonding of units [65]. In

Table 2.1: Analysis of coal, straw pellets and wood pellets

	Bituminous coal [64]	Straw pellets [63]	Wood pellets [63]
Moisture (wt% a.r.)	5.03	7.86	6.83
Volatile content (wt%, dry)	36.71	80.91	85.24
Ash content (wt%, dry)	10.13	6.54	0.86
C (wt%, daf)	80.70	54.06	56.02
H (wt%, daf)	5.41	6.20	6.20
N (wt%, daf)	1.69	0.63	0.74
S (wt%, daf)	0.73	0.16	0.04
O (by diff, wt% daf)	11.46	38.64	37.00

coal, the major organic structures are categorized as aromatic clusters, side chains, aliphatic bridges and loops [69]. These differences in the types of bonding are responsible for the devolatilization to occur at lower temperatures for biomass as compared to coal, since the aliphatic bonds are weaker than the aromatic bonds [68].

Examples of weight loss vs. temperature curves are seen in Figure 2.1a. It is

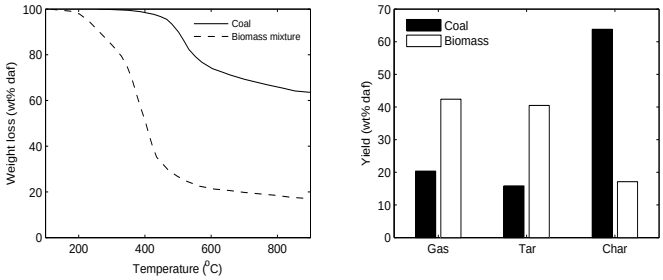

Figure 2.1: Results from pyrolysis at 30 K/min to 900 °C. The coal is a blend of HV bituminous coals, the biomass is a mix of wood, paper, sawdust and sewage sludge [70]

seen that devolatilization of biomass occurs in the temperature range 200-500 °C [71], whereas the devolatilization of coal is just initiated when the temperature reaches 450 °C. It is furthermore seen in Figure 2.1b that the yield of char is considerably higher for coal than for biomass, as expected. The differences in the bonding structure and in the volatile content will thus lead to differences in the behavior during pyrolysis.

Biomass particles employed in pulverized fuel combustion are often larger than the pulverized coal particles [72]. This is due to the fact that biomass is difficult and expensive to grind, due to a high content of fibres [73] and because it is possible to handle larger biomass particles in existing furnaces with a given residence time, due

to the high volatile content of these [74]. In pulverized coal combustion 70-75% of the particles are smaller than 75 μm [75]. In comparison, biomass particles used in suspension-firing are up to 2 mm in diameter [63, 76]. Additionally, biomass particles are irregularly shaped compared to the coal used in suspension-fired plants. Biomass often have aspect ratios (height:width) in the range 2-15 and the assumption of isothermal spherical particles, often used in modeling of coal combustion, may thus not be valid [72].

Char from biomass is chemically similar to char from coal in the sense that they both consists mainly of C and contain only minor amounts of heteroatoms (O, H, S and N) [77]. However, during devolatilization coal softens and form spherical particles, whereas biomass particles may in some cases retain their initial form which is irregular in shape [78, 79]. There are thus large physical differences such as shape, size and porosity which result in different surface area, density and thermal conductivity [77]. The result of these differences is that the chars from wood generally are found to be more reactive with respect to char oxidation, than chars from coal. This is mainly due to a less ordered carbon structure [78, 79] which is caused by a higher content of oxygen in the chars and by the higher content of volatiles in the original fuel [79].

With respect to ash formation, there are significant differences in the nature of coal and biomass ashes and thus also in the mechanism of ash formation [67, 80]. The differences origin in the different combustion behavior and in the content and speciation of inorganic elements of the fuels. The contents of inorganic elements of coal, wood and straw are seen in Figure 2.2. It is seen that the ash forming matter of coal

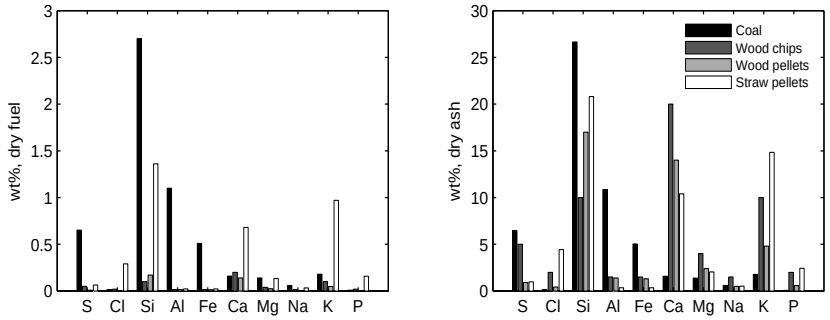

Figure 2.2: Content of inorganic elements in four selected fuels. Left figure; contents as wt% of dry fuel, Right figure; contents as wt% of ash fraction. The coal is a bituminous coal (10.1 wt% ash) [64], the biomasses are typical wood chips (1 wt% ash) [81] along with wood pellets (1 wt% ash) [59] and straw pellets (6.5 wt% ash) [63] used in suspension-firing.

is mainly silicon and aluminum along with sulfur and iron. This inorganic matter is either found as discrete mineral grains such as quartz, clay (kaolinite), carbonates or

sulfides (pyrite) or found as organically bound inorganic matter. The mineral grains may be included (inside coal matrix) or excluded mineral matter [7, 67, 82].

In coal combustion the ash formation occurs mainly through fragmentation and coalescence [82–84]. Ash formation from included minerals occurs through coalescence and agglomeration during char burnout, when the mineral grains become closer as the carbon matrix is oxidized [67, 82, 85]. The formation of ash particles by coalescence may be limited by fragmentation of the burning char particle [83] and the competition between these mechanisms thus determines the particle size distribution of the formed ash. The occurrence of fragmentation is found to be dependent on coal rank [80, 85, 86] and on macroporosity of the fuel particles [83, 84]. The formation of ash particles from excluded minerals may occur due to a rapid heating causing pressure to increase inside the particle which leads to fragmentation [67, 82]. The occurrence of fragmentation however depends on the thermal behavior of the individual mineral grains since e.g. silica and pyrite particles are found to behave differently [87, 88]. The ash formation from included and excluded minerals results in ash particles with mass mean diameters in the range 1-30 μm and account for most of the ash produced [89], often with a bimodal size distribution [84].

In addition to ash formation from included and excluded minerals, evaporated elements also contribute to the ash formation during pulverized coal combustion. Volatile elements like Na, As and Sb may evaporate from the coal while refractory oxides (CaO, MgO, SiO_2 and Fe_2O_3) may be reduced to volatile suboxides. These two groups of vapors may contribute to the formation of a fume of submicron particles as indicated in Figure 2.3A. The submicron fraction of the fly ash formed may only account for 1 wt% of the ash formed, but accounts for a large fraction of the surface area [89]. In Figure 2.3B a tri-modal particle size distribution of the ash formed during pulverized coal combustion. The particulate matter is usually categorized in three groups; PM10, PM2.5 and PM1 (particulate matter less than 10, 2.5 and 1 μm, respectively) [90].

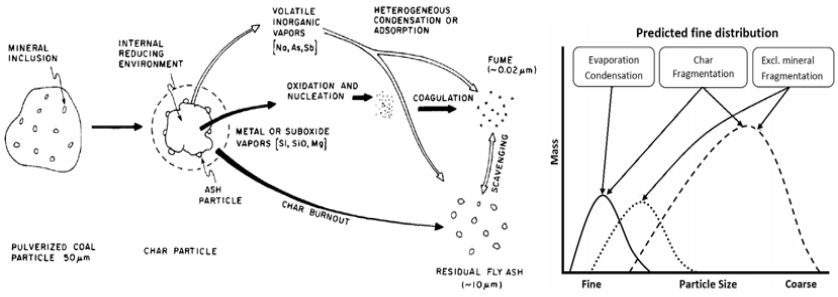

Figure 2.3: A: Schematic diagram of ash formation during pulverized coal combustion [89]. B: Predicted size distribution of ash from ash formation mechanisms occurring during coal combustion. Adapted from [90]

The inorganic compositions of three biomasses are also seen in Figure 2.2. As compared to coal, all three biomasses has high contents of alkali or alkaline earth metals and Cl and lower contents of Si, Al, S and Fe. The inorganic matter in biomass is classified in three groups: (*i*) ionically bound (as salts), (*ii*) organically bound to the carbonaceous material or (*iii*) included minerals in the fuel structure. Furthermore, minerals from e.g. soil or clay may be present in connection with the biomass and contribute to the ash. The ash formation mechanisms occurring during biomass combustion are illustrated in Figure 2.4.

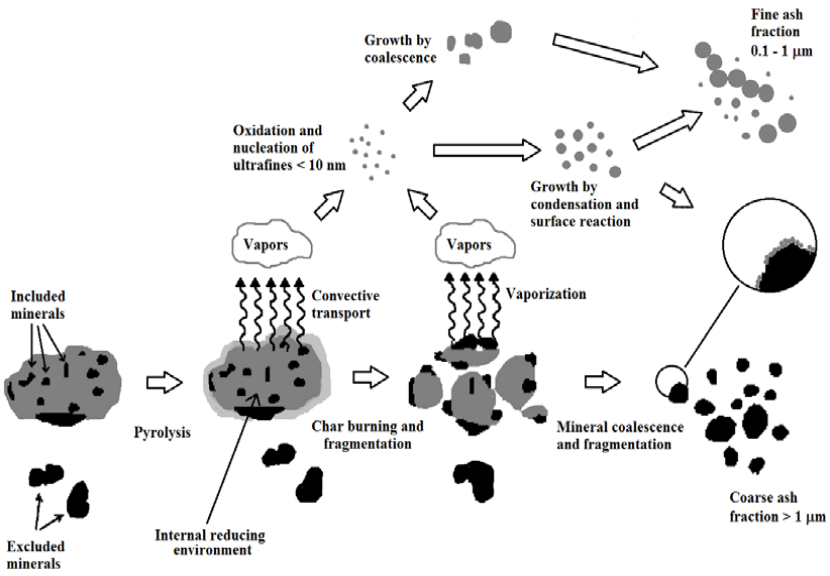

Figure 2.4: Ash formation mechanism for biomass combustion. Adapted from refs [74, 91]

As indicated in Figure 2.4, the ash formation in biomass combustion occurs via two routes, resulting in a bimodal size distribution of the ash. One route includes vaporization of volatile inorganic elements (mainly K, Cl and S) followed by condensation and agglomeration/coagulation [67]. This route leads to a concentration of sub micron particles which is found to be greater than observed for coal [74]. The fine sub micron particles are usually found to have a mean average size in the range 0.2-0.7 μm and consist almost completely of alkali, Cl, S and P with the dominant species being KCl and K_2SO_4, when firing wood pellets or straw pellets [74, 92, 93]. The other route includes mineral coalescence and fragmentation of the inorganic elements, retained in the particles and leads to a coarse ash fraction of super micron particles [92]. As a consequence of these ash formation mechanisms, the ash formation likely to occur during biomass combustion cannot be estimated by just by

definition of included or excluded minerals. The composition of the inorganic matter also have a significant role [67].

With respect to chemistry, the main differences in coal and biomass ashes are that coal ash is mainly alumino-silicates with clay and quartz, whereas biomass ash is mainly Ca- and Si- rich particles and inorganic salts of phosphates, sulfates and chlorides [67]. The components K and Na found in biomass may be part of unfavorable reactions with sulfates and chlorides forming ash prone to fouling and slagging [67]. These alkali species often found in relatively high concentrations in biomass combustion have low melting temperatures which make them sticky. Once the particles or gas phase components are condensed on a surface, they enhance further deposition due to their stickiness [48, 74].

Based on the combustion characteristics briefly reviewed in this section it can be concluded that there is significant differences in the combustion behavior and ash formation mechanism of a bituminous coal and biomasses. Although the steps in combustion are similar the differences in particle characteristics alter the overall combustion behavior and ash formation. This will naturally have implications for the deposit formation also.

2.2 Biomass Combustion Characteristics

In the following the combustion characteristics of biomass will be reviewed with special focus on the particle alterations observed for small particles in conditions similar to suspension-firing conditions. The alterations of the particles is in focus as these serve as precursors for ash formation and thus influence the characteristics of the ash. A significant amount of research has been conducted with respect to ash and deposit formation from biomass firing on a grate, mainly with respect to straw as fuel [8, 19, 51, 53–58, 94] but also some with woody biomass [71, 95, 96]. These are included for comparison.

On a grate, relatively large particles of biomass (5-100 mm or larger [97]) are combusted by leading primary air through the bed from below. Drying, gasification and char combustion thus takes place on the grate and the volatiles burn after the injection of secondary air in the freeboard of the furnace. The maximum fuel bed temperature during combustion of biomass is 1000-1200 °C and the residence time on the grate is in the order of several minutes. Comparatively, in pulverized biofuel combustion the particles are small (< 2 mm) and the residence time is in the order of seconds. The flame temperatures in the furnace is commonly 1500-1700 °C (peak temperature) [76]. This implies that the fuel particles in grate combustion are heated slowly to a low temperature as compared to pulverized fuel combustion.

2.2.1 Biomass as Fuel

The major organic components of biomass are cellulose, hemicellulose and lignin [65–67]. Besides these are some extraneous materials such as extractive organic matter and inorganic minerals. The contents of cellulose, hemicellulose and lignin influence the characteristics of the biomass combustion behavior. During thermal treatment, the hemicellulose is degraded in a lower temperature range (200-260 °C) than cellulose (240-350 °C) and lignin (280-500 °C). The products of the three compounds furthermore differs as the hemicellulose produces more volatiles than cellulose and lignin. The lignin produces the most char of the three compounds [65].

The biomasses typically used in combustion can be divided into 4 categories [66, 67, 74]. The first three categories listed mainly differs in their structural composition of cellulose, hemicellulose and lignin and in their content of inorganic elements [66].

1. Wood and woody materials
2. Herbaceous and other annual growth materials (straws, grasses, leaves)
3. Agricultural byproducts and residues (shells, hulls, pits, animal manure)
4. Refuse derived fuels (RDF) and waste

Woods are further divided in two classes; hardwood and softwood. The term 'hardwood' is used for the angiospermae trees, which is usually trees with broad leaves, whereas the term 'softwood' is used for gymnospermae trees with needle like leaves [65, 71]. Compositions of biomass with respect to cellulose, hemicellulose and lignin are listed in Table 2.2.

Table 2.2: Biomass compositions (wt% dry basis) with respect to the major organic components.

		Cellulose	Hemicellulose	Lignin	Reference
Hardwoods	Beech	48	28*	24	[98]
	Maple	40	23	22	[99]
	Oak	35	40*	25	[98]
Softwood	Pine	50	27*	23	[98]
Straws	Barley	46	23	15	[81]
	Wheat	45	24	16	[81]
	Rye	51	21	17	[81]
Various	Sugarcane Bagasse	36	17	17	[99]
	Olive husk	22	33*	45	[98]

* Extractive and ash contents are included as hemicellulose

2.2.2 Char Yield

The release of volatiles from biomass is found to be dependent on heating rate [79, 100–103]. This is seen in Figure 2.5 where the char yield obtained from pyrolysis of pine and beech particles by slow and fast heating rate is shown as function of pyrolysis temperature [79].

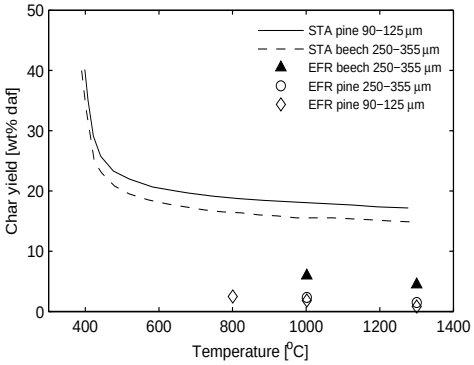

Figure 2.5: Wood char yield as function of pyrolysis temperature. Heating rate STA: 20 °C/min, Heating rate EFR: 10^4-10^5 °C/s. Adapted from Dall'Ora et al. [79]

It is seen that the char yields from the experiments in Simultaneous Thermal and Gravimetric Analyzer (STA) are significantly higher than the yield from the experiments in the Entrained Flow Reactor (EFR) and more volatiles has thus been released in the EFR. This is in agreement with results obtained by Zanzi et al. [100] who found differences in char yield as a result of differences in heating rate for birch, white quebracho, straw pellets and bagasse [100]. Jimenés et al. [104] has examined the volatile yield from fast devolatilization of thistle particles in an EFR, and found that the yield is independent of final temperature within the range 800-1175 °C. It is considered by Zanzi et al. [100] that in fast pyrolysis, the char yield remains constant above a certain temperature.

Zanzi et al. [100] explains the difference in yields by the following considerations; In slow pyrolysis in a TGA, the volatiles formed leave the particles slowly and secondary reactions (cross linking) forming char are thus possible. In fast pyrolysis, the volatiles are rapidly removed from the char and secondary reactions are thereby limited [100].

The differences in char yield as a result of heating rate can also be explained by the degradation of cellulose. At temperatures lower than 300 °C, the cellulose is dehydrated and the stable anhydride forms more char than volatiles. Contrary, at higher temperatures (> 300 °C), the cellulose is depolymerized forming volatiles. A long residence time at low temperatures will thus lower the volatile yield [100, 103].

Dall'Ora et al. [79] explain the difference in the results from pine and beech

(Figure 2.5) by their difference in inorganic contents. Ash contents are thought to influence the release of volatiles [79, 100, 105, 106]. Especially, the contents of K and Ca are considered to catalyze cross linking. The difference in the results from pine and beech, with respect to char yield, can thus be explained by the fact that beech contain more K and Ca than pine, and cross linking may thus be catalyzed by these elements [79].

Zanzi et al. [100] has examined the char yield of four biomasses; birch, white quebracho (South American hardwood), straw pellets and bagasse. For the woods (birch and white quebracho) the difference observed in char yield is ascribed to differences in the chemical composition, as the ash contents are similar. Char yield is said to be increased with high carbon content, low oxygen content, low H/C ratio, and high contents of lignin. As the chemical composition with respect to these contents are similar for the birch and straw used in the experiments, the high char yield obtained from straw pyrolysis is explained by the higher ash content [100]. It is generally found that straw and other agricultural residues give higher yields of char during pyrolysis [107].

2.2.3 Morphological Changes

It is claimed by some researchers that biomass particles retain their shape during pyrolysis [78, 105, 106]. This is found to be true only for some operational conditions and fuel types. In Figure 2.6 the morphological changes of softwood particles pyrolysed by slow and fast heating rate can be compared.

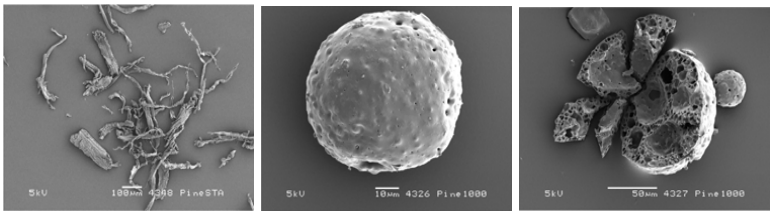

(a) Particles from STA (b) Whole particle from EFR (c) Broken particle from EFR

Figure 2.6: SEM pictures of 90-125 μm pine particles after pyrolysis in N_2 in either a STA (10 K/min to 1100°C, 30 min holding time) or in an EFR (Rapid heating to 1000°C). From Dall'Ora et al. [79]

It is seen in Figure 2.6a that the char particles obtained at a low heating rate are needle like and the fibrous structure of the wood is unaltered [79]. It is generally found that during pyrolysis at low heating rates, the volatile products are released through the natural porosity of the particle and the changes in morphology are limited [107, 108]. Contrary, is is seen in Figure 2.6b and c that the structure of the pine particle is largely altered during fast pyrolysis in the EFR. The particles are

spherical, porous, with a smooth surface and large internal cavities [79] and must have gone through a liquid phase. Melting of particles and loss of original structure in similar conditions has also been observed by other authors [107, 109, 110]. It is concluded that as the volatiles are released fast an internal overpressure is produced and small pores coalescence. Large internal cavities and thereby a more open structure is obtained [110]. The difference in morphology of chars prepared in slow and fast heating rates is thus found in the micropore structure of chars from slow heating rates and the macropore structure in chars from fast heating rates [107].

The melting behavior observed during fast pyrolysis varies with different types of biomass [79, 101, 109]. Dall'Ora et al. [79] has also conducted experiments with beech (hardwood) particles, which does not show the same degree of melting or softening as the softwood pine particles (Figure 2.6) pyrolysed in the same conditions. For Beech wood pyrolysed in the EFR, the internal structure of the char particles is somewhat similar to that of the original beech wood, whereas the surface is smooth and thus show some signs of melting. Cetin et al. [109] have tested three types of biomass and find that pine (softwood) is more prone to melting than Eucalyptus (hardwood), which again melts more readily than sugar cane bagasse (agricultural by-product) [109].

Again, the difference in results from different fuels can to some extent be explained by the catalytic effect of K and Ca enhancing cross linking. With increased cross linking during devolatilization, the melting behavior is limited [79]. The catalytic effects of potassium in the thermal degradation of wood has been examined by Jones et al. [105] and Nowakowski et al. [106] by comparison of raw willow particles (hardwood) with willow particles which where either impregnated with potassium or demineralized. In particles where K is present the particles retain their shape until the end of char oxidation where they collapse and shrink. The demineralized particles were found to melt and the size was decreased already during devolatilization [105].

The final temperature may also influence the degree of melting. For the pine particles pyrolysed by Dall'Ora et al. [79], there was not observed any difference in morphology of the particle from three temperatures (800, 1000 and 1300 °C). There was however observed an effect of temperature on morphology for beech wood particles. The alterations of the wood particles are greater at the high pyrolysis temperature (1300 °C) than at the low temperature (1000 °C). The degree of shrinkage for this type of wood follows the degree of alterations.

Finally, particle size may also influence the morphological changes. Small particles quickly reach the gas temperature, whereas larger particles are heated more slowly and large internal temperature gradients in the particle may occur [111]. This naturally influences the degree of alterations.

2.2.4 Char Combustion

The char reactivity is found to be strongly dependent on the heating conditions applied during devolatilization. Chars prepared with a high heating rate generally has a higher reactivity than the chars prepared with a slow heating rate [79, 100, 103, 107, 110].

The difference in reactivities is explained by the major transformations of the particle occurring during fast pyrolysis. These transformations affect both the mineral and the carbon structure of the chars. The chars from fast pyrolysis have less time to attain ordered structure and this results in more active sites for oxidation and thereby a higher reactivity than chars from slow pyrolysis [68, 79, 107, 110].

The final temperature also influences the reactivity of the char as a high final temperature may reduce the char reactivity. The effect of a high final temperature is also structural ordering and thermal deactivation (thermal annealing) of the char thus occurs [79, 107, 110].

Inorganic matter, especially K and Na, may also act as catalyst in char oxidation and thus influence char reactivity [105–107]. Experiments with leached biomasses lead to the the conclusion that the presence of inorganic matter is more important in determining char reactivity than the surface area of the char. Leached biomass chars have higher surface areas, but substantially reduced reactivities [112].

It is discussed by Di Blasi [107] that variations in reactivities among biomass samples is a consequence of the difference in the inorganic matter naturally present in the biomass, rather than differences in type of biomass.

2.2.5 Combustion Characteristics

It is seen in this chapter that the combustion behavior of biomass varies greatly. The characteristics of char formed depend strongly on the pyrolysis conditions in which the char is formed [79, 101, 107, 109, 110]. The morphology and amount of char is determined by the parent fuel, the rate of heating and in some cases also the final temperature. The pyrolysis condition furthermore influence the char particle size and the reactivity of the char.

During char combustion, further alterations of the particles naturally occur. For coal combustion, the particle alterations leading from char particles to ash are reasonably well understood and models are available for prediction of the transformations [8, 67]. For biomass, the understanding of the ash forming process is limited [8]. Some observations on the ash morphology [39], the particle size distribution [17] and the ash chemistry [14, 17, 39, 62] are however available. These contribute to gaining an insight to the possible ash formation mechanisms and will be reviewed in the following sections.

2.3 Release of Ash Forming Elements

The ash formed during combustion is composed of the inorganic elements originally present in the fuel. In order to describe the ash formation during biomass combustion, it is important to understand how the distribution of these elements among the gas phase, aerosols (fine particulate matter) and coarse ash particles is. In this section it is reviewed in which form the inorganic elements are found in the biomass fuel matrix, and also how the elements are either released to the gas phase or retained in the particles during suspension-firing of biomass.

The amount and composition of the inorganic contents of biomass may vary significantly, even for the same type of fuel. In Figure 2.7, examples of inorganic contents of four biomasses are shown [14].

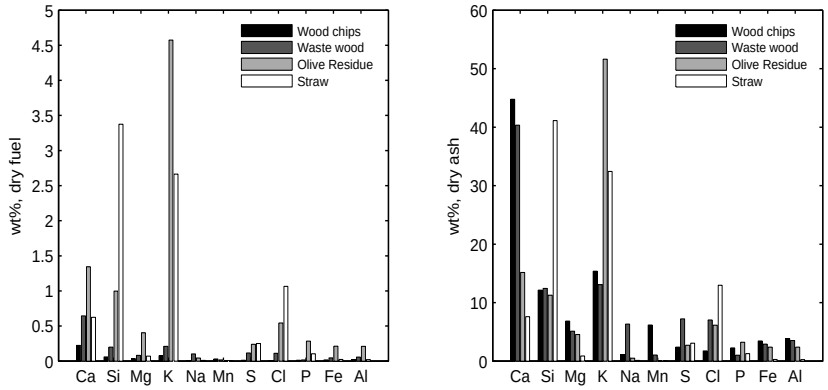

Figure 2.7: Contents of inorganic elements in four biomasses. From Korbee et al. [14]

There is quite a difference in the contents of inorganic elements of woody biomasses and straw or olive residue, as seen in Figure 2.7. The woods only contain 0.5-1.6 wt% ash (dry base) and the contents of inorganic elements are generally lower than those of straw or olive residue. The main ash constituents of the woods are Ca, Si and K. The olive residue and straw have comparable amounts of ash, approximately 8 wt% (d.b.). The main ash element for olive residue is K followed by Ca and Si. The straw contains maily Si, K and Cl.

It is generally found that both the total amount of ash, but also the chemical composition of the ash are important factors in ash and deposit formation [14, 113]

2.3.1 Ash Speciation in Biomass

The chemical forms of ash forming elements in biomass, determines to a large extent the ash formation of the biomass during combustion. The classification of the in-

organic elements has been studied thoroughly [91, 113, 114]. The studies are based on chemical fractionation (CF) analysis in which a biomass sample is leached subsequently in water, ammonium acetate (buffer solution) and HCl, as illustrated in Figure 2.8. The amount of inorganic elements leached in each solution or retained in the fuel is determined between each step [91, 113].

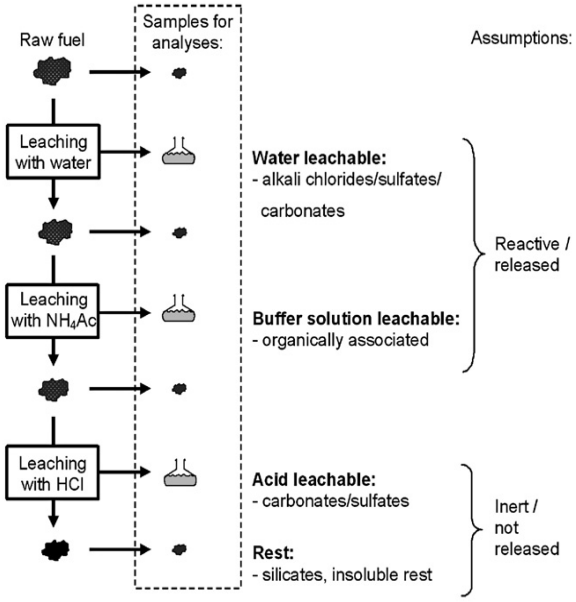

Figure 2.8: Schematic illustration of the CF analysis procedure. From Frandsen et al. [115]

Based on the CF analysis the inorganic matter in biomass can be classified into three groups: (i) salts which are ionically bound and can be leached in water, typically alkali chlorides, sulfates and carbonates, (ii) elements which are organically bound to the carbonaceous material and can be leached by ion exchange in the buffer solution, typically Ca and Mg along with some Na and K or (iii) included minerals in the fuel structure which are acid soluble, typically carbonates or sulfates of Ca and Mg, or insoluble, typically Si and Al [67, 91, 113].

In Figure 2.9 examples of results from CF analysis of wood [114] and straw [113] are seen. It should be noted that the results are obtained at different laboratories and differences in handling may cause differences in results, even for the same fuel [113]. The CF analysis has been supplemented with ion chromatography and methylene blue sorption analysis [114] and SEM/EDX [91] to gain further insight to the chemical form of the inorganic elements in the fuels.

It is seen in Figure 2.9, that the refractory materials, Si and Al are to a large

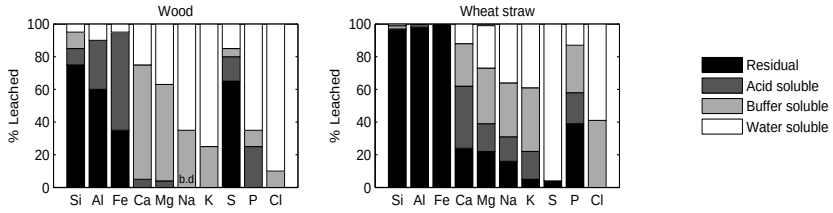

Figure 2.9: Examples of results of CF analysis for woods [114] and straw [113]. For the Na in wood, the amount leached in buffer or acid solution was below detection limits.

extent retained in the fuel or only soluble in the acid solution. These elements occur in the plants primarily as oxides. Si is an important part of especially straws, where is important for the strength of the straw [113]. In woods, Si is found to be present as included or possibly excluded minerals [114].

The alkaline earth metals, Ca and Mg, are mainly leached by buffer solution or acid. The elements leached in buffer (or water) are found as organically associated ions in the biomass. The acid soluble or retained Ca and Mg are found as discrete minerals; calcite or calcium oxalate [15, 114].

K and Na are mainly leached in the water or buffer solution and are found in the biomass as either salts or organically associated ions [114]. In the analysis of the straw seen in Figure 2.9B, some acid soluble or residual K and Na are found. It is discussed by Baxter et al. [113] that these contents may origin from soil contamination as Illite, the most prevalent form of clay, contains K and Na.

Cl is in the CF analyses leached in the water or buffer solution and is determined to be found as salts in biomasses [114].

No clear trend on leaching of S can be observed in Figure 2.9. In the work by Baxter et al. [113] 15 straws, shells and pits were examined by CF analysis. No clear trend of the behavior of S from biomasses in CF analysis can be detected from these results, even for the same type of biomass [113]. Werkelin et al. [114] found that the majority of the S in wood ($\approx 75\%$) is associated with the organic matrix by covalent bonds, while the remaining S is found as salts.

The release of inorganic elements during combustion is influenced by the origin of the element in the fuel, as also indicated in Figure 2.8. Thus, water and buffer soluble elements are expected to be reactive and possibly released during combustion. This implies that Cl, Na and K are expected to be very susceptible for vaporization, while Ca and Mg are less readily released. Si and Al are expected to remain in the fuel particle. S is an exception to this rule as S is expected to be almost quantitatively oxidized during combustion [113].

In the following sections, experimental release studies will be reviewed to see if these expectations hold.

2.3.2 Release Studies

The release of ash forming elements has been studied under conditions resembling those of grate-firing [9–11] and is reasonably well characterized [8]. However, for suspension-firing conditions the heating rate, the particle density, final temperature and the residence time differs greatly from that of grate-firing. This was found to have implications for the volatile release and char oxidation and may thus also influence the release of the inorganic elements and their subsequent interactions. The release of inorganic elements has been studied under conditions resembling those of suspension-firing in a Lab-scale Combustion Simulator (LCS) by Shah and co-workers [14, 15, 116] and in an entrained flow reactor (EFR) by Damoe et al. [16].

In the experiments by Shah and co-workers [14, 15, 116], biomass particles are combusted in a drop tube furnace at approximately 1700 °C. The release is quantified by sampling particles with an oil-cooled quenched gas/particle probe and subsequently dividing the particles into eleven size fractions (< 0.3 μm - > 50 μm) by a cascade impactor. The samples are analyzed, and the release of inorganic matter is determined as the difference between the amount of element in the fuel feed and in the recovered ash particles. In this determination, the particle fraction with diameters <1 μm (aerosols) is mathematically treated as released [14, 15, 116].

In the experiments by Damoe et al. [16], pulverized wood and straw pellets were combusted at 1200 °C or 1400 °C in an entrained flow reactor. Gas/particle samples was collected at various residence times [0.25-2 s] using a cooled and quenched gas/particle sampling probe. The gas and particles was separated by passing the sample through a cyclone with a cut-off diameter $\approx$ 1.5 μm and through a 0.1 μm PE filter. When quantifying the release of elements, it is assumed that particles in the PE filter (< 1.5 μm) has been released/volatilized during combustion. In addition to this, water soluble K, Cl and S in the cyclone ash is also assumed to be released elements, which have subsequently been attached to surfaces of larger particles [16].

The results obtained in the experiments by Shah and co-workers [14, 15, 116] and Damoe et al. [16] are reviewed in the following, along with mechanisms of release described in literature. The mechanisms of release has been described by examination of experimental results from grate-firing conditions supplemented with thermodynamic equilibrium calculations. The latter is used to gain insight on the thermodynamically 'desired' forms of selected inorganic elements [11, 17, 117]. In a suspension-fired combustion system, total equilibrium is not obtained, mainly due to short residence times and limited mixing (limited gas/solid or fuel/oxidizer contact). The calculation however provides insight to the forms, the elements are likely to be found in.

The programs used for the calculations are MINGTSYS (used by Nielsen 1998 [117]) only including ideal gases and pure solid and liquid phases and FACTSAGE 6.0 or 6.1 (used by Johansen et al. [11] and Nordgren et al. 2011 [17]) including models for non-ideal solutions of solids and liquids. Taking the age of the model and the fact that non-ideal solutions are included in the FACTSAGE models, the results

from this software may be considered more reliable.

Sulfur

The release of S is nearly complete (> 90 wt%) for six biomasses (wood chips, waste wood, bark, saw dust, straw and olive residue) tested in the LCS reactor at 1700 °C by Shah et al. [15]. A high release > 90 wt% of sulfur from wood and straw combusted in an EFR at 1200 °C and 1400 °C was also observed by Damoe et al. [16].

There is a general agreement that the organically associated S (≈75 % for woods [114]) is released as SO_2 as the particle decomposes during devolatilization [8–11, 15]. Under conditions similar to grate-firing, this fraction of S is released at temperatures lower than 500 °C. The remaining S is anticipated to react with alkalis, forming a slag of alkali sulfates [15], provided that oxygen is present [117]. The alkali sulfate is stable up to 1070 °C in pure form. However at temperatures around 800-900 °C, the alkali may be incorporated into silicate structures, and SO_2 can be released to the gas phase [9, 118]. Therefore, at higher temperatures the remaining S in the char will be released by either decomposition or evaporation of K_2SO_4 at oxidizing conditions [9–11, 15]. At reducing conditions the release of S from biomass is limited to the release occurring at low temperatures [11].

Thermodynamic equilibrium calculations made for S are seen in Figure 2.10. The

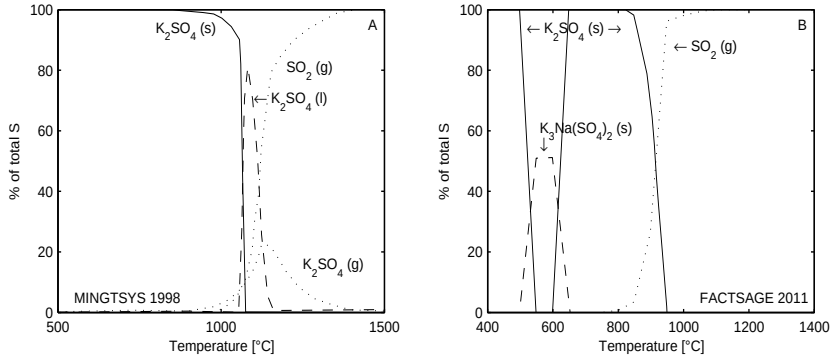

Figure 2.10: Predicted forms of S based on thermodynamic equilibrium calculations with excess oxygen present. A: Predictions by Nielsen [117] for straw with 2S/K molar ratio = 0.36. B: Predictions by Johansen et al. [11] for corn stover with 2S/K molar ratio = 0.14

thermodynamic equilibrium calculations are made for different fuels; straw and corn stover, and with different calculation software, which result in some difference in the predictions. However, the prediction agree in the sense that at low temperatures the S is found as solid K_2SO_4 and at high temperatures the only stable form of S is SO_2 (g). There is a disagreement on the temperature at which the K_2SO_4 melts or

decomposes in the two equilibrium calculations, which may be ascribed to influence of other elements in the two fuels, which influence equilibrium.

In the thermodynamic equilibrium calculations for straw (Figure 2.10A), liquid and gaseous K_2SO_4 is predicted at high temperatures. This is not present when calculations are made for corn stover, which is probably due to a low 2S/K molar ratio for this fuel. The K is thus expected to be found in other forms. According to Nielsen [117], liquid K_2SO_4 is only formed when the partial pressure of K_2SO_4 (g) is exceeded, which is clearly not the case for corn stover in Figure 2.10B. Nordgren et al. [17] has utilized FactSage for thermodynamic equilibrium calculations on straw, straw/bark mixture and straw/wood mixture at 1000 °C and 1200 °C. At these temperatures, small contents of liquid and gaseous K_2SO_4 is predicted [17].

The experimental results on S release in pf combustion by Shah et al. [15] and by Damoe et al. [16] were obtained at temperatures above 1200 °C. At these temperatures the equilibrium calculations show that the thermodynamically desired form of S is SO_2 at oxidizing conditions and the full release observed in the experiments is in agreement with this.

Chlorine

The release of Cl as compared to the fuel content of six biomasses is seen in Figure 2.11.

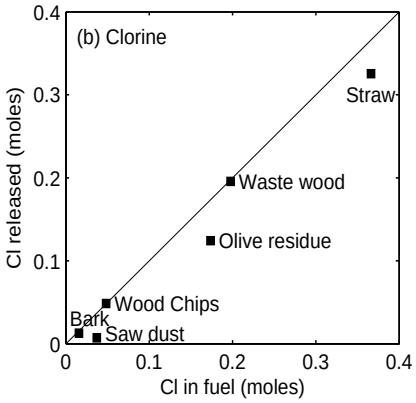

Figure 2.11: Release of Cl vs. content in fuel for 6 biomasses combusted LCS reactor at 1700 °C. The diagonal lines indicate full release. Adapted from Shah et al. [15]

It is seen in Figure 2.11 that the release is complete for three of the biomasses examined; bark, wood chips and waste wood. For the remaining three biomasses; sawdust, olive residue and straw, some Cl seem to be retained in the fuel [15]. The form of the retained Cl was not examined. In the experiments performed by Damoe et al.

[16] full release of Cl from straw and wood was observed in the EFR at both 1200 °C and 1400 °C combustion temperature [16].

Thermodynamic equilibrium calculations predict that above ≈700 °C, KCl(s) sublimates and all Cl is predicted to be in the gas phase as KCl(g), HCl(g), $(KCl)_2$(g) or NaCl(g), depending of the molar ratio of the individual elements [11, 17, 117].

During experiments resembling grate-firing, it was found that part of the Cl is released at temperatures 200-400 °C [11, 118]. At low temperatures <500 °C, the release of Cl is considered to occur by vaporization of HCl simultaneously with the devolatilization of the fuel as a consequence of reaction between KCl and proton-donating sites of the organic matrix [9, 11, 71]. The availability of proton-donating sites thus influences the release. It has been observed that fuels with a high Cl content release a smaller fraction of the Cl as HCl in this stage. The fraction of Cl retained in the biomass after devolatilization is expected to be released as KCl when the vapor pressure of this compound becomes significant above 700 °C and complete release of Cl is obtained above 800 °C [9, 71, 118]. Knudsen et al. [9] discussed that complete release of Cl may not occur if short residence times, poor gas-solid contact or a fuel with a high Cl content is applied [9]. This may partly explain the lower Cl release from at least olive residue and straw measured by Shah et al. [15]. In the work by Shah et al. [15] the release of Cl was plotted against the molar ratio Cl/(Na + K + Si + Al + 2S) with a R^2>0.96 linear regression, indicating that there is a (direct or indirect) connection between the release mechanisms of the elements. Ca and Mg has however not been included in the analysis of these connections for Cl.

The release of Cl as function of residence time have been tracked under conditions resembling those of suspension-firing. In experiments by Korbee et al. [14] (equivalent to those by Shah et al. [15]), a fraction of the Cl release was observed already at a residence time of 20 ms and nearly complete at 90 ms. A further slight increasing release with residence time was observed [14]. In the experiments by Damoe et al. [16], the release of Cl from wood and straw in the EFR was close to complete at 250 ms residence time.

Alkali Metals

The release of K from biomasses has been examined under conditions resembling those of grate-firing. The fuels utilized was woods [10], straws [9, 118] and corn stover [11]. It was generally observed that the release of K was dependent on temperature and on the presence of other inorganic compounds such as Cl, S and Si. Indirect effects of e.g. Ca has also been explored by Novakovic et al. [119], which is discussed later. An example of the experimental results on K release obtained during grate-firing is seen in Figure 2.12.

The release of K from biomasses combusted in grate-firing conditions was found to occur in steps depending on temperature [9–11, 118]. Below 600-700 °C it was found that the release of K was insignificant (0-10%). Below these temperatures,

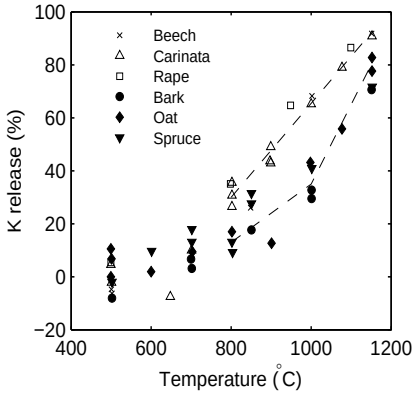

Figure 2.12: Release of K from 6 biomasses under grate-firing conditions. Open points: Fuels with low Si/K ratio, Closed point: Fuels with high Si/K ratio [10].

organic associated K may be rearranged within the char and become attached to phenol groups or transformed to K_2CO_3(s). The K_2CO_3(s) was stable up to 850 °C [10, 118].

In the range 700-800 °C, K was released as KCl by vaporization, provided that the fuel had a high Cl/K molar ratio [9–11]. It was found by Johansen et al. [11], that there was a correlation between the release of K and Cl at these temperatures. When K was in stoichiometric excess to Cl, the availability of Cl determined the quantity of K released [11].

At temperatures above 800 °C, the main mechanism of K release was vaporization of K(g) or KOH(g) from the decomposition of K_2CO_3(s) or organic structure, regardless of the amount of Cl originally present in the fuel [9, 74].

K may also be transformed to K_2SO_4 or K-silicates during the devolatilization stage and released from these at high temperatures [9, 11, 118]. The influence of S and Si present in the fuel has been examined by use of thermodynamic equilibrium calculations.

In Figure 2.13 the thermodynamic equilibrium calculations for K are seen for both oxidizing (upper figures) and reducing conditions (lower figures) [11, 17, 117]. It is seen that at low temperatures (<700 °C), KCl(s), K_2SO_4 (s), K-silicate or possibly K_2CO_3 are stable forms of K. Nielsen [117] has examined the desired forms of K and found that depending on availability, the desired solid forms of K are K_2SO_4 (s) > KCl(s) > K-silicate > K_2CO_3 at temperatures <700 °C. K_2SO_4 is however only stable at oxidizing conditions.

The fraction of K found as KCl(s) sublimates into KCl(g) at 700-800 °C, possibly via $(KCl)_2$(g). Both K_2SO_4 and K-silicates melt at temperatures within 800-1000 °C. Again - there is discrepancy within the models with respect to the behavior

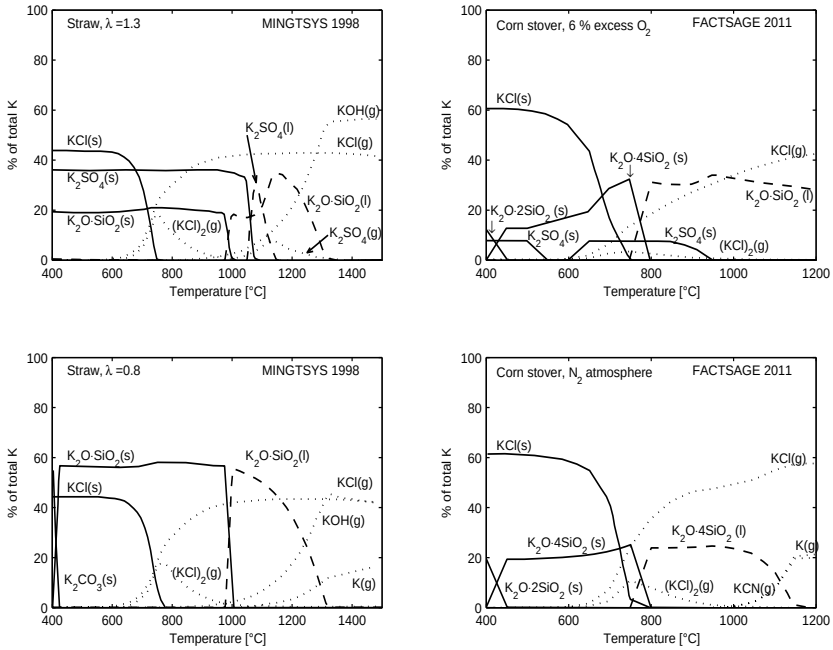

Figure 2.13: Predicted forms of K based on thermodynamic equilibrium calculations. Upper figures: oxidizing conditions, lower figures: reducing conditions. Left figures: Predictions by Nielsen [117] for straw. Right figures: Predictions by Johansen et al. [11] for corn stover.

of K_2SO_4. There is however agreements that the K from K_2SO_4 is incorporated into K-silicates at temperatures above 1000 °C. The model by Nielsen [117] predicts that the K-silicates decomposes in the temperature range 1150-1300 °C, forming KOH at oxidizing conditions and KOH(g)/K(g) at reducing conditions. Johansen et al. [11] ends the calculation at 1200 °C where molten K-silicates are still predicted to exist under oxidizing conditions. At reducing conditions the decomposition of K-silicates is predicted to occur in the temperature range 1000-1200 °C, forming K(g) and KCN(g) [11].

As can be observed from the equilibrium calculations, the release of K may be limited by the presence of silicates as alkali-metal oxides may be incorporated into silicate structures and become less volatile [9–11, 15]. The formation of K-silicates is kinetically limited at temperatures below 700-800 °C [9, 118]. Above this temperature it was found that the content of Si influences the release of K, as the release is found to be lower from fuels with a high Si/K molar ratio. This behavior observed for grate-firing conditions is seen in Figure 2.12 [10] .

The formation of K-silicates may however be limited at high temperatures due

to competition with the evaporation reaction or by physical limitations [9]. The physical limitations arise from the origin of K and Si within the particle. The K salts are precipitated as discrete salts in the pores of the char matrix or attached to the organic structure of the char. Si is mainly found on the char surface [118]. The incorporation of K in silicate structures is thus hindered by the organic material and the K is probably unable to react with silicon before the organic matrix is at least partly converted [9].

Presence of Ca may also influence the release of K [119]. The influence of Ca on K release has been examined by Novakovic et al. [119] by heating K-Ca-Si mixtures. In a mixture of K_2CO_3-CaO-SiO_2, it was found that SiO_2 preferentially reacts with CaO, when this was present in the mixture, leading to limited capture of K by silicate [119]. Thus, the presence of Ca increases the release of K, while low Ca contents may lead to a higher degree of K capture by silicates.

The above described observations on K release from biomasses were made for grate-firing conditions. A few studies have quantified K release from biomass in suspension-firing conditions [14–16, 116]. Results are seen in Figure 2.14

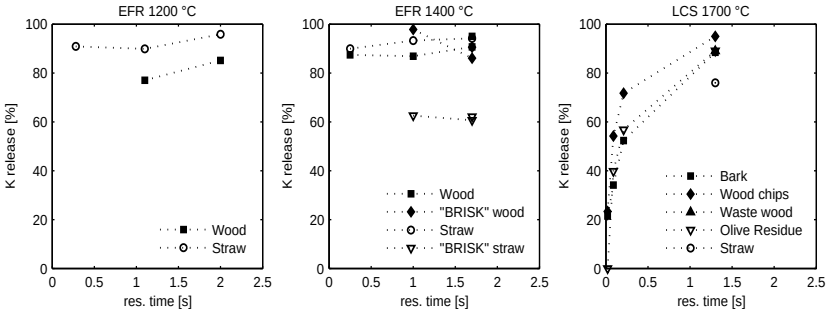

Figure 2.14: Release of K during pf combustion

It is seen that in conditions resembling suspension-firing, the release of K from biomasses is generally high, > 85%, when the residence time exceeds 1 second, except for two straws ('BRISK' straw in 1400 °C EFR and straw in 1700 °C LCS). It is furthermore seen that there is an increasing release with residence time. This is in line with results from grate-firing, where K release was primarily observed during char oxidation. The release of K occuring during char oxidation has also been observed by Jones et al. [105] who examined K release from a single burning particle and by Wornat et al. [68] who studied release of K and Na from pine and switchgrass during devolatilization and char oxidation in a laminar flow reactor.

Nordgren et al. [17] has examined the ash formation from combustion of straw, straw/bark and straw/wood in a pilot scale suspension-firing. It was found that the major part of the K (estimated close to 80 wt%) was released even when Si was present in the fuel particle. Compared to other studies [9, 10, 118] with conditions

similar to grate-firing the K release was much higher in the pilot scale suspension-firing for comparable fuels. The release was also higher than what was predicted by equilibrium calculations on the chemical components of the biomass at 1000 °C and 1200 °C. The reasons for the observed differences was most likely (*i*) a high heating rate, (*ii*) high fuel particle temperature, (*iii*) high Cl/K ratios and (*iv*) limited mixing. The limited mixing inhibits the Si and K interactions [17].

Wornat et al. [68] found that the K release from pine and switch grass chars were quite similar when the fuels were combusted in conditions resembling pf combustion. This was observed even though the Si/K molar ratio of the switch grass char was higher than for the pine char [120]. The effect of Si may thus be less pronounced for conditions resembling those of suspension-firing than for grate-firing conditions.

Low release of K from two straws as compared to other fuels was observed by both Damoe et al. [16] and Korbee et al. [14]. This can in both cases be explained by, high Si/K molar ratios along with limited content of Ca [15, 16]. The low Ca content facilitates a higher degree of K-silicate formation.

The release of Na is generally expected to be similar to the release of K, due to their chemical similarities. However, for the biomasses of interest the content of Na is relatively low - at least compared to K - and the release will not be discussed in further detail.

Alkaline Earth Metals, Silicon and Aluminum

The release of Si, Al, Ca and Mg are generally found to be negligible for grate-firing conditions [74]. The release of these elements may however occur by convective transport [12, 18]. For pf combustion conditions with biomass, Si and Al are also found to be retained in the fuel, whereas Ca and Mg may be released for some fuels [14, 15]. The release of Ca and Mg from 6 biomasses are seen in Figure 2.15
It is seen that Ca and Mg are retained in three fuels; Saw dust, olive residue and straw. For the remaining three fuels; bark, wood chips and waste wood, which initially have high Ca contents, a partial release is observed.

In biomasses, part of the Ca will be dispersed in the organic matrix, bound to the carboxylic groups. During thermal treatment this organic bound Ca may form superfine CaO(g) aerosols, as a consequence of decomposition of crystalline Ca-oxalates [15]. However, in fuels with a high Si content (such as saw dust, olive residue and straw) the release of Ca is limited due to the capture of Ca in Ca-silicates [15]. The remaining Ca (and Mg) in the biomass is found as discrete minerals, calcite or calcium oxalate. These decompose promptly during thermal treatment, releasing finely dispersed CaO(s), likely as super micron particles. The same occurs for Mg [15, 74].

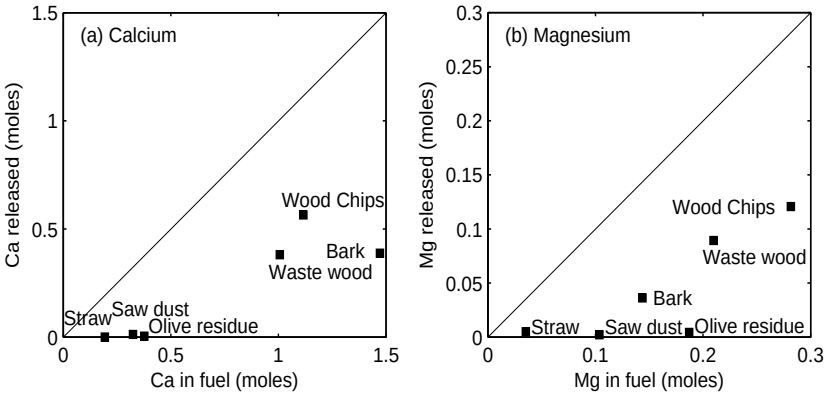

Figure 2.15: Release of Ca and Mg from LCS reactor vs. content in fuels. The diagonal lines indicate full release. Adapted from Shah et al. [15]

2.3.3 Summary

In this section the release of inorganic elements as expected based on CF analysis, observed from grate-firing, analyzed by thermodynamic equilibrium calculations and finally measured in suspension-firing experiments has been reviewed. In experiments resembling suspension-firing, the release of S and Cl was in most cases close to complete, which was as expected. However, in two cases the Cl release was incomplete, which may be explained by high chlorine contents of the fuel and/or interconnection with other release mechanisms.

In the CF analysis, it was found that K and Na are almost quantitatively leached in water or buffer solution, suggesting that these elements are released during combustion. During grate-firing experiments, it was found that K release is dependent on temperature, and a high release was observed at high temperatures ≈1200 °C. In experiments resembling suspension-firing, the release was generally >85 wt%, independent of temperature (when >1200 °C), but with some dependence of residence time. The release of K, expected based on CF analysis is thus observed.
In grate-firing, retention of K by silicates was significant for temperatures in the range 800-1200 °C. For suspension-firing, the role of silica seem to be less pronounced, probably due to limited possibility of contact between K and Si in the chars. However, it may not be disregarded completely, especially when Ca contents are low.

In experiments resembling suspension-firing, partial release of Ca and Mg was observed from woods with high contents of these elements along with a low Si content. In fuels with high Si content the Ca and Mg was retained. Expectations on release based on CF analysis, suggesting that some organically bound Ca and Mg are susceptible for vaporization, are thus realistic, provided that Ca and Si interactions does not occur. It is thus important to know both the fraction of organically bound

Ca and the Si content of the fuel, when formulating expectations on Ca release.

Si and Al are retained in the particles in all types of combustion experiments with biomass. This is in line with CF analysis.

2.4 Formation of Aerosols and Fly Ash

It was seen in the previous section that some of the inorganic elements present in biomass is released to the gas phase during combustion, while others are retained in the particles. The released elements may form aerosols, which can be observed as fine particulate matter with particle diameters less than 1 μm. This behavior will result in a bimodal (or possibly trimodal) size distribution of the ash as the particles with retained elements will form ash particles with diameters larger than 1 μm [92].

In the following the formation of each of these two size fractions and the resulting chemistry and particle size distributions will be reviewed.

2.4.1 Aerosols in Biomass Combustion

Particle size distributions of aerosols collected during combustion of wood and straw in grate or suspension-firing are seen in Figure 2.16. It is seen that in all combustion cases a peak in the sub micron particle concentration is found in the range 0.2-0.7 μm. In the results shown here, it seems that the aerosols from wood combustion are smaller (peak around 0.2 μm) than the aerosols from straw combustion (peak around 0.5-0.7 μm). Whether is a general trend cannot be established based on this comparison. However, it is likely that the higher ash load in straw combustion and more material available for aerosol agglomeration could result in larger aerosol particles.

Chemical analysis of the aerosol particles collected in the combustion systems have been conducted with SEM/EDS, in one case coupled with XRD analysis [17]. It is in all cases found that the aerosols are dominated by K, Cl and S [17, 93, 121, 122]. The XRD analysis showed that the aerosols contained KCl, K_2SO_4 and $K_3Na(SO_4)_2$ in a pilot scale suspension-firing of straw, straw/bark mixtures and straw/wood mixtures [17].

During combustion of wood on a grate Obernberger [122] detected some Zn and Pb along with minor contents of Na and Ca in the aerosols from softwood. In the aerosols from hardwood Zn was also detected along with a significant amount of Ca [122]. During full scale suspension-firing of wood, Damoe et al. [93] found increasing amount Ca with increasing particle size in the range 0.2-2.6 μm. In 1 μm particles, the Ca content is $\approx$5 wt% [93].

As discussed in Section 2.3.2, CaO aerosols may be released from fuels (primarily woods) with a high content of Ca bound to carboxylic groups in the fuel matrix, along with a low Si content, limiting retention of Ca [15]. CaO grains may also origin from

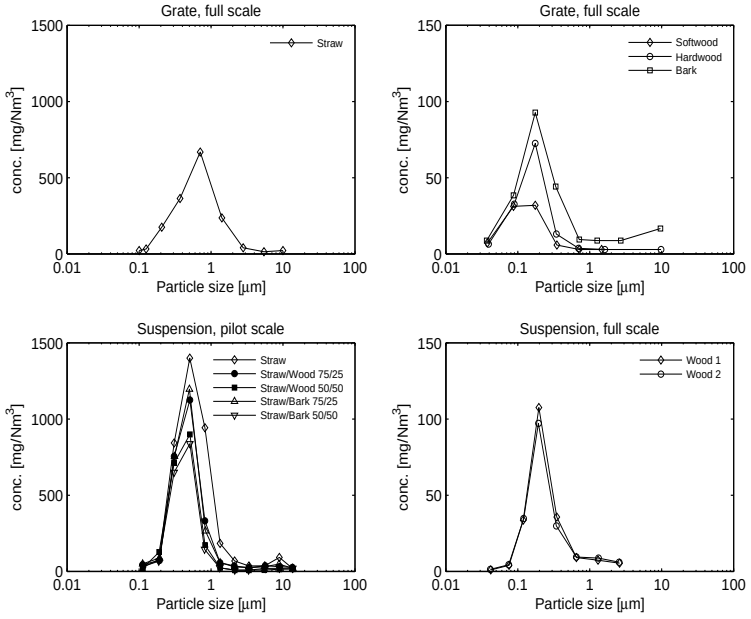

Figure 2.16: Examples of aerosol particle size distribution from straws (left figures) and woods (right figures) in grate-firing (upper figures) and suspension-firing (lower figures) [17, 93, 121, 122].

fractionation of mineral grains in the fuel matrix [17]. During full scale suspension-firing of wood, Skrifvars et al. [123] also detected Ca in the aerosol particles 0.06-1 μm and in agreement with Damoe et al. [93] found an increase in the Ca content with increasing particle sizes.

The release of Zn and Pb from woods were discussed by van Lith et al. [10] to occur when a reducing environment surrounding a fuel particle leads to reduction of the solid metal oxide to a gaseous metal. This occurs for both Zn and Pb at temperatures above 500 °C.

In this section, the aerosols formed in four different combustion scenarios, was observed to be reasonably similar in the sense that they all have a concentration peak in the range 0.2-0.7 μm and are primarily composed of K, Cl and S, most likely as KCl and K_2SO_4. The aerosol formation is a result of reactions between the inorganic elements vaporized during combustion. The mechanism of formation, which is considered to be valid for the four combustions will be reviewed in the following.

Aerosol Formation and Characteristics

The release of K from biomasses was observed in section 2.3.2, to occur primarily by release of K(g), KCl(g) and KOH(g), depending on temperature and molar ratios of the fuel. The released K(g) will react and form KCl or KOH depending on the K/Cl molar ratio, the temperature and the H_2O partial pressure [9]. K_2SO_4 may then be formed in a reaction between KCl (or KOH) and SO_2. The reaction between alkali chlorides and gaseous sulfur has been excessively discussed in literature [8, 74]. It has been discussed whether the reaction occurs by a homogeneous mechanism in the gas phase [124–126] or by a heterogeneous mechanism in which gaseous SO_2 reacts with condensed KCl [127]. However, recent experiments conducted in a rigorously homogeneous system support the homogeneous mechanisms [128]. The homogeneous mechanism is further supported by the fact that the heterogeneous mechanism may be too slow to occur within the residence time of pf combustion systems [74, 124, 125] and that pure K_2SO_4 particles (without traces of KCl) has been detected [8, 129]. The homogeneous mechanism occur via two routes:

$$KCl \rightarrow KSO_3Cl \rightarrow KHSO_4 \rightarrow K_2SO_4$$

This route is valid for high temperatures ($\approx 1100\,^{\circ}C$), with conversion of SO_2 to SO_3 being the rate limiting step, which becomes too slow at low temperatures, $< 800\,^{\circ}C$ [125]. The second route is valid at lower temperatures:

$$KCl \rightarrow KOH \rightarrow KHSO_3 \rightarrow KHSO_4 \rightarrow K_2SO_4$$

This route is found to be significant with the conversion of sulfite to sulfate being the rate limiting step [126]. The homogeneous reaction is found to be kinetically limited at low temperatures ($<800\,^{\circ}C$) and may be limited by equilibrium at high temperatures ($> 1000\,^{\circ}C$). A high conversion may thus only be expected at moderate temperatures ($\approx 900\,^{\circ}C$) [124].

Once K_2SO_4 is formed in the flue gas the formation of aerosols is initiated during cooling by homogeneous nucleation of K_2SO_4 from the gas phase, when the partial pressure of K_2SO_4 in the flue gas exceeds the saturation limit. KCl and K_2SO_4 then condense/nucleate on the surface of the sulfate seeds [92, 129, 130].

The number of particles formed is thus mainly dependent on the concentration of K_2SO_4 whereas KCl mainly influences the mass concentration and size distribution. The mechanism is considered valid for both grate-firing and pf combustion and furthermore for other biomasses although the processes may be onset at different temperatures depending on the partial pressure of KCl and K_2SO_4 in the gas [74].

With respect to description of the sub micron particle formation, some models are available in the literature. Christensen and Livbjerg [130] has developed a plug flow model for the aerosol nucleation and growth in a flue gas containing alkali species. This model includes gas phase reactions, homogeneous and heterogeneous

nucleation and coagulation. Though simplifying assumptions are made with respect to flow patterns and temperature- and composition gradients the model is considered to provide realistic results [130]. The predictions by the model has subsequently been compared to experimental results with various biomasses combusted in an EFR by Jiménes and Ballester [92, 129]. Good agreement between the model and the experimental results are found [92, 129].

Pictures of aerosols, revealing the irregular shape resulting from nucleation, condensation and aggregation of the vaporized inorganic species have been obtained from full scale suspension-firing of wood [93], Figure 2.17A and B, and from straw combustion in an EFR [39], Figure 2.17C.

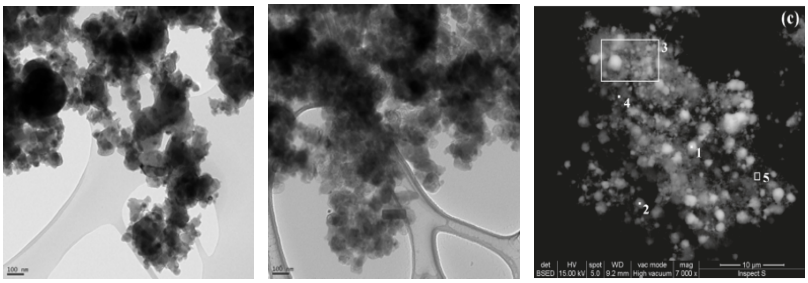

(a) wood, mean dp = 0.67 μm (b) wood, mean dp = 0.20 μm (c) straw, filter ash

Figure 2.17: Aerosols. A and B: TEM pictures of aerosols from full scale suspension-firing of wood [93]. C: SEM picture of filter ash (dp<2.5 μm) from straw combustion in EFR [39]

2.4.2 Coarse Ash Particles

As described in Section 2.2.1, the morphology and size distribution of the combusting particles may be difficult to describe as the particle alterations occurring during combustion are greatly dependent on specific fuel type, original particle size and shape, thermal history, etc. This naturally result in difficulties in describing the ash characteristics. Only scarce data on the particle size distributions of coarse ash particles from suspension-firing of biomass are available in the literature. This can naturally be ascribed to the limited amount of experiments performed with dedicated biomass suspension-firing. There are however some experimental observations available on the morphology, size distribution and chemistry of the coarse ash fraction, both from laboratory scale and full scale, which will be reviewed in the following [5, 6, 14, 16, 39]. In section, only observation from suspension-firing are included. In grate combustion the majority of the coarse ash fraction remains on the grate.

Ash Morphology and Chemical Composition

The morphology and chemical composition of ash formed from suspension-firing of straw has been studied in an EFR by Wu et al. [39] and in full-scale by Bashir [5].

In the EFR, the coarse ash fraction was collected in a cyclone with a cutoff diameter of 2.5μm, while the ash obtained in full scale suspension-firing was collected in the ESP (electrostatic precipitator). SEM pictures of the ashes are seen in Figure 2.18.

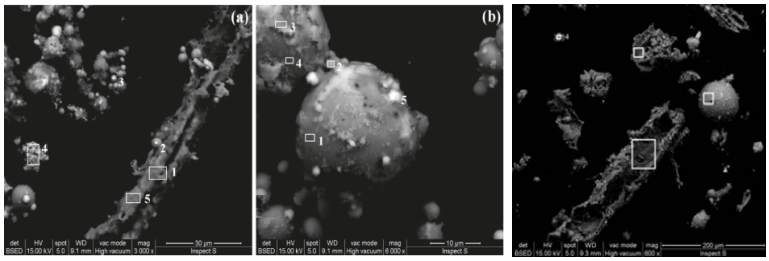

Figure 2.18: SEM pictures of fly ashes from straw combustion; A and B: Cyclone ash (> 2.5 μm) collected in EFR [39], C: Fly ash from full scale suspension-firing collected in ESP [5].

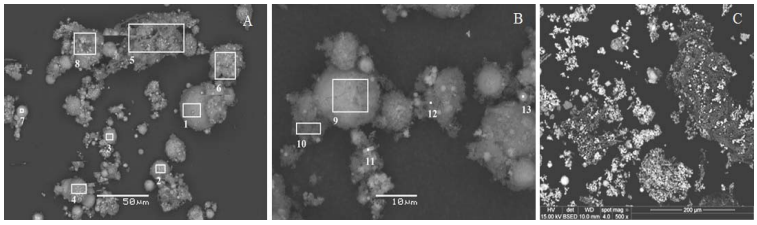

Figure 2.19: SEM pictures of fly ashes from wood combustion; A and B: Fly ash from full scale suspension-firing collected in ESP [6], C: Cyclone ash (> 1.5 μm) collected in 1400 °C EFR [16].

From both EFR and full scale combustion, three types of particles were observed by SEM, as seen in Figure 2.18; (*i*) molten or partially molten spherical particles often consisting of K-silicates or K-Ca-silicates, (*ii*) Smaller spherical particles, rich in Si, P, K and Ca and (*iii*) flake shaped or irregular particles with a high Si content (>90 wt%) [5, 39]. The appearance of the flake shaped particles can be explained by the high melting temperature of silicon oxide compared to the lower melting temperatures of the alkali silicates found in the spherical particles [39].

The coarse ash fraction formed from combustion of wood in suspension-firing has been studied in full scale by Wu et al. [6] and in an EFR by Damoe et al. [16]. SEM

pictures of the fly ashes from these combustion systems are seen in Figure 2.19. The fly ash from the EFR are seen in Figure 2.19C. Some irregular ash/char particles are present in the fly ash and appears in the SEM picture (the organic content of the ash is 19 wt%). Otherwise, the ash particles with sizes in the range 10-100 μm are described as spherical particles composed of Si, Ca and a varying content of K [16]. The fly ash from full scale suspension-firing of wood, seen in Figures 2.19A and B, are in similarity with the ashes from the EFR composed mainly of spherical particles. These vary greatly in size within the range 1-50 μm and are composed of mainly Si, Ca and K.

The chemistry of various size fractions of ash formed during full-scale pf combustion of wood has been examined by Skrifvars et al. [123]. It was found that fly ash particles with diameters below 1 μm are rich in alkali sulfates and -chlorides which is in line with the previously mentioned observations on aerosols. Silicon is found in large particles (>10μm). In the particle size range 1-10μm, calcium is found to be enriched.

Based on these observations on straw and wood fly ashes from suspension-firing, it seems that observations made in an EFR corresponds well with observations made in full scale. The ashes from the two fuels in all cases contains molten or partially molten particles composed of Si, Ca and K, with varying composition. In addition to that, the fly ash from straw also contained flakes or irregular particles rich in Si and K. The varying compositions of the K, Ca and Si particles are caused by different fuel ash compositions and the bulk ash compositions of ashes from straw- and wood combustion are not similar [16]. The bulk ash compositions has been explored further as part of this work, see Chapter 3.

In the following, available particle size distributions of ashes will be reviewed.

Particle Size Distribution

The particle size distributions of the cyclone ashes from wood and straw combusted in an EFR with various residence times are seen in Figure 2.20 along with the particle size distribution of the original fuel. For both wood (upper figures) and straw (lower figures), the fuel has a broad particle size distribution with a peak concentration around 4-500 μm. During the first stages of combustion of wood ($\approx<$ 1 s) the concentration of large particles are increased. This is by Damoe et al. [16] considered to be an expression of the small particles being converted faster than large particles. As the combustion proceeds, the concentration of large particles decreases and a new intermediate size peak with maximum within 30-50 μm is developed, possibly due to fragmentation. Damoe et al. [16] has utilized the particle size distributions and SEM/EDS of collected particles at the various residence times to gain insight to the occurrence of fragmentation, coagulation and agglomeration during combustion. It is discussed that the intermediate sized particles in wood combustion are formed as a result of fragmentation of char and included minerals as well as melting and

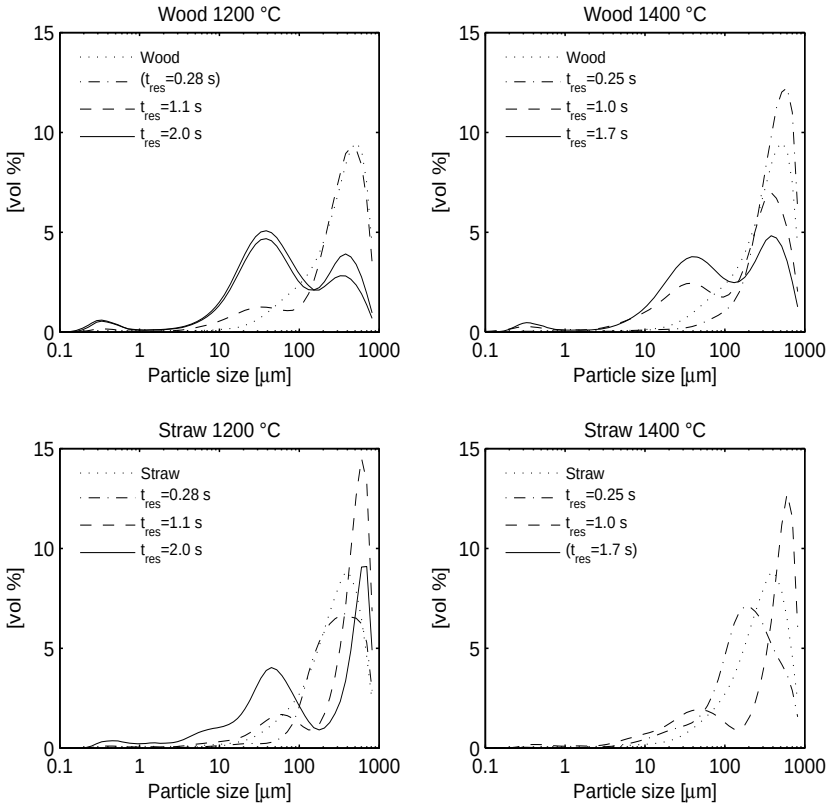

Figure 2.20: Particle size distributions obtained during combustion in an EFR [16].

coagulation of small ash droplets. At the end of combustion in the EFR (residence time 1.7 or 2 s), the super micron fly ash has an bimodal particle size distribution. It should be noted, that at this point, the cyclone ashes still contain organic matter (19-30 wt% in wood) and further developement of the PSD may occur with longer residence times.

For the straws (lower figures in Figure 4.4), the large particle size peak is contrary to that for wood initially decreased slightly, which could indicate some initial fragmentation. Then the peak narrows and move toward larger particle sizes. This could be due to agglomeration of smaller particles, but this was not evident from the SEM investigations. It could be due to smaller particles reducing in size faster than large particles, as observed for woods. When the residence time exceeds 1 s, an intermediate size peak with maximum within 30-50 μm is developed, as also observed for woods. The intermediate sized particles are a mixture of spherical particles (similar to those from wood) along with irregular particles rich in K and Si and agglomerates

of KCl aerosols. The bimodal particle size distribution of particles > 1 μm observed for woods are also evident from straw combustion. Here, the organic content at the exit of the EFR is 10-12 wt%.

Korbee et al. [14] has also examined the development of particle size distribution for different fuels (coals, woods, olive residue and straw) in an EFR and made conclusions on the type of fragmentation occurring. In agreement with Damoe et al. [16], it was found that small particles reduce in size faster than large particles in the early stages of combustion. A significant increase in aerosol concentration early in the combustion (20-90 ms) suggest occurrence of attritive fragmentation by which small particles are shedded from the surface of larger particles. At later stages of combustion (above 60-70 % conversion) the particles are observed to fragment by breakage or percolative fragmentation [14]. In percolative fragmentation the solid network of the particle is progressively eroded by oxidative attack. Finally the solid phase becomes spatially discontineous and fragmentation occur [131] as the partice disintegrates into an array of large and small particles [14]. Korbee et al. [14] found that fuels with a high ash content and high volatile matter content (olive residue and straw) has a lower conversion and lower degree of fragmentation in the early stages of combustion than wood. The conversion and fragmentation is accelerated at later stages of combustion. For straw, a high Si content seem to lower the extent of devolatilization and fragmentation as compared to olive residue [14].

In coal combustion, the ash formation mechanisms in terms of fragmentation and coalescence occurring in suspension-fired boilers is well described and can be modeled relatively accurate [8]. Two limiting models has been presented by Charon et al. [132]. In the first limiting case it is assumed that each mineral grain in a fuel particle forms an ash particle during combustion. This approach is known as the 'no coalescence' model. Contrary, it can be assumed that the mineral grains in the fuel particle coalescence to one ash particle as the carbon network is combusted. This approach is used in the 'full coalescence' model [8]. The formation mechanism occurring rely on the structure of the char particle as illustrated by Wu et al. [133] in Figure 2.21.

The full coalescence model has been applied to three biomasses; orujillo, chestnut and eucalyptus, combusted in an EFR by Jiménes and Ballester [92]. The model was not able to describe the size reductions observed [92]. It is generally found that the models derived for coal are not applicable to the ash formation in biomass combustion [67]. However, a 'break-up' model derived for coal combustion by e.g. Sarofim et al. [85], was found by Jiménes and Ballester [92] to be a possible tool for predicting the particle size distribution observed by Jiménes and Ballester [92], although with some moderations in the empirical constants describing the number of fragments per particle [92].

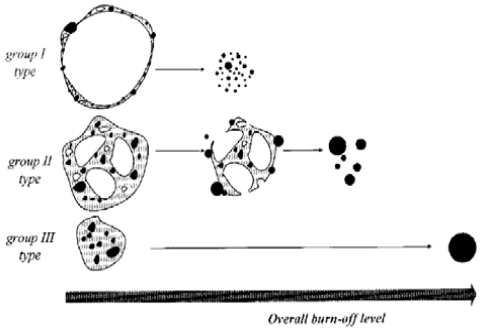

Figure 2.21: Mechanisms for ash formation from char particles with different structures. From Wu et al. [133].

2.4.3 Coarse Ash

The coarse ash fraction formed during suspension-firing of biomass was found to be quite similar for straw and wood in the sense that it is dominated by molten or partially molten particles of Si, K and Ca with peak diameters in the range 30-50 μm. Straw ash however also contained flakes rich in Si. It should however be noted that the bulk ash compositions of ashes from straw- and wood combustion are not similar, due to differences in the fuel ash composition [134]. This has been explored further as part of this work, see Chapter 3.

The coarse ash fraction is considered to be formed via some degree of fragmentation of the particles during combustion. However, no models for the description of particle size distributions are currently available for biomass. This is naturally needed before deposit formation can be modeled, and is included as part of this work, see Chapter 4.

Chapter 3

Deposit Probe Measurements in Full Scale Boilers

To investigate biomass ash deposit formation and removal in power plant boilers, probe measuring campaigns have been conducted in straw-fired grate boilers [51–58], in FBC plants [135, 136], in suspension boilers co-firing coal and biomass [75, 137, 138] and lately also in dedicated biomass-fired (wood and/or straw) suspension boilers [5, 6, 59–63]. The measuring campaigns with focus on deposit formation and shedding have primarily been conducted in Danish boilers. To our knowledge, only a few full-scale deposit probe measuring campaigns conducted with biomass as fuel in other countries have been described in publications [123, 135, 139].

In this chapter, a review of reported full scale biomass boiler deposit investigations is presented. The campaigns conducted in grate-fired and suspension-fired units with dedicated biomass-firing (straw and/or wood) are included [5, 6, 51–63]. The focus of the review is to gain knowledge on the ash transformation, deposition rates and shedding behavior occurring in the two boiler types. A further objective is to summarize the influence of operational parameters on deposit chemistry, deposit formation rates and shedding by comparing results from campaigns with a relatively broad range of flue gas temperatures and fuel compositions for each firing technology. When relevant, the experiences from lab-scale or pilot-scale experiments are included for the purpose of comparison.

This chapter is build on the review paper "Deposit Probe Measurements in Large Biomass-Fired Grate Boilers and Pulverized-Fuel Boilers" written by the author, see Appendix A.

3.1 Full-Scale Measurements Reviewed

The measurements reviewed in this study have been conducted at several combined heat and power (CHP) plants, both grate-fired boilers (including a so-called cigar-

fired boiler) and suspension-fired boilers. The primary difference among these boiler types is found in the combustion zone; in grate boilers, the fuel is fed to a grate on which the combustion takes place by leading primary air through the grate [76]. In a cigar boiler, whole straw bales are introduced to the furnace and burn along the surface of the bale, where primary air is introduced by several jets [51]. In suspension-firing, the fuel is milled in order to obtain small particle sizes before being blown into the furnace together with primary air [76]. Some operational differences are highlighted in Table 3.1.

Table 3.1: Selected operational characteristics of three boiler types firing biomass

Boiler type	Fuel size	Res. time combustion	Fly ash	Bottom ash	Ref.
Grate	Whole straws	Minutes	$< 20\%$	$> 80\%$	[76, 117]
Cigar	Bale of straw	Minutes	$\approx 30\%$	$\approx 70\%$	[51]
Suspension	< 2 mm	Few seconds	$\approx$ 75-80%	$\approx$ 20-25%	DONG Energy[a]

a: Measured by plant owners during 10-day experimental campaign with wood-firing.

An important difference seen in Table 3.1, is the distribution of the fuel ash into fly ash and bottom ash fractions, which is important for the fly ash characteristics and thereby for deposit formation. The difference is relatively small for grate-fired boilers and cigar boilers, while a great difference is observed between these boiler types and the suspension-fired boilers. For this reason, for the purpose of comparison in this study cigar boilers are treated as grate-fired units.

Measuring campaigns with deposit probe measurements have been conducted at several power plant boilers. Table 3.2 gives an overview of the plants mentioned in this study. The table lists the main boiler data and the year and reference of the measuring campaigns conducted. It should be noted that Avedøre Unit 2 comprises two boilers, a straw-fired grate boiler and a wood/oil/gas-fired suspension-boiler, which feed steam to a joint steam turbine. The deposit measurements obtained in the full-scale boilers were made by introducing a deposition probe into the furnace chamber or the superheater area of the boiler. For grate-fired boilers, the investigations included both analyses of deposits collected on probes with short exposure times and also a few mature deposits collected from superheater tubes [54, 55]. The latter deposits may have exposure times up to a year [54]. The data set includes quantification of the rate of deposit formation [51, 56–58], chemical analyses of fuels, ash and deposits [51, 53–57], and in a few cases corrosion studies [53] and shedding observations [57, 58]. In suspension-fired units, only probe deposits have been examined, until now. The focus of these examinations has been on the rate of deposit formation [6, 59–63, 123], fuel chemistry, ash and deposits [6, 59, 60, 62, 63, 123] and shedding observations [6, 60, 63].

Both relatively simple probes as well as more advanced probes for in-situ deposit measurements and soot blowing have been applied in the measuring campaigns. In

Table 3.2: Power plants mentioned in this study; boiler data and year/reference of the measuring campaigns. Some plant data not mentioned in the campaign documentations were found elsewhere [3].

Power plant	Firing system	Fuel	Therm input [MW_{th}]	Steam T[°C]/ P[Bar]	Com. operation	Camp. Year	Ref.
Haslev	Cigar fired	Straw	23	450/67	1989	1997	[51, 52]
Slagelse	Grate	Straw	31	450/67	1990	1997	[51, 52]
Rudkøbing	Grate	Straw	10.7	450/60	1990	1998	[53]
Masnedø	Grate	Straw	33	522/92	1996	2000	[54]
						2004	[55]
Ensted	Grate	Straw	100	470/200	1998	2004	[55]
						2006	[56]
Avedøre 2	Grate	Straw	100	545/310	2001	2004	[57]
						2006	[56, 58]
Avedøre 2	Suspension	Wood	800	560/300	2001	2008	[59]
						2011	[6, 60]
Amager 1	Suspension	Straw /wood	350	540/185	1971/2008	2011	[63]
Amager 2	Suspension	Straw /wood	250	480/110	1972/2003	2007	[61]
						2011	[62]
Jordbro	Suspension	Wood	80		1968	2004	[123]

the early experiments, mainly simple water and air cooled deposit probes were used. The probe is a stainless steel probe with thermocouples placed along the probe surface. The probe temperature is controlled for a given set-point by adjusting the air flow-rate inside the probe. The deposit mass is determined by extracting the probe after each experiment, and subsequently removing the deposits for weighing and analysis [51, 54].

In later studies, an advanced in situ shedding probe (Figure 3.1) was utilized. The probe is equipped with a load cell, and online quantification of mass and heat uptake is possible. The flue gas temperature was measured by a thermocouple, and the deposit formation and shedding was observed using a video camera. Often, the thermocouple temperature measurements were supported by suction pyrometer measurements [5, 57, 60, 63].

In a few experiments [57, 140] a soot blower probe was used along with the in-situ deposition probe in order to provide information about the removability of the deposits formed. The soot blowing probe was equipped with a nozzle for blowing high-pressure air onto the deposit probe surface. By adjusting the air pressure through the nozzle and the distance between the soot blowing probe and the deposits, the jet peak impact pressure (PIP) needed for removal of deposits could be determined [57, 140].

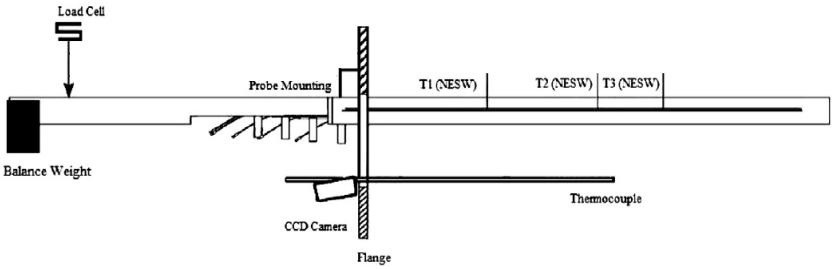

Figure 3.1: Illustration of the advanced deposit probe [62].

3.2 Results and Discussion

This section discusses and reviews the results of the reported full-scale measuring campaigns. The focus is on the chemistry of the deposits formed, the rate of deposit formation, the observations made on shedding events along with an evaluation of the measuring techniques used to quantify rates of deposition. When examining the full-scale experimental results it should be kept in mind that full-scale boilers are not very well-controlled with respect to operational parameters. Large variations in fuel composition, flue gas flow, temperatures, etc. may occur within a relatively short period of time. Thus, only major factors influencing operational parameter changes may be observed. However, by comparing the results from several different measuring campaigns, it is possible to provide relatively solid conclusions.

3.2.1 Chemistry of Ash and Deposits

This section reviews the influence of fuel type and boiler operation parameters on fly ash and deposit chemistry. The chemical examinations in this study mainly focus on the five major ash forming elements in biomass combustion; Si, Ca, K, Cl and S.

Fly Ash Chemistry

The firing technology strongly influences the fly ash formation process. As mentioned earlier, there is a large difference in the ash split occurring in grate-fired and suspension-fired boilers [76, 117]. This may influence the distribution of elements among bottom and fly ash fractions.

In Figure 3.2, fuel ash and fly ash compositions are compared for each of the two firing technologies, grate-firing (including cigar-firing) and suspension-firing, to gain an idea on how the ash split occurs in the furnace chambers. It is seen in Figure 3.2 that for grate-firing, the fly ash composition is quite different from the fuel ash composition, as almost no points are placed near the diagonal line, which would indicate similar composition of the fuel ash and fly ash. The fly ash from grate-firing of straw is rich in K, Cl and S and depleted of Si and Ca compared to the fuel ash.

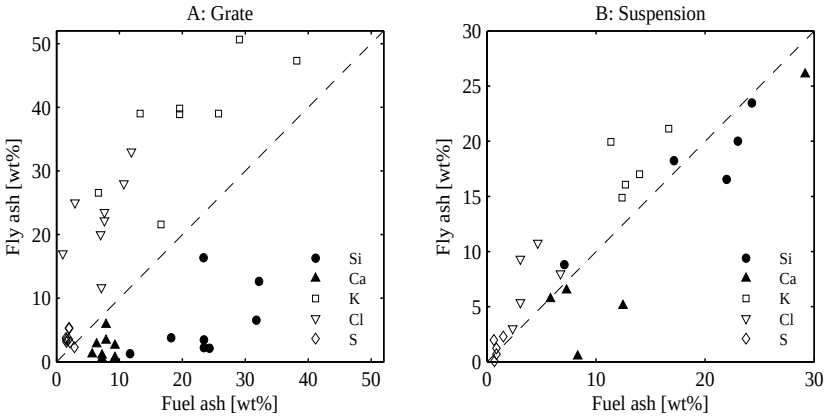

Figure 3.2: Fly ash composition vs. fuel ash composition. Elemental content is calculated as wt% dry ash based on data available in references. Points on or near the diagonal line indicate similar fuel ash and fly ash compositions. A: Grate and cigar; straw as fuel [51, 52, 57]. B: Suspension; straw and/or wood as fuel [62, 63, 123]

In suspension-firing, the fly ash resembles to a large extent the fuel ash, as seen by the distribution of points relatively close to the diagonal line in Figure 3.2B. Only a slight enrichment of K, Cl and S is found in this combustion system. The fly ash formation process is different in the two combustion systems. As K, Cl and S are volatile elements in the fuel, these are partly released to the gas phase in the combustion zone, while Ca and Si are retained in the solid fuel (or ash) particles [7]. In grate-firing most of the solid ash particles remain at the bottom of the furnace. Ca and Si are thus only found in the fly ash to a limited extent. This is in contrast to suspension-firing where a large fraction of the ash particles is entrained, which leads to the quite similar composition of the fuel ash and the fly ash. This will for straw-firing in suspension boilers lead to fly ash dominated by Si and K, and with a high content of Ca and Cl [62, 63], while wood-firing in suspension boilers leads to fly ash dominated by Ca and Si and with a high content of K [60, 123]. Examples of fly ash compositions from various combustion conditions, featuring these characteristics, are seen in Table 3.3.

Deposit Chemistry

Biomass deposits are formed by fly ash appearing as particles, aerosols and gaseous species (mainly KCl and K_2SO_4). The deposit chemistry and characteristics are thereby influenced by the characteristics of fly ash and the ability of the fly ash to impact and stick to heat transfer surfaces at the prevailing local conditions. Generally, the structure of deposits formed in biomass boilers is characterized by a salt-rich

Table 3.3: Examples of chemical composition of fly ash formed under various combustion conditions. Composition given as wt% of dry ash.

Boiler type	Si	Ca	K	Cl	S	Ref.
Grate, straw[a]	5.64	1.95	40.89	23.75	3.48	[51]
Suspension, straw	20.00	6.49	17.00	8.00	2.30	[62]
Suspension, wood	17.70	20.80	6.26	0.20	1.08	[6, 60]

[a]: Mean composition of four experiments.

inner layer, typically rich in KCl and/or K_2SO_4, and outer layer(s) containing Si and Ca along with salt components [54, 55, 62].

In this study, three parameters, which may influence deposit chemistry, are considered for each firing technology and fuel choice; exposure time, probe temperature and flue gas temperature.

The influence of exposure time and probe temperature (400-550 °C) on deposit chemistry and morphology (thickness and porosity of layers) has been examined by Hansen et al. [54], Jensen et al. [57] and Michelsen et al. [53]. The results indicate that both exposure time and probe temperature mainly influence the morphology of the deposits, whereas the bulk chemical composition of the deposits remain relatively unaltered. Based on these results, it seems reasonable to assume that variations in probe exposure time and probe temperature (within 400-550 °C) can be excluded as important parameters in the analysis when examining the influence of flue gas temperature on deposit bulk chemistry.

The influence of flue gas temperature on deposit chemistry has been examined in a few measuring campaigns [51, 55, 60]. In the campaign conducted in the straw fired cigar- and grate boilers in Haslev and Slagelse [51, 52], corresponding samples of fuel, fly ash and deposits were examined in order to obtain knowledge about the ash transformation occurring within the boilers. During the measuring campaign, probes were inserted at two positions in the boilers to observe differences in deposit chemistry and rate of formation with variations in the local flue gas temperature.

In Figure 3.3 the fly ash composition is compared to the bulk compositions of the deposits formed in the furnace chamber at mean flue gas temperatures of around 850 °C (Figure 3.3A), and to the deposits collected near the superheaters at mean flue gas temperatures near 650 °C (Figure 3.3B). It is seen that in the furnaces (850 °C), the deposits contain more Ca and Si and less K and Cl compared to the fly ash. At the probes near the superheaters, where the flue gas temperature is 650 °C, the points are placed around the diagonal line and the deposit chemical composition is thus close to that of the fly ash. This seems to suggest a shift in the deposition behavior with flue gas temperature for grate-firing, and the deposit chemical composition is influenced by local flue gas temperatures.

In order to expand the analysis of the influence of flue gas temperature on deposit

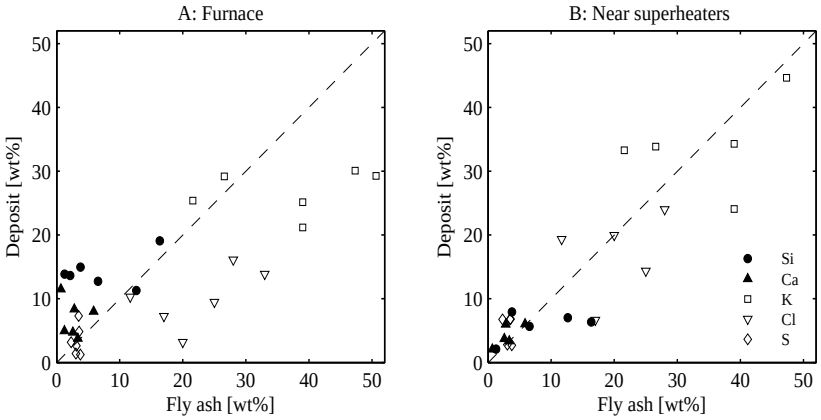

Figure 3.3: Deposit probe compositions vs. fly ash compositions in straw-fired grate boilers. Deposits are obtained on 510 °C probes with 8-hour exposure time. A: In the furnaces (flue gas 850 °C). B: Near the superheaters (flue gas 650 °C). Data from Haslev and Slagelse [51, 52]. The symbol legends shown in 4B are common for the two composition plots.

chemical composition, an enrichment factor for each element has been calculated as follows.

$$\text{Enrichment factor} = \frac{\text{wt\% in deposit}}{\text{wt\% in fuel ash}}$$

The enrichment factor is influenced by both the fly ash formation process and the deposit formation process. The deposit compositions used in the calculations are compositions of the bulk deposits or of separate layers, depending on availability. The enrichment factors of the five main ash forming elements are seen as a function of local flue gas temperatures for grate-firing of straw in Figure 3.4A and for suspension-firing of straw or wood in Figure 3.4B. The data generally fluctuate although some general trends can be identified.

For grate-fired systems (Figure 3.4A, left column), it is seen that for Si and Ca, the enrichment ratio is low at the low temperatures and approaches an enrichment factor around 1 at higher temperatures, except for the downstream deposits. The enrichment factors for K seem relatively steady, though with a slight decrease with increasing flue gas temperatures. For Cl, the enrichment factor is high (≈4) at low temperatures and then decreases with increasing flue gas temperatures. It is seen that deposits formed at high flue gas temperatures can be expected to be depleted of Cl. For S, a behavior similar to that of Cl is observed, though with a much larger scattering of the data. For K, Cl and S a point (marked with *) with high enrichment factor is seen where the flue gas temperature is around 900 °C. This point originates

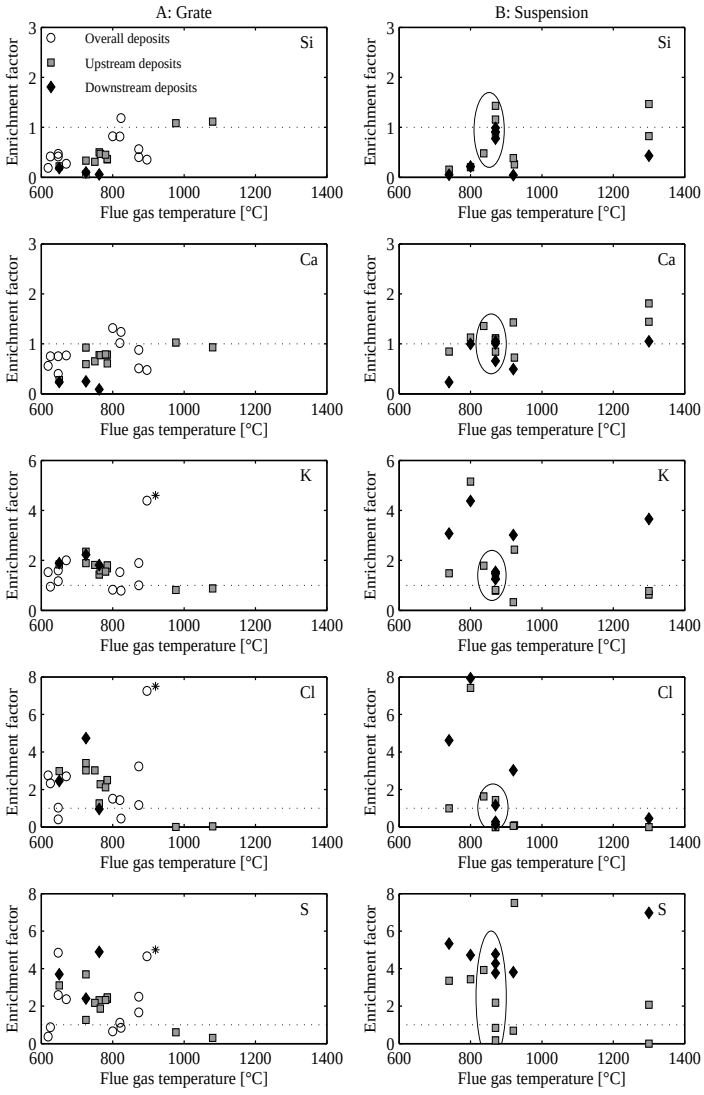

Figure 3.4: Enrichment factors for the five main ash forming elements as a function of flue gas temperature. A (left figures): Data from straw-fired grate boilers [51, 52, 56, 57]. B (right figures): Data from suspension-fired boilers. The points marked with a circle are from straw/wood ($>$ 45 wt% straw) or straw firing [62, 63]. The remaining suspension data are from wood firing [6, 59, 60, 123]. The data points for K, S, and Cl marked with a $\star$ originate from a naturally washed straw.

from naturally washed straw (rainfall in the field before baling [51]), where the fuel ash was low in these elements before combustion.

From the enrichment factors observed for grate-firing it is found that at low flue gas temperatures deposits are rich in K, Cl and S, while at higher temperatures, Si and Ca are present in the deposits to a higher degree. The influence of temperature on the deposit chemistry can be explained by the deposit mechanisms involved in deposit build-up. The increase of the enrichment factors for Ca and Si with increasing flue gas temperatures can be explained by increased deposit formation by inertial impaction with increasing temperatures. This increase is caused by a higher melt fraction of the coarse fly ash particles containing Si and Ca and of the deposit surface at high flue gas temperatures. When the melt fractions increase, the particles are more prone to stick on the probe surface upon impaction. The decrease in the K, Cl and S enrichment factors with increasing flue gas temperature can be explained by reduced condensation at high temperatures and by the dilution effects of the increased content of Ca and Si.

The enrichment factors calculated for suspension firing are seen in Figure 3.4B (right column). Both pure wood and straw/wood mixtures (where co-firing ash in many cases is dominated by straw ash) have been utilized as fuels in suspension-fired boilers. The data from measurements with straw or straw/wood mixtures as fuel are marked with circles in Figure 3.4B. Data with this fuel mixture are only obtained at flue gas temperatures around 850 °C and no influence of flue gas temperature on enrichment factors can be observed. For the measurements with wood as fuel, the enrichment factors for Si and Ca increase with flue gas temperatures, while enrichment factors for Cl decrease. For S and K, the data are scattered, and no influence of flue gas temperature can be observed. The physical effects, believed to apply to ash in grate-fired boilers are expected to apply also to ash in suspension-fired boilers. The data from wood-firing seem to support this.

It is thus seen that the local flue gas temperature influences the chemical composition of the deposits formed. To gain an overview of the implications of these influence, examples of chemical compositions of deposits are shown in Table 3.4. This allows clearer observations of differences in deposit compositions among different firing technologies, fuels and local flue gas temperatures. Table 3.4 lists the composition of three deposits obtained during grate firing of straw at various flue gas temperatures. It is seen that the low temperature deposit is rich in K, Cl and S. As the local flue gas temperature increases, the content of these three elements decreases, whereas the content of Si and Ca increases, as expected. The high temperature deposits obtained during grate-firing of straw are thus dominated by Si, K and Ca.

For suspension firing with straw in the fuel, deposits have only been collected at mean flue gas temperatures near 800-900 °C, see Table 3.4. This deposit composition can be compared to the composition of the deposits obtained during grate firing of

Table 3.4: Examples of chemical composition of deposits formed under various combustion conditions. Composition given as wt% of dry deposit.

Boiler type, fuel	T_{fg}	Si	Ca	K	Cl	S	Ref.
Grate, straw [a]	650 °C	4.94	3.06	37.59	13.64	5.44	[51]
Grate, straw [a]	873 °C	12.88	6.25	28.42	8.44	4.01	[51]
Grate, straw	1080 °C	29.00	6.70	14.00	0.21	0.57	[56]
Suspension, straw/wood [b]	870 °C	21.54	8.51	16.30	1.81	2.12	[62]
Suspension, wood	800 °C	3.44	15.08	24.75	3.19	3.09	[60]
	1300 °C	24.90	25.30	3.04	0.09	0.07	[60]

a: Data are the mean composition of 3 or 4 experiments.

b: Min. 45 wt% straw. Mean composition of all layers.

straw at similar flue gas temperatures (870 °C). It is seen that a shift in technology influences the deposit chemistry as the deposits from suspension firing have high contents of Si and Ca and a very low content of Cl and S as compared to the deposits from grate-firing. Thus it is seen that differences in fly ash composition observed between grate and suspension-firing are also observed in the deposit composition. The deposits in a suspension boiler have a higher content of Si and Ca, as compared to those in a grate boiler.

For suspension-firing of wood, it is seen that at the low flue gas temperature, 800 °C, the deposits are dominated by K and Ca. Increasing the temperature to 1300 °C leads to deposits which are dominated by Si and Ca, with a very low content of K, Cl and S. A similar shift from deposits dominated by Ca and K at low temperatures toward deposits dominated by Ca and Si at higher temperatures was observed by Skrifvars et al. [123] by collection of deposits at mean flue gas temperatures of 740 °C and 920 °C in a wood-fired suspension boiler.

3.2.2 Rates of Deposit Build-up

In the section below, the rates of deposit build-up measured in the full-scale boilers will be presented and influence of operational parameters on the rates will be examined. In some measuring campaigns, a simple probe was applied. From these campaigns, only a single quantification of the deposit mass on the probe, determined at the end of the measurement (after 4-24 hours), is available for each experiment. In other campaigns, an advanced probe was applied. From these campaigns, detailed information about the mass on the probe as a function of residence time is available. Thereby, occurrence of shedding events can be identified from the mass changes measured. Due to these differences, the applied measuring techniques will be evaluated before examining the influence of operational parameters on build-up rates.

Discussion of Applied Measuring Technique

Two definitions of the deposit build-up rate [g/m^2/h] are applied: (*i*) the Integrated Deposit Formation rate (IDF-rate) and (*ii*) the Derivative-based Deposit Formation rate (DDF-rate), as defined by Bashir et al. [5, 63]. The IDF-rate is determined by using the deposit mass obtained at a defined time divided by the probe surface area and the exposure time. The DDF-rate is determined by calculating the time derivative of the deposit mass uptake [g/h] between two shedding events and divided by the probe surface area. Using this method, only small shedding events which cannot be separated from the measuring noise, are included in the measured DDF-rate [5, 63]. Figure 3.5 shows the IDF- and DDF-rates for a firing case with frequent shedding events. As seen from the slopes of the lines in Figure 3.5, the DDF-rate

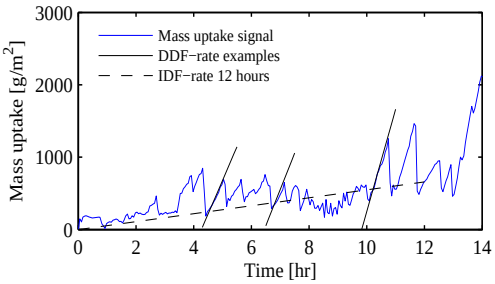

Figure 3.5: Original signal from combustion of straw/wood (flue gas 800 °C) and examples of Integrated Deposit Formation (IDF) and Derivative-based Deposit Formation (DDF) rates.

obtains much higher values (900-1400 g/m^2/h) than the IDF-rate (55 g/m^2/h), for this firing case. When shedding occurs within the exposure time chosen for determination of the IDF-rate, the IDF-rate will always obtain a value between 0 and the DDF-rate. The IDF-rate may be seen as a somewhat uncertain value, as it is greatly influenced by the choice of residence time and occurrence of shedding events within that time. However, the IDF-rate still represents valuable information, as it is an estimate of the amount of deposit accumulated on the probe. The DDF-rate may be regarded as the 'true' deposit build-up rate. However, additional information on the occurrence of shedding is needed for the DDF-rate to be of value in relation to boiler operation.

Figure 3.5 shows a firing case with occurrence of shedding events and therefore a relatively large difference in DDF- and IDF-rates was shown. In cases with no or limited shedding, the IDF-rate and the DDF-rate will be similarly. From the data obtained with the advanced probe, both DDF- and IDF-rates can be obtained and it is to some extent possible to identify whether shedding events influence the IDF-rate. This information is not available for data obtained with the simple probe where only

the IDF-rate can be obtained. In the following it will be evaluated whether IDF-rates obtained by simple probes can be assumed to be approximately equal to the DDF-rate (no/limited shedding occurring), or whether a value between 0 and the DDF-rate will be obtained (shedding occurring). This is done by examining the weight uptake signal from some of the advanced probe measurements obtained from campaigns with comparable conditions; similar fuel, firing technology and flue gas temperature.

The simple probe has mainly been used in the early campaigns in straw-fired grate boilers [51, 56]. The probes used for IDF-rate determinations have mainly been removed after a boiler residence time of 4-12 hours.

Two representative examples of signals from the advanced probe used in straw-fired grate boilers are shown in Figure 3.6. It is seen that the deposit build-up

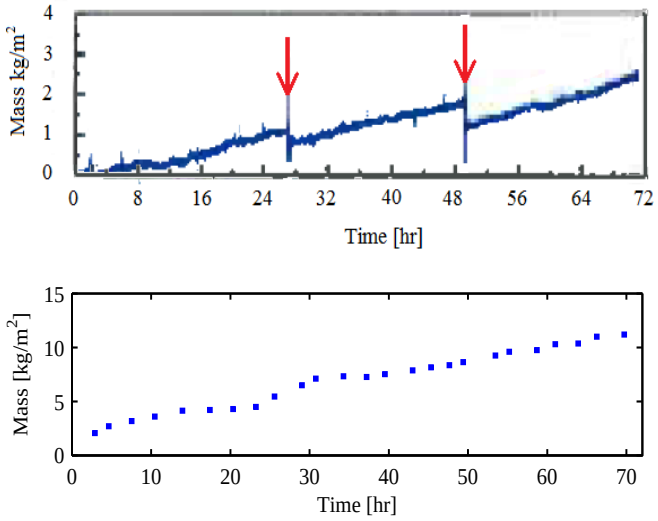

Figure 3.6: Mass uptake on the advanced probe (probe surface temperature 500 °C) in two cases of straw firing in the Avedøre grate-fired boiler. Upper figure: Mean flue gas temperature: 785 °C [57]. Lower figure: Mean flue gas temperature: 1000 °C [58]. The red arrows indicate times where operation of plant soot blowers away from the probe may influence local conditions.

is quite steady in both cases. For the flue gas temperature of 785 °C it is seen that the steady build-up is only interrupted when plant soot blowing is activated. Although a steady build-up is observed at both 785 °C and 1000 °C, the deposit mass may still be influenced by shedding. It was found by Zbogar et al. [58] that when the local flue gas temperature approaches 1000 °C in a straw fired grate boiler, melting and droplet formation occur at the deposit surface and shedding by melting is

observed. Melting is considered to occur as a continuous mass loss process, contrary to debonding, where significant mass loss occurs instantaneously. Melting may thus influence the quantification of the rate of deposit build-up, although it may not be possible to identify from the mass signal from the advanced probe. At local flue gas temperatures below ≈ 900 °C, the camera observation of the deposit surface revealed that it was composed of solid particles, and shedding by melting was not observed [58].

Consequently, it seems that the IDF-rates obtained by the simple probe during grate-firing of straw can be assumed to be approximately equal to the DDF-rate when the local flue gas temperature does not exceed 900 °C. Plant soot blowing was not activated during the experiment. At flue gas temperatures above 900 °C, shedding by melting may remove deposits and the measured IDF-rate will in that case have a value lower than the DDF-rate. This should be considered when analyzing data obtained at flue gas temperatures above 900 °C during straw-firing in grate boilers.

In the measuring campaigns conducted in suspension-fired boilers, three measuring campaigns [59, 61, 123] quantified deposition rates by use of a simple probe. The advanced probe has been applied for the majority of the data obtained in recent campaigns [60, 62, 63]. Detailed information regarding the deposit mass on the probe is thus available.

For a case of straw/wood-firing with > 80 wt% straw and flue gas temperatures near 800 °C, the mass uptake signal is seen in Figure 3.5. For this firing case the IDF-rate was significantly lower than the DDF-rate and should be regarded as an estimate of the accumulated deposit, as already discussed. For wood-firing at similar flue gas temperatures (800 °C), the mass uptake signal is seen in Figure 3.7. It is

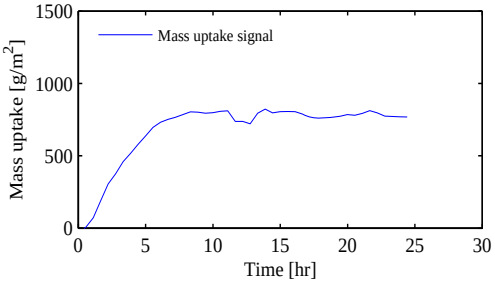

Figure 3.7: Deposit mass uptake on the advanced probe during wood-firing in suspension with a local flue gas temperature of 800 °C and a probe temperature of 530 °C [6, 60].

seen that the amount of deposit on the probe is steady after some initial build-up [60]. This shows that the determination of an IDF-rate largely depends on the choice of exposure time. If deposits are collected in a short exposure time (e.g. 5 hours), an IDF-rate close to the initial DDF-rate is obtained. This IDF-rate will

not be representative for the long-term deposit buildup behavior, however. Again, the determined IDF-rate as obtained with the simple probe is therefore a somewhat uncertain value.

A quite different deposit behavior is observed for wood-firing at high flue gas temperatures (1300 °C). Here, build-up of deposits is followed by nearly complete shedding [6, 60]. This cycle is observed repeatedly. In this case, it makes no sense to calculate an IDF-rate based on a single point.

It is concluded that IDF-rates obtained during suspension-firing of straw and/or wood at intermediate temperatures can be reasonably used as estimates of the accumulated deposit. IDF-rates should not be applied when repeated, complete shedding occurs as observed in wood suspension-firing at flue gas temperatures $> 1200\,^{\circ}\mathrm{C}$.

Deposition Rates in Grate and Suspension Boilers

In this section, the deposit build-up rates observed in grate- and suspension-firing will be compared. The focus will be on the magnitude of the IDF-rates measured. Influence of operational parameters on the deposition rates will be examined for each firing technology subsequently.

In Figure 3.8, the IDF-rates measured in grate-fired (or cigar-fired, Haslev) and suspension-fired units are seen as a function of the flue gas temperatures where the probes were placed. The IDF-rate levels for grate-fired and suspension-fired

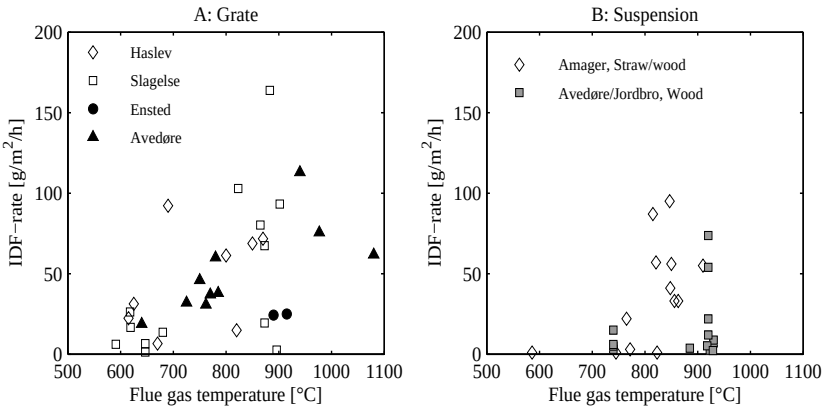

Figure 3.8: IDF-rates as a function of local flue gas temperature. A: Grate-fired units, all straw-fired [51, 56, 57]. B: Suspension fired units [5, 59, 62, 63, 123].

units are comparable, as most IDF-rates are in the range of 0-100 $\mathrm{g/m^2/h}$ for both technologies. This is not an obvious result since during grate-firing only up to 20 wt% ash is entrained whereas up to 80 wt% of the ash is expected to end up in the fly ash during suspension-firing. The ash loading of the flue gas is thus expected to be quite different in the two combustion systems.

In order to account for the differences in the fly ash loading of the local flue gas in the various boilers when examining deposition rates, the ash deposit propensity can be calculated. The ash deposit propensity is defined as the percentage of ash in the flue gas which deposits on the probe and is calculated as follows:

$$\text{Ash deposit propensity [\%]} = \frac{\pi \cdot \text{Deposit flux [g/m}^2\text{/h]}}{\text{Ash flux [g/m}^2\text{/h]}} \cdot 100\%$$

The deposit flux is the IDF- or the DDF-rate. This rate is converted from the rate based on the circumference of the probe to a rate based on the projected area (diameter of the probe) by multiplying with π. The ash flux describes the local ash flow near the probes. The ash flux is determined by the fuel flow to the boiler, the ash content of the fuel, the entrainment and the cross-section area of the boiler at the probe position. The ash flux is thus calculated as follows:

$$\text{Ash flux [g/m}^2\text{/h]} = \frac{\text{Fuel flow [g/h]} \cdot \text{Ash Content} \cdot \text{Entrainment}}{\text{Cross section area at probe position [m}^2\text{]}}$$

The ash content and the entrainment are given as fractions. Calculation of the ash flux has to rely on assumptions and should be regarded as an estimate. The fuel flow in the boilers is assumed to be equal to full load of the boiler, unless stated otherwise in the references. The ash content of the fuel is in all references either provided by analysis of the actual fuel or assumed based on earlier fuel analyses at the plant. The fraction of ash entrained in grate-fired units is found to be within 10-35%, from mass balance [57] or weighed amounts of fly ash and bottom ash [52, 141]. For suspension-fired units, the entrainment is assumed to be 80% of the fuel ash. The ash flux calculations are somewhat uncertain due to the numerous assumptions they are based on. Furthermore, the ash may not be distributed evenly across the boiler cross section area, and this will influence the local ash flux.

The calculated ash deposit propensity based on IDF-rates is seen in Figure 3.9. Note the different scales on the y-axis. It is seen from the scaling of the y-axis in Figure 3.9 that the ash deposit propensity is much higher for the grate-fired units than for the suspension-fired units. For the grate-fired units up to 20% of the ash entrained may deposit on the probe, while for suspension fired units only up to 2% is deposited on the probes. For this comparison it should be kept in mind that the ash propensity for grate-fired units may in reality be higher than 20% at high flue gas temperatures, since shedding by melting may decrease the determined IDF-rate. Furthermore, the IDF-rates obtained in suspension-firing should be regarded as somewhat uncertain values.

The difference in the ash deposit propensity of the two combustion systems may be explained by the difference in the chemical composition of the fly ash observed earlier. Due to a high content of K, Cl and S in the fly ash from grate-firing, compared to suspension-firing, the fly ash from grate-firing is expected to have a high fraction of molten and gaseous species in the temperature range 600-1000 °C. The high melt

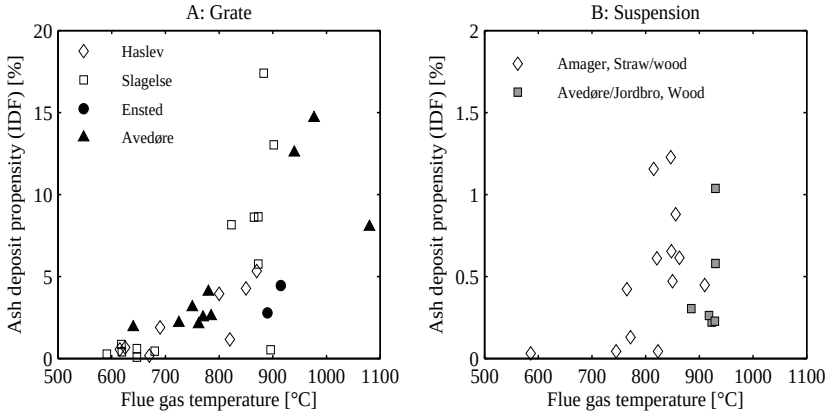

Figure 3.9: Ash deposit propensities based on IDF-rates as function of local flue gas temperature. A: Grate-fired units, all straw fired [51, 56–58]. B: Suspension fired units [5, 59, 61–63].

fraction will make the particles (and deposit surface) more sticky and thus result in higher ash propensity.

Parameters Influencing Deposit Build-up Rates in Grate-fired Boilers

In this section, the influence of operational parameters (the probe and flue gas temperatures and ash chemical composition) on the deposit build-up rates in grate-fired units is examined.

The influence of probe temperature was examined by Jensen et al. [57] for probe temperatures in the range of 400-550 °C in a series of experiments where the mean flue gas temperature was within 700-800 °C. In the temperature range examined, there was no significant effect of the altered probe temperature on deposit build-up rates [57].

In Figure 3.9A, the ash deposit propensity for the straw-fired grate boilers is seen as a function of the local flue gas temperature. It is seen that ash deposit propensity increases with increasing flue gas temperatures. The increase is quite significant at temperatures above 800 °C. The influence of temperature can be related to the melting characteristics of fly ash from grate-fired boilers (Figure 3.10). At temperatures above 800 °C, the ash contains large fractions of melt, which increase the stickiness of the particles and thereby deposit formation rates.

The chemical composition of the fly ash (and thereby also the fuel ash) may also influence the rate of deposit formation during grate-firing. In Figure 3.11 the ash deposit propensity is seen as a function of the K-content of the fuel ash (A) and of the fly ash (B). The data are from measuring campaigns where corresponding

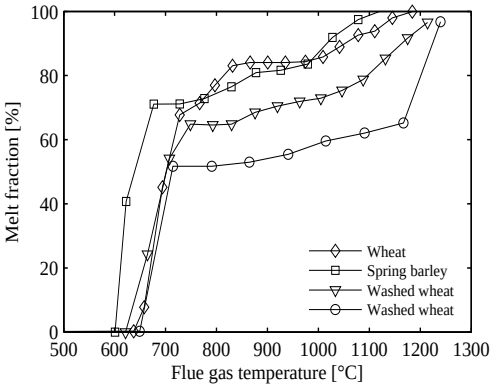

Figure 3.10: Melting curves for four fly ashes from straw grate-firing determined by STA (simultaneous thermal analysis) [48].

samples of fuel, fly ash and deposits were collected for each experiment [51, 56]. It is seen in both Figures 3.11A and 3.11B that when the flue gas temperature is low (<800 °C) the ash deposit propensity is low (< 2%) regardless of the K-content of the fuel or fly ash and no correlation is observed. For the high temperature data (T_{fg} > 900 °C) no correlation with the fuel ash K-content can be observed with these data, with only four data points available. However, for the deposits obtained at the intermediate flue gas temperatures (800-900 °C) correlations with the fuel ash and fly ash K-content can be observed. The R^2 values of the correlations are 0.44 for the fuel ash K-content and 0.93 for the fly ash K-content. The difference in the R^2 values of the correlations originate from the differences in fuel ash and fly ash compositions found in grate-firing units, as observed earlier.

Based on these examinations, it is seen that for straw-fired grate boilers an increased deposition rate can be expected when the flue gas temperature and the fuel ash or fly ash K-content increases.

Parameters Influencing Deposit Build-up Rates in Suspension-fired Boilers

In this section, the influence of flue gas temperature and fuel composition on deposit build-up rates observed in suspension-fired units is examined. As discussed earlier, the IDF-rates obtained in suspension-fired units were uncertain data due to occurrence of shedding, providing an estimate of the deposit accumulation on the probe. The DDF-rates are deposit build-up rates without influence of shedding, and these rates thus obtain higher values than the IDF-rates. In order to examine the influence of operational parameters on the rate of deposit build-up, without influence of deposit removal, DDF-rates obtained in the suspension-fired boilers are investigated.

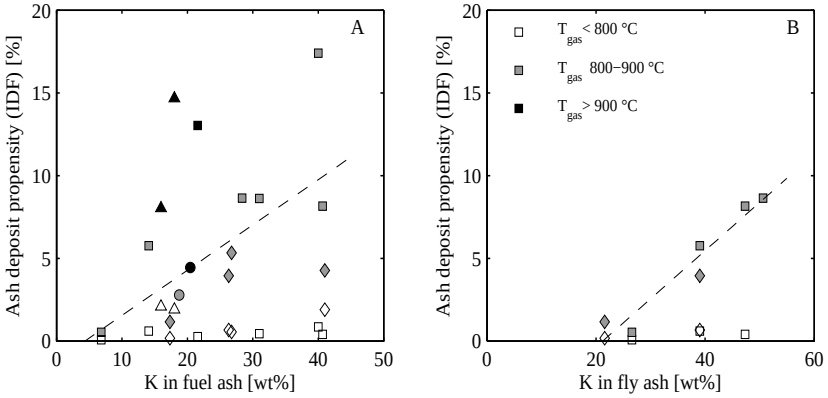

Figure 3.11: Ash deposit propensity as a function of fuel ash K-content (left figure) and fly ash K-content (right figure) for grate-fired boilers. The colored points indicate the flue gas temperatures at the probe position. Point shape indicates the boiler; ◇: Haslev, □ : Slagelse, ○: Ensted, △: Avedøre [51, 56]. The lines are linear correlations for the 800-900 °C data, obtained by least-squares analysis.

In Figure 3.12, available DDF-rates (A) and ash deposit propensity (B) are shown as a function of the local flue gas temperature. It is seen that the flue gas temperature influences the DDF-rates and the ash deposit propensity measured in suspension boilers. The deposit build-up rates increase with increasing flue gas temperatures. However, the influence of temperature on ash deposit build-up rates is quite different for straw/wood mixtures and wood as fuel. When straw is present in the fuel, a great increase in the DDF-rate and the ash deposit propensity is observed when the flue gas temperature approaches 900 °C. When pure wood is used as fuel, the DDF-rate and ash deposit propensity are low at temperatures near 800 °C and increases at temperatures >1200 °C. This difference between fuels can be explained by the differences in the melting behavior of the fly ash. Melting behavior as determined by standard ash fusion tests is seen in Table 3.5.

For suspension-firing with straw in the fuel, three melting tests have been performed for fly ash [5]. These types of fly ash have initial deformation temperatures around 800-900 °C and are completely molten at temperatures around 1200 °C. Two melting tests of laboratory fuel ash from straw are included in Table 3.5. The melting behavior of these ashes is quite similar to the melting behavior of the fly ash from straw/wood suspension-firing. This similarity can be related to the relatively similar chemical composition of fuel ash and fly ash observed previously.

For the wood fuels no melt tests of fly ash from suspension-firing were available. Table 3.5 shows melting tests of laboratory ash from wood. These are assumed to be representative for suspension-firing fly ash, based on the similar melting behaviors

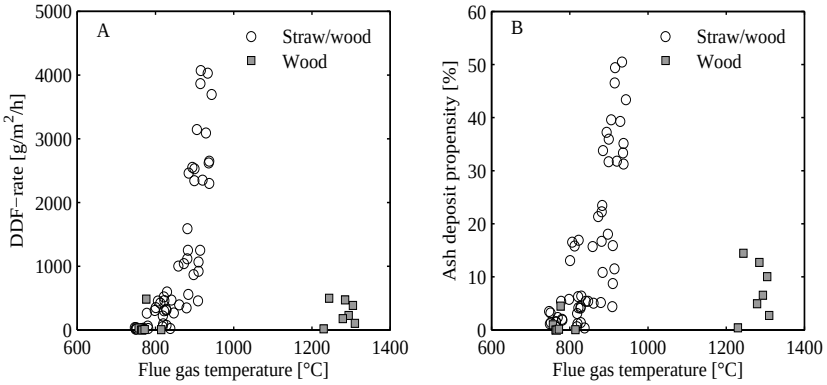

Figure 3.12: A: Derivative-based Deposit Formation (DDF) rates and B: Ash deposit propensity (based on DDF rates) obtained in suspension fired boilers [5, 6, 60, 63].

Table 3.5: Ash melting temperatures [°C] of various ashes found in literature as determined by standard ash fusion tests. The fuel ash is laboratory ash prepared at 550 °C.

Straw	Ash examined	IDT	HT	FT	Ref.
40 % straw in wood	suspension fly ash	800	1115	1260	[5]
60 % straw in wood	suspension fly ash	780	1115	1260	[5]
80 % straw in wood	suspension fly ash	865	1110	1210	[5]
Straw	fuel ash	885	1060	1225	[5]
Wheat straw	fuel ash	900	1170	1190	[142]
Woods					
Wood	fuel ash	1210	1225	1240	[5]
Forest residue	fuel ash	1150	1210	1220	[142]
Logging residue pellets	fuel ash	1170	1240	1310	[143]
Bark, birch pellets	fuel ash	1200	1230	1230	[143]

IDT: Initial deformation temp., HT: Hemisphere temp., FT: Fluid temp.

of fuel ash and fly ash observed for straw. The wood ash initiated melting at very high temperatures ≥ 1150 °C and complete melting was observed at 1220-1310 °C.

When comparing the melting temperatures in Table 3.5 to the flue gas temperatures where increases in DDF-rates and ash deposit propensity were observed in Figure 3.12, it is seen that there is quite good agreement. The differences in deposition behavior observed for suspension-firing of straw/wood mixtures and wood can thus be related to different fuel ash melting characteristics.

In the measurements with suspension-firing of straw/wood, the straw share in

the feedstock varied in the range of 0-85 wt%. Below, it is examined how the straw share affects deposit formation. In the experiments performed with suspension-firing, chemical analysis of the fuel mixture used in each experiment was not conducted, and so the deposit build-up cannot be correlated to elemental content of the fuel, as was done for the grate-fired units. However, fuel was sampled on a daily basis during the campaign and the ash fraction in the fuel mixture was measured. Based on the ash fractions, the straw share in wood was estimated by a linear correlation between the ash contents of the two pure fuels (6 wt% for straw and 0.8 wt% for wood) [63].

In the following analysis, the data are divided into three groups; (1) Straw shares <12 wt%, where wood dominates the chemical composition of the ash, (2) straw shares within 12-40 wt% and (3) straw shares > 40 wt%, where the straw dominate the chemical composition of the ash.

The DDF-rates and ash deposit propensity are seen as a function of estimated straw shares in Figure 3.13. Figure 3.13A shows the measured DDF-rates as a

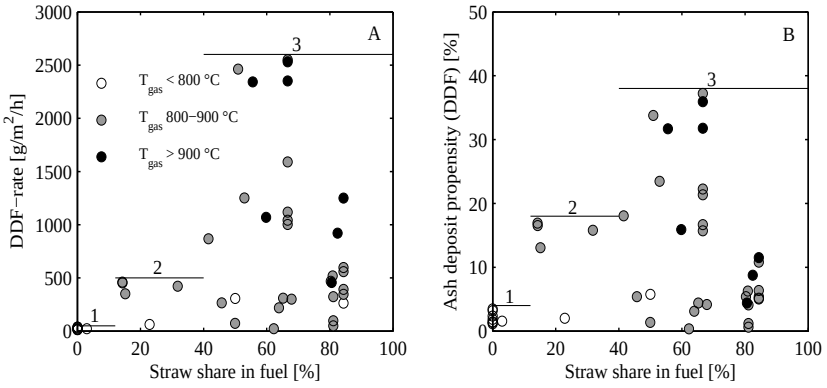

Figure 3.13: Derivative-based Deposit Formation (DDF) rates and ash deposit propensity as function of the straw share in wood for suspension-firing [63]. Data obtained at high boiler loads (>80 %) are excluded from this figure. For the remaining data the boiler load was around 60%, and the experimental conditions are thus comparable. The lines indicate maximum values for each fuel group (1: < 12% straw; 2: 12-40 % straw; 3: >40 % straw).

function of the estimated straw share in the fuel mixture. It can be observed that the data for group 1 (< 12 wt% straw) all result in low DDF-rates <50 g/m^2/h while the data for group 2 (12-40 wt% straw) have DDF-rates below 500 g/m^2/h. For straw shares > 40 %, DDF-rates up to 2500 g/m^2/h are observed. This 'stepwise' analysis indicates that increasing straw shares lead to increased deposition rates. The wide scattering of the data and the influence of temperature, however, need to be considered.

The relatively low DDF-rates obtained with 80 wt% straw share in the fuel were

not expected. In laboratory- and pilot scale experiments resembling suspension firing, increased deposit build-up has been observed with increasing straw shares in the fuel mixtures [17, 34]. Unfortunately, the observation at 80 wt% straw share cannot be explained from the available experimental data.

When the straw share is increased, both the total ash content of the fuel is increased and the chemical composition of the ash is altered. In Figure 3.13B, the ash deposit propensity is plotted as a function of straw share. Here, the increase in straw share only causes altered chemical composition since the increase in ash fraction is included in the calculation of ash deposit propensity. It is seen that the ash deposit propensity of group 1 ($<$ 12 wt% straw) is lower than 5%, while the ash deposit propensity of group 2 (12-40 wt% straw) may be up to 18%. For group 3, ash deposit propensity up to 40 % is observed. This shows that both the increased amount of ash as well as the changed ash composition, resulting from using increased fractions of straw in the fuel, cause increased deposit formation rates.

The data in Figure 3.13 are quite scattered. The scattering may to a large extent be explained by boiler operation fluctuations and by variations in the chemical composition of the fuel. The time span of the measuring campaign was approximately one month [63]. The fuel supply to the boiler will most likely have changed a number of times during that period. A few fuel samples were analyzed and showed differences in chemical composition, although the straw share was estimated to be similar [63].

Based on these examinations it is seen that for suspension-fired boilers, an increased deposition rate can be expected when the flue gas temperature and/or the straw share are increased.

3.2.3 Shedding of Deposits

Zbogar et al. [45] identify several types of shedding mechanisms; melting, gravitational shedding (including debonding), erosion etc. The occurrence of these shedding mechanisms can be related to the physical properties (degree of sintering or melting) of the deposits and they occur at various locations inside the deposits.

In this section probe shedding measurements will be reviewed and parameters influencing the occurrence of shedding will be identified when possible. In the discussion, the shedding observed is divided into two phenomena: natural and artificial shedding. Natural shedding is the shedding occurring when plant soot blowers are not in operation. Artificial shedding is thus the shedding observed when the soot blowers are active, although the blowers close to the probe position were in most cases shut off. Operation of the remaining plant soot blowers may influence local conditions and thereby the occurrence of shedding during the tests.

Shedding Observations in Full-Scale Boilers

The observations on shedding behavior made in full-scale boilers are summarized in Table 3.6. All of the observations on shedding are made with the advanced deposition probe, periodically equipped with a camera. In two campaigns [57, 140], a soot blower probe parallel to the deposit probe was applied.

During grate-firing of straw at low or intermediate flue gas temperatures ($<$ 900 °C), no natural shedding (melting, debonding or erosion) was observed [57, 58]. A soot-blower probe was applied where the local flue gas temperatures were within 700-800 °C. It was possible to remove the deposits by soot blowing, depending on the temperature and residence time of the probe [57]. These measurements are reviewed later. No soot-blowing measurements were performed for flue gas temperatures above 800 °C. At flue gas temperatures $>$ 900 °C, it was observed that the shedding of deposits took place by surface melting and droplet formation. It was found that the local flue gas temperature governs the state of the deposit. At 1100 °C or above the deposit surface layer was completely molten, and the deposits were rapidly removed from the probe as droplets [58].

For suspension-fired boilers, shedding has been examined for straw/wood mixtures [5, 140] and for wood [60]. Examples of the mass-uptake signal from the advanced probe were shown in Figures 3.5 and 3.7. The deposition behavior during straw/wood suspension firing is characterized mainly by a rapid deposit build-up followed by shedding. According to observations, the shedding mainly took place by debonding, both as natural and artificial shedding. An example of shedding by debonding is shown in Figure 3.14, where formation of a 'hammock' was observed within minutes prior to the shedding [5]. 'Hammock' formation was not observed in all shedding events by debonding. In some cases a simple break-off of a small piece was observed. It is seen in Figure 3.14 that debonding of the deposit does not occur

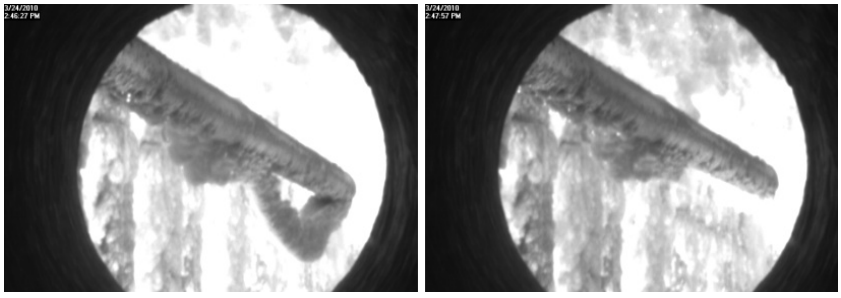

Figure 3.14: Example of observed shedding event [5]. The event is observed after 50 minutes probe exposure time during combustion of a straw/wood mixture containing 80% straw. The time frame between the photos is 1.5 minutes and 34% of the deposit was removed, according to the load cell.

Table 3.6: Shedding observations made in full scale biomass fired boilers.

Boiler	Fuel	Flue gas °C	Probe °C	Natural Shedding	Artificial Shedding	Comments	Ref.
Avedøre, grate	Straw	700-800	400-550	None	Debonding Fracture	Soot blower probe applied. The probe surface temperature and residence time influence how easily deposits are removed[a].	[57]
Avedøre, grate	Straw	800-1000	500	Melting		Flue gas temperature controls shedding by melting ≈ 900°C; Initial melt formation. ≈ 1000°C; Deposit partly molten, formation of droplets and thereby deposit removal. ≈ 1100°C; Deposit molten, rapidly removed as droplets.	[58]
Amager, suspension	Straw/ wood	600-1050	500-600	Debonding Erosion Fracture	Debonding	Incomplete shedding of deposits. Limited amount of erosion and fracture observed by visual inspection. No melting of deposits was observed, even at temperatures > 1000°C. Soot blower probe applied[b].	[5, 63]
Avedøre, suspension	Wood	800	550	Not identified		A steady mass on the probe was obtained after some initial deposit buildup. A possible shedding mechanism is erosion (not confirmed).	[6, 60]
Avedøre, suspension	Wood	1300	550	Debonding		Frequent shedding with complete removal of deposits.	[6, 60]

a: Increasing the probe surface temperature from 400°C to 550°C changed the deposit from easy removable to one requiring a high PIP soot blowing for removal.
b: Most of the deposits could be removed by soot-blowing. The required PIP to remove the deposit increased with probe temperature.

at the whole length of the probe. Some deposit remains on the part of the probe near the camera.

Besides shedding by debonding, erosion caused by impaction of non-sticky, hard fly ash particles and shedding of small deposit layers (fracture) were also observed, to a minor degree, by visual inspection of the probe during operation. Shedding by surface melting was not observed, although the flue gas temperature was $> 1000\,^{\circ}C$ for short periods of the tests [140].

Differences in the shedding behavior when straw fired on a grate and in suspension were thus observed. This difference is most likely related to the different chemical composition of the fly ash and deposits in the two combustion systems. Jensen et al. [57] have tested the strength of sintered fly ash pellets from straw-firing in grate and suspension boilers. It was found that the strength increase associated with onset of sintering occurs at low temperatures ($450\,^{\circ}C$) for fly ash from grate-firing compared to fly ash from suspension firing ($650\,^{\circ}C$). The difference was explained by differences in chemical composition of the ash. See Appendix A.1 for additional information.

For suspension-firing of wood, shedding observations were made in the Avedøre boiler at two positions where the flue gas temperatures were approximately $800\,^{\circ}C$ and $1300\,^{\circ}C$. When the flue gas was $800\,^{\circ}C$, the deposit mass on the probe became constant at a low level after some initial build-up, indicating equilibrium between deposit build-up and shedding. The type of shedding at this position was not identified, but in view of insignificant mass loss it was probably not by debonding [6, 60]. A possible mechanism in this position could be erosion, but this has not been verified. With a flue gas temperature near $1300\,^{\circ}C$, the deposit build-up was fast, and many shedding events with almost complete removal of the deposit by debonding took place [6, 60].

It can be concluded that the shedding behavior when firing wood in a suspension boiler was quite different from what was observed with the straw/wood mixture fired in a suspension boiler. A thick layer of deposit was never established on the probe during wood firing at these flue gas temperatures. Lab scale studies examining the compressive strength of sintered ash pellets from various biofuels have been conducted [57, 142, 144]. A sintering temperature, at which onset of strength increase occurs, has been defined by Jensen et al. [57]. It was found that the sintering temperatures for straw fuel ash generally were in the range $610\text{-}710\,^{\circ}C$ while the sintering temperature for wood ash was higher, $> 780\,^{\circ}C$ [57]. From the lab-scale studies [142, 144] it is observed that wood ash does not gain as much strength as straw or grass ash during sintering. See Appendix A.1

Removability of Deposits

To gain further knowledge about how difficult deposits are to remove and about the influence of time and probe temperature, a soot-blower probe was used along with the deposit probe in two of the measuring campaigns [57, 140]. Use of the soot blower

probe allowed the peak impact pressure (PIP) needed for removal of the deposits to be determined.

During the measurements in the Avedøre grate boiler, the deposit probe metal temperature was varied in the range of 400-550°C [57]. For the soot blower probe a critical PIP was defined as the pressure needed for removal of more than 75% of the deposit on the probe. Figure 3.15 shows the critical PIP measured after 100 hours of exposure (4 days) and just before the probe was removed at the end of the experiment after 260-740 hours (11-31 days). As seen in Figure 3.15, both the

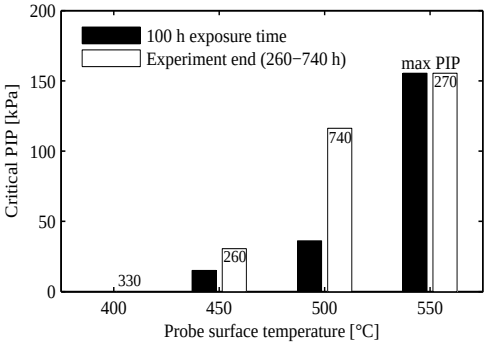

Figure 3.15: Critical PIP for removal of upstream deposit for different probe surface temperatures and exposure times [57]. At 550°C less than 25 % deposits were removed at max PIP. The flue gas temperature is within 700-800°C during the tests.

probe temperature and the exposure time influenced the removability of the upstream deposit. At a probe temperature of 400°C, the deposits were removed easily with PIP less than 0.5 kPa. Higher probe temperatures and long exposure times lead to deposits which were difficult to remove. When the probe temperature was 550°C, the maximum possible PIP (150 kPa) could only remove $< 25\%$ of the deposit, even at the short residence time (100 h). The effect of temperature and time was considered to be due to sintering and thereby increased deposit strength and possibly increased deposit-tube adhesion strength. The mechanism of removal was in all cases fracture and debonding induced by the soot blower. For the downstream deposits, it was found that these were easily removed, except at the highest temperature (550°C [57]).

A soot blower probe was also applied during straw/wood-firing in a suspension boiler. The influence of time and probe temperature was examined by measuring the PIP needed for removal of deposits at various conditions [140]. The results are shown in Figure 3.16 where it can be seen that with a probe temperature at 500°C the PIP needed for removal of deposits increased with exposure time. When the probe temperature is 600°C, the exposure time was less significant and the deposits were difficult to remove even at short residence times [140]. These results are in

line with the results obtained for the straw-fired grate boiler [57]. The soot-blower

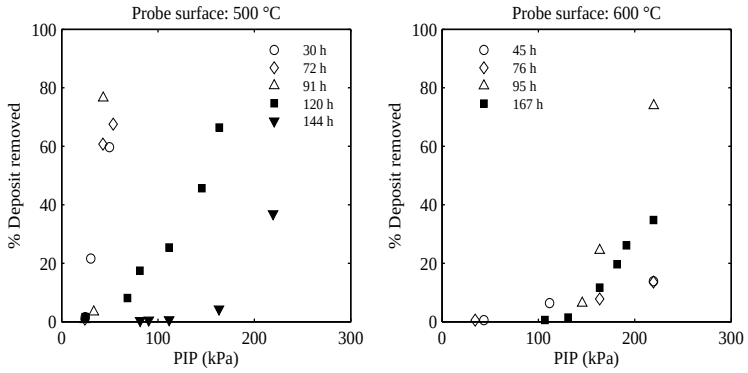

Figure 3.16: Percentage of deposits removed as a function of PIP and residence time. The deposit mass load on the probe increases with exposure time. Adapted from Bashir et al. [140].

PIP measurements demonstrated that time and probe temperature influence the strength of deposits and/or the adhesion strength between deposits and probe metal, as the deposits became difficult to remove at high probe temperatures and increased residence time.

For coal-firing, deposit strength has been correlated to deposit porosity [46]. The porosity changes by sintering reactions [45] and changes in porosity have been described as a function of time, chemical composition and temperature [145, 146]. It is considered that similar effects apply to biomass firing. Besides the strength of the deposits, the adherence strength between the deposits and the probe is considered to be important. However, very little knowledge is available on this aspect.

Parameters with Influence on Shedding

During suspension firing of straw/wood mixtures, shedding events were tracked by use of the advanced in-situ deposition probe in combination with a camera [140]. The influence of several parameters on shedding behavior was examined based on these data. Plant soot-blowers were in operation during some periods (1.7 h on average) of varying frequencies. The soot-blower close to the deposition probe was shut off, but the operation of the remaining blowers may induce fluctuations in the boiler operation, thereby influencing the deposition behavior on the probe. Therefore, before the data analysis, the shedding events observed during periods with plant soot blowing were clearly separated from the remaining data. The shedding data obtained during periods without soot blowing, termed 'natural' shedding events, will be reviewed in the following. The results obtained during soot blowing periods are

not discussed in detail, but differences or similarities to the natural shedding behavior will be noted, when relevant.

In the analysis of the shedding data, the shedding behavior has been quantified by three measures; shedding frequency [events/h], mass loss per event [g/m^2], and shedding rate [g/m^2/h], which is a product of the first two measures. In Figure 3.17 the shedding rate, given as 6-hour mean values, is seen as a function of the mean DDF-rate from the same period. A diagonal (dotted) line indicating identical rates

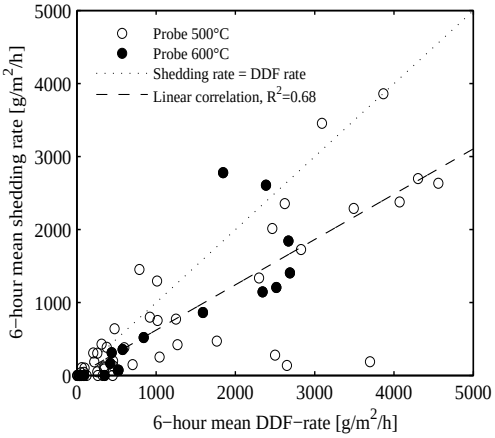

Figure 3.17: Shedding rate vs. Derivative-based Deposit Formation (DDF) rate given as six-hour mean values for straw/wood-firing. Only shedding events occurring without plant soot blowing are included [140].

of shedding and deposition is seen in Figure 3.17. For most periods the shedding rate is lower than the DDF-rates, as most points are below the dotted line. This corresponds well with the observation made earlier; during straw/wood suspension-firing large fluctuations in the deposit mass are seen, but the mass remaining on the probe increases with time. The dashed line indicates a linear correlation between the DDF-rate and the shedding rate. The slope of the line is 0.62, and hence the shedding rate corresponds on average to 62% of the DDF-rate. The linear correlation furthermore reveals that in periods with high DDF-rates, high shedding rates are often observed. When the DDF-rates are high, deposits quickly accumulate on the probe. There is thus a short time for deposit consolidation by sintering before the mass of the deposit on the probe becomes too large for the adhesion strength to keep it on the probe, and shedding occurs.

In Figure 3.18, the shedding rate observed in Figure 3.17 has been divided into a shedding frequency (Figure 3.18A) and the mean mass loss per shedding event (Figure 3.18B), both obtained in 6 hour periods. It is seen that the shedding frequency increases with increasing DDF-rate, although with large scattering of the data. The

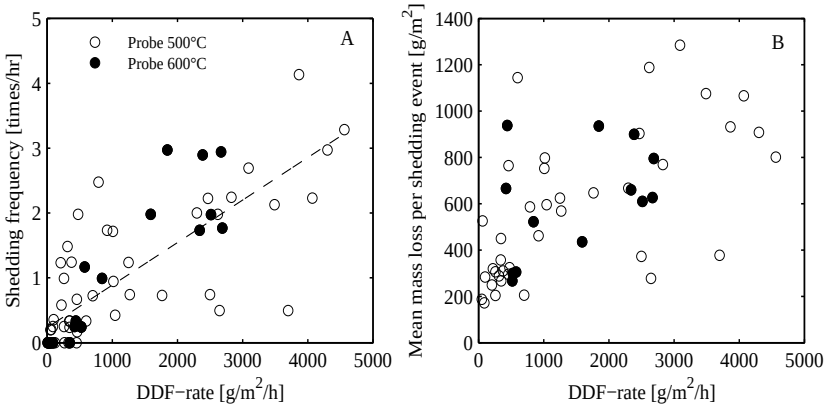

Figure 3.18: A: Shedding frequency vs. DDF rate. B: Mean mass loss per shedding event vs. DDF rate. Only shedding events occurring without plant soot blowing are included. Suspension firing of straw/wood mixtures [140]

data showing the mean mass loss per shedding event cannot be correlated with the DDF-rate. These observations imply that during periods with quick accumulation of deposits shedding occurs frequently, but the amount of deposit lost per event is not affected significantly. The mass loss per event is on average 600 g/m^2, regardless of DDF-rates, flue gas temperature or mass load of deposit on the probe [140]. Figure 3.19 shows the percentage of mass lost in a single event as a function of the time of the shedding event in five tests performed by Bashir et al. [140]. The probe residence

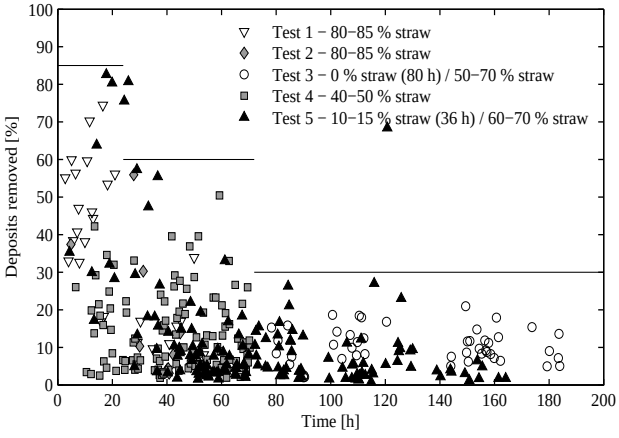

Figure 3.19: Percentage of mass lost in each single event as function of the time of the shedding event for natural shedding events [140].

time seems to influence the volume of the deposit removed in a single natural shedding event. Within the first 24 hours up to 85 % removal of the accumulated deposit may occur in a single shedding event. When the probe residence time is 24-72 hours, the maximum deposit removal is lowered to around 60% and at residence times longer than 72 hours it seems that only up to 30 % of the deposit was removed in a single shedding event. The results obtained for the periods where plant soot blowing was activated are similar to what was observed for the natural shedding. Consequently, the influence of time observed here is in agreement with the observations obtained during the experiments with the soot-blower probe discussed earlier. It is also seen that natural shedding is a stochastic process where the amount of deposit removed in a single shedding event is not easy to predict.

In Section 3.2.2 it was demonstrated that the straw share of the straw/wood mixture influences the DDF-rate. Figure 3.20A shows the shedding rate vs. straw share of the fuel. It is seen that the influence of straw share on the shedding rate

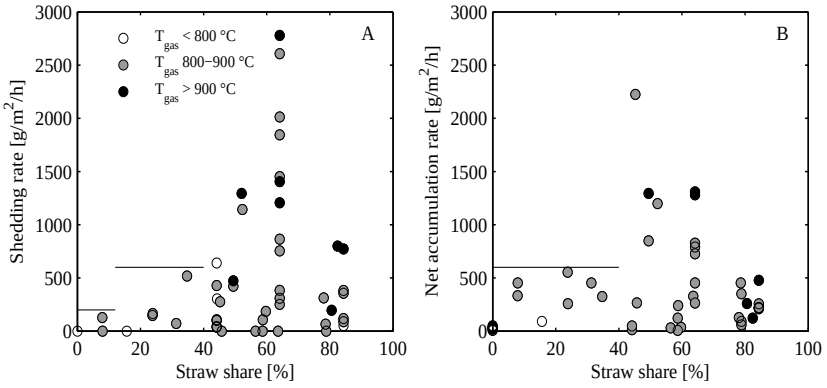

Figure 3.20: Shedding rate and net accumulation rate as function of straw share in wood [140]. Some data obtained at high boiler loads (>80 %) are excluded from this figure. For the remaining data the boiler load was around 60 %, and the experimental conditions are thus comparable. The lines indicate maximum values for each fuel group (see text).

follows the same characteristics as on the DDF-rate. When wood ash dominates the ash fraction (straw < 12%), the shedding rate is < 200 g/m^2/h. At straw shares in the range of 12-40%, shedding rates increase and may reach 500 g/m^2/h while at straw shares above 40%, where the straw ash dominates the fuel ash, high shedding rates up to 3000 g/m^2/h may be observed. As the shedding rates follow the DDF-rates, it is not possible to determine whether the straw share or the DDF-rate is responsible for the shedding rates illustrated in Figure 3.20A.

Figure 3.20B shows the net accumulation rate as a function of straw share. The net accumulation rate is calculated as the mean DDF-rate less the mean shedding

rate for a 6-hour period. It is observed that the net accumulation rate is low ($<$ 600 g/m^2/h) when the straw share is lower than 40 wt%.

The net accumulation rate has been plotted as a function of the flue gas temperature in Figure 3.21. It is seen that there is a clear correlation between the flue

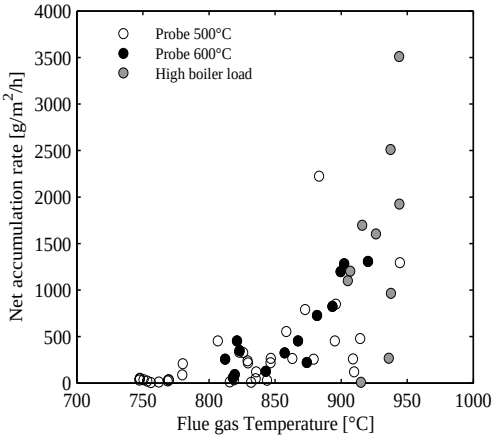

Figure 3.21: Net accumulation rate as function of flue gas temperature during suspension firing of straw/wood mixtures [140]. Data obtained at high boiler load (excluded in Figure 3.20) are indicated by grey points.

gas temperature and the net accumulation rate, which is as expected since the flue gas temperature was also an important parameter influencing the DDF-rate. This implies that during operation, high accumulation rates can be expected for high flue gas temperatures and/or straw shares.

3.3 Conclusions on Probe Measurements

A number of full-scale deposit probe measuring campaigns conducted in grate- and suspension-fired biomass boilers have been reviewed and compared. Influence of operational parameters on the chemistry of ash and deposits, on deposit build-up rates and on shedding behavior has been examined.

Firing technology and fuel type had a significant impact on the fly ash chemistry. During grate-firing of straw the fly ash was enriched in K, Cl and S compared to the fuel ash. During suspension-firing the fly ash composition largely resembled the fuel ash composition, due to a higher degree of entrainment of ash in the combustion zone. The fly ash from suspension firing of straw was thus dominated by K and Si while wood-firing in suspension boilers lead to fly ash dominated by Ca and K.

The deposit chemical composition was influenced by firing technology, fuel choice and flue gas temperature. At low local flue gas temperatures ($<$ 800 °C), the deposit

compositions were similar to those of fly ash. Increases in local flue gas temperatures increased the content of Si and Ca in the deposits and decreased the Cl content. The influence of flue gas temperature is similar for grate and suspension-firing.

The rate of deposit build-up has been defined by two measures; an IDF-rate, possibly including shedding events, and a DDF-rate, which is the build-up rate without interference from shedding events. For grate boilers limited natural shedding is expected for flue gas temperatures $< 900\,^{\circ}\mathrm{C}$. Above this temperature shedding by melting may influence IDF-rates. Shedding has significant influence on the IDF-rates in suspension boilers, and these should be regarded as uncertain estimates of the deposit accumulation. DDF-rates are currently only available from probe measuring campaigns in suspension boilers.

The IDF-rates in the two combustion systems are at similar levels; 0-100 $g/m^2/h$. Differences in the ash flux in the different boilers are included by calculating ash deposit propensity. The ash deposit propensity is an order of magnitude larger in grate-fired boilers than in suspension boilers. This can be related to differences in fly ash chemistry.

Ash deposit propensity increases with flue gas temperatures. For all boilers and fuels examined, a steep increase in ash deposition propensity was observed at flue gas temperatures close to the temperatures where melting of the fly ash was expected based on STA analysis or ash fusion tests. The rate of deposit build-up was furthermore found to increase with K content in the fuel ash and fly ash for grate-fired boilers. For suspension-fired boilers deposition rates were low for wood-firing whereas increases in deposition rates were observed with increasing straw shares.

The shedding of deposits has been monitored under various combustion conditions. During grate-firing of straw at low or intermediate flue gas temperatures ($<900\,^{\circ}\mathrm{C}$), no natural shedding (melting, debonding or erosion) was observed. At higher flue gas temperatures ($>900\,^{\circ}\mathrm{C}$), shedding of deposit took place by surface melting and droplet formation. For suspension firing of straw, natural shedding was observed to occur frequently primarily by debonding. Shedding by debonding was incomplete and increased deposit mass accumulated on the probe. Shedding by melting was not observed even at temperatures above $1000\,^{\circ}\mathrm{C}$. During wood suspension-firing, a thick layer of deposit never formed on the probe. At low flue gas temperatures, $800\,^{\circ}\mathrm{C}$, a small amount of deposit initially accumulated on the probe and the mass on the probe then remained constant. At high flue gas temperatures, $1300\,^{\circ}\mathrm{C}$, the deposition was characterized by a rapid build-up followed by complete shedding.

Soot blowing tests were conducted during grate-firing of straw and suspension-firing of straw/wood. It was in both cases found that increased probe surface temperature and residence times lead to deposits which are more difficult to remove.

Shedding behavior was closely monitored during straw/wood firing in suspension boilers. The shedding rate [$g/m^2/h$] and frequency [events/hr] increased with in-

creasing DDF-rates, whereas the deposit mass lost per event [g/m^2] seemed to be relatively stable. The percentage of deposits removed per shedding event decreased with residence time. Up to 80 % of the deposit on the probe was likely to be removed in a shedding event within the first 24 hours of exposure. Contrary, at exposure times $>$ 72 hours, only up to 30 % removal per shedding event could be expected. Camera observations revealed that the percentage of mass loss corresponded to a percentage of the probe lenght left uncovered, as the shedding occurred by debonding near the probe surface.

The net accumulation rate, calculated as the difference between the DDF-rate and the shedding rate was found to increase with increasing flue gas temperature and straw share during straw/wood firing in suspension boilers.

Chapter 4

Model for Fly Ash Formation

Before a calculation of deposit formation can be initiated, a proper description of the ash found in the flue gas is needed. During the combustion, the inorganic matter (ash) in a fuel particle is divided in two parts; a vaporized fraction and a coarse fraction, as indicated in Figure 4.1. The vaporized part (K, Cl and S) may then react and nucleate forming gaseous components and aerosols. The coarse fraction of the ash can be described by a particle size distribution and by the chemistry of the particles. Then, by knowing the chemistry and the temperature of the particles, material properties can be predicted. Part of the coarse ash will be found as large particles, which are unable to follow the gas through the reactor and will be 'lost' primarily as bottom ash.

A proper model of the fly ash should include species formulation and concentrations of gases, aerosols and coarse ash and a particle size distribution of at least the coarse ash fraction. In the following, a model for the ash formation, considering these parameters is described.

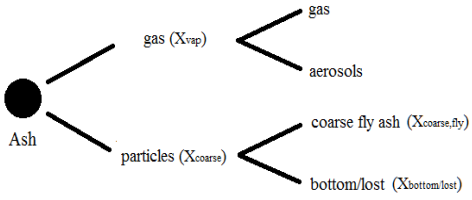

Figure 4.1: Illustration of the ash mass balance

It is in this work generally assumed that no interaction occur between the coarse ash particles and the vaporized species in the flue gas. Furthermore, it is assumed that it is only part of the large ash fraction which is lost in the reactor. All gases and aerosols are thus assumed to follow the flue gas to the position of the probe.

The ash mass balance can then be expressed as:

$$1 = X_{vap} + X_{coarse,fly} + X_{bottom/lost} \tag{4.1}$$

Where X_{vap} is the vaporized fraction of the fuel ash (forming gases and aerosols). This fraction is estimated in the model. $X_{coarse,fly}$ is the fraction of the ash found as coarse ash which follows the flue gas. This fraction is determined by either measurements or assumptions and will be described with the experiments in question.

4.1 Concentrations of Gases and Aerosols

The description of gas and aerosol concentrations occur in three consecutive steps in the model. First, the vaporized fraction (X_{vap}) is calculated, by assumptions on release of the individual elements; K, Cl and S. Then, reaction between the elements forming KCl, KOH, K_2SO_4, SO_2 and HCl is described. Finally, physical transformations of the individual species into aerosols are proposed. These steps are described in the following

4.1.1 Release of K, Cl and S

The release of inorganic elements to the gas phase has been examined in entrained flow reactor (EFR) combustion tests with various woods and straws along with olive residue by Shah et al. [15] and Damoe et al. [16]. These test were discussed in Section 2.3.2 of this thesis.

In both combustion units, a near complete release of Cl and S was generally observed. However, for some high-Cl fuels (straw and olive residue) used by Shah et al. [15], some Cl was retained in the particles. This has not been explored further. In this model, it is assumed that the fuels experience a full release of S and Cl to the gas phase.

The release of K was generally observed to be above 85 %, in both EFR experiments [15, 16]. However, for some straws and for the olive residue, a lower release (45-75 %) was observed. This was discussed to be due to high contents of Si in the fuels and a low Ca content. Thus, retaining effects of Si on the release of K may have been important, when Ca was not present in high amounts in the fuel [16]. This has been explored further, as the behavior of K in the combustion is considered important for the ash deposition behavior.

The release of K as measured by Shah et al. [15] and Damoe et al. [16] is shown as function of selected molar ratios of the fuels in Figure 4.2.

It is seen in Figure 4.2, that when the molar ratio (Ca+Mg)/Si > 0.5 (at which all Si may be found in relation with Ca or Mg), the release of K was > 85 %. In the model, it is assumed that when the molar ratio (Ca+Mg)/Si > 0.5 the release of K is 90 %.

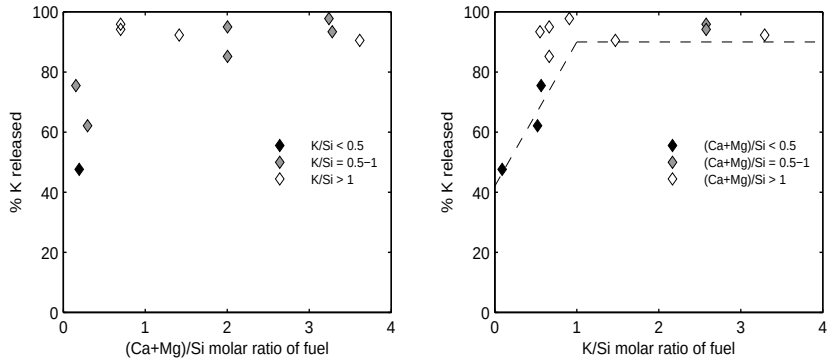

Figure 4.2: Release of K as function of molar ratios of the fuels. Data from Shah et al. [15] and Damoe et al. [16]. Fuels are 6 woods (Bark, wood chips, waste wood, saw dust, wood pellets), 3 straws and 1 olive residue

At lower molar ratios, (Ca+Mg)/Si < 0.5, some K was retained in the particles, and the release of K was lower. In these cases some Si was available for reaction with K rather than the preferred reaction with Ca or Mg. In figure 4.2B it is indicated that for fuels with (Ca+Mg)/Si < 0.5, the K/Si molar ratio influenced the release of K. There is not enough data to make clear conclusions on how the molar ratios influence the K release at these conditions. However, in the model it is assumed that the release can be described by a function of the K/Si molar ratio.

$$f_{K-release} = \begin{cases} 0.9 & \text{if } {}^{(Ca+Mg)}/_{Si} > 0.5, \\ 0.9 & \text{if } {}^{(Ca+Mg)}/_{Si} < 0.5 \quad \text{and } {}^{K}/_{Si} > 1, \\ 0.48 \cdot {}^{K}/_{Si} + 0.42 & \text{if } {}^{(Ca+Mg)}/_{Si} < 0.5 \quad \text{and } {}^{K}/_{Si} < 1. \end{cases} \tag{4.2}$$

Once $f_{K-release}$ is determined, the molar flows of the released elements are calculated.

$$\dot{n}_{S,vap} = \dot{n}_{S,fuel}, \qquad \dot{n}_{Cl,vap} = \dot{n}_{Cl,fuel}, \qquad \dot{n}_{K,vap} = f_{K-release} \cdot \dot{n}_{K,fuel}$$

The inorganic elements introduced with the fuel is given to the model as wt% dry ash in oxide scale, which sum to 100%. The total fraction of released ash from the fuel ash is calculated from the contents of K_2O, Cl and SO_3 in the fuel ash (recalculated to fractions).

$$X_{vap} = X_{SO_3,fuelash} + X_{Cl,fuelash} + f_{K-release} \cdot X_{K2O,fuelash} \tag{4.3}$$

4.1.2 Gas Phase Reactions

The volatile elements K, Cl and S was released from the particles to the gas phase during combustion. It is expected that Cl is released primarily as KCl(g), K as KCl(g), K(g) or KOH(g) while S is released as SO_2 (g). After release of the elements,

sulfation of KCl (or KOH), forming K_2SO_4 occurs. However, full reaction may not occur. At high temperatures, KCl, HCl, K_2SO_4 and SO_2 exist in equilibrium [147]. As the temperature is lowered the HCl/KCl equilibrium moves toward KCl and the K_2SO_4/SO_2 equilibrium is shifted toward K_2SO_4. The latter equilibrium is however kinetically hindered by the availability of SO_3, and equilibrium may not be reached within the residence time of a combustion plant [147]. Christensen et al. [147] states that reaction mainly occurs until the cooling has reached around 800 °C. At further cooling, only phase transitions occur.

In the modeling performed in this study, two scenarios occur; In the EFR, the concentration of SO_2 in the flue gas was measured. In the full scale combustion tests no gas measurements are available. Thus, the gas phase reactions are modeled in different ways. In the model, only the final state of the gas phase components near the deposit probe is considered. I.e. the form of the elements during the release and reaction pathways to the final form are not considered.

SO_2 Concentration Measured

When the SO_2 concentration is known, it is assumed that the S in the flue gas, not found as SO_2 will be found as K_2SO_4. The distribution of Cl among KCl and HCl is then subsequently determined by assuming that the reaction below is in equilibrium and by omitting the dimer K_2Cl_2.

$$KCl + H_2O \rightleftharpoons HCl + KOH \tag{4.4}$$

The concentrations of KCl, KOH and HCl in the flue gas is determined by solving Equations 4.5-4.7, assuming constant concentration of H_2O. $[K]_{available}$ is the amount of released K, not consumed by SO_2 in formation of K_2SO_4.

$$\frac{[KCl][H_2O]}{[KOH][HCl]} = K_c \tag{4.5}$$

$$[KCl] + [HCl] = [Cl]_{released} \tag{4.6}$$

$$[KCl] + [KOH] = [K]_{available} \tag{4.7}$$

The equilibrium constant has been derived from a detailed alkali reaction mechanism proposed by Glarborg and Marshall [125].

$$K_c = 0.465 \cdot \exp\left(\frac{1.35 \cdot 10^5}{8.314 \cdot T}\right) \tag{4.8}$$

The HCl/KCl equilibrium is shown as function of temperature for two K/Cl molar ratios in Figure 4.3. It is seen that the HCl/KCl equilibrium favors KCl at temperatures up to 900 °C. If K is in excess of Cl, HCl formation is only predicted at high temperatures.

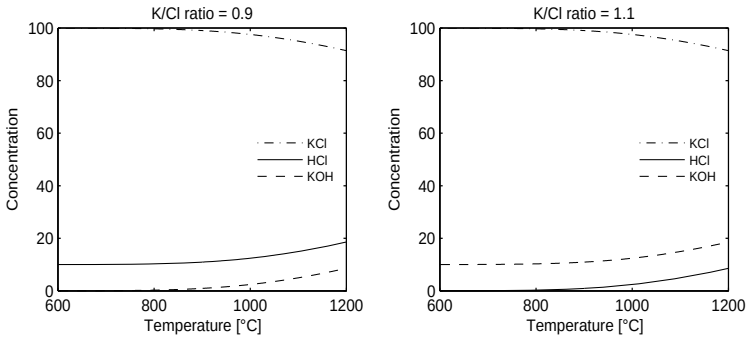

Figure 4.3: Prediction of KCl, KOH and KCl formation by Equations 4.5-4.8. Left: Cl in excess of K, Right: K in excess of Cl.

No Gas Concentration Measurements

When there is no measurement of the relevant gas phase species available, as in the full scale experiments, all the gas phase species are assumed to participate in an equilibrium.

If K is present in stoichiometric excess, all S and Cl is found to react with K and excess K is found as KOH. This observation was made for grate fired boilers [147]. It is assumed that there is enough reaction time before the probe for this to occur.

When K is not in stoichiometric excess, formation of SO_2 and HCl will occur. It was found by Christensen et al. [147], that in a grate boiler the species $K_2SO_4/SO_2/KCl/HCl$ are in equilibrium during cooling, when the temperature is above 800 °C. Christensen et al. [147] uses these four species in an equilibrium calculation valid for temperatures around 800 °C. At other temperature ranges KOH, SO_3, $KHSO_4$, etc. may influence equilibrium. At lower temperatures, the sulfation reaction is kinetically limited.

In the model, the equilibrium suggested by Christensen et al. [147], with K_c=0.25, valid at temperatures around 800 °C is applied by solving Equations 4.9-4.12.

$$K_c = \frac{[K_2SO_4][HCl]^2}{[SO_2][KCl]^2} = 0.25 \tag{4.9}$$

$$[KCl] + 2[K_2SO_4] = [K]_{released} \tag{4.10}$$

$$[KCl] + [HCl] = [Cl]_{released} \tag{4.11}$$

$$[K_2SO_4] + [SO_2] = [S]_{released} \tag{4.12}$$

The influence of temperature has not been explored further and is neglected as the majority of the deposit measurements are made at temperatures around 700-900 °C.

The estimations of the gas phase reactions presented here are quite simple. It is acknowledged that they are in fact more complicated and influenced by various

other factors such as other gas components and formation of aerosols which impact the equilibrium. However, it is anticipated that the contribution of these species in the deposit formation are small compared to the deposit formation of the coarse ash. Therefore, these simple estimates are presently considered adequate.

4.1.3 Aerosol Formation

Once the concentrations of KCl, K_2SO_4 and KOH are determined, appearance of the species as gaseous component or aerosol is estimated. If the calculated concentrations of the potassium species are above their saturation pressure, at the given flue gas temperature near the probe, the presence of aerosols is assumed. The saturation pressure in [bar] is calculated by Equation 4.13 [148].

$$\log_{10}(P_{sat}) = \frac{A \cdot 10^3}{T_{fg}} + B \cdot \log_{10}(T_{fg}) + C \tag{4.13}$$

The constants used in Equation 4.13 are seen in Table 4.1. The saturation pressures

Table 4.1: Constants used in Equation 4.13 [148]

	T_m [K]		A	B	C
KCl	1045	$T<T_m$	-12.151	-2.99	17.254
		$T>T_m$	-11.326	-4.21	20.148
K_2SO_4	1342	$T<T_m$	-19.286	-7.15	31.895
		$T>T_m$	-16.549	-5.62	25.071
KOH	679	$T<T_m$	-10.112	-3.11	16.725
		$T>T_m$	-9.723	-3.36	16.860

are then recalculated to saturation concentrations by the ideal gas law. Then, if the calculated concentrations of the K-species are above the saturation concentration, the gas concentration of the K-species is set to the saturation concentration, while the remaining of the K-species will be present as aerosol.

The aerosols present in the system are assumed to have a 0.5 μm diameter based on observations made by Zheng et al. [75] and Nordgren et al. [17]. The particle size distribution of aerosols is thus neglected.

4.2 Coarse Ash Fraction

An important parameter in modeling of ash deposition is the particle size distribution of the coarse fly ash. The only measure of particles available from the EFR experiments used for validation of the model are the particle sizes of the fuels - in most cases only provided as a single value, dp_{50}, indicating the median particle size at which 50 % (based on weight or volume) of the particles are below. A link between the dp_{50} of the fuel and a particle size distribution of the fly ash has thus been

developed as part of this work. The calculation of the ash PSD is described in the following sections.

4.2.1 Fly Ash Particle Size Distribution

The model describing the particle size distribution of the ash is based on corresponding samples of fuel and ashes obtained during combustion of straws and woods in an EFR [16].

Particle size distributions of fuels and ashes can generally be described by a Rosin-Rammler distribution (RR-distribution). The RR-distribution is a continuous probability distribution which was applied to coal particles by Rosin and Rammler [149] and subsequently described in detail by Weibull [150].

The cumulative distribution of particles ($F(dp)$) can by use of the Rosin-Rammler approach be described by Equation 4.14 in which two parameters occur. The parameters used are generally referred to as a 'shape' parameter or exponent (n) describing the shape of a distribution (or efficiency of size fractionation [85]), which is relatively constant and a 'scale' parameter, λ, which varies with the overall fineness of the particles in a sample [149] and has units similar to dp, in this case [μm].

$$F(dp) = 1 - \exp\left[-\left(\frac{dp}{\lambda}\right)^n\right] \tag{4.14}$$

The parameters of the RR-distribution are connected to the median (or dp_{50}) of the particles as given by Equation 4.15.

$$dp_{50} = \lambda(\ln(2))^{1/n} \tag{4.15}$$

Thus, when two parameters are known or assumed, the third parameter can be found. As a first step in describing the PSD of the fly ash found in suspension firing of biomass, the PSD of corresponding samples of fuel and fly ash has been described by RR distributions, to examine the variations in the RR-parameters.

4.2.2 Rosin-Rammler Parameters

The parameters λ and n for a particle sample can be determined from the cumulative distribution, by rearranging Equation 4.14 into Equation 4.16.

$$\ln(-\ln(1 - F(dp))) = n\ln(dp) - n\ln(\lambda) \tag{4.16}$$

The cumulative function is linearized in Equation 4.16 and n and λ can be obtained by plotting $\ln(dp)$ against $\ln(-\ln(1 - F(dp)))$.

Examinations on samples of fuel particles has been conducted for samples of wood and a straw fuels used in EFR experiments by Damoe et al. [16]. In these experiments, corresponding samples of the ash was also analyzed. The RR-parameters obtained for the fuels are seen in Table 4.2. In the table, calculated (from the fitted

Table 4.2: RR-parameters for fuels determined from 10-1000 μm particles. PSD of the fuels were measured by Damoe et al. [16].

Particle sample	n	λ	R^2	$dp_{50,calc}$ [μm]	$dp_{50,meas}$ [μm]
Straw	1.27	333	0.992	250	264
Wood	1.26	387.4	0.994	290	313
Wood[a]	1.30	387.7	0.990	292	309

[a]: Old wood fuel sample from similar experiments, included for comparison

n and λ) and measured values of dp_{50} are also listed. It is seen that for the fuel samples examined, the exponent n is relatively constant (within 1.26-1.30), while the scale parameter, λ, varies with the median particle size of the sample. This is in line with findings by Rosin and Rammler [149], who found that grind coal samples most often have values of n within 1 to 1.35, while larger variation was found in the scale parameter.

The ashes from the straw and wood, produced from combustion in the EFR has also been described by fitting RR-parameters to the measured PSD's. However, samples of the ashes collected had trimodal particle size distributions, which need to be considered. The three peaks appear at particle sizes (1) dp $< 1\mu$m, (2) dp within 1-100 μm and (3) dp > 200 μm. The measured PSDs of the ashes are seen in Figure 4.4. The RR-distribution can only be applied to a single peak. The cu-

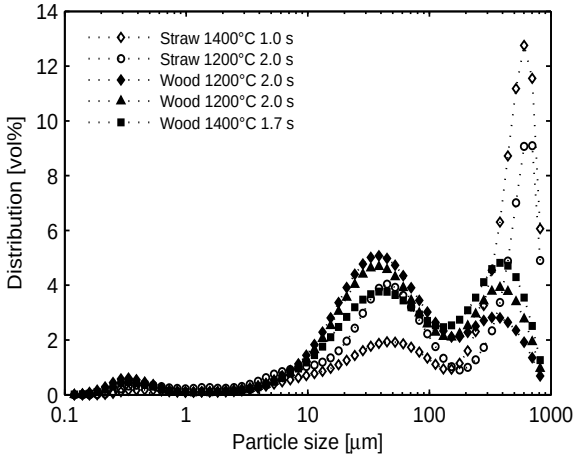

Figure 4.4: Measured particle size distributions of ashes from EFR experiments obtained at the given temperature and residence time. Data from Damoe et al. [16]

mulative distributions obtained by mathematical descriptions of different peaks can then subsequently be combined, if necessary. However, only the intermediate peak

is considered here. The peak occurring at dp < 1 μm is considered to be aerosols of vaporized species (K, Cl and S), which is not considered as part of the coarse ash. The appearance of the fraction of large particles is unexpected and not yet understood (It is possibly particles with some degree of unburnt organic material. This hypothesis is supported by chemical analysis). The fraction of large particles accounts for 25-45 wt% of the ash samples.

The cumulative distribution seen in Figure 4.4 was recalculated to only contain particles within 1 and ~150μm (the minimum between the peaks are determined for each particle sample), before fitting the RR-parameters to the distribution. In Table 4.3, the RR-parameters fitted to the fly ashes along with calculated (from the fitted n and λ) and measured values of dp_{50} are listed.

Table 4.3: RR-parameters for ashes obtained at different combustion temperatures of wood and straw. The RR-parameters and the measured dp_{50} are determined from the 1-150 μm particles. PSD of the ashes were measured by Damoe et al. [16].

Fuel	Res time [s]	Combustion T [°C]	n	λ [μm]	R^2	$dp_{50,calc}$ [μm]	$dp_{50,meas}$ [μm]
Wood[a]	2.0	1200	1.56	47	0.992	37	34
Wood[a]	2.0	1200	1.63	41	0.994	33	32
Wood	1.7	1400	1.58	42	0.994	34	33
Straw	2.0	1200	1.26	45	0.990	34	36
Straw[b]	1.0	1400	1.35	43	0.990	33	33

[a]: Repetition of ash PSD measurement from the same ash sample

[b]: No sample from the full residence (1.7) time available.

It is seen that the PSDs of the ashes are relatively independent of combustion temperature in the range examined here. The PSD of the wood ashes seem to be more narrow than the PSD of the straw ashes, since the exponent n is higher for the wood ashes. The exponent of the straw ashes is close to the exponent of the fuels observed above.

In Figure 4.5, the PSD of ashes obtained at 1200 °C are seen along with the fitted distributions. In the Figure a second distribution with a fixed exponent n = 1.30 is also shown, to examine the influence of choosing a fixed parameter to be used for all particle samples. By using a fixed parameter, the shape parameter λ is determined from Equation 4.15 with the measured dp_{50} and the fixed n value as input.
It is seen that it is reasonable to assume a constant value of the exponent n = 1.30, to fit the ash PSD. Since both the fuel and ash samples examined here can be described by a RR-distribution with $n \approx 1.30$, it seems that all particle sizes behave in a reasonable similar manner - i.e. with the same degree of coalescence or fragmentation. The same conclusion was obtained by Sarofim et al. [85] for lignite and bituminous coal.

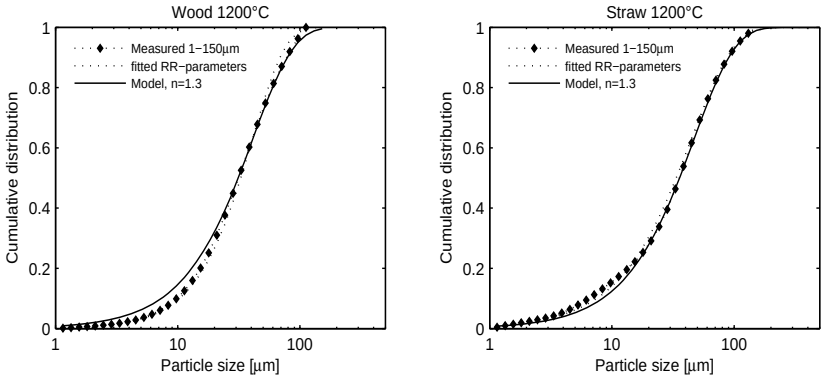

Figure 4.5: Measured PSD of wood ash (left) and straw ash (right) and PSD described by RR parameters fitted to the data and by a PSD described by a measured dp_{50} and the assumed n=1.3. Data from [16]

With the assumption that $n = 1.3$ applies to all particle samples, a PSD can be described by using a measured or calculated dp_{50} along with the fitted value of n to calculate the scale parameter, λ by Equation 4.15. In the following, it is described how the dp_{50} of the ash can be calculated from a median particle size (dp_{50}) of the fuel.

4.2.3 Ash Median Particle Size

In the ash formation model, presented here, the particle size of an ash particle is calculated from the size of the 'parent' fuel particle by taking the densities of fuel and ash into account along with the ash mass fraction of the fuel and the vaporization of K, Cl and S. Also, a parameter, describing possible breakage of the particle into a number of fragments is included.

Initially, the mass of an fuel particle is calculated.

$$m_{fuel} = \frac{1}{6}\pi \cdot \rho_{fuel} \cdot dp_{fuel}^3 \tag{4.17}$$

The mass of an ash particle formed from the fuel particle, is then calculated. Here, the number of fragments formed by each particle, N_{frag}, is included. If $N_{frag} = 1$, full coalescence of the ash within a fuel particle is assumed. The ash fraction of the fuel is corrected for the vaporized species; K, Cl and S which are not present in the particle for coalescence.

$$m_{ash} = \frac{m_{fuel} \cdot X_{ash}(1 - X_{vap})}{N_{frag}} \tag{4.18}$$

Then, the ash particle size originating from the fuel particle is calculated.

$$dp_{ash} = \sqrt[3]{\frac{6 \cdot m_{ash}}{\pi \cdot \rho_{ash}}} \tag{4.19}$$

The equations are combined:

$$dp_{ash} = \sqrt[3]{\frac{\rho_{fuel} \cdot X_{ash}(1 - X_{vap})}{\rho_{ash} \cdot N_{frag}}} \cdot dp_{fuel} \tag{4.20}$$

The number of fragments formed per particle have been calculated for the combustion experiments conducted by Damoe et al. [16], where corresponding samples of fuel and fly ash are available. This implies that corresponding values of dp_{50} of the fuel and ash are known and the vaporised fraction was furthermore quantified as part of the experiment. Therefore, Equation 4.20 can be solved for N_{frag}.

The densities of fuels and ashes has not been measured, and thus have to be assumed. The densities of the fuels are assumed based on measurements made for similar fuels with relevant particle sizes. I.e. the densities include some porosity of the particles, but are relatively close to the cell wall (skeletal) density of the fuels. The densities of the ashes are derived from the densities of the oxides in the ash and the ash composition. More details on assumption on the fuel and ash densities can be found in Appendix B.1. The densities used in the model are seen in Table 4.4.

Table 4.4: Assumed densities of fuels and ashes used in the model. See Appendix B.1 for basis of the assumptions.

	Straw	Wood
ρ_{fuel} [kg/m^3]	1300	1400
ρ_{ash} [kg/m^3]	2700	3100

The Number of fragments formed per fuel particle is for wood 3.2. For wood it is found that the correction of volatile inorganic matter has limited influence (N_{frag}=3.9 if all ash elements are included), since this fuel has a low content of K, Cl and S (X_vap=0.17). For straw, the content of these elements is high (X_vap=0.57) and a great difference in the calculated number of fragments is observed when the vaporized species is included as ash (N_{frag}=8) or corrected for as vaporized (N_{frag}=3.4). This highlight the importance of correcting for the volatile content of the fuel particles. When the vaporized species are excluded, the number of fragments formed per particle from straw are in the same range as observed for wood, just above 3.
The number of fragments calculated here, are in the same range as those calculated for lignite (N_{frag} = 3) and bituminous coal (N_{frag} = 5) by Sarofim et al. [85].

The model has been tested on particle size distributions provided by Jiménes and Ballester [92]. Here, PSD was measured on three fuels (orujillo, chestnut wood and eucalyptus wood sawdust) and their ashes after combustion in an EFR. This is seen in Appendix C.

4.2.4 Final Model for Ash PSD

In Figure 4.6, it is seen how the model performs in describing the particle size distribution of a straw ash and of a wood ash, measured by Damoe et al. [16]. In the figures, the PSD of the ash has been calculated by two methods; by the method described here, where the dp_{50} of the ash is calculated from the dp_{50} of the fuel (Equation 4.20) and a Rosin-Rammler distribution is used to describe the distribution around the dp_{50} (Equations 4.14 and 4.15). The second method in Figure 4.6 is a 'direct PSD calculation', where each particle size of the fuel PSD are used to calculate the resulting ash PSD (Equation 4.20), assuming that the ash particles will account the same fraction of the total PSD as the parent fuel particles. In both calculation approaches, N_{frag} is set to 3, the densities shown in Table 4.4 are used and X_{vap} is 0.17 for wood and 0.57 for straw. It is seen in Figure 4.6 that both

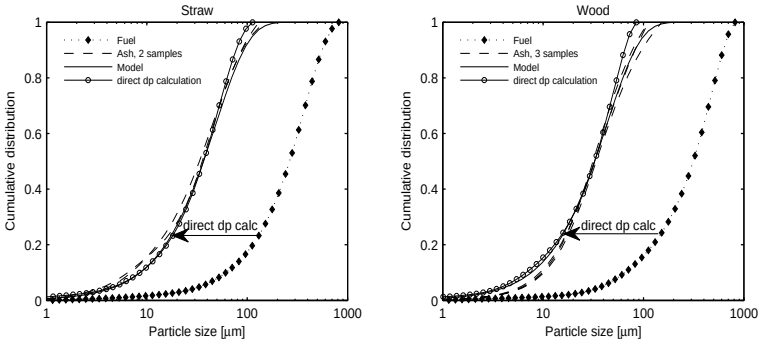

Figure 4.6: PSD model performance with N_{frag}=3 and n=1.3. X_{vap} is 0.17 for wood and 0.57 for straw. Data from [16]

calculation methods offers a good description of the PSD of the ash. The fit of the 'direct dp calculation' supports the assumption that all particles fragment to the same degree (for this range of particle sizes).

When parameters for the particle size distribution of the ash is determined (n and λ), the particle size distribution can be determined by a desired number of particle sizes. In the model, as a first approach the PSD is described by 10 size-classes (N_{part}=10), each containing 10 wt% of the ash. To do this, Equation 4.14 is rearranged to calculate the particle sizes at which 10 %, 20%, 30%, etc. of the particles are below. To calculate 10 %, $F(dp) = 0.1$

$$dp = \exp\left[\frac{1}{n}(\ln(-\ln(1 - F(dp)))) + \ln(\lambda)\right] \tag{4.21}$$

As $F(dp) = 1$ cannot be used in Equation 4.21, the upper limit is set to $F(dp) = 0.999$. Once the particle sizes separating the size-classes are found, the mean particle size of each size class is found by the average particle size of each class.

4.2.5 Chemistry of The Coarse Ash Fraction

Both the concentration and also the chemical composition of the coarse ash fraction is important in the description of deposit formation. Though it has been observed that ash particles of different sizes do not have the same chemical composition [5, 17, 39, 123], the coarse particles are in this model all assumed to have the same composition. The composition of the coarse ash particles are determined from the fuel ash chemical composition, which is corrected for the contents of the vaporized species. The molar fraction or mass fraction of each element-oxide in the ash is then recalculated to sum to 1.

Chapter 5

Deposit Build-up Model

During deposit build-up, various mechanisms of transport apply to different parts of the fly ash. The deposition mechanisms were identified by Baxter [18] for coal combustion. The mechanisms apply also to biomass combustion, but the relative importance of the individual mechanisms are different, due to the different ash characteristics [18].

Gaseous species and aerosols are transported to the heat transfer surface by diffusion. The gaseous species deposit by condensation and a concentration gradient act as driving force. The aerosols deposit by thermophoresis, where a temperature differences is the driving force. The gaseous species and aerosols considered in this work are KCl, K_2SO_4 and KOH. KCl and K_2SO_4 are expected to deposit directly forming solid KCl and K_2SO_4 (when the deposit surface temperature is below the melting point). In this model, on-site sulfation of deposited KCl is ignored. KOH may react with excess SiO_2 (not already connected to Ca, Mg, Na or K), if this is present in already formed deposit. If SiO_2 is not present in excess, KOH is expected to deposit and be present as KOH (or possibly K_2CO_3, which is not considered) and possibly react with SiO_2 in a subsequent time-step.

Solid or possibly molten particles deposit by various impaction mechanisms, depending on the particle size. Large particles will have too much inertia to follow the gas stream around a cylindrical obstacle and will therefore impact the probe and possibly stick to it. See Figure 5.1. Parameters such as particle velocity, angle of impaction, particle and surface stickiness etc. determines if the particle is deposited. The inertial impaction mechanism applies to particles larger than approximately 10 μm. Smaller particles will to a large extent follow the gas flow around the tube. Some deposition of small particles by convective diffusion may however also occur on the probe front. The impaction by these small particles is not expected to contribute greatly to the deposit mass or to the deposit characteristics. However, impaction of the small particles on the probe front is included the model.

When gas passes a cylindrical obstacle, eddies may form on the rear side of the cylinder, if Reynolds numbers are larger than ≈ 50 [151]. The small particles, which

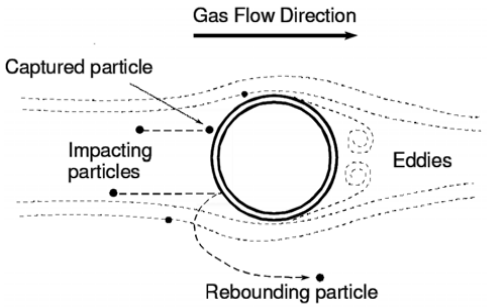

Figure 5.1: Illustration of impact/rebound of particles in flow around a cylinder [71].

follows the gas flow around the probe may be centrifuged out of these eddies and impact and deposit on the probe rear. Zhou et al. [19] has developed a model for predicting the impaction on the probe rear. This model rely on a empirical constant from the combustion system in question. The mechanism is not included as part of this model.

Five mechanisms are thus included in the deposit build-up model for the EFR; diffusion of vapors followed by condensation (C), thermophoresis (T), inertial impaction (I), convective diffusion of particles (D) and reaction (R).

$$\mathrm{Flux}_{dep}(t,\theta) = \frac{dm(t,\theta)}{dt} = \mathrm{I}(t,\theta) + \mathrm{T}(t,\theta) + \mathrm{C}(t,\theta) + \mathrm{D}(t,\theta) + \mathrm{R}(t,\theta) \tag{5.1}$$

The model is set up so the rate of deposit build-up by each mechanism in a time step is calculated for a number of positions on the probe circumference. In the model, each half of the probe circumference is divided into 40 parts where the size of each part (in radians) is:

$$\Delta\theta = \frac{\pi}{40} \tag{5.2}$$

and the angular position (in radians) of each part given by

$$\theta = \frac{\Delta\theta}{2} + (m-1)\cdot\Delta\theta \qquad m = 1...40 \tag{5.3}$$

The surface area of each part of on the probe is calculated by

$$s(\theta) = \Delta\theta \cdot r(\theta) \cdot l_{probe} \tag{5.4}$$

l_{probe} is the length of the probe exposed to the flue gas.

The radius of the surface changes as the deposit build-up. For each time step a new radius is calculated, based on the deposit flux calculated in the time step.

$$r(\theta) = \sqrt{r_0(\theta) + c_r} \tag{5.5}$$

$$c_r = \frac{2\cdot \mathrm{Flux}_{dep}(t,\theta)}{\rho_{dep}\cdot\Delta\theta\cdot l_{probe}}\Delta t \tag{5.6}$$

The total mass on the probe is calculated by summation over all angles and timesteps.

$$m_{dep} = 2 \cdot \sum_{t} \sum_{\theta} \text{Flux}_{dep}(t, \theta) \tag{5.7}$$

The deposit density is calculated from the ash density and the porosity of the deposit layer formed;

$$\rho_{dep} = \rho_{ash}(1 - \phi) \tag{5.8}$$

The porosity of the deposit layer is discussed later, in Section 5.7.

5.1 Diffusion and Condensation of Vapors

When the vapors in the flue gas approach the thermal boundary layer surrounding a heat transfer surface, deposition of vapors may occur by three mechanisms; (*i*) the vapors may traverse the boundary layer and heterogeneously condense on the heat transfer surface or deposit, (*ii*) the vapors may form a fume by homogeneous nucleation within the boundary layer and deposit on the surface by thermophoresis or (*iii*) the vapors may heterogeneously condense on particles found within the boundary layer and deposit with these particles by thermophoresis [18]. In the present model only the first mechanism with vapors traversing the boundary layer followed by heterogeneous condensation is included, for the sake of simplicity.

The rate of deposition by condensation of vapors can be described by Equation 5.9.

$$\dot{C}(t, \theta) = \sum_{j=1}^{N} k_c(j) \cdot (C_b(j) - C_s(j)) \cdot s(\theta) \tag{5.9}$$

$k_c(j)$ is the mass transfer coefficient of species j, while $C_b(j)$ and $C_s(j)$ are the concentrations of the species at the boundary layer surface (or bulk gas) and at the heat transfer surface, respectively. The concentrations on the surface are determined as the saturation concentrations calculated at the deposit surface temperature by Equation 4.13, described in Section 4.1.3. $s(\theta)$ is the surface area of the probe section of interest. The mass transfer coefficient is determined by the dimensionless Sherwood number:

$$Sh = \frac{k_c \cdot d_{probe}}{D_{j,N_2}} \tag{5.10}$$

d_{probe} is the probe diameter, while D_{j,N_2} is the diffusivity of the vapor (j) in the surrounding gas (assumed as N_2). The diffusivities of KCl, KOH and K_2SO_4 in N_2 varies with temperature and can be described by the expressions described by Equations 5.11-5.13. These expressions are derived in Appendix B.2.

$$D_{KCl,N_2} = 3.8001 \cdot 10^{-10} \cdot T^{1.7780} \quad [\text{m}^2/\text{s}] \tag{5.11}$$

$$D_{KOH,N_2} = 5.0882 \cdot 10^{-10} \cdot T^{1.7404} \quad [\text{m}^2/\text{s}] \tag{5.12}$$

$$D_{K_2SO_4,N_2} = 2.0564 \cdot 10^{-10} \cdot T^{1.8023} \quad [\text{m}^2/\text{s}] \tag{5.13}$$

Experimental data on the heat and mass transfer around a cylinder has been obtained by Sanitjai and Goldstein [152]. The data has been examined by Zhou et al. [19] and the Sherwood number was expressed as function of the angle around the probe as given by Equation 5.14 [19].

$$Sh = \begin{cases} 0.67 \cdot Re^{0.5} \cdot Sc^{0.35}(1 + \cos(\frac{\pi}{180}\theta)) & \theta \leq 85^\circ \\ 0.73 \cdot Re^{0.5} \cdot Sc^{0.35} & 85^\circ < \theta \leq 180^\circ \end{cases} \tag{5.14}$$

The Schmidt number is calculated from flue gas properties.

$$Sc = \frac{\mu_g}{\rho_g \cdot D_{j,N_2}} \tag{5.15}$$

Calculation of the flue gas properties (Cp, μ_g, λ_g, and ρ_g) are described in Appendix B.3.

5.2 Thermophoresis

Thermophoresis is a process by which particles are transported through a gas due to temperature gradients. Thermophoresis is thus expected to occur when a temperature difference between the flue gas and the heat transfer or deposit surface is found. The movement of the particle occurs when hot gas molecules collide with one side of the particle with higher energy and frequency than cold gas molecules colliding with the opposite side of the particle. This creates a pressure difference on the two sides of the particles, leading to movement of the particle in the opposite direction of the temperature gradient. The particle motion may however be influenced by temperature gradients inside the particle and slip flow effects, when the when the particles becomes larger than the mean free path of the gas [18, 153]. Thus, when thermophoresis is mathematically described, an important parameter is the Knudsen number (Kn), describing the particle size relative to the mean free path (ℓ) of the gas molecules.

$$Kn = \frac{2\ell}{d_p} \tag{5.16}$$

The mean free path is calculated as:

$$\ell = \frac{\kappa \cdot T}{\sqrt{2} \cdot \sigma \cdot P} \tag{5.17}$$

κ is the Boltzmann constant and σ is the molecular cross section of the gas molecules, which is represented by N_2 in the calculations. By using N_2 as a representative of the gas molecules, the mean free path is calculated to be 0.24-0.33 μm in the temperature range 800-1200 °C and atmospheric pressure. From particle size distributions obtained in full scale combustion units, it is found that the mean particle size of the

sub micron aerosols are ≈ 0.5 μm [5, 75] and the Knudsen numbers of interest are thus < 2.

He and Ahmadi [154] found that the Brock-Talbot equation, seen as Equation 5.18, provide good description of the thermophoretic force for particles with low Knudsen numbers < 3 . This equation includes thermal conductivities of the gas and particles along with slip flow boundary conditions. The equation was developed by Brock [155].

$$F_T = -\frac{12 \cdot \pi \cdot \mu_g \cdot \nu_g \cdot r_p \cdot C_s \left(\frac{k_g}{k_p} + C_t \cdot Kn\right)}{(1 + 3 \cdot C_m \cdot Kn)\left(1 + 2 \cdot \frac{k_g}{k_p} + 2C_t \cdot Kn\right)} \cdot \frac{\nabla T}{T} \tag{5.18}$$

The parameters C_m=1.14, C_t=2.18 and C_s=1.17 were adjusted by Talbot et al. [156]. ν_g is the kinematic viscosity (= μ_g/ρ_g), r_p is the particle radius, k_g and k_p are the thermal conductivities of the gas and particle, ∇T is the temperature gradient, and T is the temperature in the vicinity of the particle, thus the flue gas temperature.

The particle thermophoretic velocity can be determined by equating the stokes drag force (F_V) on the particle to the thermophoretic force (F_T), under the assumption that no other forces are acting on the particle (i.e. the particle does not accelerate or decelerate).

$$F = F_V + F_T = 0 \tag{5.19}$$

With the stokes drag force defined by Equation 5.20, the thermophoretic velocity can be calculated by Equation 5.21 [156].

$$F_V = \frac{6 \cdot \pi \cdot \mu_g \cdot u \cdot r}{C_c} \tag{5.20}$$

$$\Downarrow$$

$$u = \frac{C_c}{6 \cdot \pi \cdot \mu_g \cdot r} \cdot F_T \tag{5.21}$$

C_c is the Cunningham correction factor, which corrects the stokes drag force with respect to slip of gases at the particles when the particle size becomes comparable to the mean free path of the gas [157].

$$C_c(i) = 1 + Kn(i) \cdot \left(1.257 + 0.4 \cdot \exp\left(\frac{-1.1}{Kn(i)}\right)\right) \tag{5.22}$$

Equations 5.18 and 5.21 can be combined in Equation 5.23, describing the deposition velocity by thermophoresis:

$$u_T(i,\theta) = -\frac{2 \cdot \nu_g \cdot C_c(i) \cdot C_s \cdot \left(\frac{k_g}{k_p} + C_t \cdot Kn(i)\right)}{(1 + 3 \cdot C_m \cdot Kn(i))\left(1 + 2\frac{k_g}{k_p} + 2 \cdot C_t \cdot Kn(i)\right)} \cdot \frac{\nabla T(\theta)}{T} \tag{5.23}$$

The temperature gradient is found by the heat flux from the flue gas to the deposit surface (q), described by the heat transfer model (described later) and the thermal conductivity of the gas.

$$\nabla T(\theta) = \frac{q(\theta)}{k_g} \tag{5.24}$$

Once the thermophoretic velocity is determined, the thermophoretic deposition rate is described by:

$$\dot{T}(t,\theta) = \sum_{i=1}^{N} u_T(i,\theta) \cdot C(i) \cdot s(\theta) \tag{5.25}$$

In Figure 5.2, the thermophoretic velocity as function of particle size is seen. It is

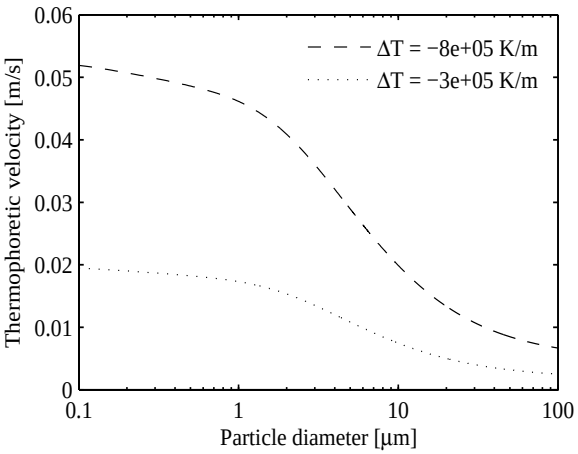

Figure 5.2: Thermophoretic velocity as function of particle size calculated for experiment S1, with T_{fg}=750°C and a temperature gradients set to $-8 \cdot 10^5$ K/m and $-3 \cdot 10^5$ K/m, relevant for the initial and final part of the experiment, respectively

seen that the thermophoretic velocity is most significant for the aerosol particles, dp < 1 μm, and then decreases for larger particles. Thermophoresis may however still contribute to the deposit formation for particles > 1 μm. For the sake of completeness, all particle sizes will be included in the calculation of deposit formation by thermophoresis. It is expected that thermophoresis will be relevant for ashes with a significant content of particles with diameters < 10 μm. All particles transported to the surface by thermophoresis are assumed to stick.

5.3 Convective Diffusion

The deposit formation by inertial impaction is only relevant for particles with Stokes numbers > 0.125, i.e. with particle sizes above ≈ 10 μm. The smaller particles may

impact by convective diffusion, or by thermophoresis, as already described.

In a simplified approach, Rosner and Tassopoulos [158] describes an capture efficiency, defined as the fraction of particles collected from the fluid volume swept by the cylinder by Equation 5.26.

$$\eta_{cap}(i,\theta) = 2\frac{Sh(i,\theta)}{Re \cdot Sc(i)} \tag{5.26}$$

The Sherwood number can be determined for a given angular position on the probe by the probe Reynolds number and the particle Schmidt number as seen in Equation 5.14, Page 88. The particle Schmidt number is calculated from flue gas properties and the particle diffusivity.

$$Sc = \frac{\mu_g}{\rho_g \cdot D_p(i)} \tag{5.27}$$

The particle diffusivity is given by the Einstein's formula:

$$D_p(i) = \frac{\kappa \cdot T}{3 \cdot \pi \cdot \mu_g \cdot d_p(i)} \tag{5.28}$$

With η_{cap} determined,

$$D(t,\theta) = \sum_{i=1}^{N} u_g \cdot C_{ash}(i) \cdot \eta_{cap}(i,\theta) \cdot s(\theta) \tag{5.29}$$

In Figure 5.3, the capture efficiencies, calculated at two temperatures are seen for particle sizes 0-10 μm. It is seen that small particles diffuse to the deposit surface

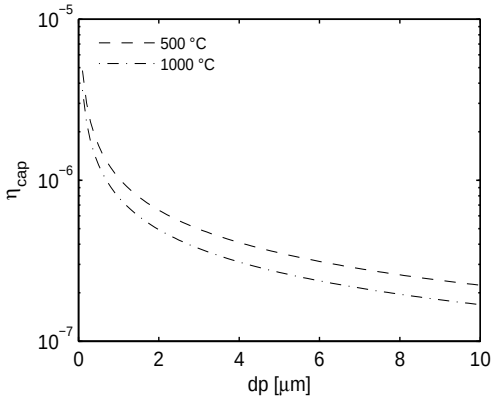

Figure 5.3: Capture efficiency of particles which may deposit by diffusion.

more easily than larger particles. However, the capture efficiency is quite low and deposition by this mechanism is not expected to be significant.

All particles transported to the surface by diffusion are assumed to stick.

5.4 Reaction

When gaseous KOH is transfered to the deposit surface, it may react with excess SiO_2 in the ash particles already found in the deposit. In this reaction, the only form of the K-silicate considered is $K_2O \cdot SiO_2$.

$$2KOH(g) + SiO_2 \rightarrow K_2O \cdot SiO_2 + H_2O(g) \tag{5.30}$$

The contents of KCl and K_2SO_4 in the deposits are disregarded in these considerations as they are observed as inert with respect to reactions and influence in viscosity. Furthermore, they are assumed to be found as solids, below the eutectic point of a KCl/K_2SO_4 mixture, 690 °C.

In the model, each angular section of the probe is observed individually. For each part, the molar content of each ash species in the probe section is calculated in each time step by adding the deposited ash to the already formed deposit. This is done for the coarse ash by the total flux of particles deposited by impaction, thermophoresis and convective diffusion and by the composition of the particles. Once the composition of the section is described by the number of moles of each oxide, the excess SiO_2 is calculated:

$$n_{SiO_2,excess} = n_{SiO_2} - n_{K_2O} - 2 \cdot (n_{CaO} + n_{MgO}) \tag{5.31}$$

The molar content of KOH transfered to the deposit is calculated by the same approach as for diffusion followed by condensation, described in Section 5.1.

If $n_{SiO_2,excess} > 0$, the molar amount of excess SiO_2 is compared to the molar amount of KOH in the probe section and reaction is assumed to occur. It is assumed that full reaction of the limited specie occur. After the amount of reaction occurring ($n_{K,react}$) has been determined, the change in the deposit chemistry is described by calculating the molar amount of K left as KOH (if in excess) and the molar amount of K_2O formed by reaction. Finally the new molar composition as mole% of each oxide is calculated for use of viscosity and surface tension calculations in the next time step.

The mass of deposit on the probe is influenced in two ways during reaction; KOH is transferred to the deposit, while the reaction product, H_2O, evaporates from the deposit.

$$\dot{R}(t,\theta) = \dot{C}_{KOH}(t,\theta) - \frac{1}{2} \cdot n_{K,react} \cdot M_{H_2O} \tag{5.32}$$

5.5 Inertial Impaction

The deposition by inertial impaction is controlled by two factors; (i) the fluid dynamics of the system, which determine whether particles will impact the heat transfer

surface and (*ii*) the ability of the particle to stick to the surface. The model used to determine the rate of inertial impaction is based on work by Wessel and Righi [159] and has also been applied by Zhou et al. [19] in a deposition model for a straw-fired grate boiler and by Rosner and Tandon [160] for coal combustion.
The rate of inertial impaction is calculated by Equation 5.33.

$$I_I(t,\theta) = \sum_{i=1}^{N} u_g \cdot C_{ash}(i) \cdot \eta_I(i,\theta) \cdot \eta_s(i,\theta) \cdot s(\theta) \tag{5.33}$$

where $\eta_I(i,\theta)$ is the local collision efficiency of each particle size $dp(i)$ at the given angle and $\eta_s(i,\theta)$ is the sticking probability.

5.5.1 Local Collision Efficiency

The local collision efficiency is defined as the flux of particles at the cylinder surface relative to the flow of particles in the free gas stream. The local collision efficiency experiences a maximum at the stagnation line (θ = 0) and decreases to zero at the maximum angle of collision (θ_{max}) on the probe.

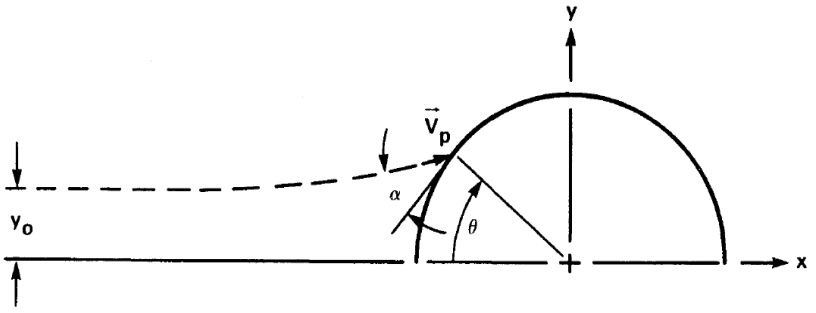

Figure 5.4: Illustration of the angles and streamlines considered for potential flow in the model of impaction by Wessel and Righi [159].

The target efficiency (η_t), the maximum angle of collision (θ_{max}) and the impact velocities at angles 0 and θ_{max} ($u_p(0)$ and $u_p(\theta_{max})$) can be determined for each particle size from correlations provided by Wessel and Righi [159], given by Equations 5.34 and 5.35 with parameters provided in Table 5.1.

$$\Gamma = \beta_1 \cdot \ln(8 \cdot Stk_{eff}) + \beta_2 \cdot (Stk_{eff} - 0.125) + \beta_3 \cdot (Stk_{eff} - 0.125)^2 \tag{5.34}$$

$$\Gamma = \left[1 + \beta_1 \cdot (Stk_{eff} - 0.125)^{-1} + \beta_2 \cdot (Stk_{eff} - 0.125)^{-2} + \beta_3 \cdot (Stk_{eff} - 0.125)^{-3}\right]^{-1} \tag{5.35}$$

The correlations are based on the effective Stokes numbers, where a non-Stokes particle drag coefficient is included [161]:

$$Stk_{eff} = Stk \cdot \psi(\mathrm{Re}_p) = \frac{\rho_p \cdot d_p^2 \cdot u_g}{9 \cdot \mu_g \cdot D} \cdot \psi(\mathrm{Re}_p) \tag{5.36}$$

The drag coefficient ($\psi(\mathrm{Re}_p)$) is calculated from the Reynolds number of the particle in the free stream by Equation 5.37 [159].

$$\psi(\mathrm{Re}_p) = \frac{3\left(\sqrt{0.158} \cdot \mathrm{Re}_p^{1/3} - \tan^{-1}(\sqrt{0.158} \cdot \mathrm{Re}_p^{1/3})\right)}{0.158^{3/2} \cdot \mathrm{Re}_p} \tag{5.37}$$

Table 5.1: Correlation coefficients for Equations 5.34 and 5.35 [159].

Parameter, Γ	Stk_{eff} range	Eq.	β_1	β_2	β_3
Target efficiency	0.125-0.5	5.34	0.01978749	0.5136545	-0.0482858
η_t	> 0.5	5.35	1.54424	-0.538013	0.2020116
Max collision angle	0.125-0.5	5.34	0.696596	-1.822407	1.1452745
$\theta_{max}/\frac{\pi}{2}$	> 0.5	5.35	0.7722744	-0.271871	0.06049905
Impact velocity	0.125-0.8	5.34	0.0209863	0.8762208	-0.403482
$\lvert u_p(0)\rvert/U$	>0.8	5.35	1.038627	-0.327754	0.1115706
Impact velocity	0.125-0.8	5.34	1.925045	-6.30525	3.796702
$\lvert u_p(\theta_{max})\rvert/U$	>0.8	5.35	-0.242589	0.2343417	-0.0446577

The local collision efficiency at a given angle can be determined by Equation 5.38 [159].

$$\eta_I(i,\theta) = \frac{\pi}{2}\frac{\eta_t(i)}{\theta_{max}(i)}\cos\left(\frac{\pi}{2}\frac{\theta}{\theta_{max}(i)}\right) \tag{5.38}$$

The impact velocity ($u_{p,impact}$) of the particle and angle of impaction (α_{impact}) at a given probe angle can be determined by Equations 5.39 and 5.40.

$$u_p(\theta) = -(u_p(\theta_{max}) - u_p(0))\cos\left(\frac{\pi}{2}\frac{\theta}{\theta_{max}}\right) + u_p(\theta_{max}) \tag{5.39}$$

$$\alpha_{impact}(\theta) = \frac{\pi}{2}\left(1 - \left(\frac{\theta}{\theta_{max}}\right)^{1/b}\right)^b \tag{5.40}$$

where

$$b = 1 + \frac{0.1851488}{Stk_{eff}} - \frac{0.0205901}{Stk_{eff}^2} + \frac{0.001530146}{Stk_{eff}^3} \tag{5.41}$$

5.5.2 Sticking Probability

In Equation 5.33, a sticking fraction, η_s, is included. This parameter describes if the particle stick or rebound upon impaction with the cylinder.

Numerous models describing the rebound or retention of particles upon impaction with surfaces or other particles have been proposed, primarily from the powder technology and aerosol technology areas [22, 32, 33, 162–176]. The models generally describe the impact by an energy balance considering the kinetic energy of the particles, the energy lost by deformations of the particle or surface, the contact area established and the adhesion energy of the contact area. The models differ in the description of the deformations and the formed contact area, depending on the material in question. Thus, models have been proposed for impact of elastic-plastic materials [22, 162–165], purely elastic materials [166–169], viscoelastic materials [32, 33] and for viscous materials (droplets) [20, 21, 29, 170–173, 177]. Besides these, models considering impact of (elastic) particles with surfaces where one part is covered by a thin viscous fluid has also been proposed [178–181].

With the aim of obtaining simple models, simple sticking criteria based on viscosity or melt fractions of the materials have been proposed for description of ash deposition. These models are described below.

The simple models do not consider particle size or velocity in their sticking criterion and may thus not be widely applicable. With the aim of obtaining a model valid for a wide range of particle sizes and velocities, models considering particle or surface properties as well as size and velocity of particles have also been reviewed.

5.5.3 Simple Sticking Models

Walsh et al. [182] examined ash deposit build-up and suggested a simple approach for estimation of the sticking probability. Walsh et al. [182] made a qualitative argument suggesting that for particles with similar surface energy and small equilibrium contact angle (angle between the deformed particle and the surface during impaction), the viscosity will determine the degree of deformation and the contact area established upon impaction of the particles with a surface. The larger the contact area, the larger is the likelihood that particles will stay attached to the surface. With this argumentation, a relationship between viscosity and sticking probability of a particle or a surface was suggested:

$$p(T, x_i) = \begin{cases} \frac{\mu_{ref}}{\mu} & \mu > \mu_{ref} \\ 1 & \mu \leq \mu_{ref} \end{cases} \tag{5.42}$$

$p(T, x_i)$ is a cumulative sticking probability for a collection of particles with varying temperature and composition. The sticking probability for a collection of particles $p(T)$ is obtained by summation over the composition distribution. μ_{ref} is a reference viscosity. Particles with viscosities lower than this reference viscosity are assumed to

be perfectly sticky. In the work by Walsh et al. [182], where this sticking probability was defined, the reference viscosity was set to 8 Pa·s, i.e. within the molten range. The model has been applied in several models for coal ash deposition, where the value of the reference viscosity has been set to e.g. 10^4 Pa·s [23, 183, 184] or 10^5 Pa·s [31, 185]. Srinivasachar et al. [186] has by observing deposition of coal particles and of soda-lime-glass spheres (which have composition relevant for ashes) shown that the critical viscosity of a deposit build-up is dependent on the particles kinetic energy - i.e. of the mass/size and velocity of the particles. See Figure 5.5.

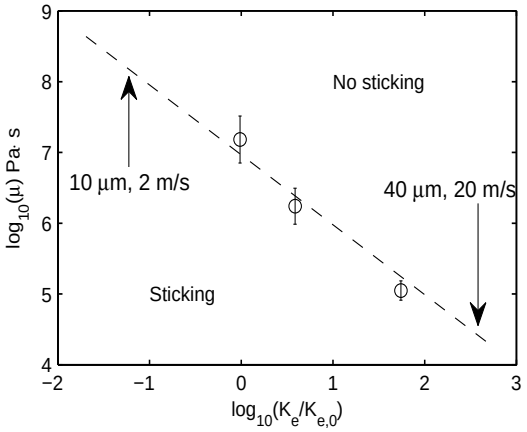

Figure 5.5: Variation of the critical viscosity of deposition as function of particle kinetic energy relative to kinetic energy of small particles. Results from experiments with soda-lime-glass spheres. Adapted from [186]

Srinivasachar et al. [186] propose that the critical viscosity in coal combustion should lie between 10^4 Pa·s and 10^8 Pa·s, because of the particle sizes and velocities used in these systems. Thus, the critical viscosity determined in one combustion system is thus not generally applicable [187], and can thus be regarded as a fitting parameter [44].

Once the sticking probabilities of particles and/or surfaces has been determined, the overall sticking probability i.e. the fraction of particles sticking to the surface upon impaction is calculated by Equation 5.43, developed by Walsh et al. [182].

$$\eta_s = \underbrace{p(T_g)}_{sticky\ particles} + \underbrace{(1-p(T_g))p_{sur}(T_s)}_{sticky\ surface} - \underbrace{k_e(1-p(T_g))(1-p_{sur}(T_s))}_{non-sticky\ particles\ and\ surface} \tag{5.43}$$

Here, $p(T_g)$ is the sticking probability of ash particles, evaluated at the gas temperature, $p_{sur}(T_s)$ is the sticking probability of the deposit surface, evaluated at the surface temperature of the deposit and k_e is the erosivity of dry particles impacting a dry surface. The basic assumption is thus that a group of particles having an av-

erage sticking probability η_s will be equivalent to a collection of particles containing a mass fraction (η_s) of particles which are perfectly sticky and a mass fraction (1-η_s) which are not [182, 184].

The erosivity of ash toward the deposit, k_e used in Equation 5.43, describes the mass of ash removed per unit mass of impacting particle. In most models, k_e is omitted (given the value 0) [19, 24, 182, 183, 188, 189]. Thus, rebound of particles upon impaction is included when both the particles and deposit surface is non-sticky, while erosion is not included. According to Walsh et al. [182], the erosivity can be empirically established.

An alternative approach for description of the sticking probability has been employed when modeling deposit build-up during biomass combustion in grate or CFB. In these combustion systems, the ash contains a significant fraction of alkali, possibly along with S and Cl, which are not completely released to the gas phase. These salt-forming components alter the sticking behavior of the ash and deposits by formation of a melt. Therefore, an approach relating the sticking probability to the fraction of melt in the ash particles have been introduced [19, 24, 48, 190]. It is in this approach assumed that particles are non-sticky when containing less than 10 % melt and completely sticky when the melt fraction exceeds 70%. Between these points, the sticking probability is assumed to be a linear function of the melt fraction. The sticking probability is thus expressed as [19]:

$$p(T) = \begin{cases} 0 & 0 \le f_{melt} < 0.1 \\ 1.67 \cdot f_{melt} - 0.167 & 0.1 < f_{melt} < 0.7 \\ 1 & 0.7 < f_{melt} \le 1 \end{cases} \tag{5.44}$$

The melt fraction of ashes has in many cases been estimated by thermodynamic equilibrium calculations, e.g. [29, 191]. In one case, presented by Zhou et al. [19], empirical correlations based on ash composition has been employed for estimation of melt fractions. The correlation was derived based on melting curves of six straw-derived fly ashes with high alkali contents (26-61 wt% K_2O) from grate combustion.

5.5.4 Detailed Models; Particles Impacting Solid Surface

As mentioned above, various models which take the particle kinetic energy into account in the prediction of capture or rebound of particles have been proposed. The models differ in the material properties used to describe the material deformation and energy loss.

Material properties of the ashes from pilot plant suspension-firing of straw and straw/wood mixtures have been analysed by Nordgren et al. [17]. They used XRD analysis for identification of crystalline phases in the ash and deposits. However, they found that fly ashes and deposits contain significant amounts of amorphous phases [17]. Amorphous phases does not undergo plastic deformations [192], and models for impact of elastic-plastic materials [22, 162–165] have been disregarded in this work.

Amorphous materials behaves like a glass at low temperatures (below the glass transition temperature), like a rubber (viscoelastic material) at intermediate temperatures and as a viscous liquid at high temperatures [192]. Models of particle impact have been proposed for have been proposed for impact of viscous materials (droplets) [20, 21, 29, 170–173, 177], and purely elastic materials [166–169]. I.e for the two ends of the scale. The ashes considered in this work are expected to be in the intermediate, viscoelastic region. These have been considered by Losurdo et al. [32, 33]. In the following, impact/rebound considerations of all three material groups will be briefly described.

Viscous Impact

Models which directly correlate the sticking or rebound of particles to viscosity, while also considering particle kinetic energy has been proposed for liquid droplets impacting a surface [20, 21, 29, 170–173, 177]. In these models, the maximum spread of the particles upon impaction is calculated from the particles Weber and Reynolds numbers, which are computed from the particle size, density, velocity, surface tension (We) or viscosity (Re) [170, 171]. The maximum spread is then used to describe the energy lost by viscous dissipation and the surface energy stored for the particles to retain their original shape and possibly rebound. These models only apply to liquids i.e. for materials with viscosities less than ≈1-10, depending on particle size. In deposit modeling, this model has been applied for silicate-rich ashes at high temperatures where the particles are molten [20, 21] and for salt-rich ashes at temperatures above the melting temperature [29, 177].

Elastic impact

In the low-temperature end of the scale, where particles are solid, deposition can be described by elastic impact models. In these models, the degree of deformation and the contact area upon impaction is determined from the particles elastic (Young's) modulus [166–169]. Possible rebound is determined from an energy balance which balance the surface tension in the formed contact area and the stored elastic energy of the particle, available for rebound. Dong et al. [167] has reviewed different elastic impact models and applied them to ash particles at low temperatures (below the glass transition temperature). They propose a critical velocity of the incoming particle, which is based on the JRK (Johnson, Kendall & Roberts) adhesion theory [167, 168].

$$u_{p,crit} = \frac{\left(\frac{\gamma}{r_p}\right)^{5/6}}{(\rho_p^3 E^2)^{1/6}} \tag{5.45}$$

γ is the surface tension and E is the Young's (elastic) modulus of the particle. The sticking criterion can then be described as:

$$p_p = \begin{cases} 1 & \text{for} \quad u_p \cdot \sin(\alpha_{impact}) < u_{p,crit} \\ 0 & \text{for} \quad u_p \cdot \sin(\alpha_{impact}) > u_{p,crit} \end{cases} \tag{5.46}$$

where p_p is the sticking probability of the particle.

The Young's modulus describe a material's elasticity. In purely elastic materials responses to stresses occur instantaneously and is described by the Young's modulus. For glasses (with compositions relevant for ashes) the Young's modulus is relatively constant physical parameter below the glass transition temperature, with values in the GPa range [32, 192]. Near the glass transition temperature, which is identified where the viscosity is 10^{12} Pa s, the elastic modulus drops approximate three orders of magnitude, due to changes in the atomic bonding [192].

Viscoelastic impact

At temperatures above the glass transition temperature, where the material is between a solid and liquid state, the material is viscoelastic; responses to stresses occur as a function of time. If a stress is applied at a high rate, the material may behave like a elastic material, whereas a slowly applied stress may result in a viscous, time dependent, response [32, 192]. Since the material behavior is still to some extent elastic, Equation 5.45 can still be employed to describe the impact, though with a proper evaluation of the Young's modulus

In this region, the Young's modulus is a function of the time and temperature and is related to the viscosity by e.g. the Maxwell Model (4 different models were presented by Losurdo [32])

$$\begin{aligned} E(t) &= E_1 \cdot \exp\left(-\frac{t}{\mu_1 / E_1|_{t=0}} \frac{\Delta T_1}{|\Delta T_1|} \right) \\ E(t=0) &= E_1 \\ \lim_{t \to \infty} E|_{T=T_1} &= 0 \end{aligned} \tag{5.47}$$

Thus, in order to describe the elastic modulus of a viscoelastic solid, it is needed to follow the time (and temperature) history of the solid. This is not attempted within this mechanistic modeling approach, but considerations in that area can be found in the CFD modeling of deposit formation presented by Losurdo et al. [32, 33].

The importance of a precise description of the Young's modulus, when applying the critical velocity described in Equation 5.45 has been examined. In Figure 5.6, the critical velocity is seen as function of Young's modulus (left) and of temperature (i.e. varied surface tension) (right). It is seen in Figure 5.6(left), that though the Young's modulus varies 5 orders of magnitude, with 1 MPa as the minimum value, the critical velocity only varies in the range 0-3 m/s for the smallest particles (10μm), while for

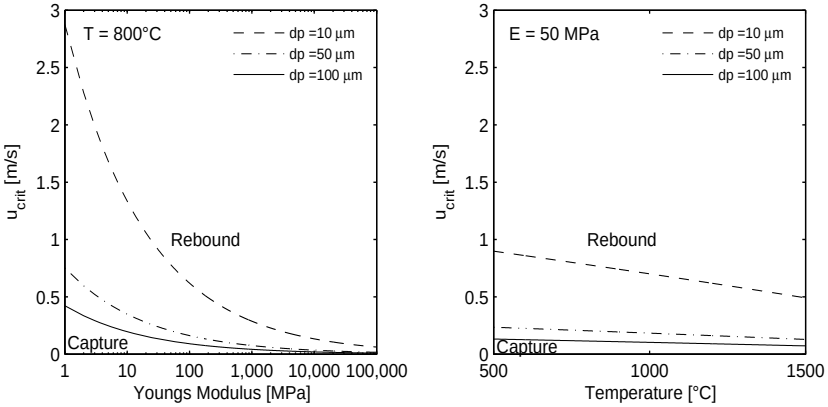

Figure 5.6: Critical velocity of three particle size as function of Young's modulus (left) and temperature (right), calculated by Equation 5.45. The calculations are made for Straw C.

larger particles (100μm) the variation in Young's modulus is only within 0-0.5 m/s. In the right figure it is seen how the temperature also have the most significant effect on the smallest particles, which is via the surface tension (calculated from temperature as described later). The major impact on the small particles as compared to larger particle sizes is caused by a higher importance of adhesive forces relative to fluid forces for small particles [166].

In figure 5.6, it is seen that in the low-E-range, i.e. where the particles are expected to be viscoelastic, the critical velocity of small particles is quite dependent on the Young's modulus, which ideally should be computed from time, temperature and viscosity. However, it is anticipated that the critical velocity can be employed with an assumed, constant value of the Young's modulus. The chosen value of the Young's modulus will primarily be significant for the smallest particles.

5.5.5 Detailed Models; Particles Impacting Captive Surface

Once a layer of deposited ash (and/or salts) has formed on a heat transfer surface, the deposit surface temperature increases, leading to lower surface viscosities and the surface may capture incoming, otherwise non-sticky particles. The capture of particles by a silicate slag or molten salt has been described by Raask [193]. In this model, the kinetic energy of the particle will be lost by resistance of a viscous drag as the particles (partly) penetrates the viscous surface. The model is found to apply to surfaces with viscosities well above the molten range (» 10 Pa·s) [193]. This model is 'opposite' the particle impact models in the sense that particles with velocity *higher* than a critical velocity will penetrate the viscous layer too much for rebound, and

will be captured.

The depth of a particle penetration into a viscous surface is approximated by [193, 194]:

$$s = \frac{2r_p^2 \rho_p u_p \sin(\alpha_{impact})}{9\mu_s} \tag{5.48}$$

μ_s is the viscosity of the deposit surface. When the surface tension forces acting on the partially penetrated particle is greater than the gravitational forces acting on the particle, the particle will be retained. A critical velocity is then found when:

$$F_s = F_g \tag{5.49}$$

$$2\pi\gamma\sqrt{2sr_p} = \frac{4}{3}\pi r_p^3 \rho_p g \tag{5.50}$$

$$s = \frac{2r_p^5 \rho_p^2 g^2}{9\gamma^2} \tag{5.51}$$

Combining equation 5.48 and 5.51 leads to a critical velocity for surface capture

$$u_{s,crit} = \frac{\rho_p g^2 r^3 \mu_s}{\gamma^2 \sin\alpha} \tag{5.52}$$

and the sticking/rebound criterion is:

$$p_s = \begin{cases} 1 & \text{for} \quad u_p > u_{s,crit} \\ 0 & \text{for} \quad u_p < u_{s,crit} \end{cases} \tag{5.53}$$

The critical velocity as function of temperature and viscosity (calculated from the temperature), calculated for three particle sizes is seen in Figure 5.7.
It is seen that with a normal impact velocity of 2 m/s (relevant for the EFR), small (10μm) particles may be captured when the viscosity of the surface is as high as 10^{10} Pa·s, well above the viscosity of a liquid material (≈10 Pa·s).

5.5.6 Model Approach

In this work; two model approaches for the sticking probability are selected;

Model #1: The simple sticking model proposed by Walsh et al. [182], using a reference viscosity to describe the sticking probability of particles and surfaces (Equation 5.42) which is combined by Equation 5.43. Looking at the experimental results for the critical viscosity in Figure 5.5, a critical viscosity in the 10^6 – 10^7 Pa·s range is expected to apply to the particles in the EFR, while it should possibly be lower for the full scale ashes, due to higher velocities and larger particles. The purpose of using this model is to test the ability of a simple model, often used in coal ash models, to describe deposit formation also for biomass ashes.

Model #2: For a detailed approach, taking particle size and velocity into account, the impact of (visco)elastic particles has been combined with the sticky surface

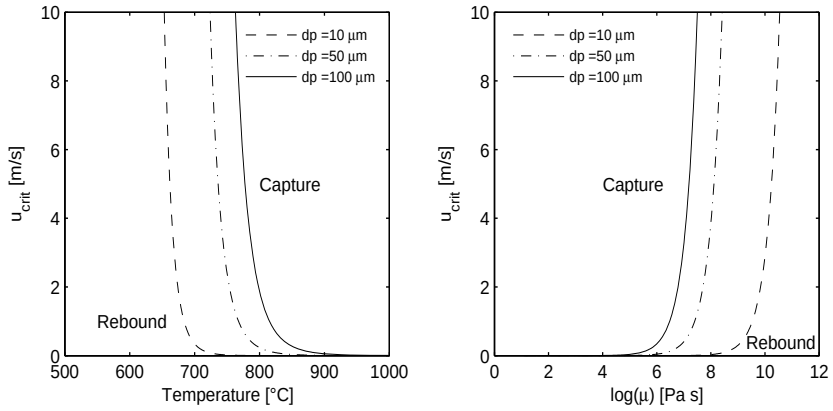

Figure 5.7: Critical velocity of three particle size as function of temperature (left) and viscosity (right), calculated by Equation 5.52. The viscosity calculations are made for Straw C.

approach. Thus, the critical velocities dcalculated by Equations 5.45 and 5.46 describing the capture of (visco)elastic particles on the solid surface and by Equations 5.52 and 5.53 for capture of particles by the viscous surface has been used to calculate the sticking probabilities of the particle and the surface; p_p and p_s. Then, the final sticking probability of the impact is:

$$\eta_s(i,\theta) = \underbrace{p_p(i,\theta)}_{sticky\ particles} + \underbrace{(1-p_p(i,\theta))\cdot p_s(i,\theta)}_{sticky\ surface} \tag{5.54}$$

The purpose of employing Equations 5.45 and 5.46 for the solid surface, in spite of the uncertain estimate of the Young's modulus, is to take into account that solid, otherwise considered 'non-sticky' particles, may also deposit in the initial phase of an experiment on a steel surface or on high-viscous surfaces, simply due to a low kinetic energy of the approaching particle, inhibiting rebound.

5.6 Heat Transfer Model

Proper descriptions of the deposit surface temperature and of the temperature profile within the deposits are important. The deposit surface temperature is important in prediction of the rates of condensation and thermophoresis, while the temperature profile within the deposit is important for the deposit characteristics and alterations. The temperature of the deposit surface is determined by an energy balance, described by Equation 5.55. In this energy balance heat development by e.g. reactions is

ignored.

$$q = \frac{k_{eff}}{\delta_{eff}}(T_s - T_t) = h(T_{fg} - T_s) + \alpha\sigma T_{fg}^4 - \epsilon\sigma T_s^4 \tag{5.55}$$

By assuming that Kirchoff's law applies to the deposit, the absorbance equates the emissivity, $\alpha = \epsilon$, and Equation 5.55 can be written as Equation 5.56, which can be solved by an iterative procedure.

$$\frac{k_{eff}}{\delta_{eff}}(T_s - T_t) = h(T_{fg} - T_s) + \epsilon\sigma(T_{fg}^4 - T_s^4) \tag{5.56}$$

The first term describes the heat conducted through the deposit and k_{eff} is the effective thermal conductivity of the deposit while δ_{eff} is the thickness. The second term describes the heat transported to the deposit surface by convection, where h is the local convective heat transfer coefficient. The last term describes the heat transported toward the deposit surface by radiation, where ϵ is the emissivity of the deposit surface and σ is the Stefan-Boltzmann constant. Thus, three parameters needs to be estimated; k_{eff}, h and ϵ.

The local heat transfer coefficient, h, can be determined from the Nusselt number, Nu, the probe diameter and the thermal conductivity of the gas;

$$\mathrm{Nu} = \frac{h \cdot d_{probe}}{k_g} \tag{5.57}$$

Experimental data on the heat and mass transfer around a cylinder has been obtained by Sanitjai and Goldstein [152]. The data has been examined by Zhou et al. [19] and the Nusselt number was expressed as function of angle around the probe as given by Equation 5.58.

$$\mathrm{Nu} = \begin{cases} 0.67 \cdot \mathrm{Re}^{0.5} \cdot \mathrm{Pr}^{0.35}(1 + \cos(\frac{\pi}{180}\theta)) & \theta \leq 85^\circ \\ 0.73 \cdot \mathrm{Re}^{0.5} \cdot \mathrm{Pr}^{0.35} & 85^\circ < \theta \leq 180^\circ \end{cases} \tag{5.58}$$

The Reynold and Prandtl's numbers are calculated from flue gas properties, found in Appendix B.3.

$$\mathrm{Re} = \frac{u_g \cdot d_{probe} \cdot \rho_g}{\mu_g} \tag{5.59}$$

$$\mathrm{Pr} = \frac{\mu_g \cdot C_{p,g}}{k_g} \tag{5.60}$$

The effective thermal conductivity and the emissivity are parameters, which depend on the deposit characteristics such as chemistry, porosity, degree of sintering, particle size, etc. The thermal conductivity of coal ashes has been experimentally examined by Rezaei et al. [195]. It was concluded, that the degree of sintering and the porosity are parameters with the main influence on thermal conductivity. The

influence of chemical composition is secondary as the influence of chemical composition is mainly via the influence of sintering temperature [195].

A deposit may be observed as a packed bed. Zbogar et al. [196] has in an extensive review compared numerous models describing the thermal conductivity and/or emissivity of packed bed. The models are ranging from rather simple to very detailed. These models are generally based on a somewhat detailed knowledge of the bed material and structure. Parameters which are mainly unknown for a deposit.

In most deposit models, a quite simple model for the thermal conductivity, based on the deposit porosity has been applied [19, 24]. The effective thermal conductivity of the deposit is described by Equation 5.61 [183].

$$k_{eff} = (1 - F) \cdot k_s + F \cdot k_g \tag{5.61}$$

k_s and k_g are the thermal conductivities of the solid and gas phase, respectively. F is the fraction of the conductivity attributable to the gas, calculated by Equation 5.62.

$$F = \frac{2^n}{2^n - 1}\left(1 - \frac{1}{(1+\phi)^n}\right) \tag{5.62}$$

n is an empirical parameter set to 6.5 and ϕ is the porosity of the deposit. In the calculation of surface temperature, the initial porosity is used for calculation of the thermal conductivity at all times. It inner most porous layer will act as a limiting barrier for the heat transport, in most cases. Only at high temperatures, with extensive sintering, where a thick dense outer layer is formed, will the thermal conductivty of the deposit differ significantly from this approximation. The deposit porosity and sintering is described later.

The thermal conductivity of the solid phase and the emissivity of the surface are described in the following section along with other relevant physical properties of the ash and deposits.

5.7 Physical Properties of Ash and Deposit

In this section, the modeling of the viscosity, the surface tension, the Young's modulus, the thermal conductivity and the emissivity is described. Initially, the compositions of the ashes in question are viewed.

The ashes and deposits formed in biomass suspension-firing (with straw and/or wood) are observed to have chemical compositions different from those observed in grate-firing of straw [134]. Since the release of K, Cl and S from biomass particles in suspension-firing is found to be high, it can be assumed that salts are found as gases and aerosols, while the coarse ash particles are 'salt-free'.

In Table 5.2, the molar composition of the ashes formed in the EFR, calculated after release of volatiles according to the model presented i Chapter 4 are seen.

Table 5.2: Molar composition of ashes in the EFR after release of volatiles

	Straw A	Straw B	Straw C	Straw D	Bark	Pine	Beech	WW
SiO_2	74.19	72.42	70.89	71.65	47.18	33.39	8.53	16.33
Al_2O_3	0.27	0.77	0.79	0.93	5.73	2.01	0.49	4.80
Fe_2O_3	0.14	0.19	0.51	0.42	1.90	1.03	0.17	1.02
CaO	12.59	13.50	14.58	15.69	35.34	45.09	57.03	49.78
MgO	4.57	4.19	5.85	6.15	6.54	16.03	20.65	11.23
Na_2O	0.31	0.46	0.62	2.04	1.58	0.78	8.19	14.36
K_2O	6.22	5.20	3.55	3.42	0.60	0.61	2.19	1.20
P_2O_5	1.71	3.28	3.21	4.62	1.14	1.05	2.76	1.28

It is seen that the straws contain high amount of SiO_2, ≈70-75 mole%, along with moderate amounts of CaO, 12-15 mole%. The summarized contents of MgO, Na_2O and K_2O is around 10 mole%. For the woody fuels, the contents of SiO_2 are low, <50 mole%, and the contents of CaO are high, >35 mole%. In addition to that, the summarized contents of MgO, Na_2O and K_2O is within 8-30 mole%.

In Table 5.3, the composition of the fuel pellets used in the full scale campaigns are seen.

Table 5.3: Molar composition of ashes used in the full scale experiments after release of volatiles

	Straw	Wood
SiO_2	61.31	54.14
Al_2O_3	0.54	2.32
Fe_2O_3	0.26	1.04
CaO	21.52	31.31
MgO	6.96	8.83
Na_2O	0.92	0.97
K_2O	5.25	0.55
P_2O_5	3.24	0.84

It is seen that the straw contains less SiO_2 than the straws used in the EFR, while the wood ash (when K, Cl and S is subtracted) has a high SiO_2 content as compared to the woods used in the EFR.
In the model, the viscosity and surface tension of the deposits are calculated from the coarse ash composition, possibly corrected by the KOH reaction.

5.7.1 Viscosity

Numerous models for predicting viscosities of ash slags have been proposed. These have been reviewed by Vargas et al. [197]. However, most of the models are developed for high temperatures and ashes rich in SiO_2, Al_2O_3 and Fe_2O_3/FeO. They are thus not expected to be valid for straw ashes with low contents of Al_2O_3 and relatively high contents of CaO , MgO, Na_2O and/or K_2O at moderate temperatures; 500-1000 °C.

Three models have been reviewed with the aim of finding a model able to describe viscosities of straw (and possibly wood ashes) at 500-1000 °C. The model performances have been evaluated by viscosity data found in the literature [197–200], with compositions relevant for straw and/or wood ashes; < 75 mole% SiO_2, <5 mole% Al_2O_3 and including varying amounts of CaO , MgO, Na_2O and K_2O. An overview of the viscosity data used is seen in Table 5.4.

Table 5.4: Overview of experimental data where viscosity is measured as function of temperature and composition. These data are considered relevant for the coarse ash fraction (after vaporization of K, Cl and S) in the biomass suspension-firing experiments.

	Lakatos 1	Lakatos 2	Tanigushi	Karlsson
Temperatures [°C]	530-1450	770-1500	700-1600	420-1200
Viscosities $\log \mu$ [Pa·s]	1-11.5	1-5	0.13-13.1	2.4-12.3
No. of mixtures	33	35	3	18
Molar compositions [%]:				
SiO_2	61-77	68-78	50-55	40-70
Al2O3	0-5	0.4-3	0.2-2.5	0
Fe2O3	0	0	0	0
CaO	8-14	6-13	25-28	10-23
MgO	1-3[a]	0-3	5-25	0-7
Na2O	10-15	2-14	0	0-25
K2O	0-6	0-9	0	0-10
P_2O_5	0	0	0	0-3
Others	-	Li_2O, BaO, ZnO, PbO: 0-7	-	B_2O_3: 0-3
Ref	[199]	[200]	[197][b]	[198]

[a] one exp with 10 %

[b] Data from compilation found in ref [197]

SS model

Senior and Srinivasachar [201] developed a model valid for viscosities in the range $10^4 - 10^8$ Pa·s. This was done to take into account that ashes may deposit even if viscosities are higher than $10^2 - 10^3$ Pa·s, where flow occurs [186]. The model is based on the mole fractions of oxides in the ash and the empirical parameters was determined from 428 viscosity measurements found in published literature [201]. The viscosity measurements was made from silicate glasses with 35-99 mole% SiO_2. It is however stated that the low-SiO_2 measurements were predominantly made at high temperatures. The model is described by Equation 5.63, with viscosity as Pa·s.

$$\log\left(\frac{\mu}{T}\right) = A + \frac{10^3 B}{T} \tag{5.63}$$

where the parameters A and B are determined from empirical correlations employing three composition-dependent constants;

$$\mathrm{NBO/T} = \frac{\mathrm{CaO} + \mathrm{MgO} + \mathrm{FeO} + \mathrm{Na_2O} + \mathrm{K_2O} - \mathrm{Al_2O_3} - \mathrm{FeO_3}}{\mathrm{SiO_2}/2 + \mathrm{Al_2O_3} + \mathrm{Fe_2O_3}} \tag{5.64}$$

$$N = \mathrm{SiO_2} \tag{5.65}$$

$$\alpha = \frac{\mathrm{CaO}}{\mathrm{CaO} + \mathrm{Al_2O_3}} \tag{5.66}$$

The model thus uses the molar content of CaO in relation to Al_2O_3 in the description of viscosity. The individual differences in the influences of e.g. K_2O, Na_2O and MgO are not considered.

Lakatos Model

Lakatos et al. [199, 200] has in various investigations examined the relationship between temperature and viscosity for soda-lime-glasses with 61-78 mole% SiO_2 and compositions as seen in Table 5.4. The viscosity model derived from the data is based on a Vogel-Fulcher-Tamann (VFT) equation, with viscosity in Pa·s:

$$\log\mu = A + \frac{B}{T - C} \tag{5.67}$$

where the constants was determined as [200]:

$$\begin{aligned} A =& 1.5183 \cdot \mathrm{Al_2O_3} - 1.6030 \cdot \mathrm{CaO} - 5.4936 \cdot \mathrm{MgO} \\ &+ 1.4788 \cdot \mathrm{Na_2O} - 0.8350 \cdot \mathrm{K_2O} - 2.4550 \\ B =& 2253.4 \cdot \mathrm{Al_2O_3} - 3919.3 \cdot \mathrm{CaO} + 6285.3 \cdot \mathrm{MgO} \\ &- 6039.7 \cdot \mathrm{Na_2O} - 1439.6 \cdot \mathrm{K_2O} + 5736.4 \\ C =& 294.4 \cdot \mathrm{Al_2O_3} + 544.3 \cdot \mathrm{CaO} - 384.0 \cdot \mathrm{MgO} \\ &- 25.07 \cdot \mathrm{Na_2O} - 321 \cdot \mathrm{K_2O} + 471.3 \end{aligned} \tag{5.68}$$

where e.g. Al_2O_3 represent the molar content of Al_2O_3 per mole SiO_2 (Al_2O_3 = moleAl_2O_3 /mole SiO_2).

Karlsson Model

Karlsson and Rönnlöf [198] examined the viscosity of bioactive glasses with 40-70 mole% SiO_2. See range of compositions in Table 5.4. The model derived is based on an Arrhenius equation with viscosity as Pa·s:

$$\log \mu = A + \frac{B}{T} \tag{5.69}$$

where the constants A and B (corrected to yield units Pa·s) are:

$$\begin{aligned} A = &- 56.707 + 0.597 \cdot Na_2O + 0.597 \cdot K_2O + 0.604 \cdot MgO + 0.516 \cdot CaO \\ &+ 0.429 \cdot P_2O_5 + 0.387 \cdot SiO_2 \\ B = &- 91.463 \cdot Na_2O + 162.861 \cdot CaO + 485.020 \cdot B_2O_3 + 249.2 \cdot P_2O_5 \\ &+ 285.212 \cdot SiO_2 \end{aligned} \tag{5.70}$$

here, the oxide contents are given as wt%.

The three models have been used to describe the viscosity data listed in Table 5.4. The results are seen in Figure 5.8, where the data has been divided into four groups according to the molar content of SiO_2 in the sample. For SiO_2 contents >60 mole% (two lower Figures in Figure 5.8), it is seen that both the SS Model and the Lakatos Model offers good predictions of the measured viscosities. The Karlsson Model generally underestimated these data. When the SiO_2 is lowered to 50-60 mole%, the SS Model is only able to predict the viscosity at high temperatures; above 1200 °C. At lower temperatures, the model is not able to take individual effects of CaO , MgO, Na_2O and/or K_2O into account. The Karlsson Model offers a generally good description of the 50-60 mole% data, but fails in describing viscosity data from mixtures containing >1 mole% Al_2O_3, as Al_2O_3 is not included in the model. The Lakatos model describes the data well, although some underestimation is observed for data containing B_2O_3 (and possibly P_2O_5). This is however not considered to be relevant for this validation. The low-SiO_2 data (<50 mole%) are only described well by the Karlsson Model, which vas derived from these data. The data with < 50 mole% SiO_2 all contain P_2O_5 and possibly B_2O_3, which are not included in the Lakatos Model.

Due to the overall best performance of the Lakatos Model, this model is used to describe the viscosities of straw ashes in the deposit formation model and the wood ash used in full scale.

The wood ashes in the EFR have very low SiO_2 contents and the viscosity model is not expected to be able to describe the viscosity of these ashes. However, In Figure 5.9B, calculations for bark and pine are shown. For the two remaining woods, the viscosity model cannot be applied due to the low SiO_2 content. Takahashi et al. [202] has examined the glass transition temperatures ($\mu = 10^{12}$ Pa·s) for SiO_2–Al_2O_3–CaO mixtures with 10-60 mole% SiO_2 and varying Al_2O_3/CaO molar ratio (0-1.5). It is

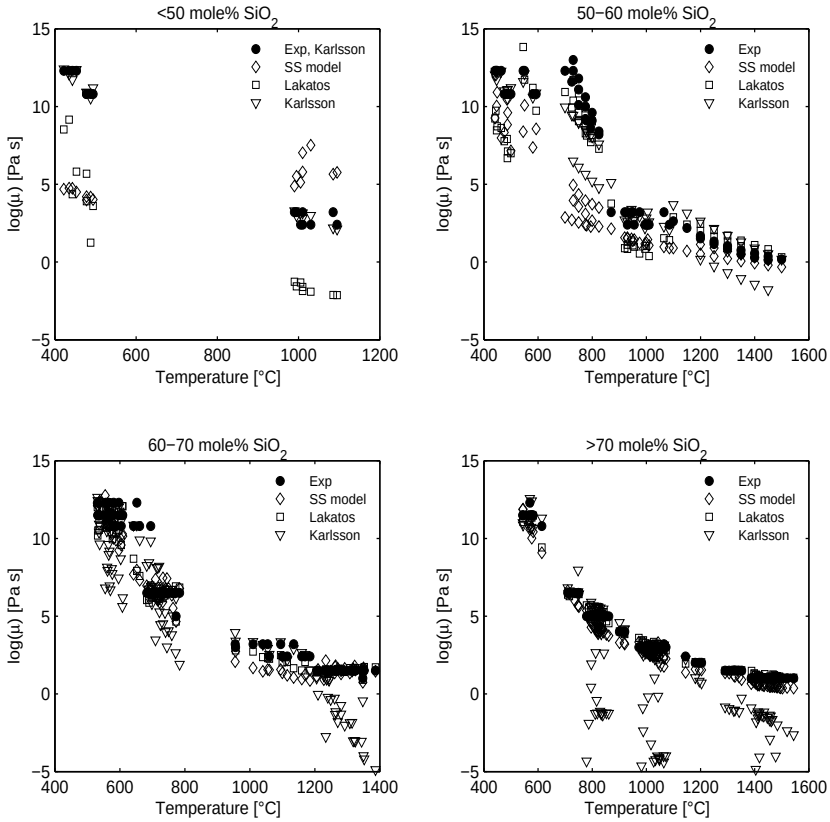

Figure 5.8: Comparison of three models (open points) in the description viscosity data (black dots). An overview of the data are seen in Table 5.4. The four figures show data with different contents of SiO_2.

found that at low Al_2O_3/CaO molar ratios the glass transition temperatures (defined where μ = 10^{12}Pa·s) are in the range 760-820 °C, increasing with decreasing SiO_2 content. In the EFR experiments, the wood ashes are all deposited at temperatures close to 800 °C, where the viscosities, according to the study by [Takahashi] and to the predictions seen in Figure 5.9B can be expected to be close to or above 10^{12} Pa·s. At the deposit surface temperatures, the viscosities will be higher. At these viscosities the wood ash will thus not contribute to deposit formation by viscosity-related mechanisms.

In the model, the viscosities of all the wood ashes in the EFR is set to μ_{wood} = 10^{12} Pa·s, and thus above the viscosity range where capture of impacted particles by a viscous surface will occur.

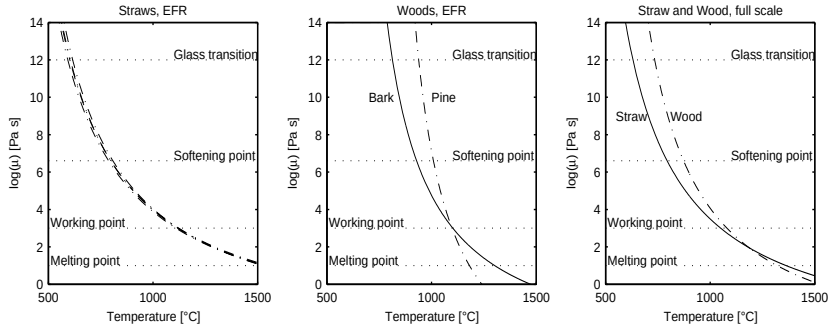

Figure 5.9: Model predictions of viscosities by the Lakatos model for the fuels used in the experiments, both EFR and full scale. The specific points in the viscosity scale, as used in glass processing are indicated [192].

5.7.2 Surface Tension

The surface tension of the ashes is described by a model proposed by Mills [203], which computes the surface tension from a weighted average of the surface tension of the individual oxides based on the molar composition of the ash.

$$\gamma = \sum y_i \bar{\gamma}_i \tag{5.71}$$

The model however takes into account that some oxides are surface active and their contribution is described by parabolic functions of the mole fraction (y_i). The parabolic functions are seen in Table 5.5 along with the partial surface tensions of the remaining oxides, both valid at 1500 °C.

Table 5.5: $y_i\bar{\gamma}_i$ for surface active ash components and $\bar{\gamma}_i$ for remaining oxides, both valid at 1500 °C [203]

$y_i\bar{\gamma}_i$ [mN/m]				$\bar{\gamma}_i$ [mN/m]	
Oxide	$y_i < N$	N	$y_i > N$	Oxide	
Fe_2O_3	-3.7-2972y_i+14312y_i^2	0.125	-216.2+516.2y_i	SiO_2	260
Na_2O	0.8-1388y_i+6723y_i^2	0.115	-115.9+2412.9y_i	Al_2O_3	655
K_2O	0.8-1388y_i+6723y_i^2	0.115	-94.5+254.5y_i	CaO	625
P_2O_5	-5.2-3454y_i+22178y_i^2	0.12	-142.5+167.5y_i	MgO	635

The temperature dependence of the surface tension is according to Mills [203] 15 mN/m per 100 °C and the surface tension in N/m of the ash at the given temperature (T_c in °C) by Equation 5.72.

$$\gamma(T) = 0.001 \cdot \gamma(1500) + 0.00015 \cdot (1500 - T_c) \tag{5.72}$$

5.7.3 Young's Modulus

Wain et al. [46] measured the Young's modulus for various coal ash slags at room temperature. They found that the Young's modulus was in the range 5-85 GPa, depending on porosity. It is generally acknowledged that porosity is a key factor in determining the Young's modulus, as increased porosity leads to lower Young's modulus [192]. The Young's modulus for the coal ashes are in the range of the Young's modulus for soda-lime-glasses which is found to be 69 GPa [192]. However, near the glass transition temperature, the the Young's modulus decrease approximately three orders of magnitude [32, 192] and values in the MPa range are expected. However, as mentioned previously, above the glass transition temperature the ashes are expected to be viscoelastic, and the Young's modulus is a function of particle history (time) and viscosity [32, 33]. In this model, the Young's modulus of the straws are assumed to by a constant value, 50 MPa. The influence of the Young's modulus is explored in a parameter study and a sensitivity analysis in Chapter 6.

For the woods in the EFR, the ashes (at least from bark and pine) are expected to be close to the glass transition temperature and values in both the GPa and the MPa range can be expected. For consistency with the straws, the Young's modulus is also set to 50 MPa for the woods.

5.7.4 Thermal Conductivity

The thermal conductivity of the gas phase within the deposit is calculated by the same temperature dependence as thermal conductivity of the flue gas, described in Appendix B.3. For the solid phase, no direct measurement of the thermal conductivity of biomass ashes have been made. Richards et al. [183] uses a constant value of 4 W/m/K while Robinson et al. [204] set the constant value to 3 W/m/K, both claimed to be representative of silica-containing materials at high temperatures. Rezaei et al. [195] have developed an empirical relation between temperature and the thermal conductivity of a sintered coal ash, based on measurements and curve fitting.

$$k_s = 0.0015 \cdot T^{1.1} \tag{5.73}$$

This relation estimating the thermal conductivity to be within 2-4 W/m/k in the temperature range 500-1000 °C is employed in the current model.

5.7.5 Emissivity

The emissivity of the deposit surface is according to Boow and Goard [205] influenced mainly by the particle size of the last deposited particles. A correlation between the particles on the deposit surface and the emissivity was suggested for real ash deposits [193, 205]:

$$\epsilon = 0.30 \cdot \log(d_p) + 0.16 \tag{5.74}$$

where d_p is given in μm. The relation is valid for particle sizes 7-420 μm. In the model, this correlation is used by employing the median particle size of the ash, $dp_{50,ash}$. The calculated emissivity of a surface of e.g. 45 μm particles is then 0.65.

5.7.6 Porosity and Sintering

In the model, the porosity of the deposits formed is an important parameter for the description of the deposit thickness and the deposit thermal conductivity. Both of these parameters influence the prediction of the deposit surface temperature. Thus, both the choice of the initial deposit porosity (i.e. the packing of the particles upon impaction) and subsequent sintering within the deposit is important.

The initial porosity of ash deposits has been measured to values within 0.6-0.9. Robinson et al. [204] measured the initial porosity to values near 0.9 for the very initial layer of deposit on a 3-400 °C probe, obtained during the first 2.5 hours in an experiment with combustion of a coal/straw mixture [204]. Richards et al. [183] states that a porosity of 0.6 can be expected from powdery or lightly sintered deposits, while Raask [206] uses an initial porosity of 2/3 (0.67), claimed to be relevant for ash deposited on boiler tubes. In the model, the initial porosity is set to 0.8. The influence of this parameter will be explored. In the model, sintering of the deposit surface is included. Rezaei et al. [146] described liquid phase mobility sintering by Equation 5.75. This was derived for coal ashes, but is assumed to apply also to biomass ashes in this work. Naturally, this need further examinations.

$$\phi = \frac{\left(1 - \frac{9 \cdot \gamma \cdot t_{sint}}{4 \cdot \mu \cdot r_0}\right) \phi_0}{\left(1 - \phi_0 + \left(1 - \frac{9 \cdot \gamma \cdot t_{sint}}{4 \cdot \mu \cdot r_0}\right) \phi_0\right)} \tag{5.75}$$

γ is the surface tension (function of composition and temperature), μ is the viscosity and t_{sint} is the time for sintering [146]. The influence of the sintering time is examined in Figure 5.10. Here, the calculation is shown for one straw used in the EFR experiments examined later, Straw C. It is seen that at viscosities around 10^7 Pa·s (around 800 °C for straw C) complete sintering may occur within 100 seconds. By lowering the viscosity to approximately 5 Pa·s (i.e. below the softening point by increasing the temperature to $>$ 900 °C) sintering is found to occur fast and full sintering may occur within a few seconds. This implies that the time for sintering is mainly important for temperatures within 800-900 °C for this ash.

In the model, t_{sint} is set to 10 sec, to occur in the outer layers. By setting the time for sintering to a fixed value, the 'final porosity' of the deposit layer is considered already when the added thickness of deposit in a time step is calculated.

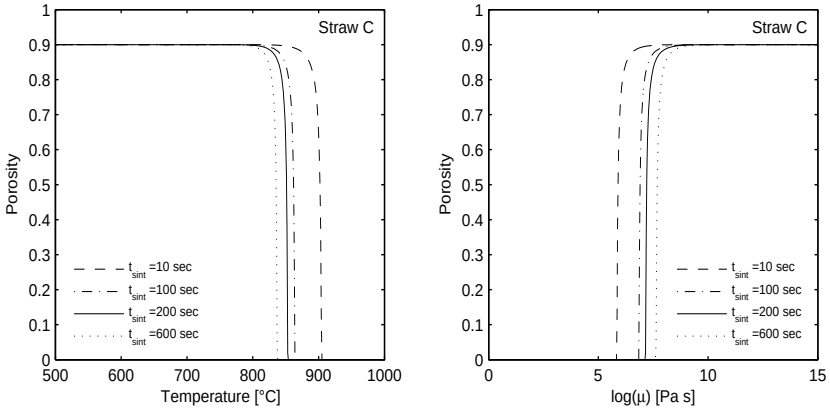

Figure 5.10: Sintering as function of Temperature and of viscosity, when the viscosity and surface tension is calculated from the composition of straw C and the temperature

Chapter 6

Model Evaluation by Use of EFR Experiments

The models for fly ash characteristics (Chapter 4) and for deposit formation (Chapter 5) are in this chapter used to describe a series of experiments conducted with combustion of straw or wood in an entrained flow reactor (EFR). The experiments were conducted in 4 experiment series over the years 2002-2004 [37, 50, 207] and 2009 [39, 49]. In these experiments, a deposit probe was placed near the reactor exit for quantification of deposit formation at a range of probe- and flue gas temperatures.

The aim of using the model to describe these experiments is to make a relatively broad validation in a controlled setup, i.e. where temperatures, flows, fuels etc. are known.

6.1 EFR Experiments

The combustion experiments were conducted in an entrained flow reactor (EFR), which was designed to simulate environment of a suspension-fired boiler [39]. Figure 6.1 shows a schematic drawing of the experimental setup.

The setup consisted of a reactor and a bottom chamber. The reactor was composed of a fuel feeding system, a gas preheater, and a vertical tube reactor electrically heated by 7 thermal elements. In the bottom chamber a controlled gas and particle extraction system, a bottom ash cup and a particle deposition system was found. Detailed information of the experimental setup can be found elsewhere [37, 39, 49].

During the experiments, pulverized biofuel particles (~850 g/h) were fed into the reactor by the primary air, which was around 15 % of the total air supply. After injection, the fuel particles were entrained with preheated secondary air in the reactor. For each experiment, the temperature of the preheater was controlled at 900 °C and the wall temperatures of the tube reactor were set from 1000 °C to 1300 °C, simulating the temperature profile in a boiler. The residence time in the reactor was

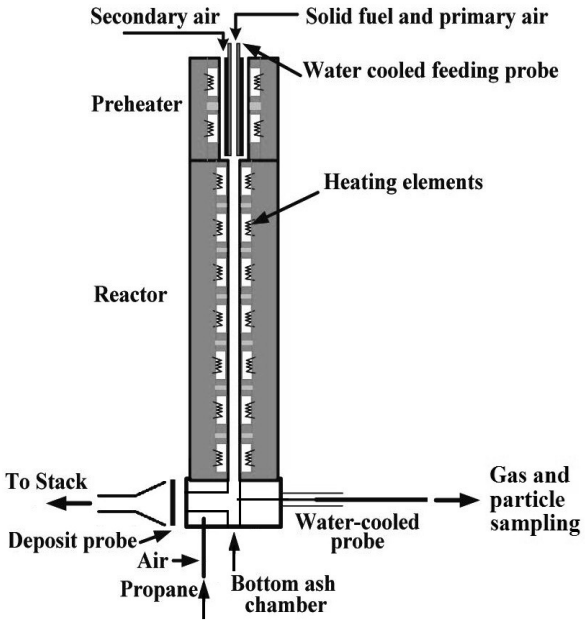

Figure 6.1: Sketch of the EFR used for deposition experiments

approximately 1 s.

Ash residues from combustion was lead with the flue gas to the bottom chamber. As the gas entered the bottom chamber it was cooled rapidly to approximately 800 °C. In the bottom chamber, the bottom ash was collected and the flue gas was separated into two fractions. A main part of the flue gas was directed to an air cooled deposition probe, while a minor part of the flue gas was drawn to an extraction system though a water-cooled probe.

The flue gas sampled in the extraction system was first lead through a cyclone with cutoff diameter 2.5 μm, where the coarse ash particles were collected. Then, the sampled gas passed through an aerosol filter with pore size of 0.1 μm where remaining fine particles were gathered. The concentration of CO, CO_2, O_2, SO_2 and NO in the dry gas was continuously measured by two gas analyzers. During the experiments, the cyclone, filters and extraction lines were heated to 95 °C to avoid condensation of water.

In the bottom chamber, the main part of the flue gas was lead through a 4x8 cm duct toward a deposit probe. In the duct, a propane burner was mounted to ensure a flue gas temperature of approximately 800 °C just before the probe, for the most experiments. The probe is a Ø = 1 cm stainless steel probe, where 8 cm (of total 10 cm) is exposed to the flue gas. The surface temperature of the probe was measured and registered by thermocouples mounted under the deposits probe tube

wall. By adjusting the temperature of cooling air, the surface temperature of the tube wall was maintained at a desired temperature, within 450-600°C, during the experiments.

The experiments reviewed for this modeling approach were conducted in four different experiment series [37, 39, 49, 50, 207]. The fuels used in the experiments are four different straws used in 19 different experiments (S1-S19) and four woods (bark, pine, beech and waste wood (ww)) used in five experiments (W1-W5). The proximate and ultimate analysis of the fuels are seen in Table 6.1. It is found that straws C and D had ash compositions similar to a typical danish straw [81], whereas straws A and B had lower contents of K and Cl. The wood ashes had a significant variation in the ash compositions, which is observed in nearly all the elements.

Table 6.1: Analysis of the fuels used in the EFR experiments

Fuel	Straw A	Straw B	Straw C	Straw D	Bark	Pine	Beech	WW
Exp nr:	S1-2	S3	S4-17	S19	W1-2	W3	W4	W5
As received moisture and ash: [wt% wet]								
Moist.	7.22	13.1	6.7	5.94	7.1	6.4	7	6.32
Ash	4.17	3.82	7.23	5.93	2.69	0.47	0.47	0.62
Proximate analysis [wt% dry fuel]								
Ash	4.49	4.40	7.75	6.30	2.90	0.50	0.50	0.66
C	47.5	46.5	47.5	46.39	50.7	49.7	48.7	49.87
H	6	6	5.9	6.17	6.3	6.3	6.2	6.43
O	43.49	42.1	37.95	39.84	39.9	43.5	44.4	42.18
S	0.08	0.12	0.20	0.26	0.026	<0.022	<0.022	0.014
N	0.43	0.83	0.7	1.04	0.18	0.01	0.12	0.08
Cl	0.156	0.097	0.72	0.673	0.023	0.011	0.045	0.042
Ultimate analysis [wt% dry ash][a]								
SiO_2	57.58	55.73	38.57	38.01	40.17	27.60	5.20	12.34
Al_2O_3	0.36	1.00	0.73	0.84	8.28	2.81	0.50	6.16
Fe_2O_3	0.29	0.39	0.74	0.60	4.30	2.27	0.28	2.05
CaO	9.11	9.68	7.39	5.96	28.04	34.74	32.40	35.06
MgO	2.38	2.16	2.14	1.73	3.74	8.89	8.44	5.69
Na_2O	0.24	0.36	0.35	1.12	1.38	0.67	5.15	11.19
K_2O	18.92	15.69	30.25	28.42	7.99	7.89	20.91	14.23
SO_3	4.48	6.81	6.43	8.62	2.81	<10.90	<12.72	4.99
P_2O_5	3.14	5.97	4.13	5.79	2.29	2.05	3.98	2.29
Cl	3.50	2.20	9.27	8.93	1.00	2.18	10.42	5.99
Ref	[39]	[37]	[50]	[49]	[37]	[37]	[37]	[49]

[a] SO_3 and Cl determined from fuel analysis and recalculated.

Details of the experimental conditions (flows etc.) are seen in Appendix D, while the key input parameters and the experimental results are seen in Table 6.2. In the experiments with straw, variations in probe- and flue gas temperatures were used, whereas the experiments with woods were made with similar temperatures.

Table 6.2: Key operation parameters and measured deposit results in terms of deposit mass/rate and deposit chemistry. Numbers in () are assumed values based on similar experiments (repetitions).

	Fuel			Measured values					Deposit		Water soluble content			
Exp no. & Ref.	Type	dp_{50} μm	Ash wt% dry	T_{fg} °C	T_{probe} °C	time h	SO_2 ppm[a]	$X_{coarse,fly}$ %[b]	Mass g	Rate g/cm^2/h	K wt%	Na wt%	Cl wt%	SO4 wt%
S1 [39]	Straw A	285	4.49	752	468	1.50	22.57	56.2	0.67	0.018	7.10	0.04	3.60	3.15
S2 [39]	Straw A	285	4.49	749	468	1.50	24.63	21.8	0.61	0.016	7.05	0.04	3.60	3.15
S3 [37]	Straw B	350	4.40	799	551	2.50	59.31	17.2	0.25	0.004	20.85	0.18	8.61	9.46
S4 [50]	Straw C	440	7.75	739	500	1.50	49.34	5.3	0.75	0.020	25.30	0.10	17.70	11.38
S5 [50]	Straw C	440	7.75	814	561	1.37	63.37	10.4	0.77	0.022	25.64	0.16	18.41	5.74
S6 [50]	Straw C	440	7.75	809	543	1.35	63.36	5.8	0.76	0.022	28.80	0.15	21.37	6.90
S7 [50]	Straw C	230	7.75	694	450	1.67	52.21	5.6	0.96	0.023	20.90	0.10	15.40	7.79
S8 [50]	Straw C	230	7.75	724	440	1.50	55.74	2.0	0.98	0.026	17.10	0.10	12.30	6.59
S9 [50]	Straw C	230	7.75	(700)	(450)	1.50	69.81	6.6	0.90	0.024	-	-	-	-
S10 [50]	Straw C	230	7.75	789	496	1.60	58.59	4.5	1.13	0.028	25.50	0.13	21.00	5.17
S11 [50]	Straw C	230	7.75	743	487	1.63	43.30	3.5	1.07	0.026	17.80	0.10	11.80	3.40
S12 [50]	Straw C	220	7.75	785	464	1.42	71.06	7.8	0.79	0.022	18.15	-	10.10	4.31
S13 [50]	Straw C	220	7.75	920[c]	577[c]	1.82	31.81	7.9	1.09	0.024	16.62	0.12	11.14	3.36
S14 [50]	Straw C	220	7.75	795	485	1.58	54.74	12.8	1.08	0.027	18.75	0.13	12.84	4.13
S15 [50]	Straw C	220	7.75	783	550	1.50	36.40	14.1	1.25	0.033	18.19	0.11	11.80	4.75
S16 [50]	Straw C	220	7.75	904	664	1.50	48.76	16.2	1.38	0.037	16.77	0.16	7.16	7.00
S17 [50]	Straw C	220	7.75	1020	607	1.50	41.58	9.1	1.58	0.042	18.55	0.29	8.17	5.78
S18 [49]	Straw D	250	6.30	800	550	1.50	65.95	18.7	1.01	0.027	8.74	0.00	4.28	3.21
S19 [49]	Straw D	250	6.30	802	548	0.78	107.10	18.4	1.14	0.058	8.74	0.00	4.28	3.21
W1 [37]	Bark	330	2.90	833	591	3.50	23.58	32.5	0.36	0.004	7.20	-	3.32	4.36
W2 [37]	Bark	330	2.90	831	582	3.50	21.97	28.5	0.37	0.004	5.70	-	2.10	3.60
W3 [37]	Pine	330	0.50	807	541	6.00	22.88	73.2	0.23	0.002	5.45	0.23	0.82	2.88
W4 [37]	Beech	240	0.50	801	551	4.50	30.76	49.8	0.29	0.003	12.95	1.84	6.07	5.29
W5 [49]	WW	220	0.66	803	550	1.50	7.52	26.1	0.15	0.004	1.51	0.00	2.05	1.31

[a] at 6%O_2, dry flue gas

[b] % Insoluble cyclone and filter ash as % of the total ash fired, after recalculation to total flue gas flow

[c] Temperatures lowered to T_{fg}=753°C and T_{probe}=416°C after 30 min in experiment S13

6.2 Flue Gas and Fly Ash in the EFR

The general model for description of the flue gas and fly ash was described in Section 4. Here, the description of the flue gas and fly ash in the EFR will be briefly described, as some measurements made during the experiments are used.

Flue Gas Flow

The flue gas flow is calculated from the fuel flow and composition (C, H, O, N and S) and the air flow supplied to the EFR. It is assumed that full combustion occurs. Thus, the only combustion products considered are CO_2, H_2O, SO_2 and NO. Once the total molar flow of flue gas is determined ($\dot{n}_{fg}$), the normal volumetric flue gas flow is calculated at the standard temperature and pressure (273.15 K, 101325 atm).

$$\dot{V}_{fg,STP} = \dot{n}_{fg} \cdot 22.413\,[\mathrm{Nm^3/kmol}] \tag{6.1}$$

In the flue gas duct in the bottom chamber, a propane burner was mounted. The purpose of this burner was to maintain an adequate flue gas temperature for deposit formation experiments. The propane burner provided additional flue gas to the duct, and thereby increased the flue gas volumetric flow and velocity and lowered the concentrations of fly ash and inorganic gas species. In the model, the amount of additional flue gas from the propane burner is calculated by assuming complete combustion. The calculated volumetric flue gas flow from the propane burner is then added to the original flow.

In the bottom chamber a sample of the flue gas is extracted. In the model, this flow is assumed to be representative with respect to the concentrations of fly ash, aerosols or gas species in the flue gas. The sample flow influenced only the amount of flue gas present in the duct toward the probe, and thereby the flue gas velocity. Thus, when the flue gas velocity near the probe is calculated from the volumetric flue gas flow, the sample flow is subtracted.

With these alterations, the flue gas flow used in the calculations of concentrations near the probe is:

$$\dot{V}_{tot\,fg,STP} = \dot{V}_{fg,STP} + \dot{V}_{fg\,propane,STP} \tag{6.2}$$

The flue gas volume used for calculating the flue gas velocity at the duct exit is:

$$u_{fg,duct} = \frac{\dot{V}_{tot\,fg,STP} - \dot{V}_{sample,STP}}{A_{duct}} \cdot \frac{T_{fg}}{273.15} \tag{6.3}$$

Gas Phase Species and Aerosols

During the EFR experiments, the SO_2 concentration in the sampled flow was measured. This measurement is used to estimate the concentration of K_2SO_4 in the flue gas. This is done with the assumptions that all S not measured as SO_2 is found

as K_2SO_4 and that no further reaction occured in the duct leading the flue gas ($\approx 800\,^{\circ}C$) toward the deposit probe. In the measurements, the SO_2 concentration is given as ppm in a dry flue gas at 6 % O_2. This concentration has been recalculated to the corresponding concentration in the flue gas with the calculated content of H_2O and O_2.

The distribution of Cl between KCl and HCl is assumed to be in equilibrium and the concentrations are determined by Equations 4.5-4.7, found in Chapter 4. The equilibrium calculation is made at the reactor temperature (1200 °C) and assumed to be unaltered near the probe. It is thus assumed that the gas phase reactions are quenched when the gas reaches the bottom chamber due to a rapid cooling to ≈800 °C at a rate estimated to be well above 2000 °C/s.

Coarse ash

In the experiments, the fly ash concentration in the duct toward the probe was measured by collection of ash particles in the sample flow in a cyclone and a filter. These collected ash samples were weighed and analyzed in terms of water soluble contents (K, Na, Cl and SO_4). The water soluble content can be regarded as originally present as gases and aerosols in the flue gas. These have most likely condensed during sampling, where the temperature in the sample line was kept at 95 °C. From the analyzed samples, the amount of coarse, insoluble ash in the flue gas can be determined. The amount of insoluble ash is given by $X_{coarse,fly}$; the fraction of the total ash supplied to the EFR, found as coarse insoluble ash in the flue gas flow. This quantity is used to calculate the concentration of the coarse ash in the flue gas.

$$C_{coarse\,ash} = \frac{\dot{m}_{fuel} \cdot X_{ash,fuel} \cdot X_{coarse,fly}}{\dot{V}_{tot,fg}} \tag{6.4}$$

The particle size distribution of the coarse fly ash is determined by the model described in Chapter 4.

PSD of Fly Ash After the Bottom Chamber

After the combustion in the vertical reactor, the flow is turned 90° in the bottom chamber and lead toward the deposit probe. As the flow is turned, a fraction of the ash will not be able to follow the gas flow and will be removed as bottom ash. A model of the bottom chamber has been used to describe the alterations in the particle size distribution occurring in the turn since large particles deposit to a higher degree than small particles.

In the literature, two simple models for particles behavior in bend flow are found; particles in an impactor and particles in a bend pipe. Simple analysis of particle curve linear motion has been performed for both systems by Hinds [208] and by Crane and Evans [209]. It is found that the impaction efficiency of particles on the impaction

plate or on the pipe wall, is determined by the flow into the bend. The impaction efficiency (fraction of particles impacting) for a 90° bend is calculated by the Stokes number of a particle in the inlet.

$$I_{bend} = \frac{\pi}{4} Stk = \frac{\pi}{4} \frac{\rho_p d_p^2 u}{18 \mu_g r_{pipe}} \qquad (6.5)$$
$$(I_{bend} = 1 \text{ for } Stk > 1.27)$$

Naturally - the analyses performed for the two systems are simplified and approximate, but they serve as good preliminary estimates of the impaction efficiencies [209]. The gas velocity and the dimension of the nozzle before the bend determine if a particle of a given size will follow the curved streamlines of the gas, or impact on the plate or pipe wall.

The gas flow occurring in the bottom chamber is quite complicated, due to changes in temperature and different dimensions of the reactor and the duct. Besides this, the flow was further complicated by ash deposits near and within the bottom chamber. However, the simple model presented by Equation 6.5 has been used to estimate the fraction of each particle size which will impact in the 90° turn and thereby estimate the alterations to the particle size distribution of the ash. In Figure 6.2, the PSD of the ash formed in the reactor and the PSD of the ash after the bend are shown. The PSD's are calculated for experiment S1, where the dp_{50} of the fuel was 285 μm. It is seen that an ash with $dp_{50,ash}$ = 50 μm is formed in the reactor. In

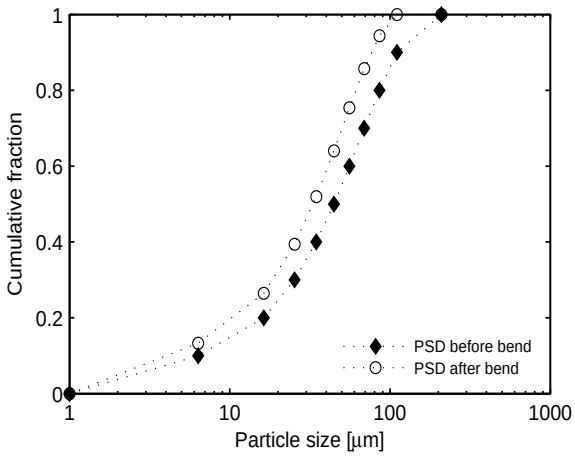

Figure 6.2: PSD of ash before and after the 90° bend in the bottom chamber, calculated for experiment S1.

the bend, the PSD is shifted toward smaller particle sizes as $dp_{50,ash}$ is reduced to 33 μm and particles above approximately 100 μm are expected to completely deposit

in the bottom chamber.

In the model the fraction of the total coarse ash occupied by each size-class of particles is calculated, and the concentration of each size class can then be determined from the total coarse ash concentration.

6.2.1 Model Prediction of Fly Ash

In this section the results of the calculations describing the gas flow and ash concentrations are shown before the results of the deposit build-up model are presented in the following sections.

In Figure 6.3, the results of the ash mass balance calculations based on the data shown in Table 6.2 are shown; the vaporized fraction, the fraction of the coarse ash found in the flue gas and the ash lost in the reactor, calculated by

$$X_{bottom/loss} = 1 - X_{vap} - X_{coarse,fly} \tag{6.6}$$

where $X_{coarse,fly}$ is the fraction of the ash found as coarse fly ash, measured during experiments by the sampling in the cyclone and the filter (the insoluble part of the ash sampled), while X_{vap} is the amount of vaporized ash, estimated from fuel compositions, as described in Chapter 4.

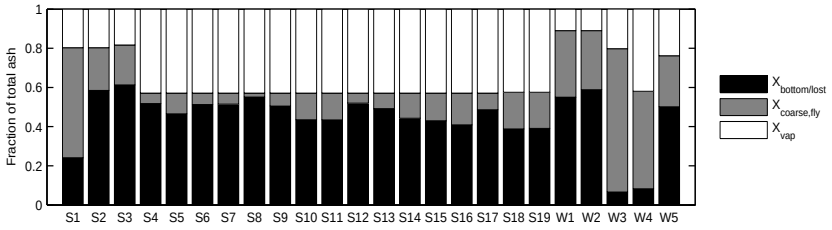

Figure 6.3: Results massbalance; $X_{bottom,lost}$ is calculated by Equation 6.6, $X_{coarse,fly}$ is measured and X_{vap} is estimated based on fuel composition.

It is seen in Figure 6.3 that the vaporized fraction is between 0.11-0.43 (depending on the ash composition) and that the ash loss in the system is calculated to be in the range 0.24-0.61, except for two woods.

In some experiments, the amount of ash collected in the bottom ash cup was weighed. In Figure 6.4 the calculated ash loss is compared to the amount of ash collected in the bottom chamber. Experiments S4-S11 are not represented since no measurements of bottom ash were recorded in these experiments. It is seen in Figure 6.4 that the calculated ash losses are above the amounts measured in the bottom ash cup. This is in line with observations made during experiments; that ash loss occurred also in other positions in the reactor and duct as well as in the bottom ash cup. In two wood experiments, the calculated ash losses are much lower than the ash

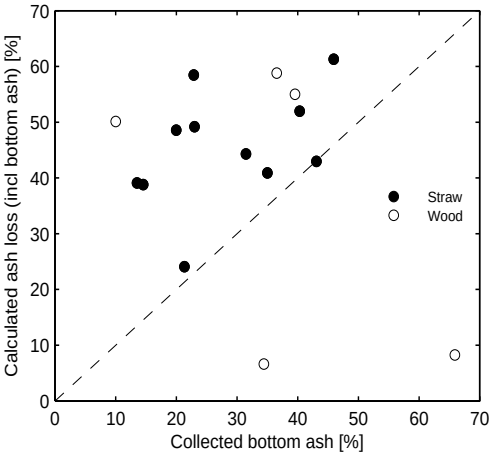

Figure 6.4: Measured bottom ash vs. calculated ash loss (incl. bottom ash). Experiments S4-S11 are not included due to lack of data.

loss measured in the bottom ash cup. In these two experiments the measured ash concentrations exceeded the amount of ash supplied and the ash out/ash in ratio is 1.3-1.4. In the remaining experiments this ratio is 0.45-0.95. Mass balance closure has not been obtained in any of the experiments. The measured ash concentrations should therefore be regarded as estimates. It is the measured ash concentrations seen in Figure 6.3 which are used in the deposit build-up model.

In Table 6.3, the calculated concentrations of the coarse ash, the aerosols and the gaseous species, calculated for the conditions near the probe, are shown along with the calculated median particle size of the ash (calculated before the bend). It is seen, that in most experiments - except for some low-temperature cases - K_2SO_4 is found as aerosols, while KCl and KOH are present in the gas phase. The fly ash concentrations seen in Table 6.3 are determined from the measured ash concentration ($X_{coarse,fly}$) during experiments, which has subsequently been diluted to various extents by the propane burner flue gas (maximum around a factor 0.2, which is the relative amount of flue gas from the propane burner). It is seen that there is a great variation in the fly ash concentrations ranging from 200-2700 mg/Nm^3, which cannot be explained by variations in the propane flue gas dilution. Variations in fuels can explain some variation. However, experiments S1-S2 and experiments S7-S17 were made under similar conditions; similar fuels, fuel flow and air supply. Within these experiment series variations in the concentrations are also observed; 1000-2700 mg/Nm^3 and 200-1300 mg/Nm^3, respectively.

In EFR experiments, mass balance closures are difficult to obtain, even in setups where the flow is not bend, due to deposition of the ash components in various po-

Table 6.3: Calculated concentrations of coarse ash, aerosols and gases [mg/Nm^3]

		Coarse ash		Aerosols		Gases				
	T_{fg} [°C]	dp_{50} [μm]	Conc.	KCl	K_2SO_4	KCl	K_2SO_4	KOH	HCl	SO_2
S1	752	50	2700	0	348	340	0	192	6	43
S2	749	50	1047	0	338	341	0	198	6	46
S3	799	60	843	0	352	178	0	97	6	95
S4	739	83	526	1313	1020	602	0	1116	7	136
S5	814	83	936	0	886	1705	0	1008	6	129
S6	809	83	512	0	886	1705	0	1008	6	129
S7	694	43	555	1724	1064	190	0	1088	7	119
S8	724	43	198	1499	1039	415	0	1104	7	129
S9	700	43	654	1692	951	223	0	1160	7	161
S10	789	43	1201	0	908	1705	0	994	6	121
S11	743	43	1210	1041	997	663	0	937	7	88
S12	785	41	429	0	802	1626	0	988	6	138
S13	920	41	664	0	1004	1623	4	855	7	62
S14	795	41	1072	0	883	1618	0	929	6	107
S15	783	41	1174	0	977	1607	0	860	6	69
S16	904	41	1324	0	890	1578	3	887	6	93
S17	1020	41	695	0	887	1578	41	864	6	80
S18	800	44	1210	0	1124	1186	0	305	13	120
S19	802	44	1191	0	922	1194	0	430	9	194
W1	833	51	813	0	13	48	0	159	1	38
W2	831	51	722	0	22	48	0	154	1	35
W3	807	27	296	0	4	15	0	21	2	34
W4	801	18	202	0	0	76	0	34	6	45
W5	803	20	142	0	29	55	0	23	7	12

sitions within the reactor and inaccurate particle sampling equipment [16]. In the setup used here, the flow is bend which makes mass balance closures even more difficult to obtain. Furthermore, the flue gas was sampled within the bend, which in itself represents an non-uniform flow zone. This was further complicated by ash deposits build-up observed just above the measuring position, where the bottom chamber was mounted to the reactor. The ash deposition at this position has possibly altered the flow patterns in the bottom chamber from experiment to experiment. This implies that even though effort was made in terms of cleaning of the reactor, positioning of the sampling probe to obtain correct measurements, variations could not be avoided in this set-up.

Though the data for the coarse ash concentration shown in Table 6.3 has been identified as uncertain, they are still used in the model validation, rather than introducing assumptions on e.g. a fixed value of $X_{coarse,fly}$. The variations in the coarse ash fraction thus need to be kept in mind during the model evaluation.

6.3 Model Results on Deposit Formation

In the following, the model for deposit formation is used to predict the deposits formed in the EFR experiments, and the model results are compared to the experimental results. Two models, which differ in the prediction of particle sticking were proposed in Chapter 5; Model #1 uses a reference viscosity to describe an overall sticking probability valid for all particle sizes (Equation 5.42). Model #2 combines impaction of (visco)elastic particles on a solid surface (Equations 5.45 and 5.46) with particle capture by a viscous surface (Equations 5.52 and 5.53). A critical velocity is calculated from particle size, velocity and angle of the impact along with physical properties of the particle in terms of Young's Modulus and of the surface in terms of viscosity.

The input to the model is the flue gas and fly ash characteristics described above. The input is also summarized in Table 6.4. With this input, the model describes the deposit formation in terms of KCl, K_2SO_4, insoluble ash and total amount of deposit.

Initially, the total amount of deposit formed on the probe as predicted by the two models is evaluated. The result of the calculations are shown in Table 6.5 and compared to the results obtained in the individual experiments in Figure 6.5.

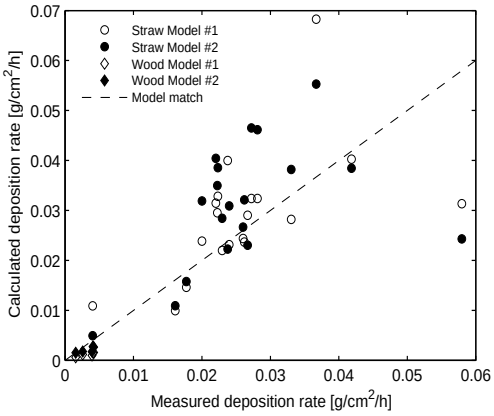

Figure 6.5: Results of calculations with Models #1 and #2 using values of the model parameters shown in Table 6.4.

It is seen in Figure 6.5, that both models are able to describe the magnitude of the deposits formed, as most of the results are distributed along the diagonal line, indicating a model match. There is however some scattering of the results, which is not similar for the two model approaches.

During the experiments, the deposits obtained were analyzed in terms of water soluble content; K, Na, Cl and SO_4 as seen in Table 6.2. These results have been re-

Table 6.4: Model input to the deposit formation model for description of the EFR experiments

	Paramter	Value	Comment
Probe	Length	8 cm	
	Diameter	1 cm	
	Temperature	440-664 °C	Table 6.2
Flue gas	Temperature	694-1020 °C	Table 6.2
	Gas velocity near probe	1.8-2.9 m/s	
	Diffusion coefficients	$f(T_{fg})$	App. B.2
	Phys prop $(\mu_g, \rho_g, C_p, k_g)$	$f(T_{fg})$	App. B.3
Fuel	Ash content straws	4.4-7.75 wt% dry	Table 6.2
	Ash content woods	0.5-2.9 wt% dry	Table 6.2
	Density $\rho_{fuel,straw}$	1300 kg/m^3	App. B.1
	Density $\rho_{fuel,wood}$	1400 kg/m^3	App. B.1
Fly ash	Concentrations		Table 6.3
	dp_{aero}	0.5 μm	
	$dp_{50,ash}$	18-83 μm	Table 6.3
	Particle sizes used n_{part}	10	
	Density $\rho_{ash,straw}$	2700 kg/m^3	App. B.1
	Density $\rho_{ash,wood}$	3100 kg/m^3	App. B.1
Deposit	Initial porosity	0.8	
	Time for sintering	10 s	
	Conductivity, k_s	$f(T)$	Eq. 5.73
	Emissivity, ϵ	$f(dp_{50,ash})$	Eq. 5.74
Model parameters	Ref. viscosity (Model #1)	10^6 Pa·s	Model #1
	Young's modulus (Model #2)	50 MPa	Model #2
	Comput. cells on semicylinder	40	
	Time step	2 s	

calculated to corresponding contents of KCl and K_2SO_4. Then, the model prediction in terms of deposited KCl, K_2SO_4 and insoluble ash content can be compared to experiment and the individual deposit formation mechanisms can be evaluated. In this comparison, the coarse ash in the model is assumed to represent the insoluble ash. In Figure 6.6 the results of the individual mechanism contributions of KCl, K_2SO_4 and insoluble ash to the deposits are shown for each experiment. It is seen that the deposition of KCl is generally overestimated for all experiments, while deposition of K_2SO_4 is quite well described for straws and underestimated for woods. The predicted mass of KCl and K_2SO_4 on the probe are quite similar from the two models.

The prediction of insoluble ash varies greatly for both models; both under- and overestimations are found. Furthermore; the two models do not show a similar behavior in the description of the insoluble ash deposition. In the following, the prediction of each of the ash components, KCl, K_2SO_4 and insoluble ash will be

Table 6.5: Results of calculations. Total mass of deposit and rate of deposit formation. Measured and calculated by Models #1 and #2.

	Experiments		Model #1		Model #2	
	mass	rate	mass	rate	mass	rate
	g	g/cm^2/h	g	g/cm^2/h	g	g/cm^2/h
S1	0.67	0.018	0.552	0.015	0.595	0.016
S2	0.61	0.016	0.375	0.010	0.411	0.011
S3	0.25	0.004	0.685	0.011	0.308	0.005
S4	0.75	0.020	0.898	0.024	1.203	0.032
S5	0.77	0.022	1.130	0.033	1.328	0.039
S6	0.76	0.022	1.002	0.030	1.187	0.035
S7	0.96	0.023	0.922	0.022	1.194	0.029
S8	0.98	0.026	0.919	0.024	1.005	0.027
S9	0.90	0.024	0.872	0.023	1.165	0.031
S10	1.13	0.028	1.301	0.032	1.857	0.046
S11	1.07	0.026	0.969	0.024	1.315	0.032
S12	0.79	0.022	1.123	0.032	1.442	0.040
S13	1.09	0.024	1.828	0.040	1.018	0.022
S14	1.08	0.027	1.285	0.032	1.846	0.047
S15	1.25	0.033	1.064	0.028	1.440	0.038
S16	1.38	0.037	2.574	0.068	2.084	0.055
S17	1.58	0.042	1.518	0.040	1.448	0.038
S18	1.01	0.027	1.095	0.029	0.868	0.023
S19	1.14	0.058	0.614	0.031	0.476	0.024
W1	0.36	0.004	0.136	0.002	0.243	0.003
W2	0.37	0.004	0.137	0.002	0.232	0.003
W3	0.23	0.002	0.092	0.001	0.228	0.002
W4	0.29	0.003	0.131	0.001	0.200	0.002
W5	0.15	0.004	0.037	0.001	0.066	0.002

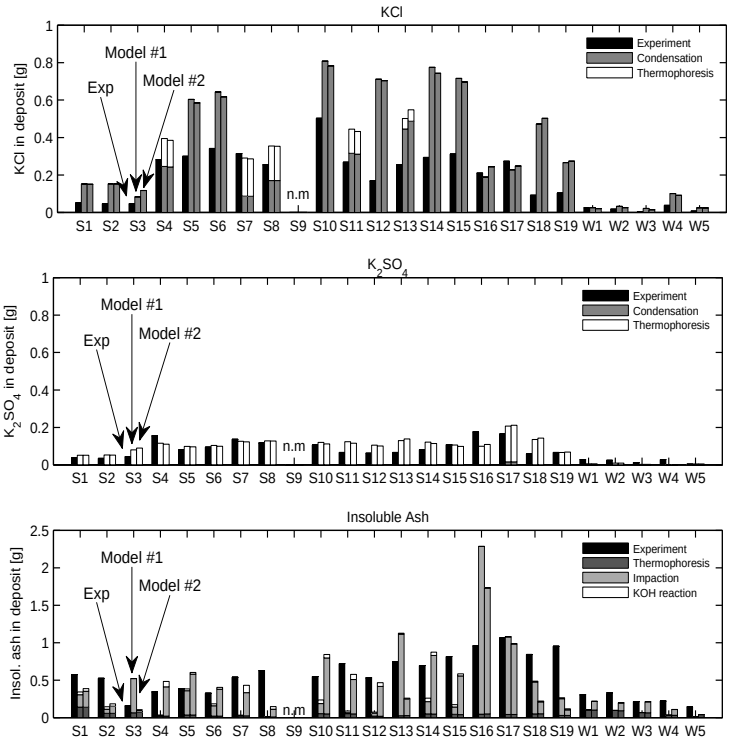

Figure 6.6: Contribution of the individual transport mechanisms to the formation of (a) KCl, (b) K_2SO_4 and (c) Insoluble ash. For each experiment is shown the experimental results (left bar), prediction by Model #1 (middle bar) and prediction by Model #2 (right bar).

further examined and for the latter case, the difference in the model predictions will be explored.

6.3.1 Prediction of KCl

In Figure 6.7A, the predicted amounts of KCl in the deposits are compared to the measured amounts, to see if there is any trend in the overestimations observed in Figure 6.6. It is seen in Figure 6.7A, that the overestimations appear to be quite systematic. This has been explored further; In the model the diffusion coefficients of the gas species are dependent on temperature ($D_{j,N_2} \propto T^{1.8}$). The diffusion coefficients have in the calculations been determined at the flue gas temperature. In Figure 6.8, the effect of using the deposit surface temperature in the calculation of the diffusion coefficient is seen. It is seen that the diffusion coefficient has a significant impact

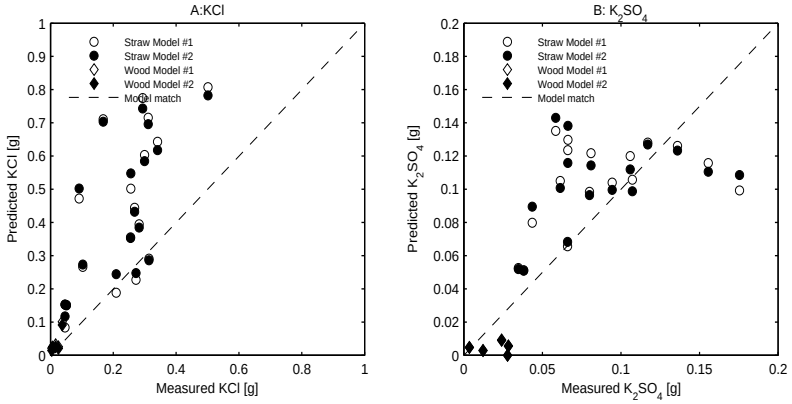

Figure 6.7: Predicted vs. measured (a) KCl and (b) K_2SO_4 in the deposits.

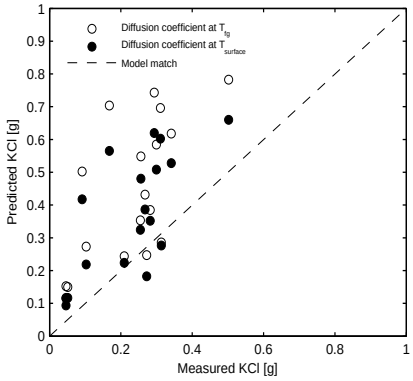

Figure 6.8: Predictions of KCl deposition when calculating the diffusion coefficients at the flue gas temperature and at the deposit surface temperature. Calculations are made with Model #2.

in description of KCl deposition. By using the diffusion coefficient calculated at the deposit surface temperature, the calculations offer predictions closer to the measured values. The KCl contents in the deposits are however still overestimated. Other explanations for the overestimations could be that only the most simple mechanism is considered; direct condensation. It is possible that if aerosol formation in the boundary layer and subsequent thermophoresis is included, the rate would be lowered. Furthermore, the model only considers the monomer KCl and not the dimer K_2Cl_2. The dimer is a larger molecule with lower diffusion coefficient, which would experience a lower rate of condensation. Finally, the concentrations of KCl may also be overestimated; These are described based on a combination of a assumed

K release, a measured SO_2 concentration, a KCl/HCl equilibrium assumption and possible loss of KCl in the reactor is ignored. The parameters with most influence on the KCl deposition in the current model are identified in a sensitivity analysis later.

6.3.2 Prediction of K_2SO_4

In Figure 6.6 it is seen that the amount of K_2SO_4 in the deposits are well predicted for straw. Contrary, the amount of K_2SO_4 is underestimated for woods. In Figure 6.7B, the predicted amounts of K_2SO_4 in the deposits are compared to the measured amounts. It is seen that for most of the straw experiments, the predicted amount of K_2SO_4 is above the measured amount. However, for the straw experiments with large amounts of measured K_2SO_4, the model underestimates the amounts formed. For woods, the underestimation is anticipated to be related to uncertainties in the measured SO_2 concentrations in the experiments. These were high compared to the wood S content, and $>$ 80 % of the S in the flue gas was measured as SO_2. For the straw experiments, only on average 25% of the S was measured as SO_2. Experimental uncertainties can not be disregarded in evaluation of the K_2SO_4 deposition, as the K_2SO_4 concentration in the flue gas is determined from the measured SO_2 concentrations. Furthermore, the parameters and assumptions in the thermophoresis model, such as temperature gradients, aerosol particle size, etc., may naturally also influence the predictions. This is explored in a sensitivity analysis later.

6.3.3 Prediction of Insoluble Ash

In Figure 6.9, amounts of insoluble ash in the deposits predicted by the two models are compared to the measured amounts. It is seen that the models tend to underes-

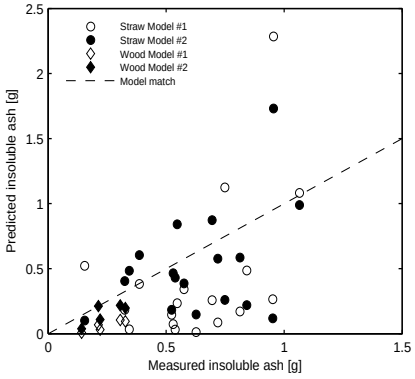

Figure 6.9: Predicted vs. measured amount of insoluble ash in the deposits.

timate the amount of insoluble ash deposited and that the data are quite scattered. Again, it is also observed that the models differ in their predictions, as the results

does not show the same pattern in the scattering.

In the following the insoluble ash deposition as predicted by the two models is evaluated individually.

The examinations in the following are performed for Straw C, which was used in 14 experiments (S4-S17). Only results with Straw C are included, to exclude variations in chemical composition (Experiments S9 and S13 are excluded due to lack of deposit analysis and to variations in temperature during experiment, respectively). Straw C was milled to three particle sizes during experiments; 220, 230 and 440 μm. The experiments with the large particles (440μm) are marked with gray points in the following figures, while the two small particle sizes are regarded as similar. The main variation in these experiments are thus the fly ash concentration (partly due to different dilution with the propane burner) and the flue gas temperature.

In the evaluation, the deposit formation is examined by two measures; by the rate of insoluble ash deposit formation [g/m^2/h] and by the ash deposit propensity [%], where the percentace of ash in the flue gas which deposits is calculated. The ash flux near the probe [g/m^2/h] is calculated from the coarse ash concentrauion and the flue gas velocity.

6.3.4 Evaluation of Model #1

In Model #1, using a reference viscosity to describe the sticking probability, the concentration of coarse ash in the flue gas and the sticking probability (a function of flue gas temperature) are considered the main parameters influencing deposit formation by impaction, which is the primary mechanism for deposition of insoluble ash (see Figure 6.6). The cause of the large variation in the prediction of deposit formation has been explored for the straw experiments, by examining the influences of temperature and ash concentration.

In Figure 6.10, the calculated and measured rates of deposit build-up and ash deposit propensities are seen as function of the flue gas temperature for Straw C. It is seen in Figure 6.10, that the measured deposit rates increase slightly with the flue gas temperature. Contrary, the model predicts a drastic increase in the deposit formation rates just above 800 °C, leading to underestimation of the deposit rates at lower temperatures and to high deposit rates at temperatures above 800 °C.

The model response to temperature can be related to the predicted sticking probability of the ash particles and deposit surface. In Figure 6.11, the sticking probability calculated for straw C, using a reference viscosity 10^6 Pa·s, at the front of the deposit ($\theta = 0°$) are seen. By comparing Figures 6.10 and 6.11 it is seen that the submodel describing the sticking probability of the particles at impact is responsible for the drastic response to temperature predicted by the model. The calculations shown here are obtained with a reference viscosity of 10^6 Pa·s. Changing this value to e.g 10^5 or 10^7 Pa·s moves the drastic response to temperature to higher or lower temperatures and an overall better model fit is not obtained.

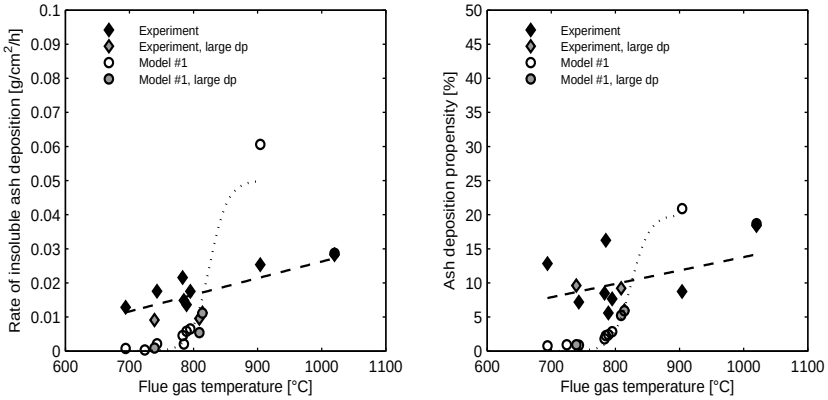

Figure 6.10: Flue gas temperature vs. predicted and measured (a) rates and (b) deposition propensities of coarse ash deposition for Straw C, described by Model #1. KCl and K_2SO_4 are not include in these rates. The lines are indications of response to temperature.

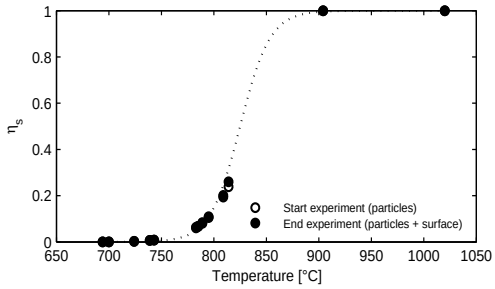

Figure 6.11: Sticking probability calculated for straw C at the front of the deposit ($\theta = 0$).

The coarse fly ash concentration is also considered a major factor influencing the deposit formation by impaction. The coarse ash concentration is in this model determined from ash sampling during experiments, which is considered to be uncertain, as discussed earlier. In Figure 6.12, the rate of deposit formation is seen as function of the coarse fly ash concentration. It is seen that for the experiments, there is no correlation between the ash concentration and the rate of deposit build-up. This is contrary to expectations, and supports the idea that the measurements of coarse ash concentrations are uncertain. In Figure 6.12 (right), it is seen that the model predict that the rate of deposit formation is influenced by the coarse fly ash concentration level, as well as temperature

Variations in the porosity by changes in initial porosity and/or time for sintering

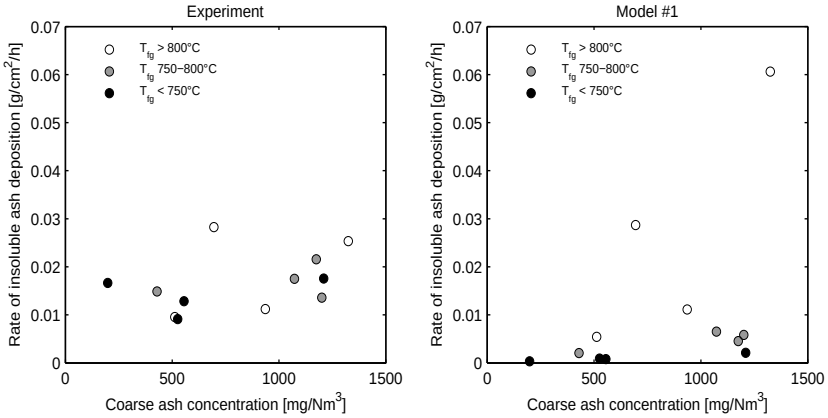

Figure 6.12: Coarse ash concentration vs. (left) measured and (right) predicted rates of coarse ash deposition for Straw C. KCl and K_2SO_4 are not include in these rates. The colors indicate flue gas temperature.

in the model have been examined as these affects the thickness and surface temperature of the deposit. It is found that variations in these parameters do not alter the observed effect of temperature predicted by the model (not shown).

From this evaluation of Model #1, it is seen that the model predicts a strong response to temperature, which is not observed in the rates measured in the experiments. This conclusion can be drawn irrespectively of the uncertainties in the measured fly ash concentrations.

6.3.5 Evaluation of Model #2

The results of Model #2, using a combination of elastic impact of particles and capture by a viscous surface, is examined in this section. As in the evaluation of Model #1, variation in the prediction of deposit formation (observed in Figure 6.9) has been explored for the experiments with Straw C, by initially examining the influences of temperature and ash concentration.

In Figure 6.13, the calculated and measured rates of deposit build-up are seen as function of the flue gas temperature for Straw C. It is seen that Model #2 is able to describe a moderate increase in deposit formation rate and/or deposit propensity with increase of flue gas temperature, as also observed in the experiments. Lines computed from linear regression analysis of the data (both calculations and experiments) have low R^2 coefficients in the range 0.4-0.7 which imply that other parameters also influence the rates measured and predicted.

The coarse fly ash concentration is also considered a major factor influencing the deposit formation by impaction. In Figure 6.14, the rate of deposit formation

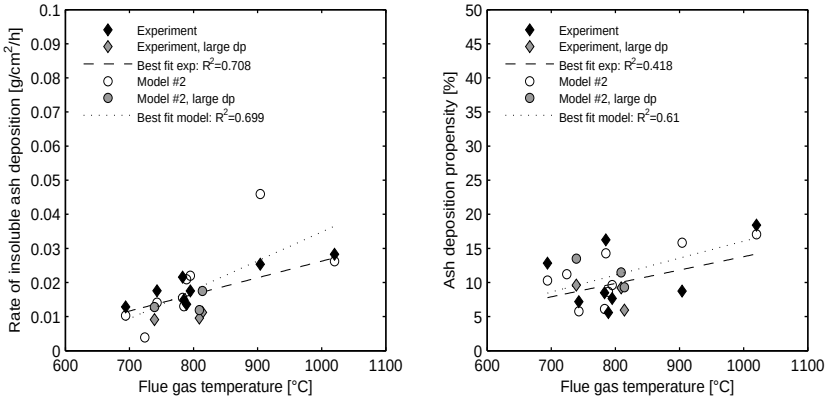

Figure 6.13: Flue gas temperature vs. predicted and measured (a) rates and (b) deposition propensities of coarse ash deposition for Straw C, described by Model #2. KCl and K_2SO_4 are not include in these rates. The lines are indications of response to temperature, computed from linear regression analysis.

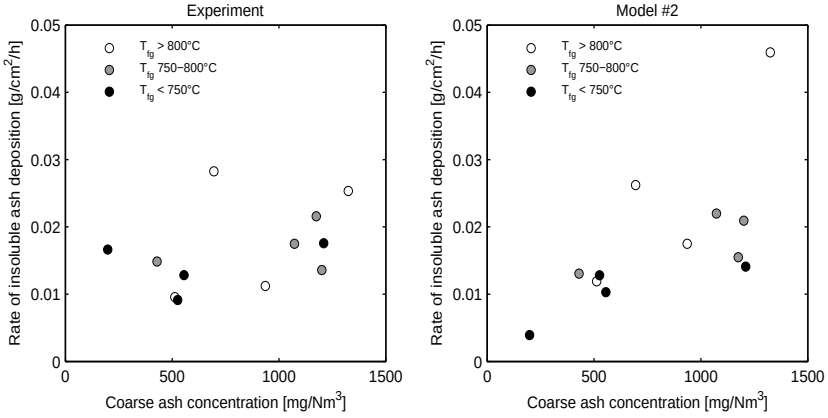

Figure 6.14: Coarse ash concentration vs. (left) measured and (right) predicted rates of coarse ash deposition for Straw C. KCl and K_2SO_4 are not include in these rates. The colors indicate flue gas temperature.

is seen as function of the coarse fly ash concentration. It is seen that the model predictions are quite dependent on the fly ash concentration, which is not observed in the experimental results. With the uncertainties present in a key parameter such as the ash concentration, the model cannot be adequately validated by this dataset. However, Model #2 clearly offers better predictions than Model #1.

6.3.6 Parameter Study with Model #2

In Figure 6.15, the deposit build-up by various mechanisms as function of time is seen for experiment S7 where a low flue gas temperature, 694 °C was employed (left) and for experiment S17 where a high flue gas temperature, 1020 °C was employed (right). The deposit surface temperature (top), fluxes (middle figures) and deposit thickness (bottom) are shown for three angles on the probe; at the front (θ = 0°), at θ = 45° and at the rear (θ = 180°). In the figure, deposition by diffusion of small coarse ash particles is excluded, as this contribution is negligible (« 1 mg/m^2/h). It is seen that the fluxes of both condensation and thermophoresis decrease as the deposit surface temperature increases. The decrease is most significant at the front, whereas at the rear, the deposit build-up is slower leading to a lower surface temperature and thermophoresis and condensation proceed for a longer time. The flux of inertial impaction is initially low, but increases when the viscosity of the surface is lowered by either a higher temperature or by formation of K-silicates by KOH reaction with excess SiO_2. The increase in the flux of inertial impaction is stepwise due to the size segregation of the fly ash into 10 size classes. The flux of KOH to the deposit occurred by diffusion and condensation. In the initial phase, KOH condensation exceeds the flux of Si rich particles and full reaction of excess SiO_2 is described, while some build-up for 'storage' of presumably liquid KOH is described in the deposit. When the flux of Si rich particles exceeds the flux of KOH, this 'stored' KOH is consumed by reaction, as it is assumed that the KOH is able to diffuse or flow from a position within the deposit to the surface of the deposit. At some point, the 'stored' KOH is used and the reaction is limited by the flux of KOH to the surface. When the reaction rate or flux is lowered, the viscosity of the surface increases slightly leading to a lower flux (less capture) of impacting particles.

As in the evaluation of Model #1, the effect of the assumed or predicted porosity has also been examined for Model #2. It is found that variation in the time for sintering (t_{sint}) does not affect the model prediction (not shown). In Figure 6.16, the effect of changing the initial porosity of the deposit is shown. It is seen that by setting the initial porosity to 0.6 instead of 0.8, the predicted amount of deposit on the probe is lower. The effect of the change in porosity is found both in the prediction of the thermal conductivity of the deposit and - more significantly - in the description of the deposit thickness which influences development of the surface temperature.

The effect of the particle's Young Modulus is seen in Figure 6.17. Here, three levels of the Young's Modulus are used; one value in the GPa range (1000 MPa), relevant below the glass transition temperature and two values in the MPa range (1 and 50 Mpa), assumed to be valid above the glass transition temperature. Two values were chosen in the MPa range, to explore the effect of variations in the Young's Modulus expected for viscoelastic materials. It is seen in Figure 6.17 that the effect of varying the Young's Modulus from 1000 MPa to 50 MPa is limited. There is

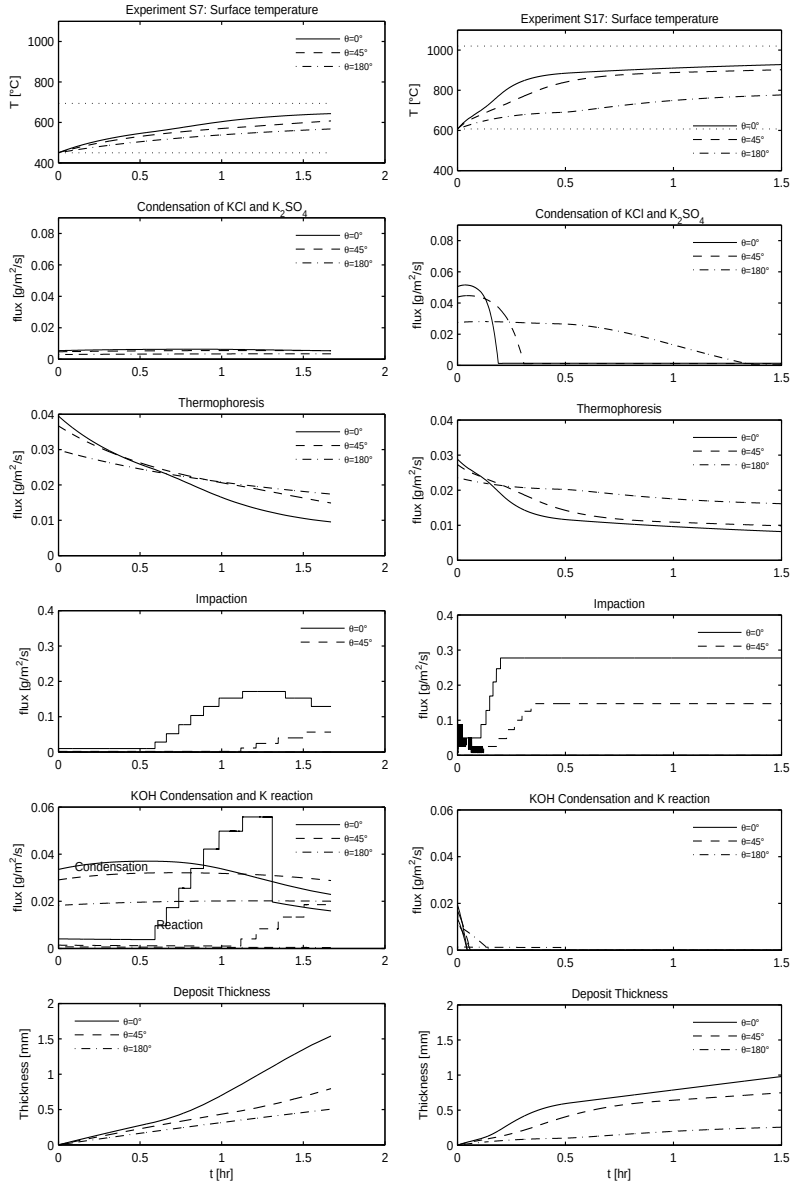

Figure 6.15: Development of surface temperature (top) and deposit thickness (bottom) and fluxes of condensation, thermophoresis, impaction and reaction as function of time during experiment S7 (left) and experiment S17 (right).

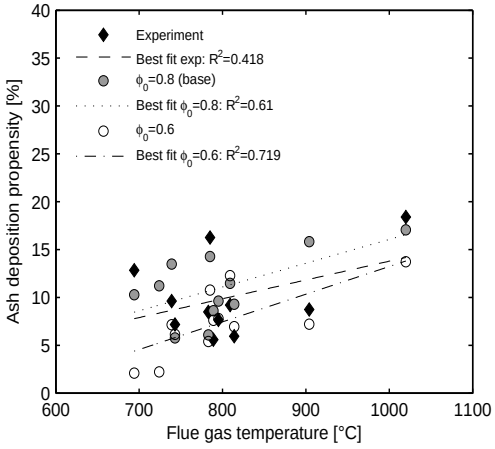

Figure 6.16: Ash deposit propensities calculated for straw C obtained by the experiments and by Model #2 with the initial porosity set to 0.6 or to 0.8. Remaining parameters are as given in Table 6.4.

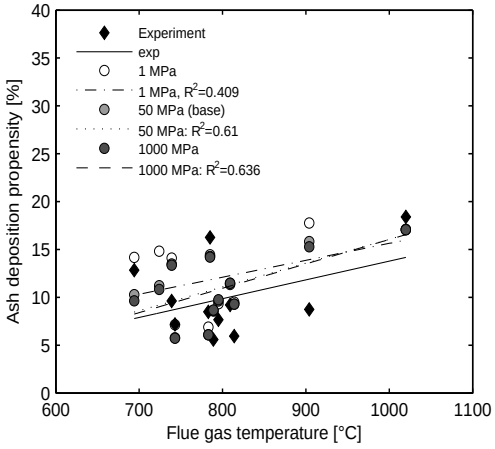

Figure 6.17: Ash deposit propensities calculated for straw C obtained by the experiments and by Model #2 with three values of the Young's modulus is used. Remaining parameters are as given in Table 6.4.

however an effect of further decreasing the Young's Modulus to 1 MPa, i.e. within the range of the viscoelastic behavior of the particles. The effect of Young's Modulus is important in the initial phase of the deposit formation, where the probe is clean. The Young's Modulus then is an important factor in determining the time needed before a sufficient layer of deposit has build-up for increase the surface temperature

to levels where the viscosity is low enough for surface capture to occur.

Another important mechanism is the reaction between SiO_2-rich particles and gaseous KOH at the deposit surface. This reaction has two effects: (*i*) adding mass to the deposit (KOH) and (*ii*) lowering the viscosity by formation of K-silicates. In the model full reaction of all available KOH and/or excess SiO_2 (not already combined with K, Na, Ca or Mg) is assumed. Thus, physical hindrances are ignored, as it is assumed that KOH is able to diffuse within the deposit. In Figure 6.18 the influence of the excluding the effect of K-silicate formation on the surface is examined. The results 'excluding' reaction are obtained by still including the reaction in terms of mass, but the viscosity and surface tension of the deposit surface is calculated from the coarse ash composition and the surface temperature. It is seen that there

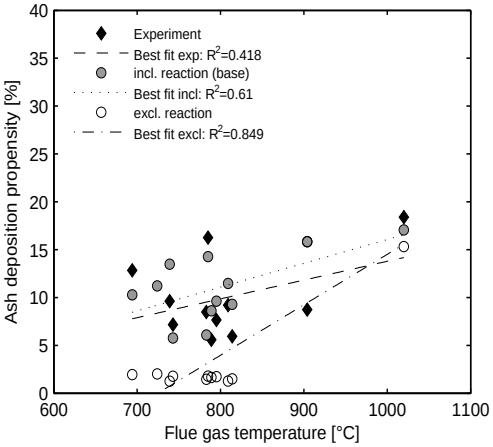

Figure 6.18: Ash deposit propensities calculated for straw C obtained by the experiments and by Model #2 when reaction of KOH with SiO_2 is included or excluded in the determination of deposit surface viscosity. Remaining parameters are as given in Table 6.4.

is a significant effect of including reaction at the surface and adjusting the deposit surface composition accordingly. The effect of reaction is most pronounced in the initial phase of the experiment, where the surface temperature is low and KOH diffuses to the surface. Once impaction by surface capture is initiated the transport of KOH to the surface will in most cases be insignificant compared to the transport of SiO_2.

Based on this evaluation of Model #2 it can be concluded that this model offers a promising approach to description of the deposit build-up of straw ashes. However, better experiments are needed in order to make a complete model validation. Furthermore, ash and deposit physical properties such as viscosity, initial porosity, sintering and Young's Modulus need to be evaluated for relevant ashes and deposits.

In the previous, only Straw C was used in the evaluation of the impaction models. However, it is expected that the other straws used in the experiments, follow the same conclusions.

6.3.7 Evaluation of Wood Ash Deposition

For the wood experiments, it was anticipated (Section 5.7.1), that the viscosities of the wood ashes are high ($\geq 10^{12}$ Pa·s) at the temperatures near or below 800 °C used in the EFR experiments. This was calculated for bark and pine, while it was assumed for beech and waste wood. For the two latter ashes the model could no be applied due to low contents of SiO_2 in the ashes. Thus, at the prevailing probe and deposit surface temperatures, the viscosity will be high and particle capture of a viscous surface is not considered to occur. The only deposit mechanisms included for wood ash particles are then thermophoresis and elastic impact. It was seen in Figure 6.6c, that both model #1 and #2 describe that thermophoresis contributes significantly to the deposition of wood ash. Impaction of larger particles are only included in Model #2. The model underestimates the amount of deposit formed, except for pine wood (W3). In Figure 6.19, the model behavior with variations in the Young's Modulus and initial porosity is seen. It is seen that the value of the Young's modulus influences

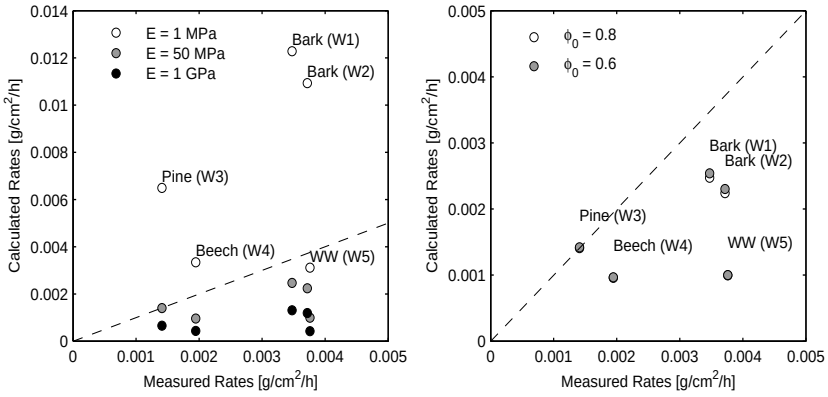

Figure 6.19: Calculated vs. measured rates of insoluble ash formation for the wood experiments. left: ϕ_0=0.8 and varied Young's Modulus. (right): E=50 MPa and varied initial porosity

the rate of deposit formation, whereas the initial porosity has no effect. The fact that the deposit surface properties are not considered in the wood experiments causes the limiting effect of the initial porosity. The effect of the Young's Modulus leads to the suggestion that the elastic properties of wood ashes and of deposit surfaces should be examined. In the model considered here, the surface properties are not considered

with respect to the elastic impact. As deposit is formed the surface becomes soft (as compared to the steel tube); this will influence the critical velocity for rebound of the impacting particle.

6.4 Sensitivity Analysis with Model #2

The sensitivity analysis of the model parameters in Model #2 is performed by employing a Morris Screening in which important parameters are identified. A Morris Screening is a global analysis which implies that the model output is computed for a large range of parameter values within given boundaries, rather than just examining the effect of a single parameter.

6.4.1 Morris Screening

In a Morris Screening, the parameters used in the model have to be given a minimum and a maximum value. These values may be known as variances around a mean value determined from uncertainty analysis, they may be estimated by expert knowledge or they may be given as arbitrarily chosen ranges around an estimated value. In the Morris method the parameter values are then randomly varied within these given boundaries in a Morris sampling. The parameters are varied one at a time and the elementary effects of the parameter change is monitored. In that step the Morris screening is similar to a local method. However, the Morris is repeated a number of times and the mean and standard deviation of the elementary effects are used in the evaluation of the sensitivity. As the Morris screening thereby covers the whole range of the parameter input value, the Morris screening becomes a global sensitivity analysis.

In the Morris screening it is ensured that the whole value range for a single parameter is employed by using a discretized approach. The input is thus assumed to vary in p levels, including the endpoints. To obtain a uniform sampling it is given that the perturbation coefficient used in the sampling should be [210]:

$$\Delta = \frac{p}{2(p-1)}$$

with $p = 4$ the perturbation coefficient thus becomes $\Delta = 2/3$. In a normalized parameter range with endpoints [0;1] and $p = 4$, the points [0, 1/3, 2/3, 1] are thus employed. It is stressed by Morris [210], that p should be an even number e.g. $p = [4, 6, 8]$

The sampling is often repeated 5-15 times to ensure that a uniform sampling is obtained. In the choice of number of repetitions, the number of parameters should be considered. The total number of calculations with the model depends on both the number of repetitions (r) and the number of parameters (k) as these are varied

one at a time in each repetition.

$$Calculations = r \cdot (k + 1)$$

In this case, with k = 19 the number of calculations is 100, 200 or 300 for r = 5, 10 or 15, respectively. In these calculations it is chosen to use p = 4 and r = 15. The sampling is performed in a Matlab function (morris.m) adopted from Sin et al. [211].

Once the calculations with the model are performed the effects of the parameter changes can be calculated. The Elementary Effects on each variable by each parameter (EE_{ij}) are calculated by initially identifying which parameter is varied in the calculation as compared to the previous calculation and then calculating the elementary effect of that parameter.

$$EE_{ij} = \frac{y_j(\theta_i + \Delta) - y_j(\theta_i)}{\Delta}$$

θ = input parameter, y = model output
In order to be able to compare results of elementary effects, the relative effect is calculated by sigma-scaling:

$$SEE_{ij} = EE_{ij} \cdot \frac{\sigma_{\theta,i}}{\sigma_{y,j}}$$

The elementary effects on each variable are calculated for each of the parameters and for each of the repetitions. Then the repetitions is used to calculate the mean and the standard deviation of the elementary effect of each parameter on each variable.

To evaluate the results of the Morris screening, a plot is constructed for each output variable. The plot illustrates the standard deviation vs. the mean of each elementary effect. Furthermore, the standard error of the mean (SEM) is calculated and lines indicating ± 2 SEM and ± 1 SEM are plotted. (See Figure 6.20). Points lying outside the wedge formed by these lines are considered to have significant effect on the variable. The parameters with points outside the ± 2 SEM are the most significant in the prediction by the model.

Morris Screening on Deposit Formation Model

The model described in the previous sections can be divided into two parts; (*i*) an input model, describing the flue gas and fly ash characteristics, which serve as input to the second part of the model; (*ii*) the deposit build-up model. In the first part of the model a lot of input parameters, e.g. flows of fuel, air, propane, sample etc. influence the flue gas velocity and fly ash concentration, which are then submitted to the deposit formation model.

The sensitivity analysis performed in this study mainly deals with the deposit formation model. Thus, rather than examine how all the individual flows (which ultimately determine the flue gas velocity) influence the deposit build-up, the flue gas

velocity is examined as a parameter. There is however an exception to this 'rule'; the fly ash particle size distribution is described as part of the input model, based on the parameters $dp_{50,fuel}$, $X_{K-release}$, N_{frag}, n and n_{part}. These parameters are included in the sensitivity analysis, rather than just changing the PSD of the fly ash. The fly ash concentration is varied by the parameter $X_{coarse,fly}$, while the concentrations of KCl and K_2SO_4 are varied by the parameters $\%SO_2$ (of total S), $X_{K-release}$ and K_c (KCl/HCl equilibrium constant).

The parameters in the model, which are considered in the sensitivity analysis, are seen in Table 6.6. In the table, it is distinguished if the parameter is an input parameter, which can be altered by changing inputs to the reactor/boiler, or a model parameter, for each of the models.

Table 6.6: Parameters considered in Sensitivity analysis and their variation used in the analysis. Result of three repetitions of the Morris sampling for Straw C are also shown. The parameter significance in description of deposit mass is shown; Notation: X: Most significant (SEM > 2), x: significant (SEM > 1), -: not signficant (SEM < 1). Blank: not included in mechanism.

Input to analysis		Results: Significance on final mass			
Parameter	Variation	Total dep.	KCl	K_2SO_4	Insol. ash
Input parameters					
u_{fg}	1-5 m/s	x x X	X X X	x x X	x x x
$X_{coarse,fly}$	5-50 %	x x X			x x X
$dp_{50,fuel}$	200-400 μm	- - -			- - -
T_{fg}	700-1000 °C	x x X	X X X	X X X	- - -
T_{probe}	400-650 °C	- - -	x x x	X X X	- - -
Flue gas/ash model					
% SO_2	10-50 % of tot S	- - -		X X X	
$X_{K-release}$	0.5-0.9	- - X	x x x	- - -	- - -
K_c	± 25%	- - -	- - -		
N_{frag}	1-5	- - -			- - -
n (RR-par)	1-3	- - -			- - -
n_{part}	3-15	- - -			- - -
Deposit model					
ϕ_0	0.6-0.9	- - x	- - x	- - -	- - -
k_s	1-5 W/m/K	- - -	- - -	- - -	- - -
ϵ	0.5-0.9	- - x	- - -	x x X	- - x
D_{j,N_2}	±10%	- - x	x x x		
$dp_{aerosol}$	0.1-0.9μm	- - x		X X X	
E	1-1000 MPa	- - x			- - x
μ	±factor 10	- - -			- - -
γ	± 25%	- - -			- - -

The result of one run made with p = 4 and r = 15 for Straw C is seen in Figure 6.20. These results are obtained from one Morris sampling. As the sampling

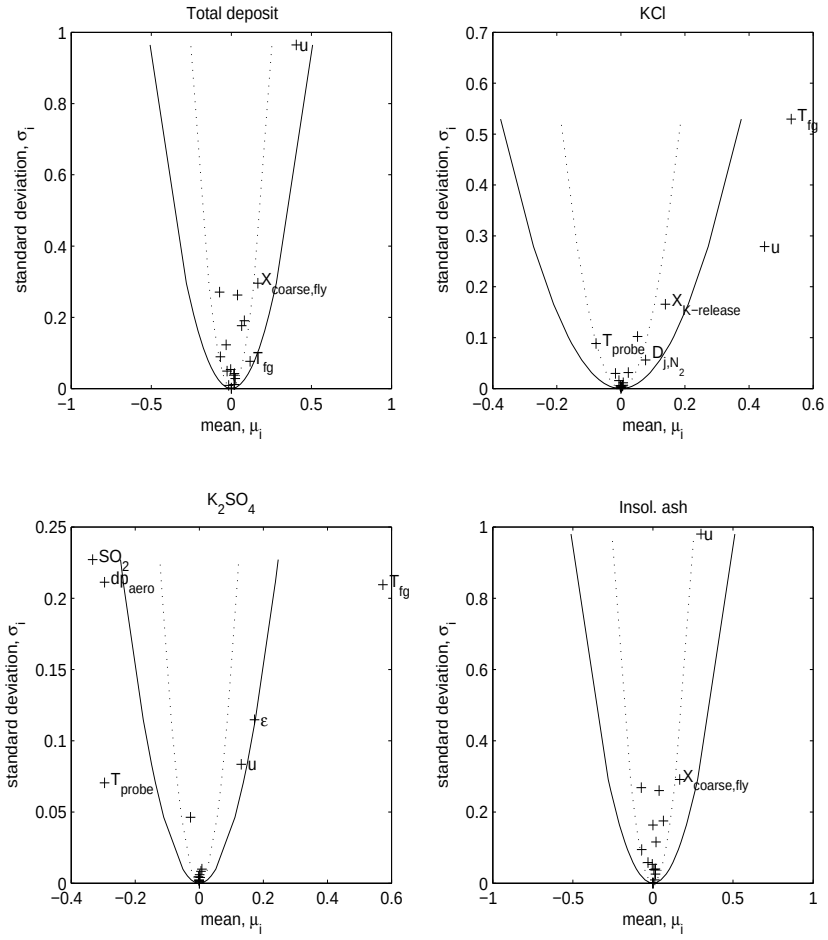

Figure 6.20: Results sensitivity analysis. Lines indicate limits for the standard error of the mean (SEM), Solid lines indicate ±2 SEM, Dashed lines indicate ± 1 SEM

is random within the parameter value range some differences may occur in different samplings - and differences in the results may follow. The sampling has thus been repeated for comparison. It is found that there are some small differences in the results. However, the parameters with large significance are unaltered. In Table 6.6, the results of three Morris samplings are shown.

It is seen that the results for insoluble ash and total deposit on the probe are quite similar, since the insoluble ash constitutes most of the deposit mass. The parameters with most influence on these are the flue gas velocity and the coarse fly ash

concentration. The flue gas temperature is not a significant parameters with respect to the total or insoluble mass of deposit, according to the sensitivity analysis. The moderate increase in deposit formation with temperature as observed in the experiments and described by the model agrees with this. Apparently the particle size distribution predicted by the input model does not have a significant impact, within the ranges explored in the sensitivity analysis. The description of viscosity within a factor 10 and of the surface tension within a factor ± 25 % are not significant, within these ranges of variation.

For KCl and K_2SO_4 nearly all parameters included in the description of condensation or thermophoresis appear to have large impact. I.e. both the flue gas velocity, the temperature and the concentrations of KCl or K_2SO_4 as determined from $X_{K-release}$ or the % of S as SO_2 are important. The model parameters D_{j,N_2} and $dp_{aerosol}$ are also significant. Several parameters are involved in the determination of the deposit surface temperature. The probe temperature and the emissivity appear to have the most significance in this submodel. The initial porosity is only found to have significance in one of the Morris sampling repetitions.

The sensitivity analysis has also been run for the Pine wood (Exp W3). The result is quite similar to that of straw shown here. However for wood, the Young's modulus has a significant impact for the insoluble ash deposition and the total amount of deposit.

6.5 Conclusions From the EFR

A model for description of biomass ash deposit formation process on a tube as function of local conditions in a furnace chamber has been developed. The input parameters include information on gas velocity and temperature, ash composition and ash particle size distribution. The output information from the model provides information on the deposit growth rate and the deposit composition. The model results are compared to ash deposit experiments conducted previously on the CHEC entrained flow reactor. The influence of selected parameters on the model results has been examined and a global sensitivity analysis, examining the influence of 19 input parameters on the output has been conducted. In the sensitivity analysis, four outputs were examined; KCl, K_2SO_4 and insoluble ash in deposit along with total mass of deposit.

The concentrations of coarse fly ash was measured during the EFR experiments. From these measurements, the concentration of coarse fly ash near the probe was estimated. The calculated concentrations vary significantly, within 200-2700 mg/Nm^3 for all experiments and within 200-1300 mg/Nm^3 for experiments made under similar conditions. A corresponding variation in the deposit build-up on the deposit probe was not observed and it is anticipated that the sampling of the fly ash particles is not representative. A better fly ash sampling system is needed for a proper validation of

the model, since the coarse fly ash concentration is an important parameter in the description of the deposit formation. The 90° degree bend along with gas sampling within a non-uniform flow zone leads to large uncertainties in the quantification of the ash concentration. The ash mass balance closures of the EFR deposit system were in the range 0.45-1.4, and this also indicates a large uncertainty of the fly ash sampling system.

Two models were set up, both including deposit build-up by condensation, thermophoresis, diffusion, impaction and reaction. The models differ in the description of sticking probability of impacting particles. Model #1 employs a reference viscosity in the description of sticking probability and all particles with a given viscosity is assumed to have the same sticking probability, regardless of particle size, velocity and impact angle. Model #2 combines impaction of (visco)elastic particles on a solid surface with particle capture by a viscous surface. A critical velocity is calculated for each mechanism and the sticking probability is then related to particle size, velocity and impact angle along with physical properties of the particle in terms of Young's Modulus and of the surface in terms of viscosity.

Both models are able to describe the overall magnitude of the deposits formed in the EFR, though with considerable scattering. When the deposit formation is examined in terms of composition, where the deposit is divided into KCl, K_2SO_4 and insoluble ash, differences occur in especially the description of the deposition of insoluble ash by the two models.

In both models, the condensation of KCl was overestimated. It was found that the temperature used for calculating the diffusion coefficient has a significant impact on the prediction of KCl deposition. It is also considered that some overestimation is a result of using a quite simple model describing direct condensation of vapors after diffusion of these to the deposit surface. A sensitivity analysis revealed that with the current model, the release of K from the fuel is an important parameter along with the temperature and velocity of the flue gas, which appear to be most significant.

Thermophoresis of K_2SO_4 was found to be overestimated at experiments where low rates were observed and underestimated at high rates. Almost all parameters involved in the description of thermophoresis were found to be significant in the sensitivity analysis. One of these parameters is the surface temperature of the deposit.

The surface temperature of the deposit is calculated by a heat transfer model. In the sensitivity analysis the most significant parameters from the temperature model are the emissivity along with the probe- and flue gas temperatures.

In the description of insoluble ash in the deposit, i.e. the modeling of impacting ash particles, Model #1 does not describe the variation in deposit rates observed with varying temperature. A too steep increase in deposit formation rates was observed and linked to a steep increase in sticking probability with temperature. The conclusion that Model#1 is unsuitable for description of ash deposition at these conditions can be drawn regardless of the uncertainties in the fly ash concentration.

Model #2 is able to describe the observed variation in deposit formation with temperature reasonably well. However, the uncertainties in the coarse ash concentration measurements and in the physical parameters of the ash and deposit inhibit a complete model validation. A parameter study made with Model #2 shows how the Young's modulus of the particles, the viscosity of the deposit surface (which is influenced by composition and temperature of the surface), and initial deposit porosity influences the model predictions.

A sensitivity analysis shows that the parameters with most significance for insoluble ash deposition are the flue gas velocity and the concentration of coarse ash. For woods, the Young's modulus is also an significant parameter. This was found in both a parameter study and in the sensitivity analysis.

Chapter 7

Model Validation by Use of Full Scale Tests

A model for ash formation and two models for deposit build-up were set up and described in Chapters 4 and 5. Both models for deposit build-up include diffusion and condensation of vapors, thermophoresis and convective diffusion of aerosols and small particles, impaction of larger particles and reaction in the prediction of deposit formation. The models differ in the description of sticking probability of impacted particles.

Model #1 employs a reference viscosity in the description of sticking probability. This model was not able to describe the influence of temperature observed in the EFR experiments, considered in the previous chapter, and will not be discussed further.

Model #2 combines impaction of (visco)elastic particles on a solid surface with particle capture by a viscous surface. A critical velocity is calculated from particle size, velocity and angle of impact along with physical properties of the particle in terms of Young's Modulus and of the surface in terms of viscosity. This model showed promising results when used for the experiments in the EFR.

The aim of this chapter is to evaluate the ability of Model #2 to describe also deposit formation occurring in full scale suspension-firing of biomass. The model is used to describe six full scale tests, conducted with deposition probes in the Amager and Avedøre power plants by Bashir et al. [5, 63] and Wu et al. [6]. These tests were discussed in the review of full scale experiences in Chapter 3. In the tests, various straw and wood mixtures were combusted and deposit formation was quantified at a range of probe- and flue gas temperatures. The aim is thus to provide a further validation of the model in full scale firing.

7.1 Tests

The tests were conducted by introducing an advanced deposit probe into a full scale suspension-fired boiler. The advanced probe offers in situ measurements of probe and flue gas temperature, deposit mass on the probe and heat flux to the probe. These data can be coupled with boiler operation data (flows of fuel, air, etc.) in the examination of deposit buildup behavior. Details of the tests are described by Bashir et al. [63] and Wu et al. [6]. The tests were also included in the review of full scale experiences, described in Chapter 3 [134]. An overview of the tests are seen in Table 7.1.

Table 7.1: Overview of full scale tests

Exp. no.	1	2	3	4	5	6
Power plant	Amager	Amager	Amager	Amager	Amager	Avedøre
Duration [h]	55	45	184	73	168	30
T_{fg} mean [°C]	869	803	797	917	873	779
T_{fg} range [°C]	762-944	715-855	730-910	820-978	766-1001	737-821
Probe T [°C]	476-632	586-637	473-496	435-492	448-653	508-536
Ash [wt% a.r.]	5.09-5.26	2.0-5.0	1-4.28	3.34	1.63-4.3	1
Straw share[a] [wt%]	81-85	20-80	0-65	48	12-65	0

[a]: Estimate for exp 1-5 as described below

In the campaign conducted at the Avedøre power plant, the probe was also used in the furnace at flue gas temperatures near 1300 °C. These tests were included in the discussion in Chapter 3. However, due to problems with the probe leading to disturbances of the weight uptake signal, the high-temperature tests cannot be included in this model evaluation.

7.2 Fuels

In test 6, the only fuel used was wood pellets, whereas a mixture of wood and straw pellets was used in tests 1-5. However, due to problems at the storage facility at the plant, the exact mixture of straw- and wood pellets could not be monitored during the test campaign. Instead, the biomass was sampled from the mills regularly during each test and the ash content of the biomass determined. The ash content of the sample has then been used to estimate the straw/wood composition of the biomass (described by f_{straw}), by linear interpolation between the ash contents of the pure fuel (6.03 % for straw and 1.0 % for wood) as determined from samples from the fuel silos.

$$f_{straw} = \frac{X_{ash,sample} - X_{ash,wood}}{X_{ash,straw} - X_{ash,wood}} = \frac{X_{ash,sample} - 1}{6.03 - 1} \tag{7.1}$$

E.g. in test 1, the ash content is measured to 5.09-5.26 % estimating a straw share of 81-85 %.

In the model, both fuel and ash composition are needed as part of the input. The fuel composition described by C, H, O, N, S, Cl and moisture is estimated by a weighted average of the fuels, e.g.;

$$C_{mix} = f_{straw} \cdot C_{straw} + (1 - f_{straw}) \cdot C_{wood} \tag{7.2}$$

The ash composition is also determined from a weighted average, taking the different ash contents of the fuels into account, e.g:

$$SiO_{2,mix} = \frac{f_{straw} \cdot X_{ash,straw} \cdot SiO_{2,straw} + (1 - f_{straw}) \cdot X_{ash,wood} \cdot SiO_{2,wood}}{X_{ash,sample}} \tag{7.3}$$

The compositions of the pure fuels are seen in Table 7.2. Here, the wood is the wood used at Avedøre power station in experiment 6 [6]. For experiment 1-5, the wood fuels vary among four types. The composition of these fuels are not provided by Bashir [5] and the composition of the wood used in experiment 6 is therefore assumed to be representative of the unknown wood fuels.
In Figure 7.1, the calculated variations in ash compositions are seen (lines). In the Figure, also results of samples taken during the test campaign are seen (points). The

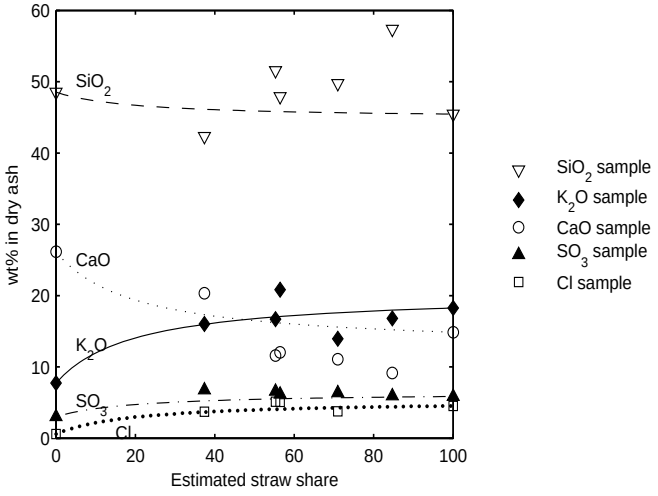

Figure 7.1: Modeled (lines) and measured (points) contents of Si, Ca, K, Cl and S in the fuel ash used in the full scale tests.

results of the fuel samples are not used in the model. They are introduced here to illustrate the extent of fuel variations observed at only a few points during the test

Table 7.2: Composition of pure fuels used in the model for the full scale tests. Ash composition is normalized to 100 %

	Straw	Wood
Moist	7.86	5.8
Ash (as rec.)	6.03	1.00
Ash (dry)	6.54	1.06
Fuel comp (wt% dry fuel)		
C	50.52	46.84
H	5.79	5.91
O	36.11	40.53
N	0.59	0.094
S	0.15	0.009
Cl	0.29	0.004
Ash comp (wt% dry ash)		
SiO_2	45.46	48.54
Al_2O_3	0.67	3.53
Fe_2O_3	0.51	2.48
CaO	14.87	26.16
MgO	3.46	5.31
Na_2O	0.70	0.90
K_2O	18.26	7.72
$^{a}SO_3$	5.85	3.00
P_2O_5	5.68	1.77
^{a}Cl	4.53	0.57

^{a}: SO_3 and Cl determined from the fuel composition

campaign. This implies, that the fuel composition used in the model can at best be regarded as rough estimates.

During small period of the tests, oil has been fired for support. There was no data available for the oil used in the test. Thus, it has been assumed that the oil can be represented by a crude oil with heating value 45 MJ/kg and roughly assuming an oil with a 16-chain C_nH_{2n+2} (84 wt% C and 15 wt% H) composition along with 1% sulfur. In test 6, natural gas was used as support fuel. The composition of this is given by Wu et al. [6] and has been recalculated to be composed of 76 wt% C and 24 wt% H.

7.3 Model Input; Flue Gas and Fly Ash

The input to the model has been taken from the test log files extracted from the the power plant control and monitoring system and from the probe data aquisition. The

data used are: Biomass load [kg/s], oil load [MJ/s] or natural gas load [kg/s], air load [kg/s], fuel ash content [% a.r.], probe temperature [°C] and flue gas temperature [°C]. The inputs changes during the tests which each run for 30-184 hours. To take these variations into account, the average flows and temperatures are calculated for each hour of the test from the log files.

For each hour of the model calculations, the flue gas amount and velocity along with the concentration of ash species are calculated. The amount of flue gas is calculated by assuming full combustion. The flue gas is assumed to be distributed evenly across the boiler cross section in the calculation of velocity. The release of volatiles and distribution of elements among gases and aerosols are described by the model presented in Chapter 4. In the full scale measurements, no measurement of the SO_2 concentration was available, so the concentrations of KCl, HCl, K_2SO_4, SO_2 (and possibly KOH), are described by the equilibrium approach presented by Equations 4.9-4.12.

The concentration of the coarse ash fraction rely on assumptions as no data on the partitioning of the ash is available from the full scale tests. Thus, the ash loss to the bottom has to be assumed. It is assumed to be 20 % of the ash fired to the boiler and X_{bottom} in the ash mass balance is set to 0.2. This value of the ash split was measured in a suspension-fired boiler by DONG Energy during at 10-day testal campaign with wood-firing [intern documentation]. This value is assumed to apply also to straw-firing in a different boiler. $X_{Coarse,fly}$ used for calculation of the coarse ash concentration is thus determined by rearranging the ash mass balance;

$$1 = X_{vap} + X_{Coarse,fly} + X_{Bottom} \tag{7.4}$$

$$X_{Coarse,fly} = 1 - X_{vap} - X_{Bottom} = 1 - X_{vap} - 0.2 \tag{7.5}$$

The model for ash particle size distribution described in Chapter 4 has been used for prediction of the particle size distribution of the ash in the full scale tests. The fuel has been sampled for particle size distribution analysis during test 1. From this sample, the fuel dp_{50} was determined to be 500 μm. This is assumed to apply to all the full scale tests. From this fuel dp_{50}, the particle size distribution of the ash for the initial part of experiment 1 (with 81 % straw in the fuel) has been determined by use of the PSD model. In this calculation, X_{vap} = 0.22 and N_frag = 3, which leads to a dp_{50} of the ash equal to 91 μm. In Figure 7.2 the particle size distributions of the fuel (A) and ash (B) are seen. In both figures, the PSD's are described by a Rosin-Rammler distribution, with exponent n = 1.3. In Figure 7.2B, the model prediction is compared to ash samples collected from the electrostatic precipitator (ESP) during Test 1, analyzed by laser diffraction (Malvern Mastersizer). In the figure, a small peak in the sampled PSD found at $d_p < 1\mu$m is ignored.

In the deposit build-up model, the PSD is described by 20 size fractions each containing 5 % of the coarse ash. A higher number of particle sizes are included in the full scale modeling than in the EFR, since the PSD covers a broader range of

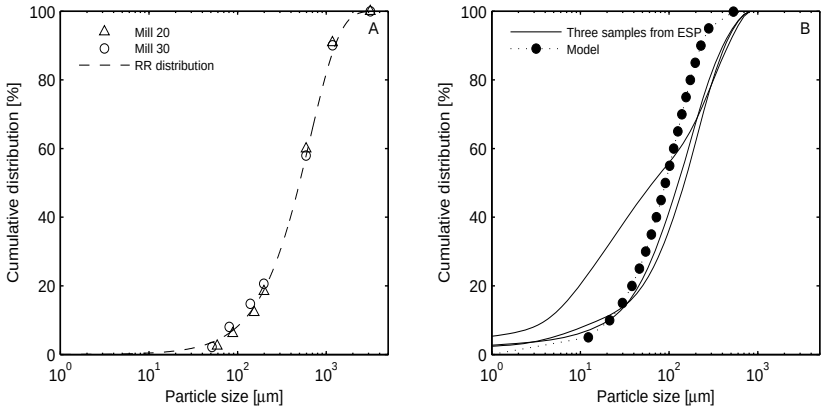

Figure 7.2: A: PSD of fuel sampled from 2 mills during test 1 and fitted by a RR-distribution. B: PSD of the ash in test 1. Model prediction and ash samples from ESP. Data from [5]

particle sizes (up to 600 μm), due to a higher median particle size of the ash (96 μm).

7.3.1 Shedding

In the full scale tests (no. 1-5), shedding was observed to occur, leading to a reduction of the mass on the probe. The shedding was observed to occur mainly as debonding, where a piece of deposit detach from the probe and the break occur near the probe surface [5, 140]. The shedding by debonding did not occur at the whole deposit probe length in each event. The shedding events have been tracked by Bashir et al. [140], and the time of the shedding event along with the mass loss has been noted. The results are seen in Figure 7.3.

In the determination of deposit rates, shedding have been accounted for by tracking of the deposit weight signal and excluding shedding events from the determination of build-up rates. The rates determined by this method was termed DDF-rates in previous work [5, 63, 134], including Chapter 3. The measured DDF-rates are used for the model validation. However, by visual inspection during the tests, shedding by erosion was observed to also occur to a minor degree [5]. This phenomenon has not been quantified, but has most likely influenced the DDF-rates measured to some extent. This needs to be considered during the model validation.

The model developed in this thesis does not include shedding, but reduction of the mass on the probe needs to be considered when the model is used to describe the full scale observations. Otherwise, the deposit mass on the probe will quickly reach unrealistic high levels. This will lead to a large surface area and a high deposit sur-

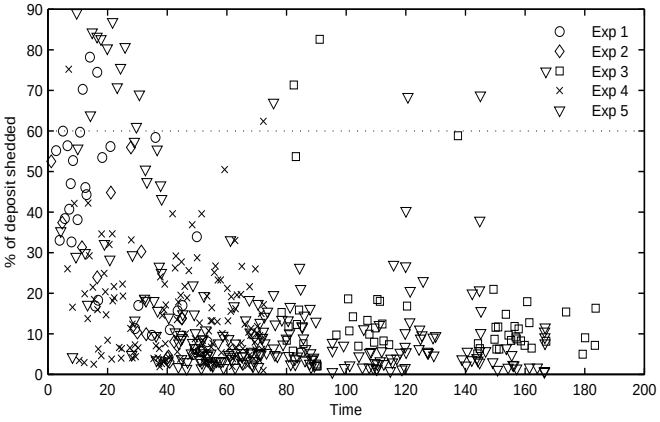

Figure 7.3: Time for shedding and % of deposit mass lost during tests 1-5. Both natural shedding and soot blower indiced shedding events are included.

face temperature and thereby unrealistic high impaction induced deposit formation rates. In the calculations with the model, the mass on the probe has been adjusted in two ways, which are explained below.

1: Mass adjusted each hour For each hour, when the input parameters (flows, temperatures etc.) are adjusted to new measured values, the mass on the probe is adjusted to the measured mass.

2: Using shedding events the adjustment is made at the time of a recorded shedding event by adjusting the mass by a recorded percentage.

In the first approach, only the rate of the deposit buildup can be compared to the values obtained in the tests, as the mass is continuously adjusted to the 'real' value. However, this approach has the advantage, that possible discrepancies in the description at one time-step are not erroneous transfered onto the next time-step, leading to further discrepancies made on a false basis. Thus, by adjusting the mass each hour, the rates of deposit formation predicted by the model, can be directly compared to those measured in the test, at the prevailing deposit mass.

In the calculations using the shedding events to adjust the mass on the probe, the adjustment is made at the time of a recorded shedding event by adjusting the mass by a recorded percentage. However, when the percentage mass-loss exceeds 60 %, complete (100 %) shedding is assumed, to take into account that the majority of the probe is empty. The advantage of this approach is that the model prediction of mass on the probe can be compared to the measured mass. The disadvantage of this approach is that rates predicted in one time-step is influenced by the rate(s) predicted in previous time-step(s).

7.4 Full Scale Model Results

The calculations are made with Model #2 for ash particle adherence, combining an elastic impact of particles on a solid surface and capture of particles by a viscous surface. The Young's modulus is set to 50 MPa as in the EFR tests. The model inputs are summarized in Table 7.3 The output from the model is the deposit mass

Table 7.3: Model input to the deposit formation model for description of the full scale tests

	Paramter	Value	Comment
Probe	Length	1.5 m	
	Diameter	4.05 cm	
	Temperature	435-637°C	Table 7.1
Flue gas	Temperature	715-1001°C	Table 7.1
	Diffusion coefficients	$f(T_{fg})$	App. B.2
	Phys prop $(\mu_g, \rho_g, C_p, k_g)$	$f(T_{fg})$	App. B.3
Fuel	Ash content	1.00-5.26 wt% dry	Table 7.1
Fly ash	Aerosol size, dp_{aero}	0.5 μm	
	Particle sizes used n_{part}	20	
Deposit	Initial porosity	0.6	
	Time for sintering	100 s	
	Conductivity, k_s	$f(T)$	Eq. 5.73
	Emissivity, ϵ	$f(dp_{50,ash})$	Eq. 5.74
Model parameters	Young's modulus (Model #2)	50 MPa	
	Comput. cells on semicylinder	40	
	Time step	2 s	

on the probe. From this mass output and the elapsed time, the deposit build-up rate can be calculated for each hour of the experiment. This rate is compared to the rate measured in the full scale tests during the following evaluation. The results of the full scale tests is in the evaluation given as hourly average values. Previously [5, 63, 134], these rates were examined as 6 hour average values. Thus, some small differences may appear in the results, as compared to previous work.

In the preliminary calculations, it was found that an initial porosity of 0.8 and/or a sintering time set to 10 s lead to unrealistic high rates of deposit build-up, primarily via the description of the deposit thickness (regardless of the calculation approach). Therefore, the initial porosity is set to 0.6 and the time for sintering has been adjusted to 100 s instead of 10 s, which was used in the EFR. A high porosity leads to a thick deposit, leading to a large surface area of the deposit. This implies that high rates became self reinforcing leading to unrealistic deposits 10-15 times thicker than observed. By setting the initial porosity to 0.6 (as was observed by Richards et al. [183] for initial and possibly lightly sintered deposits) and increasing the time for sintering, the deposit thickness described by the model is within realistic measures.

Naturally, the porosity of real biomass ash deposits needs to be examined and then, a verified value can be applied to the model.

In Figure 7.4 the results of the model calculations are shown in terms of (1) temperatures and straw share (2) coarse ash concentration and flue gas velocity (3) predicted and measured deposit formation rates and (4) predicted and measured deposit mass on the probe for test 1. In these figures, the temperatures are measurements, while the rest of the data are model predictions. Similar figures for tests 2-6 are found in Appendix E.

The reduction of deposit mass on the probe occurring during the test was included by two different calculation methods; mass adjustment eah hour and using the recorded shedding events. The model description of deposit formation rates by these two methods are seen in the 3. figure from top in Figure 7.4. When comparing the two model predictions, it is seen that these calculations differ considerably. In the calculations using the recorded shedding events, it is clear how discrepancies in the predictions made in one time-step is transfered onto the next time-step. This leads to overestimations of rates and deposit masses in tests 1 at times above 25 hours. Also, underestimations of the rates in the initial part of the tests may lead to underestimations for a long time, which is observed for the first 20 hours of test 1 in Figure 7.4. Despite these discrepancies, the model is able to capture the variations in deposit mass observed on the probe in most of the tests (see also Appendix E.

In the calculations where the deposit mass is adjusted to the measured mass, and discrepancies thereby are tied, the rates are - with some exceptions - on similar levels as those observed in the tests. In the following evaluation, only the rates obtained by these calculations are evaluated. Since the tests were conducted in full scale power plant during normal operation, the input parameters varied significantly and the tests cannot be clearly distinguished. Thus, significant variation in e.g. fuel ash content (and thereby straw share) and flue gas temperature occur in each test, as also observed in Table 7.1. Thus, the influence of parameters are difficult to evaluate from Figures 7.4 and the corresponding figures from tests 2-6, seen in Appendix E. In the following, the model performance is evaluated by considering each hour of operation during the tests. Thus, the model evaluation is made from 550 data points.

7.4.1 Model Evaluation

As the predictions are tied to the deposit mass on the probe, the influence of the deposit mass on the rate is initially examined. In Figure 7.5, the deposit build-up rate (A) and the ash deposit propensity (B) are seen as function of the deposit mass load on the probe at the beginning of the hour considered. The ash deposit propensity is defined as the percentage of ash in the flue gas which deposits on the

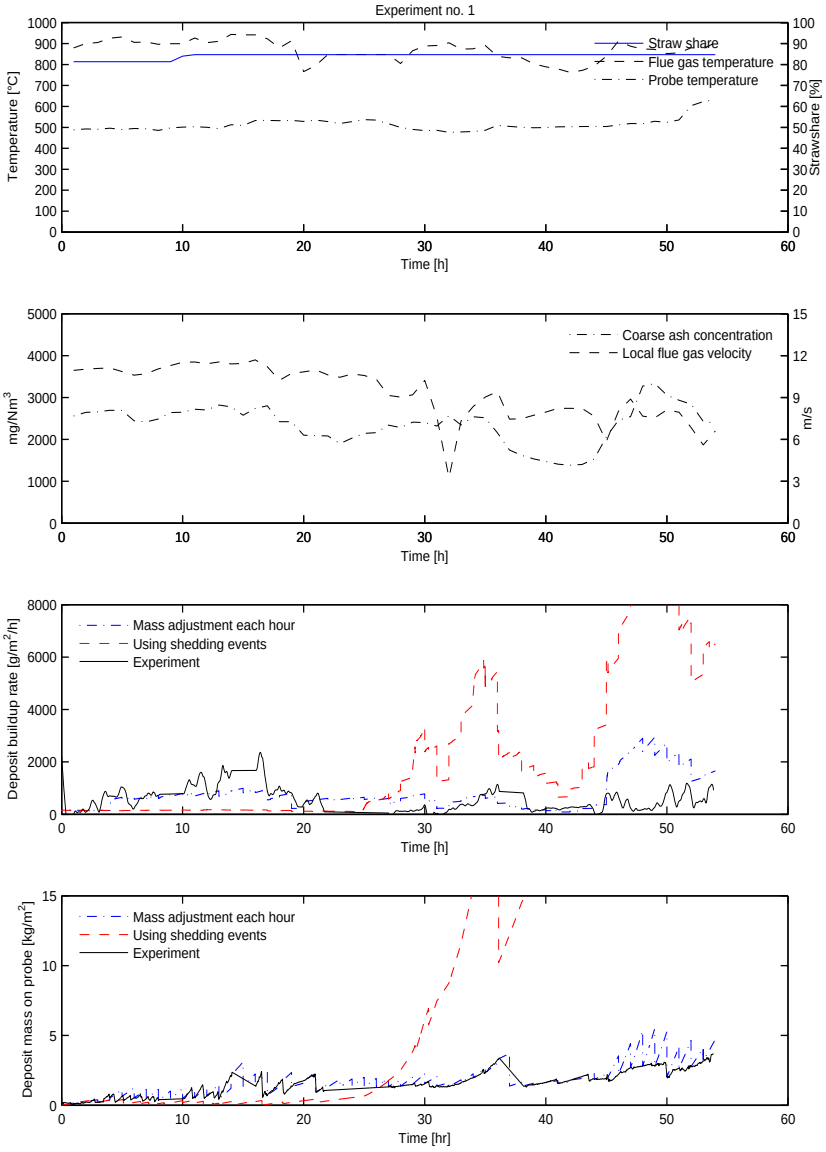

Figure 7.4: Results of full scale test 1. From the top, the figures show: (1) temperatures and estimated straw share (2) predicted coarse ash concentration and flue gas velocity (3) predicted and measured deposit formation rates and (4) predicted and measured deposit mass on the probe.

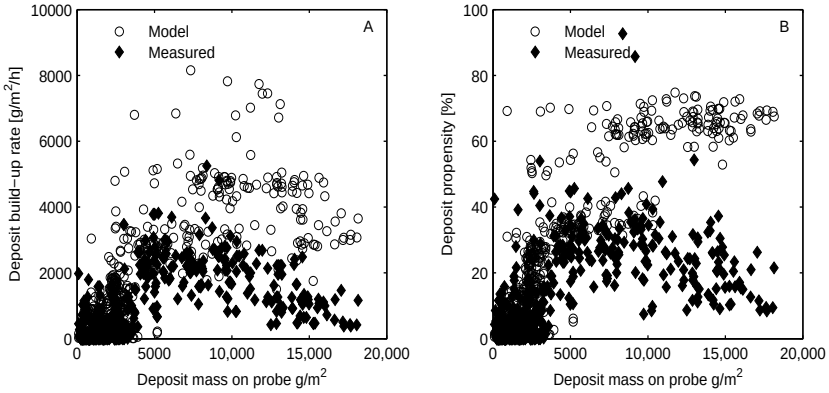

Figure 7.5: Rate of deposit formation (A) and ash deposit propensity (B) as function of the mass load on the probe.

probe and is calculated as follows:

$$\text{Ash deposit propensity}\,[\%] = \frac{\pi \cdot \text{Deposit build} - \text{up rate}\,[\text{g/m}^2\text{/h}]}{\text{Ash flux}\,[\text{g/m}^2\text{/h}]} \cdot 100\% \quad (7.6)$$

The deposit build-up rate is in Equation 7.6 converted from the rate based on the circumference of the probe to a rate based on the projected area (diameter of the probe) by multiplying with π. The ash flux is thus calculated by Equation 7.7.

$$\text{Ash flux}\,[\text{g/m}^2\text{/h}] = \frac{\text{Fuel flow}\,[\text{g/h}] \cdot \text{Ash Content} \cdot \text{Entrainment}}{\text{Cross section area at probe position}\,[\text{m}^2]} \quad (7.7)$$

It is seen in Figure 7.5 that there are significant and apparently systematically overestimations by the model when the deposit mass load is high. In the following examinations, the data have been divided into four categories with each 130-150 data points according to the mass load on the probe.

Group 1: $<$1000 g/m^2 (near empty probe)

Group 2: 1000-2500 g/m^2 (low mass load)

Group 3: 2500-7500 g/m^2 (intermediate mass load)

Group 4: $>$ 7500 g/m^2 (high mass load)

In Figure 7.6, the predicted rate of deposit formation is seen as function of the measured rate at the given time for each of the groups. The lines in the figures indicate a model match. In Figure 7.6A, it is seen that apart from a few points (which are most likely outliers), the model describes a slow rate of deposit formation on a near-empty probe as also observed in the tests. In Figure 7.6B, where the mass load on the probe

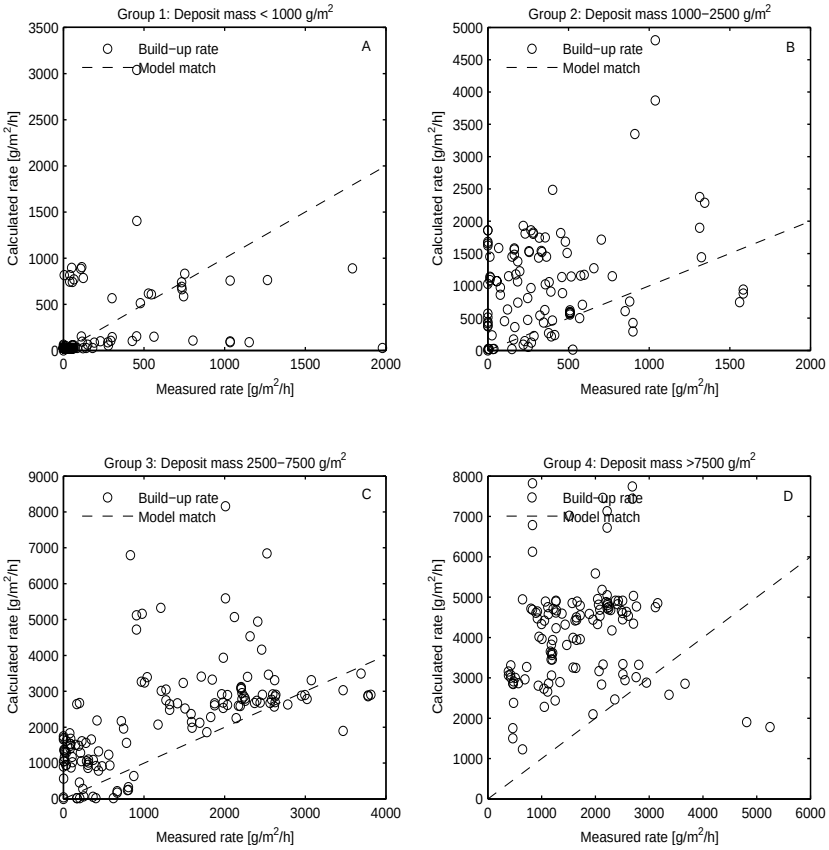

Figure 7.6: Calculated vs. measured rate of deposit formation

is low (Group 2; 1000-2500 g/m^2), the measured rates are generally < 500 g/m^2/h. These rates are overestimated by the model, where rates up to 2000 g/m^2/h are predicted. This is also observed for the intermediate mass load (Group 3) in Figure 7.6C. However rates measured to be above 1000 g/m^2/h in this group are for the most part predicted well by the model as points are found near the diagonal line, indicating a model match. For group 4, where a high mass load on the probe was found (>7500 g/m^2) the model generally overestimates the measured rates, as seen in Figure 7.6D. The overestimation is on average a factor 3.

It is thus seen that the model is able to capture the magnitude of the deposit formation rates measured in the full scale tests. Some overestimations are however found. In the following, the influence of operation parameters on the deposit formation rates measured and modeled will be examined. The aim is to test the capability of the model to predict the influence of changes in operation conditions. The rates of

deposit buildup and the ash deposit propensities are thus examined for the influences of temperature, coarse ash concentration, straw share and flue gas velocity in the following.

Initially the influence of flue gas temperature is examined. In Figure 7.7 the measured rates are shown as function of flue gas temperatures in the left column and the modeled rates are found in the right column. It is seen that for Group 1, where

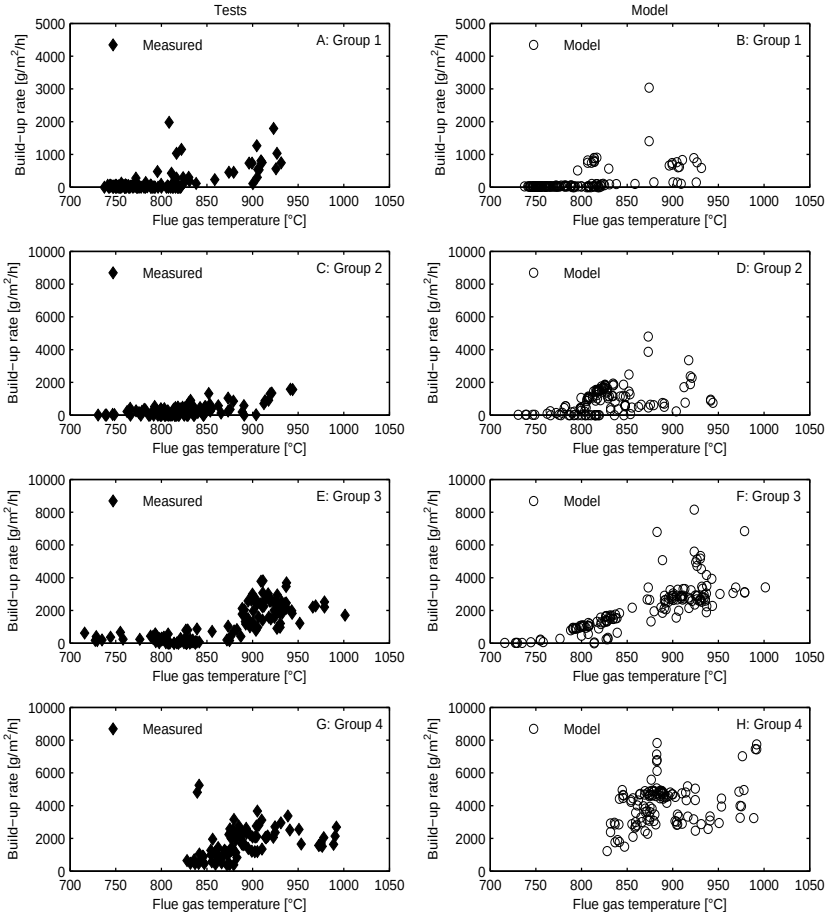

Figure 7.7: Left: Measured deposit formation rates as function of temperature. Right: Modeled deposit formation rates as function of temperature. Note differences in y-axes for group 1 in both columns.

the probe is near empty, the model prediction of the low deposit formation rates correspond well with the measured rates. Note the different scaling of the y-axis of this group. For the low and intermediate mass load data in Groups 2 and 3 it is seen

that the measured data show a low rate up to temperatures around 850 °C, where the deposit formation rates initiate an increase with temperature. This is most clearly seen for group 3. For these groups, the model predicts an increase in deposit formation rates occurring between 750 and 800 °C, leading to the overestimations of the low rates observed in Figure 7.6B, which are found to occur in the temperature range 750-850 °C. When the temperature is above 900 °C, the model prediction of deposit formation in Group 3 (intermediate mass loads) correspond well with measurements. For the high load data in Group 4, the flue gas temperatures were above 825 °C at all times. The overestimation of the model prediction seem here to occur to the same degree for all the measurements in this group.

In Figure 7.8, the results are shown as function of the calculated coarse ash concentration. It should be noted that the coarse ash concentration is the ash concentration without the vaporized ash (i.e $X_{ash,coarse}$ recalculated to concentration). The concentrations have been converted to mg/Nm^3, to exclude the influence of temperature on the concentration. It is seen in Figure 7.8 that also the coarse ash concentration influence the rate of deposit formation. An increase in the rate of deposit formation is observed with increasing concentration, both in the measured rates and the predicted rates. The increase is however much more significant in the model predictions than in the measurements. The difference in the measurements and the predictions increase with mass load on the probe and is thus highest for the data in Group 4.

There are several possible explanations for the difference in the measurements and the prediction, which possibly all contribute to some degree. First of all it should be mentioned that there are uncertainties in the coarse ash concentration used in the model. The concentration is determined based on an assumed ash split observed in a different boiler, with a different fuel. Furthermore, the flow is assumed to be uniform across the boiler cross section, which is rarely the case. If the concentrations are systematically overestimated, it could lead to the observed overestimations of the predictions. To avoid or minimize this uncertainty, CFD simulations could be used to describe the flow near the probe, prior to the use of the deposit build-up model.

It was mentioned earlier that erosion of deposit was observed during the test campaign. This may have lead to measurement of rates lower than the actual deposit build-up rate. If erosion occurred systematically, the effect naturally had the most impact at high mass loads on the probe. This is thus another explanation for the overestimation of the predictions and furthermore for the overestimations to be most significant at the high mass loads.

Finally, errors in the model may lead to the observed overestimations of the effect of the coarse ash concentration. In the model, the capture of impacting particles is affected by the viscosity and the surface tension of the deposit surface. After some initial deposit has formed, this is the governing mechanism. The viscosity and the surface tension of the surface, which describes the capture are predicted

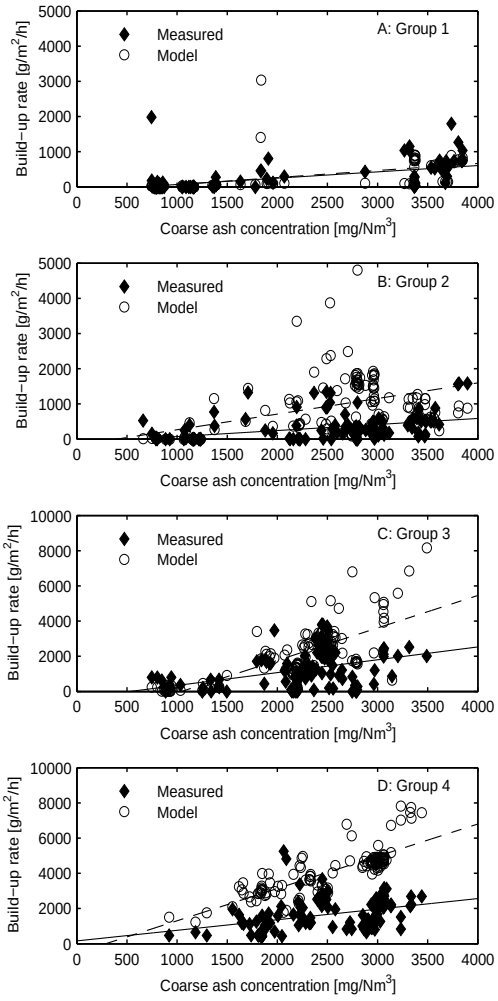

Figure 7.8: Measured and predicted deposit formation rates as function of coarse ash concentration. The lines are the best linear fit of the data. Note the difference in the y-axes.

from the chemical composition of the deposit surface and from the deposit surface temperature. Thus, four sub models are considered as possibly responsible for the overestimations of the capture of particles; (1) the description of the ash and thereby deposits chemical composition, (2) the heat transfer model which predicts the deposit surface temperature, (3) the viscosity model and (4) the surface tension model. It is recommended that the three latter sub models are investigated in future work,

where a chemical composition of the fuel can be monitored closely.

In Figure 7.9, the influence of calculated flue gas velocity is shown. It is seen in

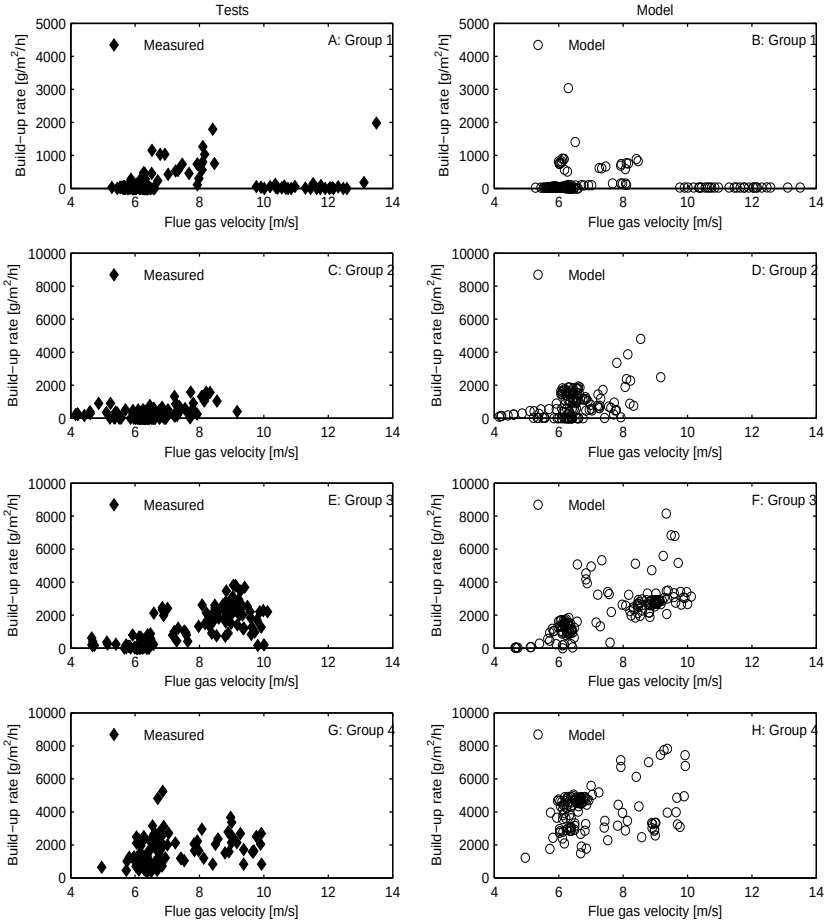

Figure 7.9: Measured and predicted deposit formation rates as function of flue gas velocity.

Figure 7.9 that the velocity of the flue gas influence the rates of deposit formation as increasing deposit rates are observed with increase in flue gas velocity. The model predictions also describe a such influence, however with the overestimations already observed. The overestimations occur at the same degree for velocities in the range 6-10 m/s, where the most data are obtained. It is considered, that the model is able to describe the influence of flue gas velocity correctly, and that the overestimations are caused by other parameters.

A final parameter examined is the estimated straw share of the fuel. The influ-

ence of the straw share on the ash deposit propensity is seen in Figure 7.10. In this figure, the influence of straw share is via the altered chemical composition of the ash, since the ash concentration is used in the calculation of the ash deposit propensity. It is seen that there is mainly observed to be an impact of the straw share when this

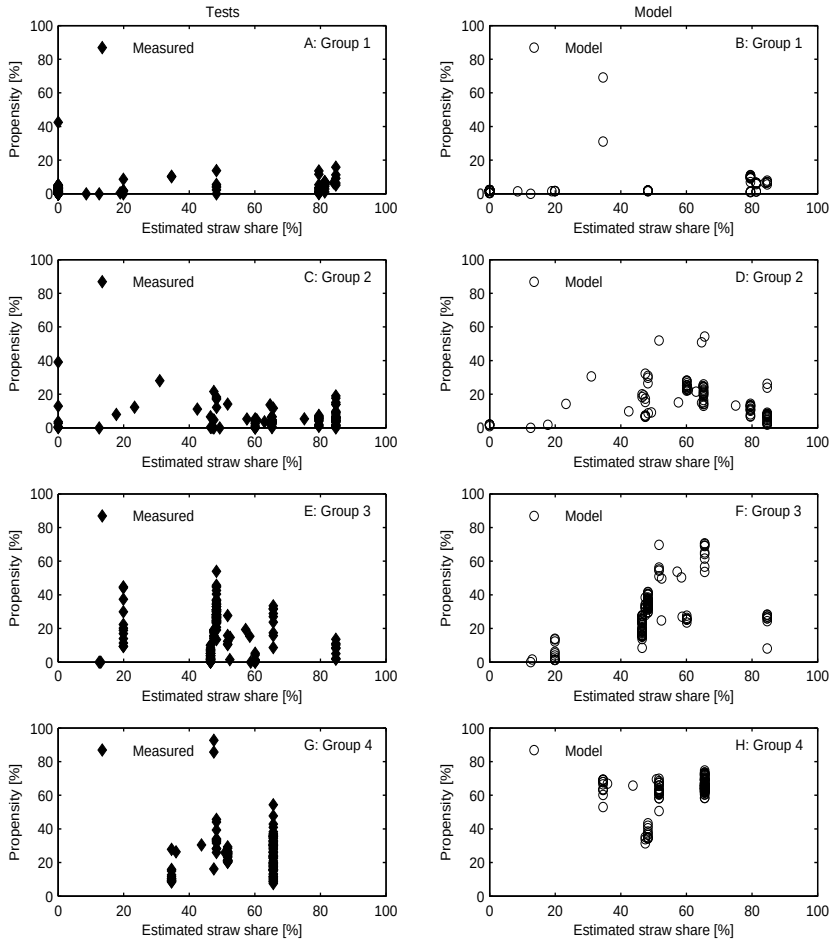

Figure 7.10: Measured and predicted ash deposit propensities as function of estimated straw share.

is increased up to around 30 %. At further increase, there is no further effect. This is related to the fact that the wood ash only influence the total fuel compotition at straw shares lower than approximately 40 % (see figure 7.1). It should be kept in mind that both the straw share and also the fuel compositions are rough estimates, which can explain the limited dependence in the test results.

7.5 Conclusions from Modeling of Full Scale Tests

The developed deposit formation model, using Model #2 for description of ash particle sticking has been used to describe deposit formation in a full scale suspension-fired biomass boiler. The model capabilities were evaluated by a comparison of the deposit formation model results and probe measurements conducted in a suspension-fired boiler. Model #2 combines impaction of (visco)elastic particles on a solid surface with particle capture by a viscous surface in the description of particle sticking or rebound. Model #2 was found to provide the most promising results for the EFR tests, and this model is the only one considered for the full scale tests.

Initially, it was found that the model predictions were quite dependent on the porosity used in the model, simply via the description of deposit geometry. A high porosity or low degree of sintering lead to unrealistic thick deposits and thereby unrealistic rates. The description of porosity and sintering of deposits formed in a biomass suspension boiler need to be examined further, so verified values can be used in the model.

Shedding was in the test campaigns found to occur frequently by debonding. This has been included in the calculations by use of two calculation methods. In the one method the testal results on shedding was used to adjust the mass on the probe, including full shedding at recorded times of shedding. It was seen that this model was able to describe some of the variations observed in the test. However, discrepancies in the prediction in one time step lead to further discrepancies in the following time-step(s) and the calculation method was thus not used for the model evaluation.

In the other calculation method the predicted deposit mass on the probe was adjusted to the measured deposit mass on the probe for each hour. Then, the rate predicted in one hour, was related to that deposit mass load and not influenced by previous occurrences. The rates obtained in this calculation was reasonably able to follow the rates observed in the tests, although with some variation, primarily as overestimations of the deposit formation rates.

The predicted and observed rates of deposit formation has been analyzed for the influence of selected parameters; flue gas temperatures, coarse ash concentration, flue gas velocity and estimated straw share. Based on these examinations it is concluded that the model in general describe the same influences as observed in the tests. The overestimations observed in the model predictions are found primarily at high mass loads on the probe. At low or intermediate mass loads the response to increases in temperature are overestimated by the model in the temperature range 750-850 °C. The model describes increased rates above ~ 775 °C, which are observed to occur above 850 °C in the test results.

It is found, that the model generally overestimate the influence of coarse ash concentration. It is considered that the captive properties of the deposit surface

are overestimated. This overestimation can occur via an incorrect description of the deposit surface temperature and/or an incorrect prediction of the parameters in the sticking model; viscosity and surface tension. This needs further examination.

Based on these examinations Model #2 can be regarded as a promising tool for description of deposit formation also in full scale combustion.

Chapter 8

Conclusions

This PhD was aimed at improving the understanding of the deposit formation process occurring in suspension-firing of biomass. This has been done in two ways. First by conducting a review of the deposit formation tests made in full scale suspension- and grate-firing of biomass. Secondly, by developing models for the ash formation and for the deposit build-up occurring in suspension-firing of biomass.

Initially, a literature review on ash formation from biomass was conducted. Here the influence of firing technology and fuel type on characteristics of the ash was examined. The focus was on the ash chemical transformations, the ash particle size and the particle morphology.

Observations from Full Scale

The review of full scale tests included both grate- and suspension-fired boilers. Here, the fly ash and deposits chemical compositions were examined along with deposit formation rates and types of shedding occurring in the two boiler types.

In the review of the full scale campaigns it was found that during grate-firing of straw, the fly ash was enriched in K, Cl and S compared to the fuel ash. During suspension-firing the fly ash composition largely resembled the fuel ash composition, due to a higher degree of entrainment of ash in the combustion zone. The fly ash from suspension-firing of straw was thus dominated by K and Si while wood-firing in suspension boilers lead to fly ash dominated by Ca and K.

The deposit chemical composition was influenced by firing technology, fuel choice and flue gas temperature. At low local flue gas temperatures (< 800 °C), the deposit compositions were similar to those of fly ash. Increases in local flue gas temperatures increased the content of Si and Ca in the deposits and decreased the Cl content. The influence of flue gas temperature is similar for grate and suspension-firing.

The net deposit build-up rates in grate and suspension-firing of biomass are at similar levels; 0-100 g/m^2/h, while the ash deposit propensity is an order of magnitude larger in grate-fired boilers than in suspension boilers. The ash deposit

propensity increases with flue gas temperatures and a steep increase in ash deposition propensity was observed near the melting temperatures of the fly ash. The rate of deposit build-up was furthermore found to increase with K content in the fuel ash and in the fly ash for grate-fired boilers. For suspension-fired boilers deposition rates were low for wood-firing and increases with increasing straw shares.

Shedding of deposits occurs by melting during straw-firing on a grate at high flue gas temperatures (>900 °C). At lower flue gas temperatures, the deposits can be removed by soot blowing. During combustion of straw/wood mixtures in suspension-fired boilers, shedding occurred by debonding with incomplete removal at flue gas temperatures within 600-1000 °C. When wood was used at fuel in suspension-fired boilers, shedding occurred by debonding with complete removal high flue gas temperatures (1300 °C), whereas no shedding events were observed at low flue gas temperatures (<900 °C). Here, a steady-state mass of deposits on the probe was observed.

It was observed for grate-firing of straw and for straw/wood firing in suspension-fired boilers that increased exposure times and probe temperatures lead to deposits which are difficult to remove.

Model for Ash Formation

Based on the observations made in a literature study, including recent experiments, and in the review of full scale campaigns, a model for ash formation was suggested. In this model, the release of K, Cl and S was assumed, simple description of the gas phase reactions was proposed along with quantification of aerosol formation. The coarse ash fraction was described by a new model for particle size distribution. The model is similar to fragmentation models suggested for coal combustion, but takes vaporization of K, Cl and S into account. It was found that after release of volatiles both straw and wood particles fragment into ~3 pieces during combustion.

Model for Deposit Build-up

Two models for deposit formation were set up. Both models include deposit build-up by diffusion and condensation of vapors, thermophoresis and convective diffusion of aerosols and small particles, impaction of larger particles and reaction. The models differ in the description of sticking probability of impacted particles.

Model #1 employs a reference viscosity in the description of sticking probability. All particles with a given viscosity is assumed to have the same sticking probability, regardless of particle size, velocity and impact angle. This model is analogous to the models often used for coal ash deposition.

Model #2 combines impaction of (visco)elastic particles on a solid surface with particle capture by a viscous surface. A critical velocity is calculated for each mechanism from particle size, velocity and angle of the impact along with physical properties of the particle in terms of Young's Modulus or of the surface in terms of viscosity.

Two sets of previously conducted experiments have been used in the model validation; EFR experiments and full scale tests. The EFR experiments were conducted with straws and woods as fuels. Besides variation in fuels, also variations in temperatures (700-1000 °C) and fuel particle sizes, was used in the straw experiments. In the description of the EFR experiments, a measured concentration of the coarse ash was used in the calculations. It was however found that the concentrations vary significantly and it is anticipated that these concentration measurements are uncertain, which is supported by poor mass balances. This uncertainty was considered during the model validation.

The full scale tests were obtained with deposit probes in combustion plants with straw/wood mixtures as fuel. In these experiments, the fuel composition supplied to the model rely on rough estimates, which is considered during model evaluation. In the six full scale experiment each running for 30-185 hours, significant variations in flows and temperatures (T_{fg}: 700-1000 °C) occurred.

In the initial model validation conducted with the EFR experiments, it was found that both models are able to describe the overall magnitude of the deposits formed. There is however a significant scattering of the results for both models. The deposit formation was examined in terms of KCl, K_2SO_4 and insoluble ash amounts in the deposit. For KCl and K_2SO_4, the predictions by the two models are similar. The condensation of KCl was generally overestimated. It was found that the temperature used for calculating the diffusivity have a significant impact on the prediction of KCl deposition. It is also considered that some overestimation is a result of using a quite simple model. Thermophoresis of K_2SO_4 was found to be overestimated at experiments where low rates was observed and underestimated at high rates.

The two models differ in the description of the deposition of insoluble ash in the EFR experiments. It was found that Model #1 does not describe the variation in deposit rates observed with varying temperature. A too steep increase in deposit formation rates was observed and linked to a steep increase in sticking probability with temperature. The conclusion that Model#1 is unsuitable for description of ash deposition during suspension-firing of biomass can be drawn regardless of the uncertainties in the measured fly ash concentration.

Model #2, combining elastic impact of particles with capture by a viscous surface, is able to describe the observed variation in deposit formation with temperature. This observation was made for both the EFR experiments and the full scale tests, though overestimations were observed in the latter case. The uncertainties in the measured concentrations of the coarse ash in the EFR inhibited a complete model validation within this set-up. In the full scale model evaluation it was found that the model predicted an increase in deposit formation rate with increased temperatures which was initiated at temperatures approximately 100 °C lower than where the increase was initiated in the tests. This lead to overestimations of the measured deposit formation rates, in the temperature range 750-850 °C.

In a parameter study conducted for the full scale tests, it was found that the model overestimate the influence of coarse ash concentration. Assuming that the predicted coarse ash concentration is correct, it is considered that the captive properties of the deposit surface are overestimated. This overestimation can occur via an incorrect description of the deposit surface temperature and/or an incorrect prediction of the viscosity or surface tension. This needs further examination.

The model predictions were quite dependent on the porosity used in the model, simply via the description of deposit geometry. This was especially found to be significant during modeling of the full scale tests. A high initial porosity or low degree of sintering lead to unrealistic thick deposits and thereby unrealistic rates. The description of porosity and sintering of deposits formed in a biomass suspension boiler thus need to be examined further, so validated values can be applied in the model

In the model, the adhesion or rebound of particles on a dry solid surface is described by an elastic impact model, employing a Young's Modulus. It is found by examinations of the EFR experiments and by a sensitivity analysis that for woods and for straws at low temperature ($<800\,^{\circ}C$), the Young's modulus is an significant parameter. The Young's modulus has in this work been given an assumed, fixed value. Ideally, this parameter should be related to temperature and ash composition.

Based on the results obtained in this thesis, Model #2, combining elastic impact of particles with capture by a viscous surface, can be regarded as a promising tool for description of deposit formation in suspension-firing across a relatively wide range of biomass fuels and temperatures.

Chapter 9

Suggestions for Further Work

This work has presented a model which was observed to be a promising tool for description of deposit build-up during suspension firing of biomass for both combustion in small scale and full scale. The model has been tested across a range of temperatures (700-1000 °C) and fuel mixtures (straw/wood). However, some parameters were rough estimates and some experimental parameters were uncertain. Thus, more work is needed for a complete model validation. Ideas for such work is provided in this chapter.

Experimental work

- The concentration of coarse fly ash needs to be measured with higher accuracy in both small and large scale combustion. In small combustion, a better fly ash sampling is needed, possibly combined with a different set-up, where a bend flow is avoided. In full scale, a closer tracking of fuel and ash composition is desired. Also the ash split into bottom ash and fly ash from the combustion plant and fuel in question will be valuable for a model validation.

- The straws used in the EFR mainly varied in the contents of K, Cl and S. After vaporisation, the bulk chemical composition of the straw ash particles were modeled to be quite similar. The woods used in the EFR all had very low Si content and very low deposition rates. The fuels in the EFR thus represented two ends of the scale. A broader fuel variation e.g. by use of a broader variation of the pure fuels and/or mixing of fuels is suggested for small scale experiments.

Physical properties

- The porosity of formed deposits - both initially and over time - should be evaluated. This is not only considered to be important for prediction of deposit build-up, but also for description deposit shedding, which is considered to be a future topic.

- The viscoelasticity of ash (and deposit) should be examined in greater detail. The Young's modulus was shown to be a significant parameter for deposit build-up during wood combustion and at low temperatures during straw combustion. The variation of this parameter with temperature and composition should be examined.

- The viscosity of ash is in this work modeled by a model from the glass technology tested against relevant compositions. This model needs to be evaluated for relevant ashes.

- The surface tension of ash and deposits was predicted by a model suggested for coal ash slags, which was assumed to apply. This assumption needs evaluation.

Nomenclature

Roman letters

$\dot{n}$	Molar flow	[kmol/s]
∇T	Temperature gradient	[K/m]
$\mathrm{C}(t,\theta)$	Rate of condensation	[kg/s]
$\mathrm{D}(t,\theta)$	Rate of diffusion	[kg/s]
$\mathrm{Flux}_{dep}(t,\theta)$	Rate deposit build-up	[kg/s]
$\mathrm{I}(t,\theta)$	Rate of inertial impaction	[kg/s]
$\mathrm{R}(t,\theta)$	Rate of mass accumulation by reaction	[kg/s]
$\mathrm{T}(t,\theta)$	Rate of thermophoresis	[kg/s]
A	Constant	
B	Constant	
C	Constant	
C_c	Cunningham correction factor	
C_j	Concentration of species j	[kg/m^3]
C_m	Parameter used in thermophoretic velocity, Eq. 5.23	
C_p	Heat Capacity	[J/(kg·K)]
C_s	Parameter used in thermophoretic velocity, Eq. 5.23	
C_t	Parameter used in thermophoretic velocity, Eq. 5.23	
d	Diameter	[m]
D_p	Particle diffusivity	[m^2/s]
D_{j,N_2}	Diffusion coefficient of species j in N_2	[m^2/s]
d_{probe}	Diameter, probe	[m]
dp	Particle diameter	[m]
dp_{50}	Median particle diameter	[m] or [μm]

E	Young's Modulus	[Pa]
F	Fraction of conductivity attributable to gas	
F_T	Thermophoretic force	[N]
F_V	Stokes drag force	[N]
$f_{K-release}$	Fraction of K vaporized	
f_{melt}	Melt fraction	
h	Heat transfer coefficient	[W/(m^{2}K)]
k	Thermal conductivity	[W/(m K)]
K_c	Equilibrium constant	[-]
k_c	Mass transfer coefficient	[m/s]
Kn	Knudsen number	[-]
l_{probe}	Length of probe (exposed to flue gas)	[m]
m	Mass	[kg]
m_{ash}	Mass of ash particle	[kg]
Mw	Molar weight	[kg/kmol]
n	Exponent in RR distribution	
N_{frag}	Number of fragments per particle	
N_{part}	Number of particle sizes used in model	
Nu	Nusselt number	
P	Pressure	[Pa]
P	Pressure	[Pa]
p	Probability (of sticking)	
Pr	Prandtl's number	
q	Heat flux	[J/(m^{2}s)]
r	Radius	[m]
Re	Reynolds number	
s	Surface area of probe section	[m^2]
Sc	Schmidt number	
Sh	Sherwood number	
Stk	Stokes number	

T	Temperature	[K]
T	Temperature	[K]
t	Time	[s]
u	Velocity	[m/s]
X_{ash}	Fraction of ash in fuel	
$X_{bottom/lost}$	Fraction of coarse ash as bottom ash (by weight)	
$X_{coarse,fly}$	Fraction of coarse ash as fly ash (by weight)	
X_{vap}	Vaporized fraction of ash (by weight)	
y	Molar fraction	
$\tilde{V}$	Molar volume	[cm^3/mol]

Greek letters

α	Absorbance	
α_{impact}	Angle of impaction	[radian]
δ	Deposit thickness	[m]
$\Delta\theta$	Length of computational cell on probe circumsphere	[radian]
ℓ	Mean free path	[m]
ϵ	Characteristic energy	[J]
ϵ	Emissivity	
η_cap	Capture efficiency	[-]
η_I	Collision efficiency	
η_s	Sticking probability	
η_t	Target efficiency	
γ	Surface tension	[N/m]
κ	Boltzmann constant = $1.3806488{\cdot}10^{-23}$	[J/K]
κ	Boltzmann's constant	[J/K]
λ	Parameter in RR distribution	[m]
μ	Viscosity	[Pa·s]
μ_{ref}	Reference viscosity	[Pa·s]
ν	Kinematic Viscosity	[m^2/s]
Ω	Diffusion collision integral	

ϕ	Porosity	[-]
ψ	Drag coefficient	
ρ	Density	[kg/m^3]
σ	Collision cross section	[nm^2]
σ_i	Characteristic diameter	[Å]
θ	Position around probe	[radian]
θ_{max}	Maximum angle of collision (on cylinder)	[radian]
M	Molar mass	[g/mol]

Subscripts

b	bulk
dep	deposit
fg	flue gas
g	gas
m	Melting point
p	particle
$probe$	probe
s	surface

Bibliography

[1] Klimakommisionen. *Green energy - the road to a Danish energy system without fossil fuels.* Danish Commission on Climate Change Policy, 2010. ISBN 978-87-7844-881-1.

[2] H. Egsgaard, U. Hansen, P.A. Jensen, P. Glarborg, and C. Nielsen. *Combustion and gasification technologies.* Risø Energy Report 2, 2003. ISBN 87-550-3261-3.

[3] Centre for Biomass Technology (CBT). *Straw for Energy Production - Technology - Environment - Economy.* Report, Ed: L. Nikolaisen. http://www.videncenter.dk/uk/, 1998. ISBN 87-90074-20-3.

[4] F.J. Frandsen. *Ash Formation, Deposition and Corrosion When Utilizing Straw for Heat and Power Production.* Doctoral thesis, CHEC Research Centre, Department of Chemical Engineering, Technical University of Denmark, 2011. ISBN 978-87-92481-40-5.

[5] M.S. Bashir. *Characterization and Quantification of Deposit Build-up and Removal in Straw Suspension-Fired Boilers.* Ph.D. thesis, CHEC Research Centre, Department of Chemical Engineering, Technical University of Denmark, 2012. ISBN 978-87-92481-88-7.

[6] H. Wu, M.S. Bashir, P.A. Jensen, B. Sander, and P. Glarborg. Impact of coal fly ash addition on ash transformation and deposition in a full-scale wood suspension-firing boiler. *Fuel*, 113:632–643, 2013.

[7] R.W. Bryers. Fireside slagging, fouling, and high-temperature corrosion of heat-transfer surface due to impurities in steam-raising fuels. *Prog. Energy Combust. Sci.*, 22:29–120, 1996.

[8] F.J. Frandsen, L. Bäfver, and A.F. Sarofim. *On the Gaps in Understanding and Quantification of Release of Critical Elements, Formation of Fly Ash and Aerosols when Utilizing Solid Fuels in Different Thermal Fuel Conversion Technologies.* Proceedings; Impacts of Fuel Quality on Power Production & Environment, Saariselkä, Lapland, Finland, August 29 - September 3, 2010.

[9] J.N. Knudsen, P.A. Jensen, and K. Dam-Johansen. Transformation and Release to the Gas Phase of Cl, K, and S during Combustion of Annual Biomass. *Energy & Fuels*, 18:1385–1399, 2004.

[10] S.C. van Lith, P.A. Jensen, F.J. Frandsen, and Peter Glarborg. Release to the Gas Phase of Inorganic Elements during Wood Combustion. Part 2: Influence of Fuel Composition. *Energy & Fuels*, 22:1598–1609, 2008.

[11] J.M. Johansen, J.G. Jakobsen, F.J. Frandsen, and P. Glarborg. Release of K, Cl, and S during Pyrolysis and Combustion of High-Chlorine Biomass. *Energy & Fuels*, 25: 4961–4971, 2011.

[12] I. Obernberger, T. Brunner, and M. Jöller. *Characterization and formation of aerosols and fly-ashes from fixed-bed biomass combustion.* Aerosols from Biomass Combustion, International Seminar at 27 June 2001 in Zurich (Switzerland), Thomas Nussbaumer(Ed), 2001.

[13] M. Jöller, T. Brunner, and I. Obernberger. Modeling of Aerosol Formation during Biomass Combustion in Grate Furnaces and Comparison with Measurements. *Energy & Fuels*, 19:311–323, 2005.

[14] R. Korbee, K.V. Shah, M.K. Cieplik, C.I. Betrand, H.B. Vuthaluru, and W.L. van de Kamp. First Line Ash Transformations of Coal and Biomass Fuels during PF Combustion. *Energy & Fuels*, 24:897–909, 2010.

[15] K.V. Shah, M.K. Cieplik, C.I. Betrand, W.L. van de Kamp, and H.B. Vuthaluru. Correlating the effects of ash elements and their association in the fuel matrix with the ash release during pulverized fuel combustion. *Fuel Processing Technology*, 91: 531–545, 2010.

[16] A.J. Damoe, F.J. Frandsen, P.A. Jensen, H. Wu, and P. Glarborg. *Residual Ash Formation during Suspension-Firing of Biomass. Effects of Residence Time and Fuel-Type.* Proceedings; 'Impacts of Fuel Quality on Power Production' Conference, Snowbird, Utah, October 26-31, 2014.

[17] D. Nordgren, H. Hedman, N. Padban, D. Boström, and M. Öhman. Ash transformations in pulverised fuel co-combustion of straw and woody biomass. *Fuel Processing Technology*, 105:52–58, 2013.

[18] L.L. Baxter. Ash deposition during biomass and coal combustion: A mechanistic approach. *Biomass and Bioenergy*, 4:85–102, 1993.

[19] H. Zhou, P.A. Jensen, and F.J. Frandsen. Dynamic mechanistic model of superheater deposit growth and shedding in a biomass fired grate boiler. *Fuel*, 86:1519–1533, 2007.

[20] S. Balakrishnan, R. Nagarajan, and K. Karthick. Mechanistic modeling, numerical simulation and validation of slag-layer growth in a coal-fired boiler. *Energy*, 81:462–470, 2015.

[21] J. Ni, G. Yu, Q. Guo, Z. Zhou, and F. Wang. Submodel for Predicting Slag Deposition Formation in Slagging Gasification Systems. *Energy & Fuels*, 25:1004–1009, 2011.

[22] Y. Pan, F. Si, Z. Xu, and C.E. Romero. An integrated theoretical fouling model for convective heating surfaces in coal-fired boilers. *Powder Technology*, 210:150–156, 2011.

[23] H. Wang and J.N. Harb. Modeling of ash deposition in large-scale combustion facilities burning pulverized coal. *Prog. Energy Combust. Sci.*, 23:267–282, 1997.

[24] S.K. Kær. *Numerical investigation of ash deposition in straw-fired boilers.* Ph.D. thesis, Institute of Energy Technology, Aalborg University, Denmark, 2001. ISBN 87-89179-39-0.

[25] P. Venturini, D. Borello, C. Iossa, D. Lentini, and F. Rispoli. Modeling of multiphase combustion and deposit formation in a biomass-fed furnace. *Energy*, 35:3008–3021, 2010.

[26] P. Venturini, D. Borello, K. Hanjalíc, and F. Rispoli. Modelling of particles deposition in an environment relevant to solid fuel boilers. *Applied Thermal Engineering*, 49: 131–138, 2012.

[27] M.U. Garba, D.B. Ingham, L. Ma, R.T.J. Porter, M. Pourkashnian, H.Z. Tan, and A. Williams. Prediction of Potassium Chloride Sulfation and Its Effect on Deposition in Biomass-Fired Boilers. *Energy & Fuels*, 26:6501–6508, 2012.

[28] M. Hupa. Ash-Related Issues in Fluidized-Bed Combustion of Biomasses: Recent Research Highlights. *Energy & Fuels*, 26:4–14, 2012.

[29] C. Mueller, M. Selenius, M. Theis, B.-J. Skrifvars, R. Backman, M. Hupa, and H. Tran. Deposition behavior of molten alkali-rich fly ashes - development of a submodel for CFD applications. *Proceedings of the Combustion Institute*, 30:2991–2998, 2005.

[30] P. Plaza, A.J. Griffiths, N. Syred, and T. Rees-Gralton. Use of a Predictive Model for the Impact of Cofiring Coal/Biomass Blends on Slagging and Fouling Propensity. *Energy & Fuels*, 23:3437–3445, 2009.

[31] M.U. Garba, D.B. Ingham, L. Ma, M.U. Degereji, M. Pourkashanian, and A. Williams. Modelling of deposit formation and sintering for the co-combustion of coal with biomass. *Fuel*, 113:863–872, 2013.

[32] M. Losurdo. *Particle Tracking and Deposition from CFD Simulations using a Viscoelastic Particle Model.* Ph.D. thesis, Delft Technical University, The Netherlands, 2009.

[33] M. Losurdo, H. Spliethoff, and J. Kiel. Ash deposition modeling using a visco-elastic approach. *Fuel*, 102:145–155, 2012.

[34] M. Theis, B.-J. Skrifvars, M. Hupa, and H. Tran. Fouling tendency of ash resulting from burning mixtures of biofuels. Part 1: Deposition rates. *Fuel*, 85:1125–1130, 2006.

[35] M. Theis, B.-J. Skrifvars, M. Zevenhoven, M. Hupa, and H. Tran. Fouling tendency of ash resulting from burning mixtures of biofuels. Part 2: Deposit chemistry. *Fuel*, 85:1992–2001, 2006.

[36] M. Theis, B.-J. Skrifvars, M. Zevenhoven, M. Hupa, and H. Tran. Fouling tendency of ash resulting from burning mixtures of biofuels. Part 3: Influence of probe surface temperature. *Fuel*, 85:2002–2011, 2006.

[37] P.A. Jensen, L.H. Sørensen, G. Hu, J.K. Holm, F. Frandsen, and U.B. Henriksen. *Combustion experiments with biomass fuels and additives in a suspension fired entrained flow reactor - Test of Ca and P rich additives used to minimize deposition and corrosion.* Energinet.dk PSO project 6515/Report R0504, CHEC Research Centre, Technical University of Denmark, 2005.

[38] J. Capablo, P.A. Jensen, K.H. Pedersen, K. Hjuler, L. Nikolaisen, R. Backman, and F. Frandsen. Ash Properties of Alternative Biomass. *Energy & Fuels*, 23:1965–1976, 2009.

[39] H. Wu, P. Glarborg, F.J. Frandsen, K. Dam-Johansen, and P.A. Jensen. Dust-Firing of Straw and Additives: Ash Chemistry and Deposition Behavior. *Energy & Fuels*, 25:2862–2873, 2011.

[40] S.S. Lokare, J.D. Dunaway, D. Moulton, D. Rogers, D.R. Tree, and L.L. Baxter. Investigation of Ash Deposition Rates for a Suite of Biomass Fuels and Fuel Blends. *Energy & Fuels*, 20:1008–1014, 2006.

[41] A.L. Robinson, H. Junker, and L.L. Baxter. Pilot-Scale Investigation of the Influence of Coal-Biomass Cofiring on Ash Deposition. *Energy & Fuels*, 16:343–355, 2002.

[42] M. Hupa. Interaction of fuels in co-firing in FBC. *Fuel*, 84:1312–1319, 2005.

[43] R. Weber, Y. Poyraz, A.M. Beckmann, and S. Brinker. Combustion of biomass in jet flames. *Proceedings of the Combustion Institute*, 35:2749–2758, 2015.

[44] R. Weber, M. Mancini, N. Schaffel-Mancini, and T. Kupka. On predicting the ash behaviour using Computational Fluid Dynamics. *Fuel Processing Technology*, 105: 113–128, 2013.

[45] A. Zbogar, F. Frandsen, P.A. Jensen, and P. Glarborg. Shedding of ash deposits. *Progress in Energy and Combustion Science*, 35, 2009.

[46] S.E. Wain, W.R. Livingston, A. Sanyal, and J. Williamson. *Thermal and mechanical properties of boiler slags of relevance to sootblowing.* In: Benson S.A., editor. Inorganic transformations and ash deposition during combustion, United Engineering Trustees, Inc., 1992. ISBN 0-7918-0657-X.

[47] A. Kaliazine, D.E. Cormack, A. Ebrahimi-Sabet, and H. Tran. The Mechanistic of Deposit Removal in Kraft Recovery Boilers. *Journal of Pulp and Paper Science*, 25: 418–424, 1999.

[48] L.A. Hansen. *Melting and Sintering of Ashes.* Ph.D. thesis, CHEC Research Centre, Department of Chemical Engineering, Technical University of Denmark, 1998. ISBN 87-90142-31-4.

[49] L.Wang, H. Wu, P.A. Jensen, K. Dam-Johansen, and J.E. Hustad. *Ash transformation and deposition behavior during co-firing biomass fuels with sewage sludge.* Proceedings; Impacts of Fuel Quality on Power Production & Environment, Puchberg am Schneeberg, Austria, September 23-27, 2012.

[50] Elsam Engineering. *Slutrapport, Halmtilsatsfyring i naturgasfyret kraftværkskedel.* Energinet.dk PSO project 3941, 2005.

[51] P. A. Jensen, M. Stenholm, and P. Hald. Deposition Investigation in Straw-Fired Boilers. *Energy & Fuels*, 11:1048–1055, 1997.

[52] P.A. Jensen, M. Stenholm, and P. Hald. *Biomasses brændsels- og fyringskarakteristika - Fyringsforsøg.* Journal nr. 1323/93-0015. dk-TEKNIK, Risø, 1996.

[53] H.P. Michelsen, F. Frandsen, K. Dam-Johansen, and O.H. Larsen. Deposition and high temperature corrosion in a 10 MW straw fired boiler. *Fuel Processing Technology*, 54: 95–108, 1998.

[54] L.A. Hansen, H.P. Nielsen, F.J. Frandsen, K. Dam-Johansen, S. Hørlyck, and A. Karlsson. Influence of deposit formation on corrosion at a straw-fired boiler. *Fuel Processing Technology*, 64:189–209, 2000.

[55] P.A. Jensen, F.J. Frandsen, J. Hansen, K. Dam-Johansen, N. Henriksen, and S. Hörlyck. SEM Investigation of Superheater Deposits from Biomass-Fired Boilers. *Energy & Fuels*, 18:378–384, 2004.

[56] J. Hansen, P.A. Jensen, and P. Glarborg. *Deposit probe measurements in the Avedøre and Ensted straw fired grate boilers.* Energinet.dk PSO project 4792/Report R0705, CHEC Research Centre, Department of Chemical Engineering, Technical University of Denmark, 2007.

[57] P.A. Jensen, H. Zhou, A. Zbogar, J. Hansen, F.J. Frandsen, and B.and Stang H. Glarborg, P.and Madsen. *Final Report - Ash Deposit Formation and Removal in Biomass-fired Boilers. Fundamental Data Provided with Deposit Probes.* Energinet.dk PSO project 4106/Report R0603, CHEC Research Centre, Department of Chemical Engineering, Technical University of Denmark, 2006.

[58] A. Zbogar, P.A. Jensen, F. Frandsen, J. Hansen, and P. Glarborg. Experimental Investigation of Ash Deposit Shedding in a Straw-Fired Boiler. *Energy & Fuels*, 20, 2006.

[59] P.A. Jensen, M. Dall'ora, W. Lin, S. Clausen, J. Hansen, P. Simonsen, M. Berg, and A.D. Jensen. *Measurements on the 800 MW_{th} Avedøre oil, gas and wood co-fired suspension boiler - Analysis of emission, burnout, deposit and FTIR measurements from April 2005.* Energinet.dk PSO project 6526/Report R0802, CHEC Research Centre, Department of Chemical Engineering, Technical University of Denmark, 2008.

[60] H. Wu, M.S. Bashir, P.A. Jensen, P. Glarborg, and F.J. Frandsen. *Full-scale deposition measurements at Avedøre Power Plant unit 2 during suspension-firing of wood with and without coal ash addition.* CHEC Report, CHEC Research Centre, Department of Chemical Engineering, Technical University of Denmark, 2012.

[61] L. Tobiasen, R. Skytte, L.S. Pedersen, S.T. Pedersen, and M.A. Lindberg. Deposit characteristic after injection of additives to a Danish straw-fired suspension boiler. *Fuel Processing Technology*, 88:1108–1117, 2007.

[62] M.S. Bashir, P.A. Jensen, F.J. Frandsen, S. Wedel, K. Dam-Johansen, J. Wadenbäck, and S.T. Pedersen. Ash transformation and deposit build-up during biomass suspension and grate-firing: Full-scale experimental studies. *Fuel Processing Technology*, 97: 93–106, 2012.

[63] M.S. Bashir, P.A. Jensen, F.J. Frandsen, S. Wedel, K. Dam-Johansen, J. Wadenbäck, and S.T. Pedersen. Suspension-Firing of Biomass. Part 1: Full-Scale Measurements of Ash Deposit Build-up. *Energy & Fuels*, 26:2317–2330, 2012.

[64] M.B. Toftegaard. *OxyFuel Combustion of Coal and Biomass*. Ph.D. thesis, CHEC Research Centre, Department of Chemical Engineering, Technical University of Denmark, 2011. ISBN 978-87-92481-58-0.

[65] D. Mohan, C.U. Pittman Jr, and P.H. Steele. Pyrolysis of Wood/Biomass for Bio-oil: A Critical Review. *Energy & Fuels*, 20:848–889, 2006.

[66] B.M. Jenkins, L.L. Baxter, T.R. Miles Jr., and T.R. Miles. Combustion properties of biomass. *Fuel Processing Technology*, 54:17–46, 1998.

[67] V. Doshi, H.B. Vuthaluru, R. Korbee, and J.H.A. Kiel. Development of a modeling approach to predict ash formation during co-firing of coal and biomass. *Fuel Processing Technology*, 90:1148–1156, 2009.

[68] M.J. Wornat, R.H. Hurt, N.Y.C. Yang, and T.J. Headly. Structural and Compositional Transformations of Biomass Chars during Combustion. *Combustion and Flame*, 100: 131–143, 1995.

[69] T.H Fletcher, A.R. Kerstein, R.J. Pugmire, M.S. Solum, and D.M. Grant. Chemical percolation model for devolatilization. 3. direct use of carbon-13 nmr data to predict effects of coal type. *Energy & Fuels*, 6:414–431, 1992.

[70] W. de Jong, G. Di Nola, B.C.H. Venneker, H. Spliethoff, and M.A. Wójtowicz. TG-FTIR pyrolysis of coal and secondary biomass fuels: Determination of pyrolysis kinetic parameters for main species and NO_x precursors. *Fuel*, 86:2367–2376, 2007.

[71] S.C. van Lith. *Release of Inorganic Elements during Wood-Firing on a Grate*. Ph.D. thesis, CHEC Research Centre, Department of Chemical Engineering, Technical University of Denmark, 2005. ISBN 87-91435-29-3.

[72] H. Lu, E. Ip, J. Scott, P. Foster, M. Vickers, and L.L. Baxter. Effects of particle shape and size on devolatilization of biomass particle. *Fuel*, 89:1156–1168, 2010.

[73] H. Spliethoff and K.R.G. Hein. Effect of co-combustion of biomass on emissions in pulverized fuel furnaces. *Fuel Processing Technology*, 54:189–205, 1998.

[74] H. Wu. *Co-combustion of Fossil Fuels and Waste*. Ph.D. thesis, CHEC Research Centre, Department of Chemical Engineering, Technical University of Denmark, 2011. ISBN 978-87-92481-55-9.

[75] Y. Zheng, P.A. Jensen, A.D. Jensen, B. Sander, and H. Junker. Ash transformation during co-firing coal and straw. *Fuel*, 86:1008–1020, 2007.

[76] S. van Loo and J. Koppejan (editors). *The handbook of Biomass Combustion & Co-firing*. Earthscan, 2008. ISBN 978-1-84971-104-3.

[77] H. Lu, W. Robert, J. Scott, P. Foster, M. Vickers, and L.L. Baxter. Comprehensive Study of Biomass Particle Combustion. *Energy & Fuels*, 22:2826–2839, 2008.

[78] R.I. Backreedy, L.M. Fletcher, J.M. Jones, L. Ma, M. Pourkashanian, and A. Williams. Co-firing pulverised coal and biomass: a modeling approach. *Proceedings of the Combustion Institute*, 30:2955–2964, 2005.

[79] M. Dall'Ora, P.A. Jensen, and A.D. Jensen. Suspension Combustion of Wood: Influence of Pyrolysis Conditions on Char Yield, Morphology, and Reactivity. *Energy & Fuels*, 22:2955–2962, 2008.

[80] Y.A. Levendis, K. Joshi, R. Khatami, and A.F. Sarofim. Combustion behavior in air of single particles from three different coal ranks and from sugarcane bagasse. *Combustion and Flame*, 158:452–465, 2011.

[81] B. Sander. Properties of danish biofuels and the requirements for power production. *Biomass and Bioenergy*, 12:177–183, 1997.

[82] L. Yan, R.P. Gupta, and T.F. Wall. The implication of mineral coalescence behaviour on ash formation and ash deposition during pulverised coal combustion. *Fuel*, 80: 1333–1340, 2001.

[83] J.J. Helble and A.F. Sarofim. Influence of Char Fragmentation on Ash Particle Size Distributions. *Combustion and Flame*, 76:183–196, 1989.

[84] S.-G. Kang, A.R. Kerstein, J.J. Helble, and A.F. Sarofim. Simulation of Residual Ash Formation During Pulverized Coal Combustion: Bimodal Ash Particle Size Distribution. *Aerosol Science and Technology*, 13:401–412, 1990.

[85] A.F Sarofim, J.B. Howard, and A.S Padia. The Physical Transformation of the Mineral Matter in Pulverized Coal Under Simulated Combustion Conditions. *Combustion Science and Technology*, 16:187–204, 1977.

[86] L.L. Baxter. Char Fragmentation and Fly Ash Formation During Pulverized-Coal Combustion. *Combustion and Flame*, 90:174–184, 1992.

[87] L.L. Baxter. The evolution of mineral particle size distributions during early stages of coal combustion. *Prog. Energy Combust. Sci.*, 16:261–266, 1990.

[88] J.J. Helble, S. Srinivasachar, and A.A. Boni. Factors influencing the transformation of minerals during pulverized coal combustion. *Prog. Energy Combust. Sci.*, 16:267–279, 1990.

[89] B.S. Haynes, M. Neville, R.J. Quann, and A.F. Sarofim. Factors Governing the Surface Enrichment of Fly Ash in Volatile Trace Species. *Journal of Colloid and Interface Science*, 87:266–278, 1982.

[90] F. Vejahati, Z. Xu, and R. Gupta. Trace elements in coal: Associations with coal and minerals and their behavior during coal utilization - A review. *Fuel*, 89:904–911, 2010.

[91] M. Zevenhoven-Onderwater. *Ash Forming Matter in Biomass Fuels*. Academic Dissertation, Faculty of Chemical Engineering, Åbo Akademi, Finland, 2001. ISBN 9521208139.

[92] S. Jiménes and J. Ballester. Particulate matter formation and emission in the combustion of different pulverized biomass fuels. *Combust. Sci. and Tech.*, 178:655–683, 2006.

[93] A.J. Damoe, H. Wu, F.J. Frandsen, P. Glarborg, and B. Sander. *Combustion Aerosols from Full-Scale Suspension Firing of Wood Pellets*. Proceedings; Impacts of Fuel Quality on Power Production & Environment, Puchberg am Schneeberg, Austria, September 23-27, 2012.

[94] R.P. van der Lans, L.T. Pedersen, A. Jensen, P. Glarborg, and K. Dam-Johansen. Modelling and experiments of straw combustion in a grate furnace. *Biomass and Bioenergy*, 19:199–208, 2000.

[95] M.A Grønli. *Theoretical and Experimental Study of the Thermal Degradation of Biomass*. Ph.D. Thesis, Norwegian University of Science and Technology, Norway, 1996. ISBN 82-471-0009-6.

[96] M.G. Grønli and M.C Melaaen. Mathematical model for wood pyrolysis - comparison of experimental measurements with model predictions. *Energy & Fuels*, 14:791–800, 2000.

[97] Y.B. Yang, V.N. Sharifi, J. Swithenbank, L. Ma, L.I. Darvell, J.M. Jones, M. Pourkashanian, and A. Williams. Combustion of a Single Particle of Biomass. *Energy & Fuels*, 22:306–316, 2008.

[98] R.S. Miller and J Bellan. A Generalized Biomass Pyrolysis Model Based on Superimposed Cellulose, Hemicellulose and Lignin Kinetics. *Combust. Sci. and Tech.*, 126: 97–137, 1997.

[99] W.S.L. Mok and M.J. Antal Jr. Uncatalyzed Solvolysis of Whole Biomass Hemicellulose by Hot Compressed Liquid Water. *Ind. Eng. Chem. Res.*, 31:1157–1161, 1992.

[100] R. Zanzi, K. Sjöström, and E. Björnbom. Rapid high-temperature pyrolysis of biomass in a free-fall reactor. *Fuel*, 75:545–550, 1996.

[101] E. Biagini, C. Fantozzi, and L. Tognotti. Characterization of devolatilization of secondary fuels in different conditions. *Combust. Sci. and Tech.*, 176:685–703, 2004.

[102] C. Di Blasi. Modeling chemical and physical processes of wood and biomass pyrolysis. *Progress in Energy and Combustion Science*, 34:47–90, 2008.

[103] G. Chen and K. Sjöström Q. Yu. Reactivity of char from pyrolysis of birch wood. *Journal of Analytical and Appied Pyrolysis*, 41:491–499, 1997.

[104] S. Jimenés, P. Remacha, J.C. Ballesteros, A. Gimenéz, and J. Ballester. Kinetics of devolatilization and oxidation of a pulverized biomass in an entrained flow reactor under realistic combustion conditions. *Combustion and Flame*, 152:588–603, 2008.

[105] J.M. Jones, L.I. Darvell, T.G. Bridgeman, M. Pourkashanian, and A. Williams. An investigation of the thermal and catalytic behaviour of potassium in biomass combustion. *Proceedings of the Combustion Institute*, 31:1955–1963, 2007.

[106] D.J. Nowakowski, J.M. Jones, R.M.D. Brydson, and A.B. Ross. Potassium catalysis in the pyrolysis behaviour of short rotation willow coppice. *Fuel*, 86:2389–2402, 2007.

[107] C. Di Blasi. Combustion and gasification rates of lignocellulosic chars. *Progress in Energy and Combustion Science*, 35:121–140, 2009.

[108] P.A. Della Rocca, E.G. Cerrella, P.R. Bonelli, and A.L. Cukierman. Pyrolysis of hardwoods residues: on kinetics and chars characterization. *Biomass and Bioenergy*, 16:79–88, 1999.

[109] E. Cetin, B. Moghtaderi, R. Gupta, and T.F. Wall. Influence of pyrolysis conditions on the structure and gasification reactivity of biomass chars. *Fuel*, 83:2139–2150, 2004.

[110] M. Guerrero, M.P. Ruiz, M.U. Alzueta, R. Bilbao, and A. Millera. Pyrolysis of eucalyptus at different heating rates: studies of char characterization and oxidative reactivity. *J. Anal. Appl. Pyrolysis*, 74:307–314, 2005.

[111] C. Dupont, L. Chen, J. Cances, J. Commandre, A. Cuoci, S. Pierucci, and E. Ranzi. Biomass pyrolysis: Kinetic modelling and experimental validation under high temperature and flash heating rate conditions. *J. Anal. Appl. Pyrolysis*, 85:260–267, 2009.

[112] G. Várhegyi, E. Mészáros, M.J. Antal Jr., J. Bourke, and E. Jakab. Combustion Kinetics of Corncob Charcoal and Partially Demineralized Corncob Charcoal in the Kinetic Regime. *Ind. Eng. Chem. Res.*, 45:4962–4970, 2006.

[113] L.L. Baxter, T.R. Miles, T.R. Miles, B.M. Jenkins, D.C. Dayton, T.A. Milne, R.W. Bryers, and L.L. Oden. *Alkali Deposits Found in Biomass Power Plants, Volume II.* NREL, Subcontract TP-433-8142, 1994.

[114] J. Werkelin, B.-J. Skrifvars, M. Zevenhoven, B. Holmbom, and M. Hupa. Chemical forms of ash-forming elements in woody biomass fuels. *Fuel*, 89:481–493, 2010.

[115] F.J. Frandsen, S.C. van Lith, R. Korbee, P. Yrjas, R. Backman, I. Obernberger, T. Brunner, and M. Jöller. Quantification of the release of inorganic elements from biofuels. *Fuel Processing Technology*, 88:1118–1128, 2007.

[116] R. Korbee and M.K. Cieplik. *Ash formation from biofuels and coal in pf systems.* Proceedings; 'Impacts of Fuel Quality on Power Production' Conference, Snowbird, Utah, October 29 - November 3, 2006.

[117] H.P. Nielsen. *Deposition and High-Temperature Corrosion in Biomass-Fired Boilers.* Ph.D. thesis, CHEC Research Centre, Department of Chemical Engineering, Technical University of Denmark, 1998. ISBN 87-90142-47-0.

[118] P.A. Jensen, F.J. Frandsen, K. Dam-Johansen, and B. Sander. Experimental Investigation of the Transformation and Release to Gas Phase of Potassium and Chlorine during Straw Pyrolysis. *Energy & Fuels*, 14:1280–1285, 2000.

[119] A. Novakovic, S.C van Lith, F.J. Frandsen, P.A. Jensen, and L.B. Holgersen. Release of potassium from the systems k-ca-si and k-ca-p. *Energy & Fuels*, 23:3423–3428, 2009.

[120] M.J. Wornat, R.H. Hurt, K.A. Davis, and N.Y.C. Yang. Single-particle combustion of two biomass chars. *Twenty-Sixth Symposium (International) on Combustion*, 26: 3075–3083, 1996.

[121] J.H. Zeuthen, P.A. Jensen, J.P. Jensen, and H. Livbjerg. Aerosol formation during the combustion of straw with addition of sorbents. *Energy & Fuels*, 21:699–709, 2007.

[122] I. Obernberger. *Aerosols from Fixed Bed Biomass Combustion. Formation, Characterization, and Particulate Emissions.* http://www.acerc.byu.edu/News /Conference/2003/Presentations/Obernberger.pdf, 2003.

[123] B. Skrifvars, T. Laurén, M. Hupa, R. Korbee, and P. Ljung. Ash behavior in a pulverized wood fired boiler - a case study. *Fuel*, 83:1371–1379, 2004.

[124] K. Iisa, Y. Lu, and K. Salmenoja. Sulfation of Potassium Chloride at Combustion Conditions. *Energy & Fuels*, 13:1184–1190, 1999.

[125] P. Glarborg and P. Marshall. Mechanism and modeling of the formation of gaseous alkali sulfates. *Combustion & Flame*, 141:22–39, 2005.

[126] L. Hindiyarti, F. Frandsen, H. Livbjerg, P. Glarborg, and P. Marshall. An exploratory study of alkali sulfate aerosol formation during biomass combustion. *Fuel*, 87:1591–1600, 2008.

[127] M. Steinberg and K. Schofield. The chemistry of sodium with sulfur in flames. *Prog. Energy Combust. Sci.*, 16:311–317, 1990.

[128] B. Li, Z. Sun, Z. Li, M. Aldén, J.G. Jakobsen, S. Hansen, and P. Glarborg. Post-flame gas-phase sulfation of potassium chloride. *Combustion & Flame*, Submitted, 2012.

[129] S. Jiménes and J. Ballester. Formation and Emission of Submicron Particles in Pulverized Olive Residue (Orujillo) Combustion. *Aerosol Science and Technology*, 38: 707–723, 2004.

[130] K.A. Christensen and H. Livbjerg. A Plug Flow Model for Chemical Reactions and Aerosol Nucleation and Growth in an Alkali-Containing Flue Gas. *Aerosol Science and Technology*, 33:470–489, 2000.

[131] R. Hurt and K. Davis. Percolative Fragmentation and Spontaneous Agglomeration. *Combustion and Flame*, 116:662–670, 1999.

[132] O. Charon, A.F. Sarofim, and J.M. Beer. Distribution of mineral matter in pulverized coal. *Prog. Energy Combust. Sci.*, 16:319–326, 1990.

[133] H. Wu, T. Wall, G. Liu, and G. Bryant. Ash Liberation from Included Minerals during Combustion of Pulverized Coal: The Relationship with Char Structure and Burnout. *Energy & Fuels*, 13:1197–1202, 1999.

[134] S.B. Hansen, P.A. Jensen, F.J. Frandsen, H. Wu, M.S. Bashir, Johan Wadenbäck, Bo Sander, and P. Glarborg. Deposit Probe Measurements in Large Biomass-Fired Grate Boilers and Pulverized-Fuel Boilers. *Energy & Fuels*, 28:3539–3555, 2014.

[135] B.-J. Skrifvars, R. Backman, M. Hupa, G. Sfiris, T. Åbyhammar, and A. Lyngfelt. Ash behaviour in a cfb boiler during combustion of coal, peat or wood. *Fuel*, 77: 65–70, 1998.

[136] H. Kassman, M. Broström, M. Berg, and L.-E. Åmand. Measures to reduce chlorine in deposits: Application in a large-scale circulating fluidised bed boiler firing biomass. *Fuel*, 90:1325–1334, 2011.

[137] L.A. Hansen, F.J. Frandsen, K. Dam-Johansen, H.S. Sørensen, and B.-J. Skrifvars. Characterization of Ashes and Deposits from High-Temperature Coal-Straw Co-Firing. *Energy & Fuels*, 13:803–816, 1999.

[138] K.H. Andersen, F.J. Frandsen, P.F.B. Hansen, K. Wieck-Hansen, I. Rasmussen, P. Overgaard, and K. Dam-Johansen. Deposit Formation in a 150 MW_e Utility PF-Boiler during Co-combustion of Coal and Straw. *Energy & Fuels*, 14:765–780, 2000.

[139] B.M. Jenkins, R.B. Williams, P.R. Bakker, S. Blunk, D.E. Yomogida, W. Carlson, J. Duffy, R. Bates, K. Stuci, and V. Tiangco. *Combustion of leached straw for power generation.* 4^{th} Biomass Conference of the Americas, Pergamon, Oxfored, UK, 1999. ISBN 0-08-04-3-0198.

[140] M.S. Bashir, P.A. Jensen, F.J. Frandsen, S. Wedel, K. Dam-Johansen, and J. Wadenbäck. Suspension-Firing of Biomass. Part 2: Boiler Measurements of Ash Deposit Shedding. *Energy & Fuels*, 26:5241–5255, 2012.

[141] Miljøstyrelsen. *Separation og genanvendelse af aske fra biobrændselsanlæg.* Miljøprojekt nr. 962, http://www.mst.dk/Publikationer/, 2004.

[142] B.J. Skrifvars, M. Öhman, A. Nordin, and M. Hupa. Predicting Bed Agglomeration Tendencies for Biomass Fuels Fired in FBC Boilers: A Comparison of Three Different Prediction Methods. *Energy & Fuels*, 13:359–363, 1999.

[143] C. Gilbe, E. Lindström, R. Backman, R. Samuelsson, J. Burvall, and M. Öhman. Predicting slagging tendencies for biomass pellets fired in residential appliances: A comparison of different prediction methods. *Energy & Fuels*, 22:3680–3686, 2008.

[144] B.J. Skrifvars, R. Backman, and M. Hupa. Characterization of the sintering tendency of ten biomass ashes in FBC conditions by a laboratory test and by phase equilibrium calculations. *Fuel Processing Technology*, 56:55–67, 1998.

[145] C.L. Senior. Predicting Removal of Coal Ash Deposits in Convective Heat Exchangers. *Energy & Fuels*, 11:416–420, 1997.

[146] H.R. Rezaei, R.G. Gupta, T.F. Wall, S. Miyamae, and K. Makino. *Modeling the initial structure of ash deposits and structure changes due to sintering.* In: Gupta R.P., Wall T.F., Baxter L.L., editors. Impact of mineral impurities in solid fuel combustion. Plenum Publishers, New York, 1999. ISBN 978-0-306-46126-2.

[147] K.A. Christensen, M. Stenholm, and H. Livbjerg. The formation of submicron aerosol particles, HCl and SO_2 in straw-fired boilers. *J. Aerosol Sci.*, 29:421–444, 1998.

[148] O. Knacke, O. Kubaschewski, and K. Hesselmann. *Thermochemical Properties of Inorganic Substances, 2nd.* Springer-Verlag, 1991. ISBN 0387540148.

[149] P. Rosin and E. Rammler. The Laws Governing the Fineness of Powdered Coal. *The Institute of Fuel*, 7:29–36,, 1933.

[150] W. Weibull. A Statistical Distribution Function of Wide Applicability. *ASME Journal of Applied Mechanics*, September:293–297, 1951.

[151] R.B. Bird, W.E. Stewart, and E.N. Lightfoot. *Transport Phenomena, 2nd ed.* John Wiley & Sons, Inc, 2007. ISBN 0-470-11539-4.

[152] S. Sanitjai and R.J. Goldstein. Forced convection heat transfer from a circular cylinder in crossflow to air and liquids. *International Journal of Heat and Mass Transfer*, 47: 4795–4805, 2004.

[153] L.L. Baxter and D.R. Hardesty. *Task 3: Fate of mineral matter during pulverized coal combustion.* Coal Combustion Science: Quaterly Progress Report. Sandia Report SAND90-8247, 1990.

[154] C. He and G. Ahmadi. Particle Deposition with Thermophoresis in Laminar and Turbulent Duct Flows. *Aerosol science and technology*, 29:525–546, 1998.

[155] J.R Brock. On the theory of thermal forces acting on aerosol particles. *Journal of Colloid Sience*, 17:768–780, 1962.

[156] L. Talbot, R.K. Cheng, R.W. Schefer, and D.R. Willis. Thermophoresis of particles in a heated boundary layer. *Journal of Fluid Mechanics*, 101:737–758, 1980.

[157] C.N. Davies. Definitive equations for the fluid resistance of spheres. *The proceedings of the physical society*, 57:259–270, 1945.

[158] D.E. Rosner and M. Tassopoulos. Deposition Rates from Polydispersed Particle Populations of Arbitrary Spread. *AIChE Journal*, 35:1497–1508, 1989.

[159] R.A. Wessel and J. Righi. Generalized Correlations for Inertial Impaction of Particles on a Circular Cylinder. *Aerosol Science and Technology*, 9:29–60, 1988.

[160] D.E. Rosner and P. Tandon. Pyrolysis of hardwoods residues: on kinetics and chars characterization. *Biomass and Bioenergy*, 16:79–88, 1999.

[161] R. Israel and D.E. Rosner. Use of a Generalized Stokes Number to Determine the Aerodynamic Capture Efficiency of Non-Stokesian Particles from a Compressible Gas Flow. *Aerosol Science and Technology*, 2:45–51, 1983.

[162] M.S. Abd-Elhady, C.C.M. Rindt, J.G. Wijers, and A.A. van Steenhoven. Modelling the impaction of a micron particle with a powdery layer. *Powder Technology*, 168: 111–124, 2006.

[163] A.G. Konstandopoulos. Particle sticking/rebound criteria at oblique impact. *Aerosol Science*, 37:292–305, 2006.

[164] S. Wall, W. John, and H.-C. Wang. Measurements of Kinetic Energy Loss for Particles Impacting Surfaces. *Aerosol Science and Technology*, 12:926–946, 1990.

[165] L.N. Rogers and J. Reed. The adhesion of particles undergoing an elasti-plastic impact with a surface. *J. Phys. D: Appl. Phys*, 17:677–689, 1984.

[166] S. Chen, S. Li, and M. Yang. Sticking/rebound criterion for collisions of small adhesive particles: Effects of impact parameter and particle size. *Powder Technology*, 274:431–440, 2015.

[167] M. Dong, J. Han, S. Li, and H. Pu. A Dynamic Model for the Normal Impact of Fly Ash Particle with a Planar Surface. *Energies*, 6:4288–4307, 2013.

[168] K.L. Johnson, K. Kendall, and A.D. Roberts. Surface Energy and the Contact of Elastic Solids. *Proceedings of the Royal Society of London. Series A, Mathematical and Physical Sciences*, 324:301–313, 1971.

[169] C. Thornton and K.K. Yin. Impact of elastic spheres with and without adhesion. *Powder Technology*, 65:153–166, 1991.

[170] T. Mao, D.C.S. Kuhn, and H. Tran. Spread and Rebound of Liquid Droplets upon Impact on Flat Surfaces. *AIChE Journal*, 43:2169–2179, 1997.

[171] P.E. DesJardin, C. Presser, P.J. Disimile, and J.R. Tucker. A droplet impact model for agent transport in engine nacelles. *NIST Special Publication 984*, 2002.

[172] S. Balakrishnan and R. Nagarajan. Role of Bouncing Potential in Molten Ash Impaction. *Chemical Engineering Communication*, 202:1360–1367, 2015.

[173] S. Schiaffino and A.A. Sonin. Molten droplet deposition and solidification at low Weber numbers. *Phys. Fluids*, 9:3172–3187, 1997.

[174] W. John. Particle-Surface Interactions: Charge Transfer, Energy Loss, Resuspension, and Deagglomeration. *Aerosol Science and Technology*, 23:2–24, 1995.

[175] R.M. Brach and P.F. Dunn. A Mathematical Model of the Impact and Adhesion of Microspheres. *Aerosol Science and Technology*, 16:51–64, 1992.

[176] S. Singh and D. Tafti. Particle deposition model for particulate flows at high temperatures in gas turbine components. *International Journal of Heat and Fluid Flow*, 52: 72–83, 2015.

[177] T.Mao, D.C.S. Kuhn, and H. Tran. Laboratory Study of Carryover Deposition in Kraft Recovery Boilers. *Journal of Pulp and Paper Science*, 23:565–570, 1997.

[178] G. Barnocky and R.H. Davis. Elastohydrodynamic collision and rebound of spheres: Experimental verification. *Physics of Fluids*, 31:1324–1329, 1988.

[179] L.J. Wibberley and T.F. Wall. *Fouling and Slagging Resulting From Impurities in Combustion Gases*. Proceedings of the 1981 Engineering Foundation Conference, July 12-17, New England College, Henniker, New Hampshire, 1981.

[180] L.J. Wibberley and T.F. Wall. Alkali-ash reactions and deposit formation in pulverized-coal-fired boilers: the thermodynamic aspects involving silica, sodium, sulphur and chlorine. *Fuel*, 61:87–92, 1982.

[181] L.J. Wibberley and T.F. Wall. Alkali-ash reactions and deposit formation in pulverized-coal-fired boilers: experimental aspects of sodium silicate formation and the formation of deposits. *Fuel*, 61:93–99, 1982.

[182] P.M. Walsh, A.N. Sayre, D.O. Loehden, L.S. Monroe, J.M. Beér, and A.F. Sarofim. Deposition of bituminous coal ash on an isolated heat exchanger tube: Effects of coal properties on deposit growth. *Prog. Energy Combust. Sci*, 16:327–346, 1990.

[183] G.H. Richards, P.N. Slater, and J.N. Harb. Simulation of Ash Deposit Growth in a Pulverized Coal-Fired Pilot Scale Reactor. *Energy & Fuels*, 7:774–781, 1993.

[184] L.Y. Huang, J.S. Norman, M. Pourkashanian, and A. Williams. Prediction of ash deposition on superheater tubes from pulverized coal combustion. *Fuel*, 75:271–279, 1996.

[185] J.R. Fan, X.D. Zha, P. Sun, and K.F. Cen. Simulation of ash deposit in a pulverized coal-fired boiler. *Fuel*, 80:645–654, 2001.

[186] S. Srinivasachar, J.J. Helble, and A.A Boni. An experimental study of the inertial deposition of ash under coal combustion conditions. *Twenty-Third Symposium (International) on Combustion/The Combustion Institute*, 1990.

[187] G.H. Richards, J.N. Harb, and C.J. Zygarlicke. *The effect of variations in particle-to-particle composition on the formation of ash deposits*. In: Benson S.A., editor. Inorganic transformations and ash deposition during combustion, United Engineering Trustees, Inc., 1992. ISBN 0-7918-0657-X.

[188] D. Borello, P. Venturini, F. Rispoli, and S.G.Z. Rafael. Prediction of multiphase combustion and ash deposition within a biomass furnace. *Applied Energy*, 101:413–422, 2013.

[189] Q. Fang, H. Wang, Y. Wei, L. Lei, X. Duan, and H. Zhou. Numerical simulations of the slagging characteristics in a down-fired, pulverized-coal boiler furnace. *Fuel Processing Technology*, 91:88–96, 2010.

[190] F.J. Frandsen, L. Hansen, H. Sørensen, and K. Hjuler. *Characterization of ashes from biofuels*. Final Report from EFP-95; The Danish Energy Research Programme, Journal no. 1323/95-0007, 1998. ISBN 87-7782-000-2.

[191] R. Backman, M. Hupa, and B.-J. Skrifvars. *Predicting superheater deposit formation in boilers burning biomasses*. In: Gupta R.P., Wall T.F., Baxter L.L., editors. Impact of mineral impurities in solid fuel combustion. Plenum Publishers, New York, 1999. ISBN 978-0-306-46126-2.

[192] W.D. Callister Jr. *Materials Science and Engineering. An Introduction. 6^{th} ed.* John Wiley & Sons, Inc, 2003. ISBN 0-471-22471-5.

[193] E. Raask. *Mineral impurities in coal combustion. Behavior, problems, and remedial measures.* Hemisphere publishing corp., Washington,D.C. ISBN 0-891-16362-x.

[194] E. Raask. Slag-coal interface phenomena. *Journal of Engineering for Power*, January: 40–44, 1966.

[195] H.R. Rezaei, R.G. Gupta, G.W. Bryant, J.T. Hart, G.S. Liu, C.W Bailey, T.F. Wall, S. Miyamae, K. Makino, and Y. Endo. Thermal conductivity of coal ash and slags and models used. *Fuel*, 79:1697–1710, 2000.

[196] A. Zbogar, F. Frandsen, P.A. Jensen, and P. Glarborg. Heat transfer in ash deposits: A modelling tool-box. *Progress in Energy and Combustion Science*, 31, 2005.

[197] S. Vargas, F.J. Frandsen, and K. Dam-Johansen. Rheological properties of high-temperature melts of coal ashes and other silicates. *Progress in Energy and Combustion Science*, 27:237–429, 2001.

[198] K.H. Karlsson and M. Rönnlöf. Property-composition relationships for potentially bioactive glasses. *Glastech. Ber. Glass Sci. Technol.*, 71:141–145, 1998.

[199] T. Lakatos, L.-G. Johansson, and B. Simmingköld. Viscosity temperature relations in the glass system SiO_2-Al_2O_3-Na_2O-K_2O-CaO-MgO in the composition range of technical glasses. *Glass Technology*, 13:88–95, 1972.

[200] T. Lakatos, L.-G. Johansson, and B. Simmingköld. The effect of some glass components on the viscosity of glass. *Glasteknisk Tidsskrift*, 27:25–28, 1972.

[201] C.L. Senior and S. Srinivasachar. Viscosity of Ash Particles in Combustion Systems for Prediction of Particle Sticking. *Energy & Fuels*, 9:277–283, 1995.

[202] S. Takahashi, D.R. Neuville, and H. Takebe. Thermal properties, density and structure of percalcic and peraluminus CaO-Al_2O_3-SiO_2 glasses. *Journal of Non-Crystalline Solids*, 411:5–12, 2015.

[203] K.C. Mills. *Estimation of Physicochemical Properties of Coal Slags and Ashes.* in 'Mineral Matter and Ash in Coal' (Ed. K.S. Vorres), Amer. Chem. Soc. Symposium Series, 301, Washington DC, 1986.

[204] A.L. Robinson, S.G. Buckley, N. Yang, and L.L. Baxter. Experimental Measurements of the Thermal Conductivity of Ash Deposits: Part 2. Effect of Sintering and Deposit Microstructure. *Energy & Fuels*, 15:75–84, 2001.

[205] J. Boow and P.R.C. Goard. Fireside deposits and their effect on heat transfer in a pulverized-fuel-fired boiler: Part III. The influence of the physical characteristics of the deposit on its radiant and effective thermal conductance. *Journal of the institute of fuel*, 42:412–419, 1969.

[206] E. Raask. Sintering characteristics of coal ashes by simultaneous dilatometry-electrical conductance measurements. *Journal of Thermal Analysis*, 16:91–102, 1979.

[207] M. Berg and P. Simonsen. *Biostøvfyring. Slutrapport - Resumé.* Energinet.dk PSO project 6515, 2006.

[208] Hinds. *Aerosol Technology. Properties, Behavior, and Measurement of Airborne Particles, 2nd edition.* John Wiley & Sons, inc., 1999. ISBN 0471194107.

[209] R.I. Crane and R.L. Evans. Inertial deposition of particles in a bent pipe. *J. Aerosol Sci.*, 8:161–170, 1977.

[210] M.D. Morris. Factorial Sampling Plans for Preliminary Computational Experiments. *Technometrics*, 33:161–173, 1991.

[211] G. Sin, A.E. Lantz, and K.V. Gernaey. Good Modeling Practice for PAT Applications: Propagation of Input Uncertainty and Sensitivity Analysis. *Biotechnology progress*, 25: 1043–1053, 2009.

[212] J.W. Nowok, S.A. Benson, M.L. Jones, and D.P. Kalmanovitch. Sintering behaviour and strength development in various coal ashes. *Fuel*, 69:1020–1028, 1990.

[213] S.Mani, L.G. Tabil, and S. Sokhansanj. Grinding performance and physical properties of wheat and barley straws, corn stover and switchgrass. *Biomass and Bioenergy*, 27: 339–352, 2004.

[214] I. Obernberger and G. Thek. *The Pellet Handbook: The Production and Thermal Utilisation of Pellets.* ISBN 9781844076314.

[215] A.J. Stamm. Density of wood substance, adsorption by wood, and permeability of wood. *Journal of Physical Chemistry*, 33:398–414, 1929.

[216] R.J. Kee, F.M. Rupley, J.A. Miller, M.E. Coltrin, J.F. Grcar, E. Meeks, H.K. Moffat, A.E. Lutz, G. Dixon-Lewis, M.D. Smooke, J. Warnatz, G.H. Evans, R.S. Larson, R.E. Mitchell, L.R. Petzold, W.C. Reynolds, M. Caracotsios, W.E. Stewart, P. Glarborg, C. Wang, and Ola Adigun. *Transport: A software package for the evaluation of gas-phase, multicomponent transport properties.* CHEMKIN Collection, Release 3.6, Reaction Design, Inc., San Diego, CA, 2000.

[217] J.H. Zeuthen. *The Formation of Aerosol Particles during Combustion of Biomass and Waste.* Ph.D. thesis, Department of Chemical Engineering, Technical University of Denmark, 2007. ISBN 978-87-91435-54-4.

[218] P. Atkins and J. de Paula. *ATKINS' Physical Chemistry, 7^{th} ed.* Oxford University Press, 2002. ISBN 0-19-879285-9.

[219] D. W. Green and R. H. Perry. *Perry's Chemical Engineers' Handbook (8th Edition).* McGraw-Hill Book Company, 2008. ISBN 9780071422949.

[220] C. R. Wilke. A Viscosity Equation for Gas Mixtures. *The Journal of Chemical Physics*, 18:517–519, 1950.

[221] H. Cheung, L. A. Bromley, and C. R. Wilke. Thermal Conductivity of Gas Mixtures. *A.I.Ch.E. Journal*, 8:221–228, 1962.

Appendix A

Article

energy&fuels

Review

pubs.acs.org/EF

Deposit Probe Measurements in Large Biomass-Fired Grate Boilers and Pulverized-Fuel Boilers

Stine Broholm Hansen,[†] Peter Arendt Jensen,*[†] Flemming Jappe Frandsen,[†] Hao Wu,[†] Muhammad Shafique Bashir,[†] Johan Wadenbäck,[‡] Bo Sander,[§] and Peter Glarborg[†]

[†]Department of Chemical and Biochemical Engineering, Technical University of Denmark Building 229, DK-2800 Lyngby, Denmark

[‡]Vattenfall A/S, Amagerværket, Kraftværksvej 37, DK-2300 Copenhagen S, Denmark

[§]DONG Energy Thermal Power, Kraftværksvej 53, DK-7000 Fredericia, Denmark

Supporting Information

ABSTRACT: A number of full-scale deposit probe measuring campaigns conducted in grate-fired and suspension-fired boilers, fired with biomass, have been reviewed and compared. The influence of operational parameters on the chemistry of ash and deposits, on deposit build-up rates, and on shedding behavior has been examined. The firing technology and the fuel utilized influence the fly ash and deposit chemical composition. In grate-firing, K, Cl, and S are enriched in the fly ash compared to the fuel ash, while the fly ash in suspension-firing is relatively similar to the fuel ash. The chemical composition of the deposits formed is determined by the fly ash composition and the flue gas temperature; increases in the local flue gas temperature lead to higher contents of Si and Ca and lower contents of Cl in the deposits. The net deposit build-up rates in grate-fired and suspension-fired boilers are at similar levels, 0−100 g/m^2·h, while the ash deposit propensity is an order of magnitude larger in grate fired boilers than in suspension-fired boilers. Deposit build-up rates were found to increase at flue gas temperatures close to the melting temperatures of the fly ash. Furthermore, the rate of deposit build-up increased with the K-content of the fuel ash and fly ash for grate-fired boilers. For suspension-fired boilers, deposition rates are comparatively low for wood-firing and increase with increasing fuel straw shares. Shedding of deposits occurs by melting during straw-firing on a grate at high flue gas temperatures (>900 °C). At lower flue gas temperatures, the deposits can be removed by soot blowing. The required soot blower impact pressure is strongly influenced by the surface temperature, such that a high surface temperature makes the deposit more difficult to remove. During straw/wood-firing in suspension-fired boilers, shedding occurred by debonding with incomplete removal at flue gas temperatures of 600−1000 °C and by debonding with complete removal during wood-firing in suspension-fired boilers at high flue gas temperatures (1300 °C). Shedding events were not observed during wood suspension-firing at low flue gas temperatures (<900 °C). Here, a steady-state mass of deposits on the probe was observed. Increased exposure times and probe temperatures lead to deposits that are difficult to remove. This was observed for grate-firing of straw and for straw/wood firing in suspension-fired boilers.

1. INTRODUCTION

In order to reduce CO_2 emissions and the dependency on fossil fuels, Danish and international energy policy has increasingly supported the use of biomass for power production during the last 20 years. Bituminous coal ash is often dominated by Si and Al, which form compounds with relatively high melting temperatures during combustion. Ash from biomass, such as straw and wood, has a high content of K as compared to coal ash. K-rich ash often has a low melting temperature and thereby forms particles that may stick to heat transfer surfaces.[1] Utilization of biomass for power production thereby increases the rate of formation of deposits that are difficult to remove, especially in the boiler chamber and on superheater coil surfaces, compared to those formed during coal-firing.[1]

The deposit behavior occurring in utility boilers is controlled by a number of consecutive steps: (i) release of critical elements (K, Na, Cl, S, etc.) from the fuel, (ii) formation of gaseous species, aerosols, and ash particles (collectively denoted as fly ash), (iii) transport and adhesion of fly ash (including gaseous species) to heat transfer surfaces, (iv) deposit build-up and consolidation, and finally, (v) shedding of deposits.[2]

The release of critical elements and formation of fly ash have been studied extensively for grate-firing conditions and is quite well understood.[3−7] In suspension-firing and fluid bed combustion (FBC), the conditions in the combustion zones differ markedly from those in the combustion zone of grate-fired boilers. This leads to altered conditions for the ash formation, and experience from grate-firing cannot always be applied to suspension-firing or fluid bed combustion. Only a few studies on the ash transformation processes have been conducted at lab scale[8,9] and pilot scale[10] for conditions resembling suspension firing. For fluid bed combustion conditions, more research on the release of ash-forming elements and ash formation processes is also desirable.[11,12]

Deposits are formed in biomass-fired boilers by at least three different mechanisms, which apply to different parts of the fly ash.[13] Inertial impaction apply to large fly ash particles (>10 μm). The impact velocity and angle, along with the stickiness of

Received: February 26, 2014
Revised: May 12, 2014
Published: May 13, 2014

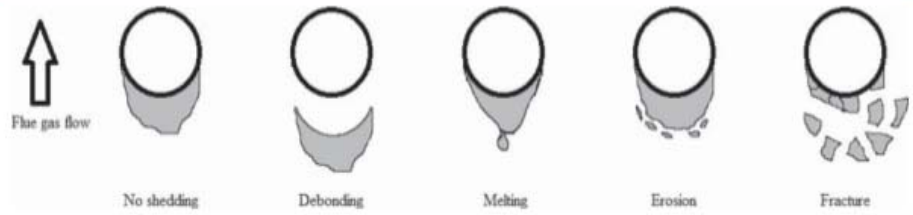

Figure 1. Illustration of shedding mechanisms.

the ash particles, determines if the particles are deposited on the heat transfer surface upon impaction.[13,14] Thermophoresis, where a temperature gradient is the driving force for the transport of the particles toward the cold heat transfer surface, applies to aerosol particles (<1 μm). Condensation on heat transfer surfaces applies to gas phase species such as KCl and K_2SO_4. In this case, a concentration gradient is the driving force for the transport.[13] The characteristics of the formed fly ash thereby influence the deposit formation rate and deposit characteristics. Various work has been conducted with the aim of describing how fuel choice and possibly use of additives influence deposition rates in laboratory or pilot scale experiments, mainly resembling suspension-firing.[10,15−21]

The amount of deposits present on boiler surfaces is influenced both by deposit formation and deposit removal processes. Shedding of deposits depends on deposit characteristics and may be caused by natural boiler events, such as tube fluctuations, or artificially by, for example, soot blowing in the boiler chamber. Various types of shedding mechanisms have been observed.[22] In Figure 1, different shedding mechanisms are shown, and in Table 1, the shedding mechanisms are summarized with respect to deposit type and place of occurrence within the deposit.

Table 1. Deposit Removal Mechanisms along with Indication of Type of Deposit and Place at Which the Shedding Occurs[22]

	place of shedding		
	tube-deposit interface	within deposit	surface removal
debonding	X		
melting			X
erosion			X
fracture		X	
thermal tensions	X	X	
mechanical tensions	X	X	

Erosion, debonding, melting, and, to some extent, thermally induced tensions can be termed natural shedding mechanisms, while artificial shedding induced by soot blowing can cause deposit fracture and debonding. Soot blowers operate by injecting jets of steam, water, or high-pressure air into the boiler, thereby inducing thermal and mechanical stresses. Besides the efficiency of the soot blower, often measured by the peak impact pressure (PIP), shedding is influenced by the strength development of the deposits. The strength can mainly be achieved by either solidification of molten or partially molten material or by sintering (fusion) of solid particles.[22] These processes depend on local temperatures, time, and the physical and chemical structure of the deposits. The strength development and shedding of deposits have been examined to some extent for deposits formed during coal-firing and for kraft recovery boilers. Only limited studies have been conducted in biomass-fired boilers.[22]

To investigate biomass ash deposit formation and removal in power plant boilers, probe measuring campaigns have been conducted in straw-fired grate boilers,[23−30] in FBC plants,[31,32] in suspension boilers cofiring coal and biomass[33−35] and, lately, also in dedicated biomass-fired (wood and/or straw) suspension boilers.[36−42] The measuring campaigns with focus on deposit formation and shedding have primarily been conducted in Danish boilers. To our knowledge, only a few full-scale deposit probe measuring campaigns conducted with biomass as fuel in other countries have been described in publications.[31,43,44]

The aim of this study is to provide knowledge on ash deposit behavior in biomass-fired power plant boilers from a review of reported full scale biomass boiler deposit investigations. The campaigns conducted in grate-fired and suspension-fired units with dedicated biomass-firing (straw and/or wood) are included.[23−30,36−42] The focus of the study is to gain knowledge on the ash transformation, deposition rates, and shedding behavior occurring in the two boiler types. A further objective is to summarize the influence of operational parameters on deposit chemistry, deposit formation rates, and shedding by comparing results from campaigns with a relatively broad range of flue gas temperatures and fuel compositions for each firing technology. When relevant, the experiences from lab-scale or pilot-scale experiments are included for the purpose of comparison.

2. FULL-SCALE MEASUREMENTS REVIEWED

The measurements reviewed in this study have been conducted at several combined heat and power (CHP) plants, both grate-fired boilers (including a so-called cigar-fired boiler) and

Table 2. Selected Operational Characteristics of Three Boiler Types Firing Biomass

boiler type	fuel size	res. time combustion	fly ash	bottom ash	ref.
grate	whole straws	minutes	<20%	>80%	47 and 45
cigar	bale of straw	minutes	≈30%	≈70%	23
suspension	<2 mm	few seconds	≈75−80%	≈20−25%	DONG Energy[a]

[a]Measured by plant owners during 10-day experimental campaign with wood-firing.

dx.doi.org/10.1021/ef500442z | Energy Fuels 2014, 28, 3539−3555

Table 3. Power Plants Mentioned in This Study; Boiler Data and Year/Reference of the Measuring Campaigns[a]

power plant	firing system	fuel	thermal input [MW_{th}]	steam T/P [°C]/[bar]	commercial operation	campaign year	ref.
Haslev	cigar fired	straw	23	450/67	1989	1997	23 and 24
Slagelse	grate	straw	31	450/67	1990	1997	23 and 24
Rudkøbing	grate	straw	10.7	450/60	1990	1998	25
Masnedø	grate	straw	33	522/92	1996	2000/2004	26 and 27
Ensted	grate	straw	100	470/200	1998	2004/2006	27 and 28
Avedøre 2	grate	straw	100	545/310	2001	2004/2006	29,28, and 30
Avedøre 2	suspension	wood	800	560/300	2001	2008/2011	36−38
Amager 1	suspension	straw/wood	350	540/185	1971/2008	2011	41
Amager 2	suspension	straw/wood	250	480/110	1972/2003	2007/2011	39 and 40
Jordbro	suspension	wood	80		1968	2004	43

[a]Some plant data not mentioned in the campaign documentations were found in other references.[54]

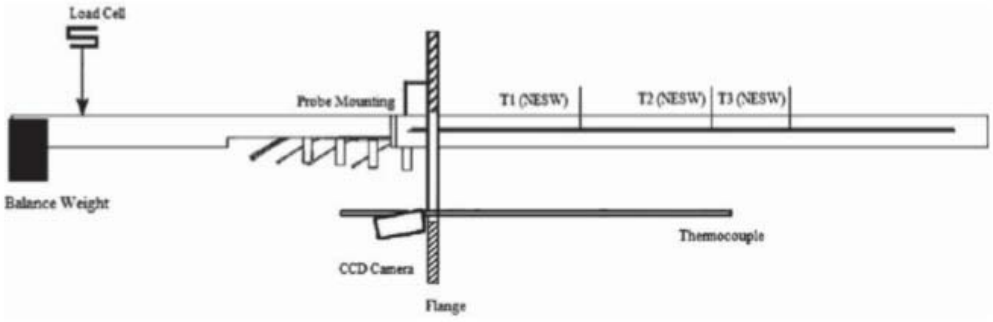

Figure 2. Illustration of the advanced deposit probe.[40]

suspension-fired boilers. The primary difference among these boiler types is found in the combustion zone; in grate boilers, the fuel is fed to a grate on which the combustion takes place by leading primary air through the grate.[45] In a cigar boiler, whole straw bales are introduced to the furnace and burn along the surface of the bale, where primary air is introduced by several jets.[23] In suspension-firing, the fuel is milled in order to obtain small particle sizes before being blown into the furnace together with primary air.[45] Some operational differences are highlighted in Table 2.

An important difference seen in Table 2 is the distribution of the fuel ash into fly ash and bottom ash fractions, which is important for the fly ash characteristics and thereby for deposit formation. The difference is relatively small for grate-fired boilers and cigar boilers, while a great difference is observed between these boiler types and the suspension-fired boilers. For this reason, for the purpose of comparison in this study cigar boilers are treated as grate-fired units.

Measuring campaigns with deposit probe measurements have been conducted at several power plant boilers. Table 3 gives an overview of the plants mentioned in this study. The table lists the main boiler data and the year and reference of the measuring campaigns conducted. It should be noted that Avedøre Unit 2 comprises two boilers, a straw-fired grate boiler and a wood/oil/gas-fired suspension-boiler, which feed steam to a joint steam turbine.

The deposit measurements obtained in the full-scale boilers were made by introducing a deposition probe into the furnace chamber or the superheater area of the boiler. For grate-fired boilers, the investigations included both analyses of deposits collected on probes with short exposure times and also a few mature deposits collected from superheater tubes.[26,27] The latter deposits may have exposure times up to a year.[26] The data set includes quantification of the rate of deposit formation,[23,28−30] chemical analyses of fuels, ash, and deposits,[23,25−29] and, in a few cases, corrosion studies[25] and shedding observations.[29,30] In suspension-fired units, only probe deposits have been examined, until now. The focus of these examinations has been on the rate of deposit formation,[36−41,43] fuel chemistry, ash and deposits,[36−38,40,41,43] and shedding observations.[37,38,41]

Both relatively simple probes as well as more advanced probes for in situ deposit measurements and soot blowing have been applied in the measuring campaigns. In the early experiments, mainly simple water and air cooled deposit probes were used. The probe is made of stainless steel with thermocouples placed along the probe surface. The probe temperature is controlled for a given set-point by adjusting the air flow rate inside the probe. The deposit mass is determined by extracting the probe after each experiment and subsequently removing the deposits for weighing and analysis.[23,26]

In later studies, an advanced in situ shedding probe (Figure 2) was utilized. The probe is equipped with a load cell, and online quantification of mass and heat uptake is possible. The flue gas temperature was measured by a thermocouple, and the deposit formation and shedding were observed using a video camera. Often, the thermocouple temperature measurements were supported by suction pyrometer measurements.[29,37,41,42]

In a few experiments[29,46] a soot blower probe was used along with the in situ deposition probe in order to provide information about the removability of the deposits formed. The soot blowing probe was equipped with a nozzle for blowing high-pressure air onto the deposit probe surface. By adjusting the air pressure through the nozzle and the distance between the soot blowing probe and the deposits, the jet peak

dx.doi.org/10.1021/ef500442z | Energy Fuels 2014, 28, 3539−3555

impact pressure (PIP) needed for removal of deposits could be determined.[29,46]

3. RESULTS AND DISCUSSION

This section discusses and reviews the results of the reported full-scale measuring campaigns. The focus is on the chemistry of the deposits formed, the rate of deposit formation, the observations made on shedding events along with an evaluation of the measuring techniques used to quantify rates of deposition. When examining the full-scale experimental results, it should be kept in mind that full-scale boilers are not very well-controlled with respect to operational parameters. Large variations in fuel composition, flue gas flow, temperatures, etc., may occur within a relatively short period of time. Thus, only major factors influencing operational parameter changes may be observed. However, by comparing the results from several different measuring campaigns, it is possible to provide relatively solid conclusions.

3.1. Chemistry of Ash and Deposits. This section reviews the influence of fuel type and boiler operation parameters on fly ash and deposit chemistry. The chemical examinations in this study mainly focus on the five major ash forming elements in biomass combustion: Si, Ca, K, Cl, and S.

3.1.1. Fly Ash Chemistry. The firing technology strongly influences the fly ash formation process. As mentioned earlier, there is a large difference in the ash split occurring in grate-fired and suspension-fired boilers.[45,47] This may influence the distribution of elements among bottom and fly ash fractions.

In Figure 3, fuel ash and fly ash compositions are compared for each of the two firing technologies, grate-firing (including cigar-firing) and suspension-firing, to gain an idea on how the ash split occurs in the furnace chambers.

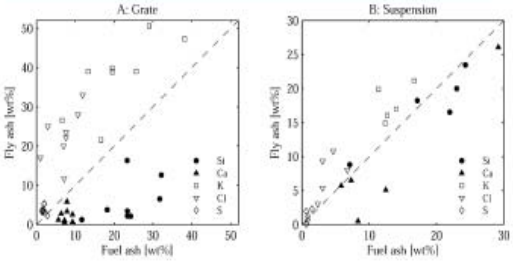

Figure 3. Fly ash composition vs fuel ash composition. Elemental content is calculated as wt % dry ash based on data available in references. Points on or near the diagonal line indicate similar fuel ash and fly ash compositions. (A) Grate and cigar; straw as fuel.[23,24,29] (B) Suspension; straw and/or wood as fuel.[40,41,43]

It is seen in Figure 3 that for grate-firing, the fly ash composition is quite different from the fuel ash composition, as almost no points are placed near the diagonal line, which would indicate similar composition of the fuel ash and fly ash. The fly ash from grate-firing of straw is rich in K, Cl, and S and depleted of Si and Ca compared to the fuel ash.

In suspension-firing, the fly ash resembles to a large extent the fuel ash, as seen by the distribution of points relatively close to the diagonal line in Figure 3B. Only a slight enrichment of K, Cl, and S is found in this combustion system. The fly ash formation process is different in the two combustion systems. As K, Cl, and S are volatile elements in the fuel, these are partly released to the gas phase in the combustion zone, while Ca and Si are retained in the solid fuel (or ash) particles.[1] In grate-firing most of the solid ash particles remain at the bottom of the furnace. Ca and Si are thus only found in the fly ash to a limited extent. This is in contrast to suspension-firing where a large fraction of the ash particles is entrained, which leads to the quite similar composition of the fuel ash and the fly ash. This will for straw-firing in suspension boilers lead to fly ash dominated by Si and K, and with a high content of Ca and Cl,[40,41] while wood-firing in suspension boilers leads to fly ash dominated by Ca and Si and with a high content of K.[37,43] Examples of fly ash compositions from various combustion conditions, featuring these characteristics, are seen in Table 4.

Table 4. Examples of Chemical Composition of Fly Ash Formed under Various Combustion Conditions[a]

boiler type	Si	Ca	K	Cl	S	ref.
grate, straw[b]	5.64	1.95	40.89	23.75	3.48	23
suspension, straw	20.00	6.49	17.00	8.00	2.30	40
suspension, wood	17.70	20.80	6.26	0.20	1.08	37 and 38

[a]Composition given as wt % of dry ash. [b]Mean composition of four experiments.

3.1.2. Deposit Chemistry. Biomass deposits are formed by fly ash appearing as particles, aerosols and gaseous species (mainly KCl and K_2SO_4). The deposit chemistry and characteristics are thereby influenced by the characteristics of fly ash and the ability of the fly ash to impact and stick to heat transfer surfaces at the prevailing local conditions. Generally, the structure of deposits formed in biomass boilers is characterized by a salt-rich inner layer, typically rich in KCl and/or K_2SO_4, and outer layer(s) containing Si and Ca along with salt components.[26,27,40]

In this study, three parameters, which may influence deposit chemistry, are considered for each firing technology and fuel choice; exposure time, probe temperature, and flue gas temperature.

The influence of exposure time and probe temperature (400−550 °C) on deposit chemistry and morphology (thickness and porosity of layers) has been examined by Hansen et al.,[26] Jensen et al.,[29] and Michelsen et al.[25] The results indicate that both exposure time and probe temperature mainly influence the morphology of the deposits, whereas the bulk chemical composition of the deposits remain relatively unaltered. Based on these results, it seems reasonable to assume that variations in probe exposure time and probe temperature (within 400−550 °C) can be excluded as important parameters in the analysis when examining the influence of flue gas temperature on deposit bulk chemistry.

The influence of flue gas temperature on deposit chemistry has been examined in a few measuring campaigns.[23,27,37] In the campaign conducted in the straw fired cigar and grate boilers in Haslev and Slagelse,[23,24] corresponding samples of fuel, fly ash, and deposits were examined in order to obtain knowledge about the ash transformation occurring within the boilers. During the measuring campaign, probes were inserted at two positions in the boilers to observe differences in deposit chemistry and rate of formation with variations in the local flue gas temperature.

In Figure 4, the fly ash composition is compared to the bulk compositions of the deposits formed in the furnace chamber at

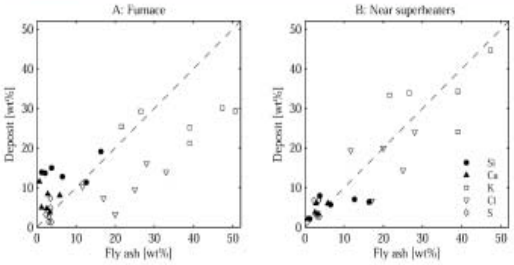

Figure 4. Deposit probe compositions vs fly ash compositions in straw-fired grate boilers. Deposits are obtained on 510 °C probes with 8-h exposure time. (A) In the furnaces (flue gas 850 °C). (B) Near the superheaters (flue gas 650 °C). Data from Haslev and Slagelse.[23,24] The symbol legends shown in part B are common for the two composition plots.

mean flue gas temperatures of around 850 °C (Figure 4A) and to the deposits collected near the superheaters at mean flue gas temperatures near 650 °C (Figure 4B).

It is seen that in the furnaces (850 °C), the deposits contain more Ca and Si and less K and Cl compared to the fly ash. At the probes near the superheaters, where the flue gas temperature is 650 °C, the points are placed around the diagonal line and the deposit chemical composition is thus close to that of the fly ash. This seems to suggest a shift in the deposition behavior with flue gas temperature for grate-firing, and the deposit chemical composition is influenced by local flue gas temperatures.

In order to expand the analysis of the influence of flue gas temperature on deposit chemical composition, an enrichment factor for each element has been calculated as follows.

$$\text{enrichment factor} = \frac{\text{wt \% in deposit}}{\text{wt \% in fuel ash}}$$

The enrichment factor is influenced by both the fly ash formation process and the deposit formation process. The deposit compositions used in the calculations are compositions of the bulk deposits or of separate layers, depending on availability. The enrichment factors of the five main ash forming elements are seen as a function of local flue gas temperatures for grate-firing of straw in Figure 5A and for suspension-firing of straw or wood in Figure 5B. The data generally fluctuate although some general trends can be identified.

For grate-fired systems (Figure 5A, left column), it is seen that, for Si and Ca, the enrichment ratio is low at the low temperatures and approaches an enrichment factor around 1 at higher temperatures, except for the downstream deposits. The enrichment factors for K seem relatively steady, though with a slight decrease with increasing flue gas temperatures. For Cl, the enrichment factor is high (≈4) at low temperatures and then decreases with increasing flue gas temperatures. It is seen that deposits formed at high flue gas temperatures can be expected to be depleted of Cl. For S, behavior similar to that of Cl is observed, though with a much larger scattering of the data. For K, Cl, and S, a point (marked with *) with high enrichment factor is seen where the flue gas temperature is around 900 °C. This point originates from naturally washed straw (rainfall in the field before baling[23]), where the fuel ash was low in these elements before combustion.

From the enrichment factors observed for grate-firing, it is found that at low flue gas temperatures deposits are rich in K,

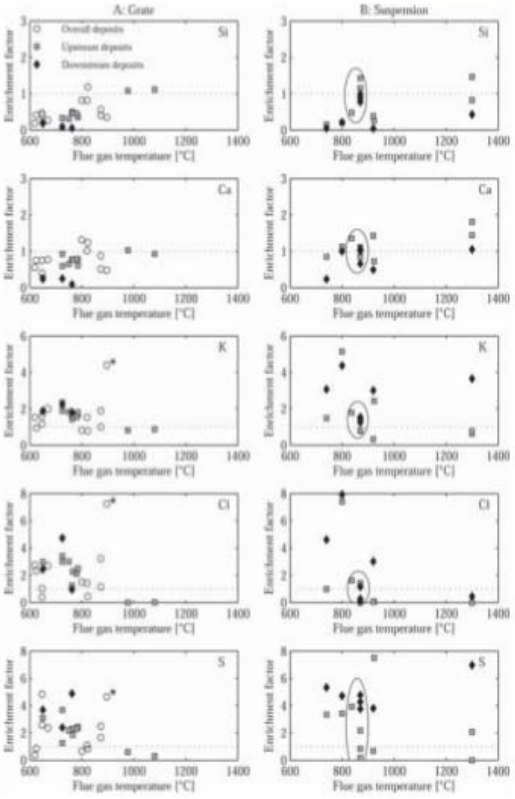

Figure 5. Enrichment factors for the five main ash forming elements as a function of flue gas temperature. (A, left figures) Data from straw-fired grate boilers.[23,24,28,29] (B, right figures) Data from suspension-fired boilers. The points marked with a circle are from straw/wood (>45 wt % straw) or straw firing.[40,41] The remaining suspension data are from wood firing.[36−38,43] The data points for K, S, and Cl marked with an asterisk (*) originate from a naturally washed straw.

Cl, and S, while at higher temperatures, Si and Ca are present in the deposits to a higher degree. The influence of temperature on the deposit chemistry can be explained by the deposit mechanisms involved in deposit build-up. The increase of the enrichment factors for Ca and Si with increasing flue gas temperatures can be explained by increased deposit formation by inertial impaction with increasing temperatures. This increase is caused by a higher melt fraction of the coarse fly ash particles containing Si and Ca and of the deposit surface at high flue gas temperatures. When the melt fractions increase, the particles are more prone to stick on the probe surface upon impaction. The decrease in the K, Cl, and S enrichment factors with increasing flue gas temperature can be explained by reduced condensation at high temperatures and by the dilution effects of the increased content of Ca and Si.

The enrichment factors calculated for suspension firing are seen in Figure 5B (right column). Both pure wood and straw/wood mixtures (where cofiring ash in many cases is dominated by straw ash) have been utilized as fuels in suspension-fired boilers. The data from measurements with straw or straw/wood mixtures as fuel are marked with circles in Figure 5B. Data with this fuel mixture are only obtained at flue gas temperatures around 850 °C and no influence of flue gas temperature on

dx.doi.org/10.1021/ef500442z | Energy Fuels 2014, 28, 3539−3555

Table 5. Examples of Chemical Composition of Deposits Formed under Various Combustion Conditions[a]

boiler type, fuel	T_{fg} (°C)	Si	Ca	K	Cl	S	ref.
grate, straw[b]	650	4.94	3.06	37.59	13.64	5.44	23
grate, straw[b]	873	12.88	6.25	28.42	8.44	4.01	23
grate, straw	1080	29.00	6.70	14.00	0.21	0.57	28
suspension, straw/wood[c]	870	21.54	8.51	16.30	1.81	2.12	40
suspension, wood	800	3.44	15.08	24.75	3.19	3.09	37
	1300	24.90	25.30	3.04	0.09	0.07	37

[a]Composition given as wt % of dry deposit. [b]Data are the mean composition of 3 or 4 experiments. [c]Min. 45 wt % straw. Mean composition of all layers.

enrichment factors can be observed. For the measurements with wood as fuel, the enrichment factors for Si and Ca increase with flue gas temperatures, while enrichment factors for Cl decrease. For S and K, the data are scattered, and no influence of flue gas temperature can be observed. The physical effects, believed to apply to ash in grate-fired boilers are expected to apply also to ash in suspension-fired boilers. The data from wood-firing seem to support this.

It is thus seen that the local flue gas temperature influences the chemical composition of the deposits formed. To gain an overview of the implications of these influences, examples of chemical compositions of deposits are shown in Table 5. This allows clearer observations of differences in deposit compositions among different firing technologies, fuels, and local flue gas temperatures.

Table 5 lists the composition of three deposits obtained during grate firing of straw at various flue gas temperatures. It is seen that the low temperature deposit is rich in K, Cl, and S. As the local flue gas temperature increases, the content of these three elements decreases, whereas the content of Si and Ca increases, as expected. The high temperature deposits obtained during grate-firing of straw are thus dominated by Si, K, and Ca.

For suspension firing with straw in the fuel, deposits have only been collected at mean flue gas temperatures near 800–900 °C, see Table 5. This deposit composition can be compared to the composition of the deposits obtained during grate firing of straw at similar flue gas temperatures (870 °C). It is seen that a shift in technology influences the deposit chemistry as the deposits from suspension firing have high contents of Si and Ca and a very low content of Cl and S as compared to the deposits from grate-firing. Thus, it is seen that differences in fly ash composition observed between grate and suspension-firing are also observed in the deposit composition. The deposits in a suspension boiler have a higher content of Si and Ca, as compared to those in a grate boiler.

For suspension-firing of wood, it is seen that at the low flue gas temperature, 800 °C, the deposits are dominated by K and Ca. Increasing the temperature to 1300 °C leads to deposits which are dominated by Si and Ca, with a very low content of K, Cl, and S. A similar shift from deposits dominated by Ca and K at low temperatures toward deposits dominated by Ca and Si at higher temperatures was also observed by Skrifvars et al.[43] by collection of deposits at mean flue gas temperatures of 740 and 920 °C in a wood-fired suspension boiler.

3.2. Rates of Deposit Build-up. In the section below, the rates of deposit build-up measured in the full-scale boilers will be presented and influence of operational parameters on the rates will be examined. In some measuring campaigns, a simple probe was applied. From these campaigns, only a single quantification of the deposit mass on the probe, determined at the end of the measurement (after 4–24 h), is available for each experiment. In other campaigns, an advanced probe was applied. From these campaigns, detailed information about the mass on the probe as a function of residence time is available. Thereby occurrence of shedding events can be identified from the mass changes measured. Due to these differences, the applied measuring techniques will be evaluated before examining the influence of operational parameters on build-up rates.

3.2.1. Discussion of Applied Measuring Technique. Two definitions of the deposit build-up rate [g/m²·h] are applied: (i) the Integrated Deposit Formation rate (IDF rate) and (ii) the Derivative-based Deposit Formation rate (DDF rate), as defined by Bashir et al.[41,42] The IDF rate is determined by using the deposit mass obtained at a defined time divided by the probe surface area and the exposure time. The DDF rate is determined by calculating the time derivative of the deposit mass uptake [g/h] between two shedding events and divided by the probe surface area. Using this method, only small shedding events that cannot be separated from the measuring noise are included in the measured DDF rate.[41,42] Figure 6 shows the IDF and DDF rates for a firing case with frequent shedding events.

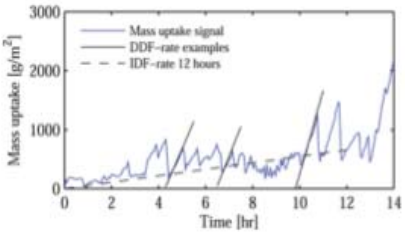

Figure 6. Original signal from combustion of straw/wood (flue gas 800 °C) and examples of integrated deposit formation (IDF) and derivative-based deposit formation (DDF) rates.

As seen from the slopes of the lines in Figure 6, the DDF rate obtains much higher values (900–1400 g/m²·h) than the IDF rate (55 g/m²·h), for this firing case. When shedding occurs within the exposure time chosen for determination of the IDF rate, the IDF rate will always obtain a value between 0 and the DDF rate. The IDF rate may be seen as a somewhat uncertain value, as it is greatly influenced by the choice of residence time and occurrence of shedding events within that time. However, the IDF rate still represents valuable information, as it is an estimate of the amount of deposit accumulated on the probe. The DDF rate may be regarded as the "true" deposit build-up rate. However, additional information on the occurrence of shedding is needed for the DDF rate to be of value in relation to boiler operation.

Figure 6 shows a firing case with occurrence of shedding events, and therefore, a relatively large difference in DDF and IDF rates was shown. In cases with no or limited shedding, the IDF rate and the DDF rate will be similar. From the data obtained with the advanced probe, both DDF and IDF rates can be obtained and it is, to some extent, possible to identify whether shedding events influence the IDF rate. This information is not available for data obtained with the simple probe where only the IDF rate can be obtained. In the following, it will be evaluated whether IDF rates obtained by simple probes can be assumed to be approximately equal to the DDF rate (no/limited shedding occurring), or whether a value between 0 and the DDF rate will be obtained (shedding occurring). This is done by examining the weight uptake signal from some of the advanced probe measurements obtained from campaigns with comparable conditions: similar fuel, firing technology, and flue gas temperature.

The simple probe has mainly been used in the early campaigns in straw-fired grate boilers.[23,28] The probes used for IDF rate determinations have mainly been removed after a boiler residence time of 4–12 h.

Two representative examples of signals from the advanced probe used in straw-fired grate boilers are shown in Figure 7. It

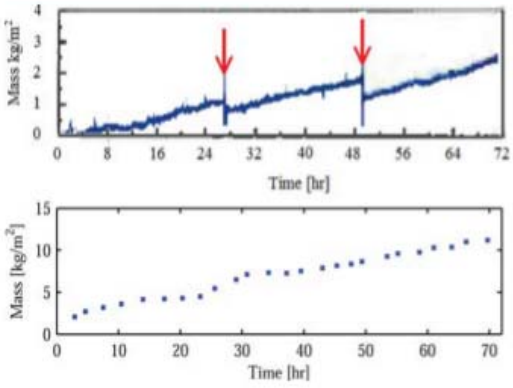

Figure 7. Mass uptake on the advanced probe (probe surface temperature 500 °C) in two cases of straw firing in the Avedøre grate-fired boiler. (Top) Mean flue gas temperature: 785 °C.[29] (Bottom) Mean flue gas temperature: 1000 °C.[30] The red arrows indicate times where operation of plant soot blowers away from the probe may influence local conditions.

is seen that the deposit build-up is quite steady in both cases. For the flue gas temperature of 785 °C, it is seen that the steady build-up is only interrupted when plant soot blowing is activated. Although a steady build-up is observed at both 785 and 1000 °C, the deposit mass may still be influenced by shedding. It was found by Zbogar et al.[30] that when the local flue gas temperature approaches 1000 °C in a straw fired grate boiler, melting and droplet formation occur at the deposit surface and shedding by melting is observed. Melting is considered to occur as a continuous mass loss process, contrary to debonding, where significant mass loss occurs instantaneously. Melting may thus influence the quantification of the rate of deposit build-up, although it may not be possible to identify from the mass signal from the advanced probe. At local flue gas temperatures below ≈900 °C, the camera observation of the deposit surface revealed that it was composed of solid particles, and shedding by melting was not observed.[30]

Consequently, it seems that the IDF rates obtained by the simple probe during grate-firing of straw can be assumed to be approximately equal to the DDF rate when the local flue gas temperature does not exceed 900 °C. Plant soot blowing was not activated during the experiment. At flue gas temperatures above 900 °C, shedding by melting may remove deposits and the measured IDF rate will in that case have a value lower than the DDF rate. This should be considered when analyzing data obtained at flue gas temperatures above 900 °C during straw-firing in grate boilers.

In the measuring campaigns conducted in suspension-fired boilers, three measuring campaigns[36,39,43] quantified deposition rates by use of a simple probe. The advanced probe has been applied for the majority of the data obtained in recent campaigns.[37,40,41] Detailed information regarding the deposit mass on the probe is thus available.

For a case of straw/wood-firing with >80 wt % straw and flue gas temperatures near 800 °C, the mass uptake signal is seen in Figure 6. For this firing case the IDF rate was significantly lower than the DDF rate and should be regarded as an estimate of the accumulated deposit, as already discussed. For wood-firing at similar flue gas temperatures (800 °C), the mass uptake signal is seen in Figure 8. It is seen that the amount of deposit on the

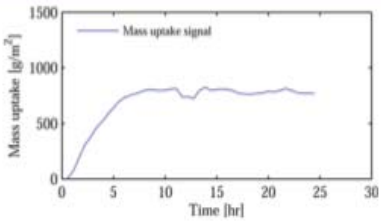

Figure 8. Deposit mass uptake on the advanced probe during wood-firing in suspension with a local flue gas temperature of 800 °C and a probe temperature of 530 °C.[37,38]

probe is steady after some initial build-up.[37] This shows that the determination of an IDF rate largely depends on the choice of exposure time. If deposits are collected in a short exposure time (e.g., 5 h), an IDF rate close to the initial DDF rate is obtained. This IDF rate will not be representative for the long-term deposit buildup behavior, however. Again, the determined IDF rate as obtained with the simple probe is therefore a somewhat uncertain value.

A quite different deposit behavior is observed for wood-firing at high flue gas temperatures (1300 °C). Here, buildup of deposits is followed by nearly complete shedding.[37,38] This cycle is observed repeatedly. In this case, it makes no sense to calculate an IDF rate based on a single point.

It is concluded that IDF rates obtained during suspension-firing of straw and/or wood at intermediate temperatures can be reasonably used as estimates of the accumulated deposit. IDF rates should not be applied when repeated, complete shedding occurs as observed in wood suspension-firing at flue gas temperatures >1200 °C.

3.2.2. Deposition Rates in Grate and Suspension Boilers. In this section, the deposit build-up rates observed in grate- and suspension-firing will be compared. The focus will be on the magnitude of the IDF rates measured. Influence of operational

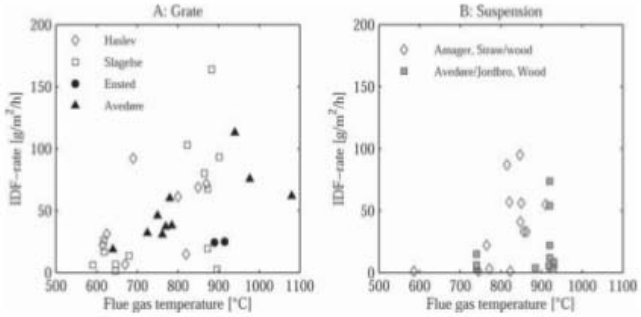

Figure 9. IDF rates as a function of local flue gas temperature. (A) Grate-fired units, all straw-fired.[23,28,29] (B) Suspension fired units.[36,40−43]

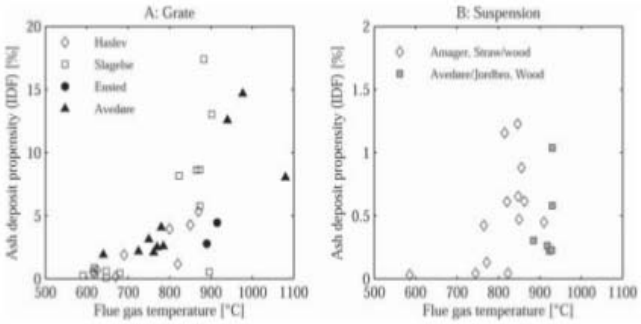

Figure 10. Ash deposit propensities based on IDF rates as a function of local flue gas temperature. (A) Grate-fired units, all straw fired.[23,28−30] (B) Suspension fired units.[36,39−42]

parameters on the deposition rates will be examined for each firing technology subsequently.

In Figure 9, the IDF rates measured in grate-fired (or cigar-fired, Haslev) and suspension-fired units are seen as a function of the flue gas temperatures where the probes were placed. The IDF rate levels for grate-fired and suspension-fired units are comparable, as most IDF rates are in the range 0−100 g/m²·h for both technologies. This is not an obvious result since during grate-firing only up to 20 wt % ash is entrained whereas up to 80 wt % of the ash is expected to end up in the fly ash during suspension-firing. The ash loading of the flue gas is thus expected to be quite different in the two combustion systems.

In order to account for the differences in the fly ash loading of the local flue gas in the various boilers when examining deposition rates, the ash deposit propensity can be calculated. The ash deposit propensity is defined as the percentage of ash in the flue gas which deposits on the probe and is calculated as follows:

$$\text{ash deposit propensity } [\%] = \frac{\pi \cdot \text{deposit flux } [\text{g/m}^2\cdot\text{h}]}{\text{ash flux } [\text{g/m}^2\cdot\text{h}]} 100$$

The deposit flux is the IDF or the DDF rate. This rate is converted from the rate based on the circumference of the probe to a rate based on the projected area (diameter of the probe) by multiplying with π. The ash flux describes the local ash flow near the probes. The ash flux is determined by the fuel flow to the boiler, the ash content of the fuel, the entrainment, and the cross-section area of the boiler at the probe position. The ash flux is thus calculated as follows:

$$\text{ash flux } [\text{g/m}^2\cdot\text{h}] = \frac{\text{fuel flow } [\text{g/h}] \cdot \text{ash content} \cdot \text{entrainment}}{\text{cross section area at probe position } [\text{m}^2]}$$

The ash content and the entrainment are given as fractions. Calculation of the ash flux has to rely on assumptions and should be regarded as an estimate. The fuel flow in the boilers is assumed to be equal to full load of the boiler, unless stated otherwise in the references. The ash content of the fuel is in all references either provided by analysis of the actual fuel or assumed based on earlier fuel analyses at the plant. The fraction of ash entrained in grate-fired units is found to be within 10−35%, from mass balance[29] or weighed amounts of fly ash and bottom ash.[24,48] For suspension-fired units, the entrainment is assumed to be 80% of the fuel ash. The ash flux calculations are somewhat uncertain due to the numerous assumptions they are based on. Furthermore, the ash may not be distributed evenly across the boiler cross section area, and this will influence the local ash flux.

The calculated ash deposit propensity based on IDF rates is seen in Figure 10. Note the different scales on the *y*-axis. It is seen from the scaling of the *y*-axis in Figure 10 that the ash deposit propensity is much higher for the grate-fired units than for the suspension-fired units. For the grate-fired units up to 20% of the ash entrained may deposit on the probe, while for suspension fired units only up to 2% is deposited on the probes. For this comparison, it should be kept in mind that the ash propensity for grate-fired units may in reality be higher than 20% at the high flue gas temperatures, since shedding by melting may decrease the determined IDF rate. Furthermore,

the IDF rates obtained in suspension-firing should be regarded as somewhat uncertain values.

The difference in the ash deposit propensity of the two combustion systems may be explained by the difference in the chemical composition of the fly ash observed earlier. Due to a high content of K, Cl, and S in the fly ash from grate-firing, compared to suspension-firing, the fly ash from grate-firing is expected to have a high fraction of molten and gaseous species in the temperature range 600−1000 °C. The high melt fraction will make the particles (and deposit surface) more sticky and thus result in higher ash stickiness propensity.

3.2.3. Parameters Influencing Deposit Build-up Rates in Grate-fired Boilers. In this section, the influence of operational parameters (the probe and flue gas temperatures and ash chemical composition) on the deposit build-up rates in grate-fired units is examined.

The influence of probe temperature was examined by Jensen et al.[29] for probe temperatures in the range of 400−550 °C in a series of experiments where the mean flue gas temperature was within 700−800 °C. In the temperature range examined, there was no significant effect of the altered probe temperature on deposit build-up rates.[29]

In Figure 10A, the ash deposit propensity for the straw-fired grate boilers is seen as a function of the local flue gas temperature. It is seen that ash deposit propensity increases with increasing flue gas temperatures. The increase is quite significant at temperatures above 800 °C. The influence of temperature can be related to the melting characteristics of fly ash from grate-fired boilers (Figure 11). At temperatures above 800 °C, the ash contains large fractions of melt, which increase the stickiness of the particles and thereby deposit formation rates.

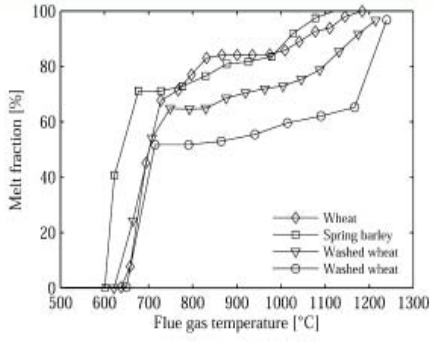

Figure 11. Melting curves for four fly ashes from straw grate-firing determined by STA (simultaneous thermal analysis).[56]

The chemical composition of the fly ash (and thereby also the fuel ash) may also influence the rate of deposit formation during grate-firing. In Figure 12 the ash deposit propensity is seen as a function of the K-content of the fuel ash (A) and of the fly ash (B). The data are from measuring campaigns where corresponding samples of fuel, fly ash, and deposits were collected for each experiment.[23,28]

It is seen in Figure 12 that when the flue gas temperature is low (<800 °C) the ash deposit propensity is low (<2%) regardless of the K-content of the fuel or fly ash and no correlation is observed. For the high temperature data (T_{fg} > 900 °C) no correlation with the fuel ash K-content can be observed with these data, with only four data points available. However, for the deposits obtained at the intermediate flue gas temperatures (800−900 °C) correlations with the fuel ash and fly ash K-content can be observed. The R^2 values of the correlations are 0.44 for the fuel ash K-content and 0.93 for the fly ash K-content. The difference in the R^2 values of the correlations originate from the differences in fuel ash and fly ash compositions found in grate-firing units, as observed earlier.

Based on these examinations, it is seen that for straw-fired grate boilers an increased deposition rate can be expected when the flue gas temperature and the fuel ash or fly ash K-content increases.

3.2.4. Parameters Influencing Deposit Build-up Rates in Suspension-fired Boilers. In this section, the influence of flue gas temperature and fuel composition on deposit build-up rates observed in suspension-fired units is examined. As discussed earlier, the IDF rates obtained in suspension-fired units were uncertain data due to occurrence of shedding, providing an estimate of the deposit accumulation on the probe. The DDF rates are deposit build-up rates without influence of shedding, and these rates thus obtain higher values than the IDF rates. In order to examine the influence of operational parameters on the rate of deposit build-up, without influence of deposit removal, DDF rates obtained in the suspension-fired boilers are investigated.

In Figure 13, available DDF rates (A) and ash deposit propensity (B) are shown as a function of the local flue gas temperature. It is seen that the flue gas temperature influences the DDF rates and the ash deposit propensity measured in suspension boilers. The deposit build-up rates increase with increasing flue gas temperatures. However, the influence of temperature on ash deposit build-up rates is quite different for straw/wood mixtures and wood as fuel. When straw is present in the fuel, a great increase in the DDF rate and the ash deposit propensity is observed when the flue gas temperature approaches 900 °C. When pure wood is used as fuel, the DDF rate and ash deposit propensity are low at temperatures near 800 °C and increases at temperatures >1200 °C. This difference between fuels can be explained by the differences in the melting behavior of the fly ash. Melting behavior as determined by standard ash fusion tests is seen in Table 6.

For suspension-firing with straw in the fuel, three melting tests have been performed for fly ash.[42] These types of fly ash have initial deformation temperatures around 800−900 °C and are completely molten at temperatures around 1200 °C. Two melting tests of laboratory fuel ash from straw are included in Table 6. The melting behavior of these ashes is quite similar to the melting behavior of the fly ash from straw/wood suspension-firing. This similarity can be related to the relatively similar chemical composition of fuel ash and fly ash observed previously.

For the wood fuels no melt tests of fly ash from suspension-firing were available. Table 6 shows melting tests of laboratory ash from wood. These are assumed to be representative for suspension-firing fly ash, based on the similar melting behaviors of fuel ash and fly ash observed for straw. The wood ash initiated melting at very high temperatures ≥1150 °C and complete melting was observed at 1220−1310 °C.

When comparing the melting temperatures in Table 6 to the flue gas temperatures where increases in DDF rates and ash deposit propensity were observed in Figure 13, it is seen that there is quite good agreement. The differences in deposition behavior observed for suspension-firing of straw/wood mixtures

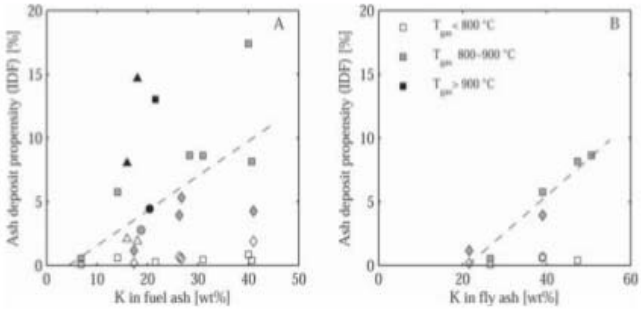

Figure 12. Ash deposit propensity as a function of fuel ash K-content (left figure) and fly ash K-content (right figure) for grate-fired boilers. The color of the points show the flue gas temperatures at the probe position. Point shape shows the boiler; ◇ Haslev, □ Slagelse, ○ Ensted, Δ Avedøre.[23,28] The lines are linear correlations for the 800−900 °C data, obtained by least-squares analysis.

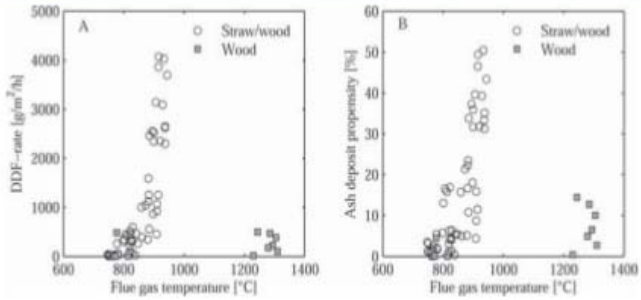

Figure 13. (A) Derivative-based Deposit Formation (DDF) rates and (B) ash deposit propensity (based on DDF rates) obtained in suspension fired boilers.[37,38,41,42]

Table 6. Ash Melting Temperatures of Various Ash Found in Literature As Determined by Standard Ash Fusion Tests[a]

	ash examined	IDT [°C]	HT [°C]	FT [°C]	ref.
	Straw				
40% straw in wood	fly ash, suspension	800	1115	1260	42
60% straw in wood	fly ash, suspension	780	1115	1260	42
80% straw in wood	fly ash, suspension	865	1110	1210	42
straw	fuel ash	885	1060	1225	42
wheat straw	fuel ash	900	1170	1190	50
	Wood				
wood	fuel ash	1210	1225	1240	42
forest residue	fuel ash	1150	1210	1220	50
logging residue pellets	fuel ash	1170	1240	1310	55
bark, birch pellets	fuel ash	1200	1230	1230	55

[a]The fuel ash is laboratory ash prepared at 550 °C. IDT: initial deformation temperature. HT: hemisphere temperature. FT: fluid temperature.

and wood can thus be related to different fuel ash melting characteristics.

In the measurements with suspension-firing of straw/wood, the straw share in the feedstock varied in the range 0−85 wt %. In the following, it is examined how the straw share affects deposit formation. In the experiments performed with suspension-firing, chemical analysis of the fuel mixture used in each experiment was not conducted, and so, the deposit build-up cannot be correlated to elemental content of the fuel, as was done for the grate-fired units. However, fuel was sampled on a daily basis during the campaign and the ash fraction in the fuel mixture was measured. Based on the ash fractions, the straw share in wood was estimated by a linear correlation between the ash contents of the two pure fuels (6 wt % for straw and 0.8 wt % for wood).[41]

In the following analysis, the data are divided into three groups; (1) straw shares <12 wt %, where wood dominates the chemical composition of the ash, (2) straw shares within 12−40 wt %, and (3) straw shares >40 wt %, where the straw dominate the chemical composition of the ash.

The DDF rates and ash deposit propensity are seen as a function of estimated straw shares in Figure 14. Figure 14A shows the measured DDF rates as a function of the estimated straw share in the fuel mixture. It can be observed that the data for group 1 (<12 wt % straw) all result in low DDF rates <50 g/m²·h while the data for group 2 (12−40 wt % straw) have DDF rates below 500 g/m²·h. For straw shares >40%, DDF rates up to 2500 g/m²·h are observed. This "stepwise" analysis indicates that increasing straw shares lead to increased deposition rates. The wide scattering of the data and the influence of temperature, however, need to be considered.

The relatively low DDF rates obtained with 80 wt % straw share in the fuel were not expected. In laboratory and pilot scale experiments resembling suspension firing, increased deposit build-up has been observed with increasing straw shares in the fuel mixtures.[10,15] Unfortunately, the observation at 80 wt % straw share cannot be explained from the available experimental data.

When the straw share is increased, both the total ash content of the fuel is increased and the chemical composition of the ash

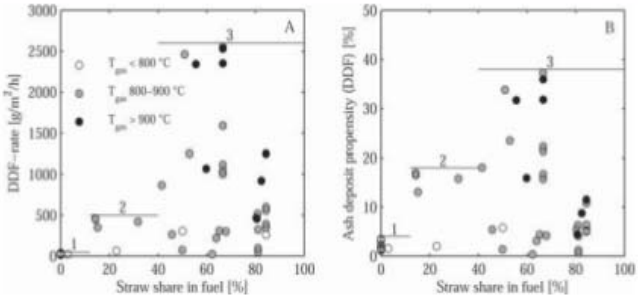

Figure 14. Derivative-based deposit formation (DDF) rates and ash deposit propensity as a function of the straw share in wood for suspension-firing.[41] Data obtained at high boiler loads (>80%) are excluded from this figure. For the remaining data the boiler load was around 60%, and the experimental conditions are thus comparable. The lines indicate maximum values for each fuel group (1:<12% straw; 2:12−40% straw; 3:>40% straw).

is altered. In Figure 14B, the ash deposit propensity is plotted as a function of straw share. Here, the increase in straw share only causes altered chemical composition since the increase in ash fraction is included in the calculation of ash deposit propensity. It is seen that the ash deposit propensity of group 1 (<12 wt % straw) is lower than 5%, while the ash deposit propensity of group 2 (12−40 wt % straw) may be up to 18%. For group 3, ash deposit propensity up to 40% is observed. This shows that both the increased amount of ash as well as the changed ash composition, resulting from using increased fractions of straw in the fuel, cause increased deposit formation rates.

The data in Figure 14 are quite scattered. The scattering may to a large extent be explained by boiler operation fluctuations and by variations in the chemical composition of the fuel. The time span of the measuring campaign was approximately one month.[41] The fuel supply to the boiler will most likely have changed a number of times during that period. A few fuel samples were analyzed and showed differences in chemical composition, although the straw share was estimated to be similar.[41]

Based on these examinations, it is seen that for suspension-fired boilers, an increased deposition rate can be expected when the flue gas temperature and/or the straw share are increased.

3.3. Shedding of Deposits. Zbogar et al.[22] identify several types of shedding mechanisms; melting, gravitational shedding (including debonding), erosion, etc. The occurrence of these shedding mechanisms can be related to the physical properties (degree of sintering or melting) of the deposits and they occur at various locations inside the deposits.

In this section, probe shedding measurements will be reviewed and parameters influencing the occurrence of shedding will be identified when possible. In the discussion, the shedding observed is divided into two phenomena: natural and artificial shedding. Natural shedding is the shedding occurring when plant soot blowers are not in operation. Artificial shedding is thus the shedding observed when the soot blowers are active, although the blowers close to the probe position were in most cases shut off. Operation of the remaining plant soot blowers may influence local conditions and thereby the occurrence of shedding during the tests.

3.3.1. Shedding Observations in Full-Scale Boilers. The observations on shedding behavior made in full-scale boilers are summarized in Table 7. All of the observations on shedding are made with the advanced deposition probe, periodically equipped with a camera. In two campaigns,[29,46] a soot blower probe parallel to the deposit probe was applied.

During grate-firing of straw at intermediate flue gas temperatures (<900 °C), no natural shedding (melting, debonding, or erosion) was observed.[29,30] A soot-blower probe was applied where the local flue gas temperatures were within 700−800 °C. It was possible to remove the deposits by soot blowing, depending on the temperature and residence time of the probe.[29] These measurements are reviewed later. No soot-blowing measurements were performed for flue gas temperatures above 800 °C. At flue gas temperatures >900 °C, it was observed that the shedding of deposits took place by surface melting and droplet formation. It was found that the local flue gas temperature governs the state of the deposit. At 1100 °C or above, the deposit surface layer was completely molten and the deposits were rapidly removed from the probe as droplets.[30]

For suspension-fired-boilers, shedding has been examined for straw/wood mixtures[42,46] and for wood.[37] Examples of the mass-uptake signal from the advanced probe are shown in Figures 6 and 8. The deposition behavior during straw/wood suspension firing is characterized mainly by a rapid deposit build-up followed by shedding. According to observations, the shedding mainly took place by debonding, both as natural and artificial shedding. An example of shedding by debonding is shown in Figure 15, where formation of a "hammock" was observed within minutes prior to the shedding.[42] Hammock formation was not observed in all shedding events by debonding. In some cases, a simple break-off of a small piece was observed.

It is seen in Figure 15 that debonding of the deposit does not occur at the whole length of the probe. Some deposit remains on the part of the probe near the camera.

Besides shedding by debonding, erosion caused by impaction of nonsticky, hard fly ash particles and shedding of small deposit layers (fracture) were also observed, to a minor degree, by visual inspection of the probe during operation. Shedding by surface melting was not observed, although the flue gas temperature was >1000 °C for short periods of the tests.[46]

Differences in the shedding behavior betweem straw-fired on a grate and in suspension were thus observed. This difference is most likely related to the different chemical composition of the fly ash and deposits in the two combustion systems. Jensen et al.[29] have tested the strength of sintered fly ash pellets from straw-firing in grate and suspension boilers. It was found that the strength increase associated with onset of sintering occurs

dx.doi.org/10.1021/ef500442z | Energy Fuels 2014, 28, 3539−3555

Table 7. Shedding Observations Made in Full Scale Biomass Fired Boilers

boiler	fuel	flue gas	probe	natural shedding	artificial shedding	comments	ref.
Avedøre, grate	straw	700–800 °C	400–550 °C	none	debonding fracture	soot blower probe applied probe surface temp. and residence time influence on how easily deposits are removed[a]	29
Avedøre, grate	straw	800–1000 °C	500 °C	melting		flue gas temp. controls shedding by melting ≈900 °C; initial melt formation ≈1000 °C; deposit partly molten, formation of droplets and thereby deposit removal ≈1100 °C; deposit molten, rapidly removed as droplets	30
Amager, suspension	straw/ wood	600–1050 °C	500–600 °C	debonding erosion fracture	debonding	incomplete shedding of deposits limited amount of erosion and fracture observed by visual inspection no melting of deposits observed, even at temp. >1000 °C soot blower probe applied[b]	41 and 42
Avedøre, suspension	wood	800 °C	550 °C	not identified		steady mass on the probe obtained after some initial deposit buildup; possible shedding mechanism = erosion (not confirmed)	37 and 38
Avedøre, suspension	wood	1300 °C	550 °C	debonding		frequent shedding with complete removal of deposits	37 and 38

[a]Increasing the probe surface temperature from 400 to 550 °C changed the deposit from easy removable to one where a high PIP soot blowing was needed for removal. [b]Most of the deposits could be removed by soot-blowing. The required PIP to remove the deposit increased with probe temperature.

at low temperatures (450 °C) for fly ash from grate-firing compared to fly ash from suspension firing (650 °C). The difference was explained by differences in chemical composition of the ash. See Supporting Information for additional information.

For suspension-firing of wood, shedding observations were made in the Avedøre boiler at two positions where the flue gas temperatures were approximately 800 and 1300 °C. When the flue gas was 800 °C, the deposit mass on the probe became constant at a low level after some initial build-up, indicating equilibrium between deposit build-up and shedding. The type of shedding at this position was not identified, but in view of insignificant mass loss, it was probably not by debonding.[37,38] A possible mechanism in this position could be erosion, but this has not been verified. With a flue gas temperature near 1300 °C, the deposit build-up was fast, and many shedding events with almost complete removal of the deposit by debonding took place.[37,38]

It can be concluded that the shedding behavior when firing wood in a suspension boiler was quite different from what was observed with the straw/wood mixture fired in a suspension boiler. A thick layer of deposit was never established on the probe during wood firing at these flue gas temperatures. Lab scale studies examining the compressive strength of sintered ash pellets from various biofuels have been conducted.[29,49,50] A sintering temperature, at which onset of strength increase occurs, has been defined by Jensen et al.[29] It was found that the sintering temperatures for straw fuel ash generally were in the range 610–710 °C while the sintering temperature for wood ash was higher, >780 °C.[29] From the lab-scale studies[49,50] it is observed that wood ash does not gain as much strength as straw or grass ash during sintering. See Supporting Information for additional information.

3.3.2. Removability of Deposits. To gain further knowledge about how difficult deposits are to remove and about the influence of time and probe temperature, a soot-blower probe was used along with the deposit probe in two of the measuring campaigns.[29,46] Use of the soot blower probe allowed the peak impact pressure (PIP) needed for removal of the deposits to be determined.

During the measurements in the Avedøre grate boiler, the deposit probe metal temperature was varied in the range 400–550 °C.[29] For the soot blower probe, a critical PIP was defined as the pressure needed for removal of more than 75% of the deposit on the probe. Figure 16 shows the critical PIP measured after 100 h of exposure (4 days) and just before the probe was removed at the end of the experiment after 260–740 h (11–31 days).

As seen in Figure 16, both the probe temperature and the exposure time influenced the removability of the upstream deposit. At a probe temperature of 400 °C, the deposits were removed easily with PIP less than 0.5 kPa. Higher probe temperatures and long exposure times lead to deposits that were difficult to remove. When the probe temperature was 550 °C, the maximum possible PIP (150 kPa) could only remove <25% of the deposit, even at the short residence time (100 h). The effect of temperature and time was considered to be due to sintering and thereby increased deposit strength and possibly increased deposit-tube adhesion strength. The mechanism of removal was in all cases fracture and debonding induced by the soot blower. For the downstream deposits, it was found that these were easily removed, except at the highest temperature (550 °C[29]).

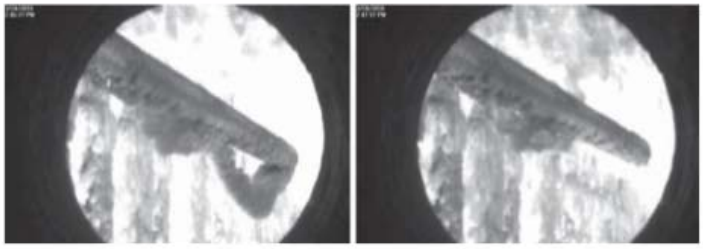

Figure 15. Example of observed shedding event.[42] The event is observed after 50 min probe exposure time during combustion of a straw/wood mixture containing 80% straw. The time frame between the photos is 1.5 min, and 34% of the deposit was removed, according to the load cell.

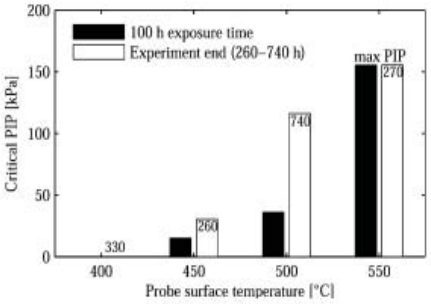

Figure 16. Critical PIP for removal of upstream deposit for different probe surface temperatures and exposure times.[29] At 550 °C less than 25% deposits were removed at max PIP.

A soot blower probe was also applied during straw/wood-firing in a suspension boiler. The influence of time and probe temperature was examined by measuring the PIP needed for removal of deposits at various conditions.[46] The results are shown in Figure 17 where it can be seen that at 500 °C the PIP needed for removal of deposits increased with exposure time. At 600 °C the exposure time was less significant and the deposits were difficult to remove even at short residence times.[46] These results are in line with the results obtained for the straw-fired grate boiler.[29]

The soot-blower PIP measurements demonstrated that time and probe temperature influence the strength of deposits and/or the adhesion strength between deposits and probe metal, as the deposits became difficult to remove at high probe temperatures and increased residence time.

For coal-firing, deposit strength has been correlated to deposit porosity.[51] The porosity changes by sintering reactions[22] and changes in porosity have been described as a function of time, chemical composition, and temperature.[52,53] It is considered that similar effects apply to biomass firing. Besides the strength of the deposits, the adherence strength between the deposits and the probe is considered to be important. However, very little knowledge is available on this aspect.

3.3.3. Parameters Influencing Shedding during Suspension Firing of Straw/Wood. During suspension firing of straw/wood mixtures, shedding events were tracked by use of the advanced in situ deposition probe in combination with a camera.[46] The influence of several parameters on shedding behavior was examined based on these data. Plant soot-blowers were in operation during some periods (1.7 h on average) of varying frequencies. The soot-blower close to the deposition probe was shut off, but the operation of the remaining blowers may induce fluctuations in the boiler operation, thereby influencing the deposition behavior on the probe. Therefore, before the data analysis, the shedding events observed during periods with plant soot blowing were clearly separated from the remaining data. The shedding data obtained during periods without soot blowing, termed "natural" shedding events, will be reviewed in the following. The results obtained during soot blowing periods are not discussed in detail, but differences or similarities to the natural shedding behavior will be noted, when relevant.

In the analysis of the shedding data, the shedding behavior has been quantified by three measures; shedding frequency [events/h], mass loss per event [g/m^2], and shedding rate [g/m^2·h], which is a product of the first two measures. In Figure 18 the shedding rate, given as 6-h mean values, is seen as a function of the mean DDF rate from the same period.

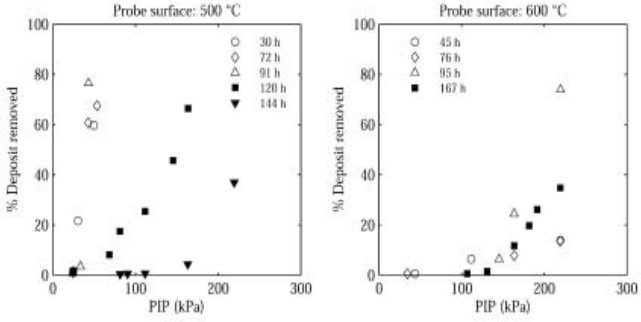

Figure 17. Percentage of deposits removed as a function of PIP and residence time. The deposit mass load on the probe increases with exposure time. Adapted from data presented in ref 46.

dx.doi.org/10.1021/ef500442z | Energy Fuels 2014, 28, 3539−3555

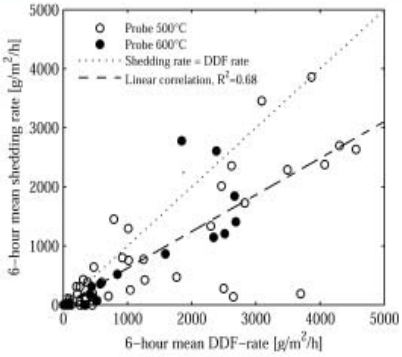

Figure 18. Shedding rate vs derivative-based deposit formation (DDF) rate given as 6-h mean values for straw/wood-firing. Only shedding events occurring without plant soot blowing are included.[46]

A diagonal (dotted) line indicating identical rates of shedding and deposition is seen in Figure 18. For most periods the shedding rate is lower than the DDF rates, as most points are below the dotted line. This corresponds well with the observation made earlier; during straw/wood suspension-firing, large fluctuations in the deposit mass are seen, but the mass remaining on the probe increases with time. The dashed line indicates a linear correlation between the DDF rate and the shedding rate. The slope of the line is 0.62, and hence the shedding rate corresponds on average to 62% of the DDF rate. The linear correlation furthermore reveals that in periods with high DDF rates, high shedding rates are often observed. When the DDF rates are high, deposits quickly accumulate on the probe. There is thus a short time for deposit consolidation by sintering before the mass of the deposit on the probe becomes too large for the adhesion strength to keep it on the probe, and shedding occurs.

In Figure 19, the shedding rate observed in Figure 18 has been divided into a shedding frequency (Figure 19A) and the mean mass loss per shedding event (Figure 19B), both obtained in 6 h periods. It is seen that the shedding frequency increases with increasing DDF rate, although with large scattering of the data. The data showing the mean mass loss per shedding event cannot be correlated with the DDF rate. These observations imply that during periods with quick accumulation of deposits shedding occurs frequently, but the amount of deposit lost per event is not affected significantly. The mass loss per event is on average 600 g/m^2, regardless of DDF rates, flue gas temperature or mass load of deposit on the probe.[46]

Figure 20 shows the percentage of mass lost in a single event as a function of the time of the shedding event in five tests

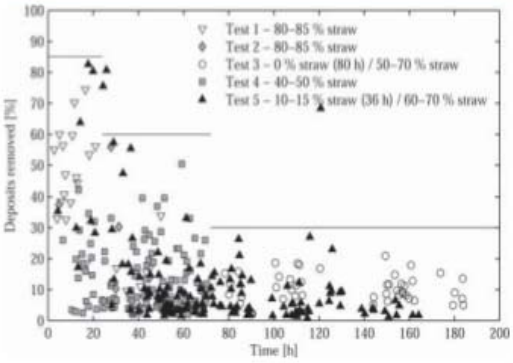

Figure 20. Percentage of mass lost in each single event as a function of the time of the shedding event for natural shedding events.[46]

performed by Bashir et al.[46] The probe residence time seems to influence the volume of the deposit removed in a single natural shedding event. Within the first 24 h up to 85% removal of the accumulated deposit may occur in a single shedding event. When the probe residence time is 24−72 h, the maximum deposit removal is lowered to around 60% and at residence times longer than 72 h it seems that only up to 30% of the deposit was removed in a single shedding event. The results obtained for the periods where plant soot blowing was activated are similar to what was observed for the natural shedding. Consequently, the influence of time observed here is in agreement with the observations obtained during the experiments with the soot-blower probe discussed earlier. It is also seen that natural shedding is a stochastic process where the amount of deposit removed in a single shedding event is not easy to predict.

Earlier in this paper, it was demonstrated that the straw share of the straw/wood mixture influences the DDF rate. Figure 21A shows the shedding rate vs straw share of the fuel. It is seen that the influence of straw share on the shedding rate follows the same characteristics as on the DDF rate. When wood ash dominates the ash fraction (straw <12%), the shedding rate is <200 g/m^2·h. At straw shares in the range 12−40%, shedding

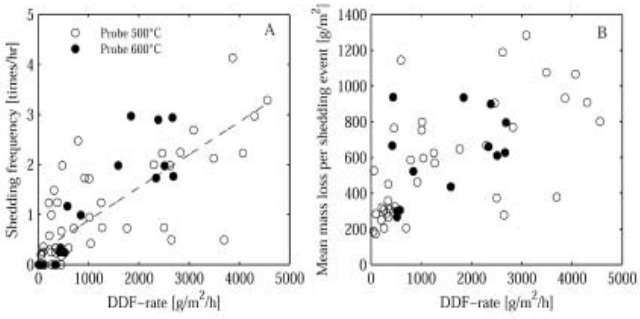

Figure 19. (A) Shedding frequency vs DDF rate. (B) Mean mass loss per shedding event vs DDF rate. Only shedding events occurring without plant soot blowing are included. Suspension firing of straw/wood mixtures.[46]

dx.doi.org/10.1021/ef500442z | Energy Fuels 2014, 28, 3539−3555

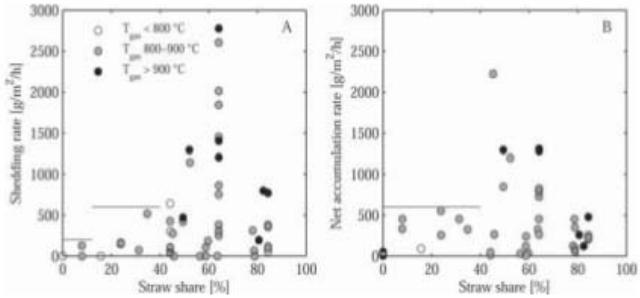

Figure 21. Shedding rate and net accumulation rate as a function of straw share in wood.[46] Some data obtained at high boiler loads (>80%) are excluded from this figure. For the remaining data the boiler load was around 60%, and the experimental conditions are thus comparable. The lines indicate maximum values for each fuel group (see text).

rates increase and may reach 500 g/m^2·h while at straw shares above 40%, where the straw ash dominates the fuel ash, high shedding rates up to 3000 g/m·h may be observed. As the shedding rates follow the DDF rates, it is not possible to determine whether the straw share or the DDF rate is responsible for the shedding rates illustrated in Figure 21A.

Figure 21B shows the net accumulation rate as a function of straw share. The net accumulation rate is calculated as the mean DDF rate less the mean shedding rate for a 6-h period. It is observed that the net accumulation rate is low (<600 g/m^2·h) when the straw share is lower than 40 wt %.

The net accumulation rate has been plotted as a function of the flue gas temperature in Figure 22. It is seen that there is a

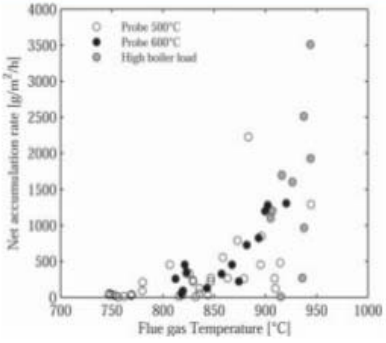

Figure 22. Net accumulation rate as a function of flue gas temperature during suspension firing of straw/wood mixtures.[46] Data obtained at high boiler load (exduded in Figure 21) are indicated by gray points.

clear correlation between the flue gas temperature and the net accumulation rate, which is as expected since the flue gas temperature was also an important parameter influencing the DDF rate. This implies that during operation, high accumulation rates can be expected for high flue gas temperatures and/or straw shares.

4. CONCLUSION

A number of full-scale deposit probe measuring campaigns conducted in grate- and suspension-fired biomass boilers have been reviewed and compared. Influence of operational parameters on the chemistry of ash and deposits, on deposit build-up rates and on shedding behavior has been examined.

Firing technology and fuel type had a significant impact on the fly ash chemistry. During grate-firing of straw the fly ash was enriched in K, Cl, and S compared to the fuel ash. During suspension-firing, the fly ash composition largely resembled the fuel ash composition, due to a higher degree of entrainment of ash in the combustion zone. The fly ash from suspension firing of straw was thus dominated by K and Si while wood-firing in suspension boilers lead to fly ash dominated by Ca and K.

The deposit chemical composition was influenced by firing technology, fuel choice, and flue gas temperature. At low local flue gas temperatures (<800 °C), the deposit compositions were similar to those of fly ash. Increases in local flue gas temperatures increased the content of Si and Ca in the deposits and decreased the Cl content. The influence of flue gas temperature is similar for grate and suspension-firing.

The rate of deposit build-up has been defined by two measures: an IDF rate, possibly including shedding events, and a DDF rate, which is the build-up rate without interference from shedding events. For grate boilers limited natural shedding is expected for flue gas temperatures <900 °C. Above this temperature, shedding by melting may influence IDF rates. Shedding has significant influence on the IDF rates in suspension boilers, and these should be regarded as uncertain estimates of the deposit accumulation. DDF rates are currently mainly available from probe measuring campaigns in suspension boilers.

The IDF rates in the two combustion systems are at similar levels; 0−100 g/m^2·h. Differences in the ash flux in the different boilers are included by calculating ash deposit propensity. The ash deposit propensity is an order of magnitude larger in grate-fired boilers than in suspension boilers. This can be related to differences in fly ash chemistry.

Ash deposit propensity increases with flue gas temperatures. For all boilers and fuels examined, a steep increase in ash deposition propensity was observed at flue gas temperatures close to the temperatures where melting of the fly ash was expected based on STA analysis or ash fusion tests. The rate of deposit build-up was furthermore found to increase with K content in the fuel ash and fly ash for grate-fired boilers. For suspension-fired boilers deposition rates were low for wood-firing whereas increases in deposition rates were observed with increasing straw shares.

The shedding of deposits has been monitored under various combustion conditions. During grate-firing of straw at low or intermediate flue gas temperatures (<900 °C), no natural shedding (melting, debonding or erosion) was observed. At higher flue gas temperatures (>900 °C), shedding of deposit took place by surface melting and droplet formation. For suspension firing of straw, natural shedding was observed to

dx.doi.org/10.1021/ef500442z | Energy Fuels 2014, 28, 3539−3555

occur frequently primarily by debonding. Shedding by debonding was incomplete and increased deposit mass accumulated on the probe. Shedding by melting was not observed even at temperatures above 1000 °C. During wood suspension-firing, a thick layer of deposit never formed on the probe. At low flue gas temperatures, 800 °C, a small amount of deposit initially accumulated on the probe and the mass on the probe then remained constant. At high flue gas temperatures, 1300 °C, the deposition was characterized by a rapid build-up followed by complete shedding.

Soot blowing tests were conducted during grate-firing of straw and suspension-firing of straw/wood. It was found, in both cases, that increased probe surface temperature and residence times lead to deposits that are more difficult to remove.

Shedding behavior was closely monitored during straw/wood firing in suspension boilers. The shedding rate [$g/m^2 \cdot h$] and frequency [events/h] increased with increasing DDF rates, whereas the deposit mass lost per event [g/m^2] seemed to be relatively stable. The percentage of deposits removed per shedding event decreased with residence time. Up to 80% of the deposit on the probe was likely to be removed in a shedding event within the first 24 h of exposure. Contrarily, at exposure times >72 h, only up to 30% removal per shedding event could be expected. Camera observations revealed that the percentage of mass loss corresponded to a percentage of the probe length left uncovered, as the shedding occurred by debonding near the probe surface.

The net accumulation rate, calculated as the difference between the DDF rate and the shedding rate was found to increase with increasing flue gas temperature and straw share during straw/wood firing in suspension boilers.

■ ASSOCIATED CONTENT

Supporting Information

Information on sintering; chemical composition and sintering temperatures (Table S8). This material is available free of charge via the Internet at http://pubs.acs.org.

■ AUTHOR INFORMATION

Corresponding Author

*Email: paj@kt.dtu.dk.

Notes

The authors declare no competing financial interest.

■ ACKNOWLEDGMENTS

Funding from the Danish Strategic Research Council (GREEN) and DONG Energy AS is gratefully acknowledged.

■ REFERENCES

(1) Bryers, R. W. *Prog. Energy Combust. Sci.* **1996**, *22*, 29−120.

(2) Frandsen, F. J.; Bäfver, L.; Sarofim, A. F. On the Gaps in Understanding and Quantification of Release of Critical Elements, Formation of Fly Ash and Aerosols when Utilizing Solid Fuels in Different Thermal Fuel Conversion Technologies. In *Proceedings: Impacts of Fuel Quality on Power Production & Environment*, Saariselkä, Lapland, Finland, Aug. 29−Sept. 3, 2010.

(3) Knudsen, J. N.; Jensen, P. A.; Dam-Johansen, K. *Energy Fuels* **2004**, *18*, 1385−1399.

(4) van Lith, S. C.; Jensen, P. A.; Frandsen, F. J.; Glarborg, P. *Energy Fuels* **2008**, *22*, 1598−1609.

(5) Johansen, J. M.; Jakobsen, J. G.; Frandsen, F. J.; Glarborg, P. *Energy Fuels* **2011**, *25*, 4961−4971.

(6) Obernberger, I.; Brunner, T.; Jöller, M. Characterization and Formation of Aerosols and Fly-Ashes from Fixed-Bed Biomass Combustion. *Aerosols from Biomass Combustion*, International Seminar; Nussbaumer, T., Ed.; Verenum: Zurich, Switzerland, 2001; pp 69−74.

(7) Jöller, M.; Brunner, T.; Obernberger, I. Modeling of Aerosol Formation during Biomass Combustion in Grate Furnaces and Comparison with Measurements. *Energy Fuels* **2005**, *19*, 311−323.

(8) Korbee, R.; Shah, K. V.; Cieplik, M. K.; Betrand, C. I.; Vuthaluru, H. B.; van de Kamp, W. L. *Energy Fuels* **2010**, *24*, 897−909.

(9) Shah, K. V.; Cieplik, M. K.; Betrand, C. I.; van de Kamp, W. L.; Vuthaluru, H. B. *Fuel Process. Technol.* **2010**, *91*, 531−545.

(10) Nordgren, D.; Hedman, H.; Padban, N.; Boström, D.; Öhman, M. *Fuel Process. Technol.* **2013**, *105*, 52−58.

(11) Hupa, M. *Energy Fuels* **2012**, *26*, 4−14.

(12) Lind, T.; Valmari, T.; Kauppinen, E.; Nilsson, K.; Sfiris, G.; Maenhaut, W. *Proc. Combust. Inst.* **2000**, *28*, 2287−2295.

(13) Baxter, L. L. *Biomass Bioenergy* **1993**, *4*, 85−102.

(14) Zhou, H.; Jensen, P. A.; Frandsen, F. J. *Fuel* **2007**, *86*, 1519−1533.

(15) Theis, M.; Skrifvars, B. J.; Hupa, M.; Tran, H. *Fuel* **2006**, *85*, 1125−1130.

(16) Jensen, P. A.; Sørensen, L. H.; Hu, G.; Holm, J. K.; Frandsen, F.; Henriksen, U. B. *Combustion Experiments with Biomass Fuels and Additives in a Suspension Fired Entrained Flow Reactor: Test of Ca and P Rich Additives Used to Minimize Deposition and Corrosion*; Energinet.dk PSO project 6515/Report R0504, CHEC Research Centre, Technical University of Denmark: Lyngby, 2005.

(17) Capablo, J.; Jensen, P. A.; Pedersen, K. H.; Hjuler, K.; Nikolaisen, L.; Backman, R.; Frandsen, F. *Energy Fuels* **2009**, *23*, 1965−1976.

(18) Wu, H.; Glarborg, P.; Frandsen, F. J.; Dam-Johansen, K.; Jensen, P. A. *Energy Fuels* **2011**, *25*, 2862−2873.

(19) Lokare, S. S.; Dunaway, J. D.; Moulton, D.; Rogers, D.; Tree, D. R.; Baxter, L. L. *Energy Fuels* **2006**, *20*, 1008−1014.

(20) Robinson, A. L.; Junker, H.; Baxter, L. L. *Energy Fuels* **2002**, *16*, 343−355.

(21) Hupa, M. *Fuel* **2005**, *84*, 1312−1319.

(22) Zbogar, A.; Frandsen, F.; Jensen, P. A.; Glarborg, P. *Prog. Energy Combust. Sci.* **2009**, *35*, 31−56.

(23) Jensen, P. A.; Stenholm, M.; Hald, P. *Energy Fuels* **1997**, *11*, 1048−1055.

(24) Jensen, P. A.; Stenholm, M.; Hald, P. *Biomasses brændsels—og fyringskarakteristika. Fyringsforsøg*; Journal nr. 1323/93-0015; dk-TEKNIK: Risø, 1996.

(25) Michelsen, H. P.; Frandsen, F.; Dam-Johansen, K.; Larsen, O. H. *Fuel Process. Technol.* **1998**, *54*, 95−108.

(26) Hansen, L. A.; Nielsen, H. P.; Frandsen, F. J.; Dam-Johansen, K.; Hørlyck, S.; Karlsson, A. *Fuel Process. Technol.* **2000**, *64*, 189−209.

(27) Jensen, P. A.; Frandsen, F. J.; Hansen, J.; Dam-Johansen, K.; Henriksen, N.; Hörlyck, S. *Energy Fuels* **2004**, *18*, 378−384.

(28) Hansen, J.; Jensen, P. A.; Glarborg, P. *Deposit Probe Measurements in the Avedøre and Ensted Straw Fired Grate Boilers*; Energinet.dk PSO project 4792/Report R0705, CHEC Research Centre, Department of Chemical Engineering; Technical University of Denmark: Lyngby, 2007.

(29) Jensen, P. A.; Zhou, H.; Zbogar, A.; Hansen, J.; Frandsen, F. J.; Glarborg, P.; Madsen, H.; Stang, B. *Final Report: Ash Deposit Formation and Removal in Biomass-fired Boilers. Fundamental Data Provided with Deposit Probes*; Energinet.dk PSO project 4106/Report R0603, CHEC Research Centre, Department of Chemical Engineering; Technical University of Denmark: Lyngby, 2006.

(30) Zbogar, A.; Jensen, P. A.; Frandsen, F.; Hansen, J.; Glarborg, P. *Energy Fuels* **2006**, *20*, 512−519.

(31) Skrifvars, B. J.; Backman, R.; Hupa, M.; Sfiris, G.; Åbyhammar, T.; Lyngfelt, A. *Fuel* **1998**, *77*, 65−70.

(32) Kassman, H.; Broström, M.; Berg, M.; Åmand, L. E. *Fuel* **2011**, *90*, 1325−1334.

(33) Hansen, L. A.; Frandsen, F. J.; Dam-Johansen, K.; Sørensen, H. S.; Skrifvars, B. J. *Energy Fuels* **1999**, *13*, 803−816.

(34) Zheng, Y.; Jensen, P. A.; Jensen, A. D.; Sander, B.; Junker, H. *Fuel* **2007**, *86*, 1008−1020.
(35) Andersen, K. H.; Frandsen, F. J.; Hansen, P. F. B.; Wieck-Hansen, K.; Rasmussen, I.; Overgaard, P.; Dam-Johansen, K. *Energy Fuels* **2000**, *14*, 765−780.
(36) Jensen, P. A.; Dall'ora, M.; Lin, W.; Clausen, S.; Hansen, J.; Simonsen, P.; Berg, M.; Jensen, A. D. *Measurements on the 800 MW_{th} Avedøre Oil, Gas, and Wood Co-fired Suspension Boiler - Analysis of Emission, Burnout, Deposit, and FTIR Measurements from April 2005*; Energinet.dk PSO project 6526/Report R0802, CHEC Research Centre, Department of Chemical Engineering; Technical University of Denmark: Lyngby, 2008.
(37) Wu, H.; Bashir, M. S.; Jensen, P. A.; Glarborg, P.; Frandsen, F. J. *Full-Scale Deposition Measurements at Avedøre Power Plant Unit 2 during Suspension-Firing of Wood with and without Coal Ash Addition*; CHEC Report, CHEC Research Centre, Department of Chemical Engineering; Technical University of Denmark: Lyngby, 2012.
(38) Wu, H.; Bashir, M. S.; Jensen, P. A.; Sander, B.; Glarborg, P. *Fuel* **2013**, *113*, 632−643.
(39) Tobiasen, L.; Skytte, R.; Pedersen, L. S.; Pedersen, S. T.; Lindberg, M. A. *Fuel Process. Technol.* **2007**, *88*, 1108−1117.
(40) Bashir, M.; Jensen, P.; Frandsen, F.; Wedel, S.; Dam-Johansen, K.; Wadenbäck, J.; Pedersen, S. *Fuel Process. Technol.* **2012**, *97*, 93−106.
(41) Bashir, M. S.; Jensen, P. A.; Frandsen, F. J.; Wedel, S.; Dam-Johansen, K.; Wadenbäck, J.; Pedersen, S. T. *Energy Fuels* **2012**, *26*, 2317−2330.
(42) Bashir, M. S. *Characterization and Quantification of Deposit Build-up and Removal in Straw Suspension-Fired Boilers*. Ph.D. thesis, CHEC Research Centre, Department of Chemical Engineering, Technical University of Denmark, Lyngby, 2012.
(43) Skrifvars, B.; Laurén, T.; Hupa, M.; Korbee, R.; Ljung, P. *Fuel* **2004**, *83*, 1371−1379.
(44) Jenkins, B. M.; Williams, R. B.; Bakker, P. R.; Blunk, S.; Yomogida, D. E.; Carlson, W.; Duffy, J.; Bates, R.; Stuci, K.; Tiangco, V. Combustion of Leached Straw for Power Generation. *4th Biomass Conference of the Americas*; Pergamon, Elsevier Science: Oxford, U.K., 1999; pp 1357−1363.
(45) *The Handbook of Biomass Combustion and Co-firing*; van Loo, S.; Koppejan, J., Eds.; Earthscan: London, 2008.
(46) Bashir, M. S.; Jensen, P. A.; Frandsen, F. J.; Wedel, S.; Dam-Johansen, K.; Wadenbäck, J. *Energy Fuels* **2012**, *26*, 5241−5255.
(47) Nielsen, H. P. *Deposition and High-Temperature Corrosion in Biomass-Fired Boilers*. Ph.D. thesis, CHEC Research Centre, Department of Chemical Engineering, Technical University of Denmark, Lyngby, 1998.
(48) Miljøstyrelsen. *Separation og Genanvendelse af aske fra Biobrændselsanlæg*; Miljøprojekt nr. 962; Miljøstyrelsen: København K, Denmark, 2004; http://www.mst.dk/Publikationer/.
(49) Skrifvars, B. J.; Backman, R.; Hupa, M. *Fuel Process. Technol.* **1998**, *56*, 55−67.
(50) Skrifvars, B. J.; Öhman, M.; Nordin, A.; Hupa, M. *Energy Fuels* **1999**, *13*, 359−363.
(51) Wain, S. E.; Livingston, W. R.; Sanyal, A.; Williamson, J. Thermal and Mechanical Properties of Boiler Slags of Relevance to Sootblowing. In *Inorganic Transformations and Ash Deposition during Combustion*; Benson, S. A., Ed.; ASME: New York, 1992.
(52) Senior, C. L. *Energy Fuels* **1997**, *11*, 416−420.
(53) Rezaei, H. R.; Gupta, R. G.; Wall, T. F.; Miyamae, S.; Makino, K. Modeling the Initial Structure of Ash Deposits and Structure Changes Due to Sintering. In *Impact of Mineral Impurities in Solid Fuel Combustion*; Gupta, R. P., Wall, T. F., Baxter, L. L., Eds.; Plenum Publishers: New York, 1999.
(54) Centre for Biomass Technology. *Straw for Energy Production: Technology - Environment - Economy*; Nikolaisen, L., Ed.; Center for Biomass Technology, Danish Energy Agency: Copenhagen, 1998; http://www.videncenter.dk/uk/.
(55) Gilbe, C.; Lindström, E.; Backman, R.; Samuelsson, R.; Burvall, J.; Öhman, M. *Energy Fuels* **2008**, *22*, 3680−3686.
(56) Hansen, L. A. *Melting and Sintering of Ashes*. Ph.D. thesis, CHEC Research Centre, Department of Chemical Engineering, Technical University of Denmark, Lyngby, 1998.

A.1 Supporting Information

Sintering

In order to understand sintering behavior and strength increase of deposits, lab-scale studies have been conducted [57]. In these studies the compression strength of fly ash pellets from straw-firing in suspension and on a grate has been compared. This was done by heat-treating fly ash pellets at different temperatures for four hours, before measuring the compression strength of the pellets. The results are seen in Figure A.1, where it is observed that for both types of fly ash pellets, the compression strength first increased and then decreased as the temperature was increased. The increase of compression strength is associated with sintering of the ash pellets, while the decrease in strength is associated with the formation of pores, due to evaporation of some salt species. This behavior may not apply completely to real deposits, where long exposure times, additional deposition and possibly collapse of deposits may alter the sintering behavior [57]. However, it is clear that for the fly ash from suspension-firing, the onset of strength increase was high (650 °C) compared to that of fly ash from grate-firing of straw (450 °C). The fly ash from suspension firing had a high content of Si and Ca, and a low content of K and Cl compared to the fly ash from grate-firing [57]. It is thus seen that both chemical composition and local temperature influence deposit strength.

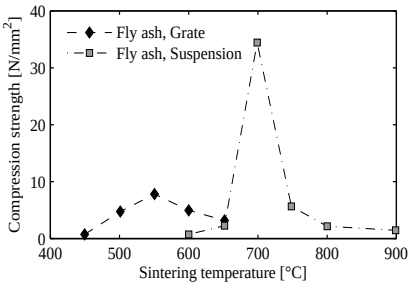

Figure A.1: Compression strength as function of sintering temperature for two fly ash from straw combustion [57]

Sintering of Various Types of Fuel Ash

In order to compare the above mentioned results with other lab-scale studies, a sintering temperature (T_{sint}) was defined by Jensen et al. [57] as the temperature at which the compression strength of deposits increases above 2 N/mm^2 [57]. Table A.1 lists sintering temperatures for various types of biomass fuel ash and coal are shown. It is seen that straw fuel ash generally has sintering temperatures in the range of 610-710 °C while wood ash with a higher content of Ca exhibits higher

sintering temperatures > 780 °C. Ash from coal or coal/straw co-firing has even higher sintering temperatures in the range of 920-1010 °C [57].

Table A.1: Chemical composition and sintering temperatures of various types of fuel ash. The sintering temperature was determined by Jensen et al. [57] based on graphical lab-scale results from the references noted.

Biomass or coal type		Composition of ash[a] [wt%]						T_{sint}
[Ref. lab-work]		SiO_2	CaO	Al_2O_3	K_2O	S	Cl	[°C]
Straw	Wheat [142]	30.6	7.9	0.5	25.3	2.9	3.7	690
	Wheat [144]	56.3	6.3	0.5	12.6	1.16	2.10	710
	Wheat [144]	34.2	9.1	0.4	24.7	0.92	3.15	660
Wood	Forrest residue [142]	24.6	25.3	4.3	6.9	1.3	0.1	[b]
	Bark [142]	12.2	33.3	1.8	7.6	1.0	0.1	[b]
	Olive [144]	44.1	6.7	5.1	16	2.1	-	930
	Branch & top [144]	7.3	44.8	1.5	11.3	0.6	-	[c]
	Willow [144]	0.6	28.8	0.1	22.5	2.36	0.18	780
Coal	Beulah [212]	27.5	27.4	14.2	1.0	n.a.	n.a.	920
	Pittsburg no. 8 [212]	50.8	5.2	20.2	2.5	n.a.	n.a.	920
	Illinois no.6 [212]	48.6	5.6	23.1	3.1	n.a.	n.a.	1020
	South American [137]	55.1	1.6	18.3	1.9	0.2	n.a.	1010
Coal/	20% straw [137]	57.3	2.9	18.4	6.1	0.4	n.a.	950
straw	20% straw [137]	55.0	3.0	15.6	5.1	0.3	n.a.	1010
	20% straw [137]	57.3	2.9	17.6	5.5	0.2	n.a.	1010

[a]: MgO, P_2O_5 and Na_2O are excluded

[b]: Compression strength did not increase above 2 N/mm^2 up to 1100 °C

[c]: Compression strength did not increase above 2 N/mm^2 up to 900 °C

Appendix B

Parameter Estimation

B.1 Density of Fuels and Ashes

The densities of fuels vary with particle sizes as cavities within the biomass fuels are reduced as the particle sizes are reduced [213]. Thus, it is important to use either a value of the density measured for a relevant particle size or to use the cell wall density along with a porosity of the particles.

Straw

The densities of wheat and barley straw particles with geometric mean diameters of the particle samples within 0.18-1.43 mm have been measured by use of a gas multipycnometer by S.Mani et al. [213]. For particles with geometric mean diameters near 300 μm, relevant for these calculations, the particle densities are:

$$\text{Wheat:} \quad \rho(280\mu m) = 1340 \text{kg/m}^3$$
$$\text{Barley:} \quad \rho(320\mu m) = 1250 \text{kg/m}^3$$

In this model, the density of straw particles are set to 1300 kg/m^3. By using this density, some the porosity of the particle is included in the density.

Wood

The density of the wood particles within a wood pellet are within 1120-1300 kg/m^3 [214]. This density includes som porosity between particles and naturally also some porosity within individual particles. Stamm [215] has measured wood densities and measured densities around 1500 kg/m^3 for wood particles < 850 μm. These measurements include little or no porosity inside the particles. In the present calculations a wood density on 1400 kg/m^3 is applied.

Ashes

The densities of the wood and straw ashes has been estimated from the densities of the oxides in the ash and the content of the individual oxides, seen in Table B.1. The composition of the ashes after release of volatile K, Cl and S has been used to estimate the density of the ashes by a weighted average. For the straws, where SiO_2

Table B.1: Densities of Oxides in Ash

Oxide	Density [kg/m^3]
SiO_2	2648
Al_2O_3	3950
Fe_2O_3	5242
CaO	3340
MgO	3580
Na_2O	2270
K_2O	2320
P_2O_5	2390

dominates the ash (>60 %), the density of the ashes is on average 2700 kg/m^3. For the wood ashes, dominated by CaO and MgO, the density is on average 3100 kg/m^3 These values are used in the model.

B.2 Diffusivity of Alkali Gases

The diffusivities of KCl, K_2SO_4 and KOH in N_2 are estimated from the Chapmann-Enskog Theory [151] and the diffusivity is thus given by:

$$D_{AB} = 0.0018583 \cdot \sqrt{\frac{1}{Mw_A} + \frac{1}{Mw_B}} \cdot T^{3/2} \cdot \frac{1}{p \cdot \sigma_{AB}^2 \cdot \Omega_{D,AB}}$$

where D_{AB} is the binary diffusion coefficient [cm^2/s] for the binary pair A in B. T is the temperature [K], M the molecular weight, P the total pressure [atm], σ_{AB} is the characteristic length and $\Omega_{D,AB}$ is the dimensionless diffusion collision integral. The collision integral is calculated by:

$$\Omega_{AB} = \frac{1.06036}{(T^*)^{0.15610}} + \frac{0.193}{\exp(0.47635T^*)} + \frac{1.03587}{\exp(1.52996T^*)} + \frac{1.76474}{\exp(3.89411T^*)}$$

where

$$T^* = \frac{\kappa T}{\epsilon}$$

The Lennard-Jones parameters (σ and ϵ/κ) are either found in the literature or calculated from the properties of the pure species at the melting temperature, seen in Table B.2 [151].

$$\sigma[\text{Å}] = 1.222 \cdot V_m^{(1/3)}$$
$$\epsilon/\kappa[K] = 1.92 \cdot T_m$$

For the mixtures the ϵ/κ and σ values are estimated as:

$$\sigma_{AB} = \frac{1}{2}(\sigma_A + \sigma_B)$$
$$\epsilon_{AB} = \sqrt{\epsilon_A \cdot \epsilon_B}$$

Table B.2: Constants used for calculation of Lennard-Jones parameters. Data in () are calculated from species properties.

	M [g/mol]	T_m [K]	ν_m[cm^3/mol]	ϵ/κ[K]	σ[Å]	Data from ref.
KCl	74.55			1989	4.186	[216]
K_2SO_4	174.25	1342	93.18	(2577)	(5.54)	[217]
N_2	28.01			91.85	3.919	[218]
KOH	56.11			1213	4.52	[216]

The diffusivities for KCl, K_2SO_4 and KOH in N_2 calculated with the parameters of Table B.2 are seen in Figure B.1.

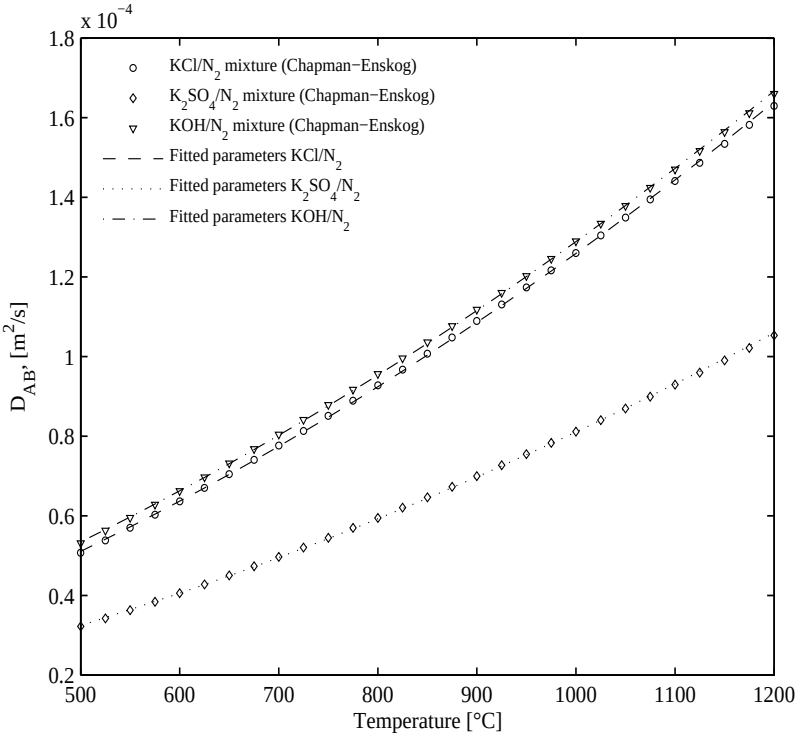

Figure B.1: Estimated diffusivities of KCl, K_2SO_4 and KOH in N_2

In order to ease calculations the calculated diffusivities has been fitted with two-parameter expressions, which will be used in the model [217]:

$$D_{AB} = A \cdot T^B$$

T is the temperature [K] and D_{AB} is calculated in [m^2/s]

Table B.3: Parameters for two-parameter fit describing diffusivities of vapors in N_2

	A [m^2/s]	B [-]
KCl/N_2	$3.8001 \cdot 10^{-10}$	1.7780
K_2SO_4/N_2	$2.0564 \cdot 10^{-10}$	1.8023
KOH/N_2	$5.0882 \cdot 10^{-10}$	1.7404

B.3 Flue Gas Properties

The major components of the flue gas produced from combustion of the straw/wood mixture [5] at an excess air ratio of 1.25 is found to be CO_2 (14%), H_2O (11%), O_2 (4 %) and N_2 (71 %). The viscosity, thermal conductivity and heat capacity of these components are functions of temperature and can be determined by correlations found in Perry's Chemical Engineers' Handbook, Tables 2-312, 2-314 and 2-156 [219].

B.3.1 Heat Capacity

The heat capacity of the gas mixture is calculated by a weighed average according to the composition (molar fractions) of the gas.

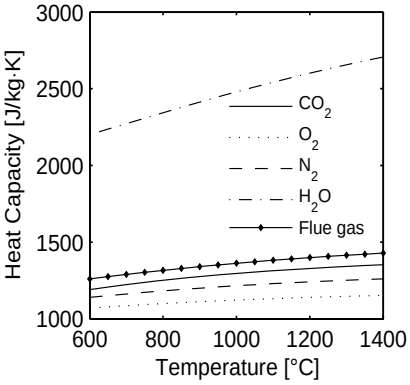

Figure B.2: Heat capacity as function of temperature for the components in a flue gas and for the mixed flue gas. Data from Green and Perry [219].

The heat capacity of the flue gas is seen to only have limited variance within the temperature range 600-1400°C and a constant heat capacity of 1340 J/(kg·K) is assumed, for simplicity in the calculations.

B.3.2 Viscosity and Thermal Conductivity

The viscosity and thermal conductivity of the gas mixture is calculated by a method of Wilke [220, 221]. For the viscosity the calculation is presented by Equations B.1-B.2

$$\mu_g = \sum_{i=1}^{n} \frac{\mu_i}{1 + \frac{1}{y_i} \sum_{j=1, j \neq i}^{n} (y_j \phi_{ij})} \tag{B.1}$$

with

$$\phi_{ij} = \frac{\left[1 + \left(\frac{\mu_i}{\mu_j}\right)^{\frac{1}{2}} \left(\frac{M_j}{M_i}\right)^{\frac{1}{4}}\right]^2}{\left[8\left(1 + \frac{M_i}{M_j}\right)\right]^{\frac{1}{2}}} \tag{B.2}$$

The equations are similar for the thermal conductivity. The results are seen as function of temperature in Figure B.3. It is seen that both the viscosity and the thermal

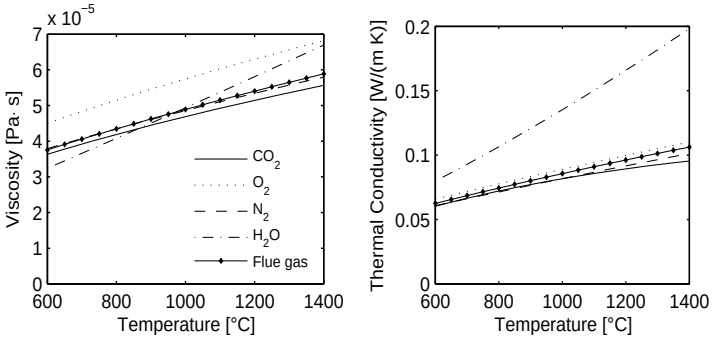

(a) Viscosity (b) Thermal Conductivity

Figure B.3: Viscosity and thermal conductivity as function of temperature for the components in a flue gas and for the mixed flue gas. Data from Green and Perry [219].

conductivity of the flue gas is close to that of N_2. In order to save computational time during modeling, the viscosity and the thermal conductivity of the flue gas are thus taken to be those of N_2. The error of this assumption is lower than 5 % in the temperature range of interest. The viscosity and thermal conductivity of the flue gas are calculated by:

$$\mu_g = \frac{6.5592 \cdot 10^{-7} \cdot T_g^{0.6081}}{1 + 54.714/T_g} \quad [\mathrm{Pa \cdot s}] \tag{B.3}$$

$$k_g = \frac{3.3143 \cdot 10^{-4} \cdot T_g^{0.7722}}{1 + 16.323/T_g + 373.72/T_g^2} \quad [\mathrm{W/(m \cdot K)}] \tag{B.4}$$

B.3.3 Density

The density of the gas phase is estimated by the ideal gas law, where the average molar weight (29.3 kg/kmol) of the gas is utilized.

$$\rho_g = \frac{357.09}{T_g[\mathrm{K}]} \quad [\mathrm{kg/m^3}] \tag{B.5}$$

The density is thus within 0.21-0.41 $\mathrm{kg/m^3}$ in the temperature range 600-1400 °C.

Appendix C

Test of Ash PSD Model

The model has been tested on particle size distributions provided by Jiménes and Ballester [92]. Here, PSD was measured on three fuels (orujillo, chestnut wood and eucalyptus wood sawdust) and their ashes after combustion in an EFR.

Initially the number of fragments have been calculated by the measured dp50 of the fuels and ashes, by the same procedure as described in Chapter 4. The fuels and ashes all have a larger value of the exponent n, when fitting Rosin-Rammler distributions on the measured PSD's. This is due to sieving of the fuels, by which a narrow PSD is obtained ($n \approx 4$ for the fuels). When using the measured median particle sizes, the orujillo is found to fragment into 3 pieces, while $N_{frag} = 2.5$ for eucalyptus and $N_{frag} = 7.8$ for the chestnut wood.

As a test, the model developed here, with $n = 1.3$ and $N_{frag} = 3$ has been applied on the PSD's of the ashes provided by Jiménes and Ballester [92]. The result is seen in Figure C.1. It is seen that the model provides a reasonable description of the PSD's of the ashes even though different values of the exponent n and of N_{frag} was determined for the three fuels.

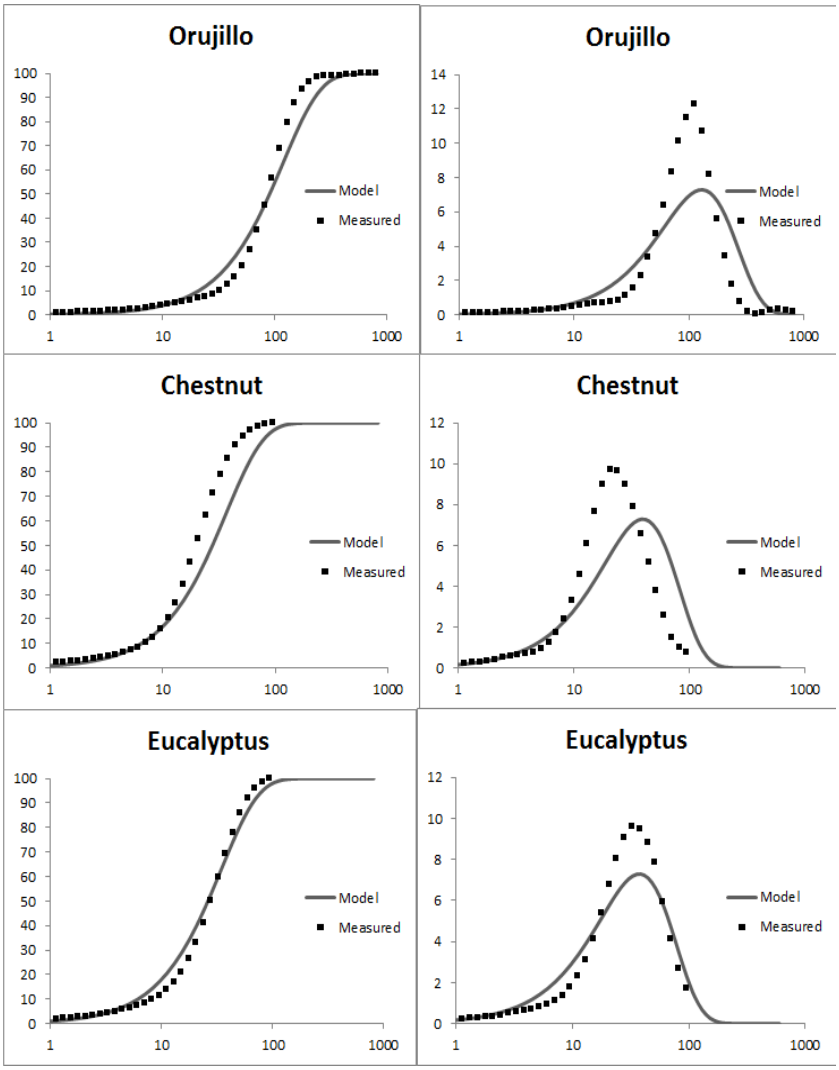

Figure C.1: Model description of the PSD of ashes from EFR combustion of orujillo, chestnut wood and eucalyptis wood. PSD's provided by Jiménes and Ballester [92]

Appendix D

EFR Details

Details of the experimental conditions in the EFR are seen in Table D.1.

Table D.1: Experimental conditions used.

Exp no	Fuel type	Ref	Fuel dp_{50} my	Fuel flow g/hr	Air flow NL/min	Propane flow NL/min	Air to propane NL/min	Cyclone flow NL/min	Filter flow NL/min	T_{fg} bottom °C	T_{fg} probe °C	T_{probe} °C	time exp h
S1	Straw A	[39]	285	850	95.0	0.7	17.0	5.8	2.8	806	752	468	1.50
S2	Straw A	[39]	285	850	95.0	0.7	17.0	6.0	3.0	811	749	468	1.50
S3	Straw B	[207]	350	800	96.0	0.7	16.5	9.1	1.0	767	799	551	2.50
S4	Straw C	[50]	440	860	95.6	0.0	0.0	8.3	1.0		739	500	1.50
S5	Straw C	[50]	440	850	96.0	0.4	10.0	8.6	0.9	1137	814	561	1.37
S6	Straw C	[50]	440	850	96.0	0.4	10.0	7.9	0.8	914	809	543	1.35
S7	Straw C	[50]	230	860	95.6	0.0	0.0	8.5	1.0		694	450	1.67
S8	Straw C	[50]	230	860	95.6	0.0	0.0	10.9	1.2		724	440	1.50
S9	Straw C	[50]	230	860	95.6	0.0	0.0	8.6	0.9		(700)	(450)	1.50
S10	Straw C	[50]	230	850	96.0	0.4	10.0	8.1	0.9		789	496	1.60
S11	Straw C	[50]	230	850	96.0	0.4	10.0	8.1	1.0	844	743	487	1.63
S12	Straw C	[50]	220	850	96.0	0.8	15.0	8.1	0.1	693	785	464	1.42
S13	Straw C	[50]	220	850	96.0	0.6	15.5	6.6	0.8	811	920	577	1.82
S14	Straw C	[50]	220	850	96.0	0.3	16.5	8.6	0.3	778	795	485	1.58
S15	Straw C	[50]	220	850	96.0	0.7	16.5	7.5	0.4	740	783	550	1.50
S16	Straw C	[50]	220	850	96.0	1.8	16.5	8.3	0.2	755	904	664	1.50
S17	Straw C	[50]	220	850	96.0	1.9	16.5	(7.4)	0.8	756	1020	607	1.50
S18	Straw D	[49]	250	800	95.0	0.7	17.0	9.9	5.9	901	800	550	1.50
S19	Straw D	[49]	250	800	95.0	0.7	17.0	8.5	4.7	884	802	548	0.78
W1	Bark	[207]	330	750	96.0	1.0	15.0	9.1	1.1	794	833	591	3.50
W2	Bark	[207]	330	750	96.0	1.0	15.0	8.3	1.1	813	831	582	3.50
W3	Pine	[207]	330	730	96.0	0.5	16.5	7.8	0.8	835	807	541	6.00
W4	Beech	[207]	240	740	96.0	0.6	16.5	9.4	0.8	808	801	551	4.50
W5	WW	[49]	220	744	95.0	0.7	17.0	10.8	7.1	939	803	550	1.50

Numbers in () are assumed based on repetitions or standard settings

Bottom chamber temperature assumed to be 800 °C if no measurement available

[a] Propane flow closed and temperatures lowered to T_{fg}=753 °C and T_{probe}=416 °C after 30 minutes in experiment S13

Appendix E

Model Description of Full Scale Tests 2-6

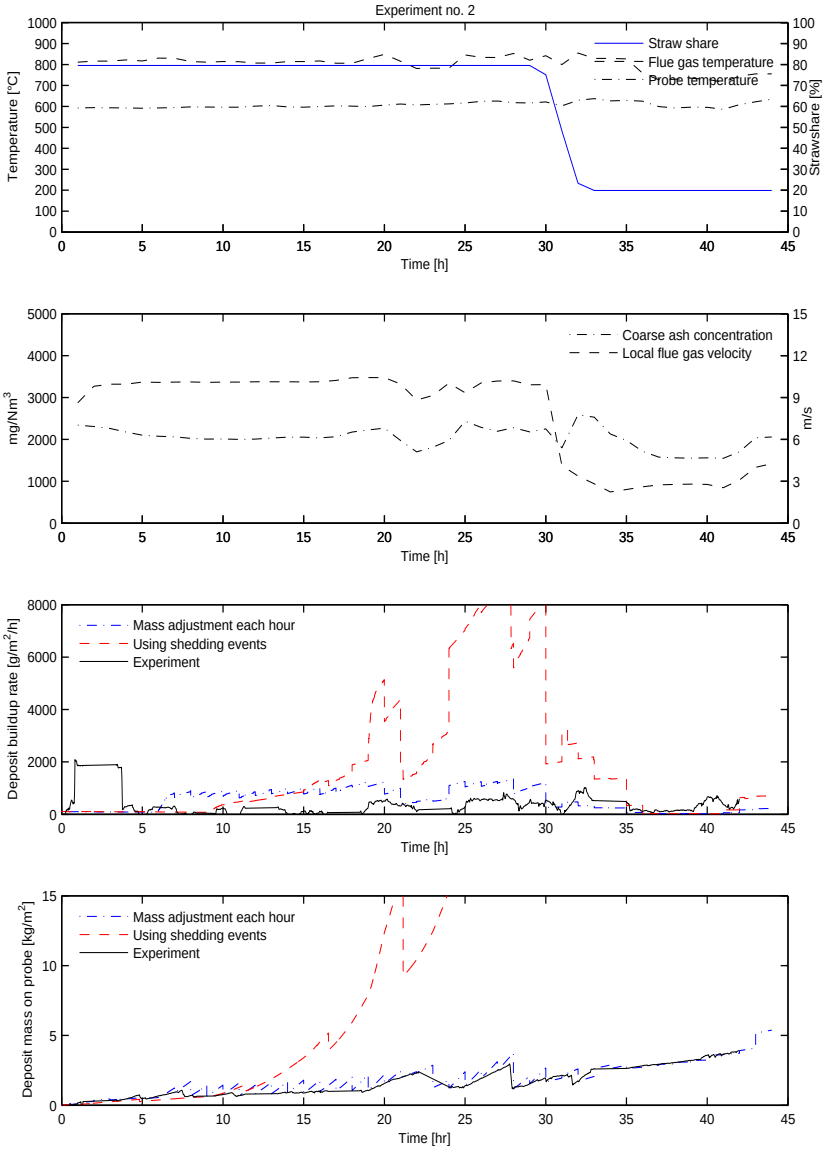

Figure E.1: Results of full scale test 2. From the top, the figures show: (1) temperatures and estimated straw share (2) predicted coarse ash concentration and flue gas velocity (3) predicted and measured deposit formation rates and (4) predicted and measured deposit mass on the probe.

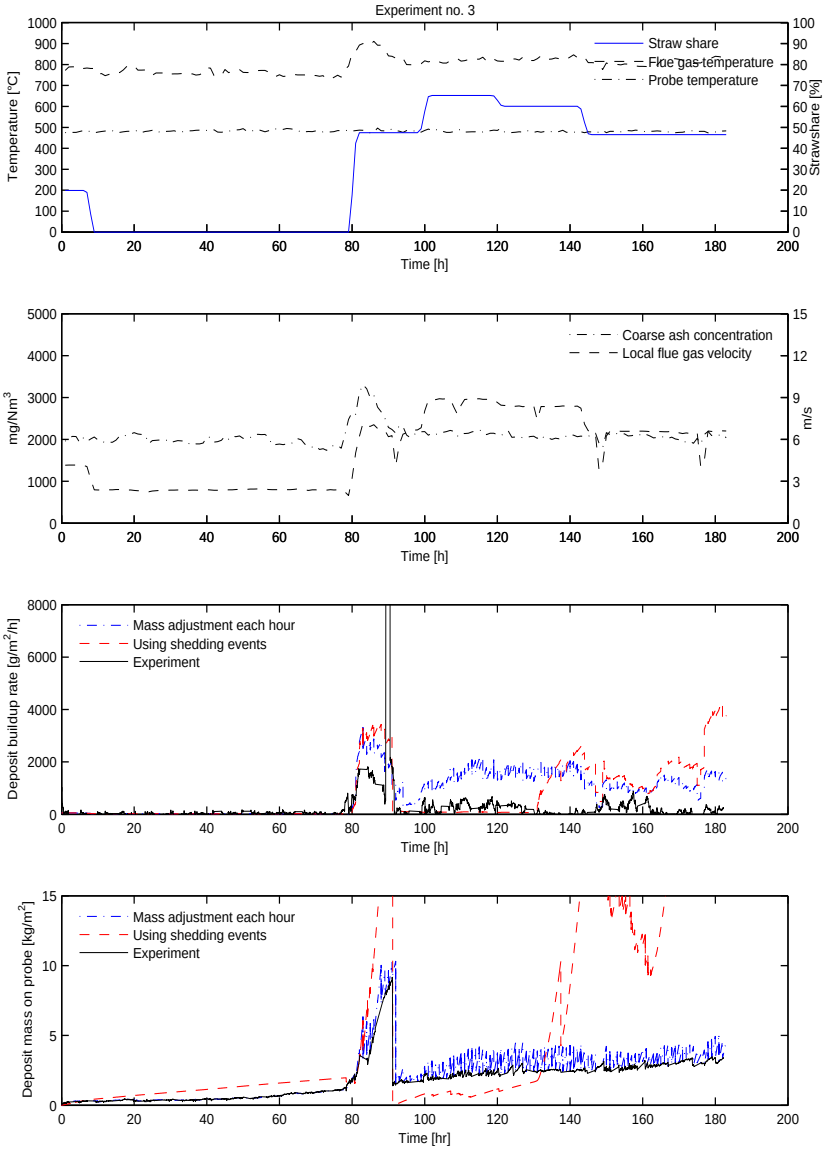

Figure E.2: Results of full scale test 3. From the top, the figures show: (1) temperatures and estimated straw share (2) predicted coarse ash concentration and flue gas velocity (3) predicted and measured deposit formation rates and (4) predicted and measured deposit mass on the probe.

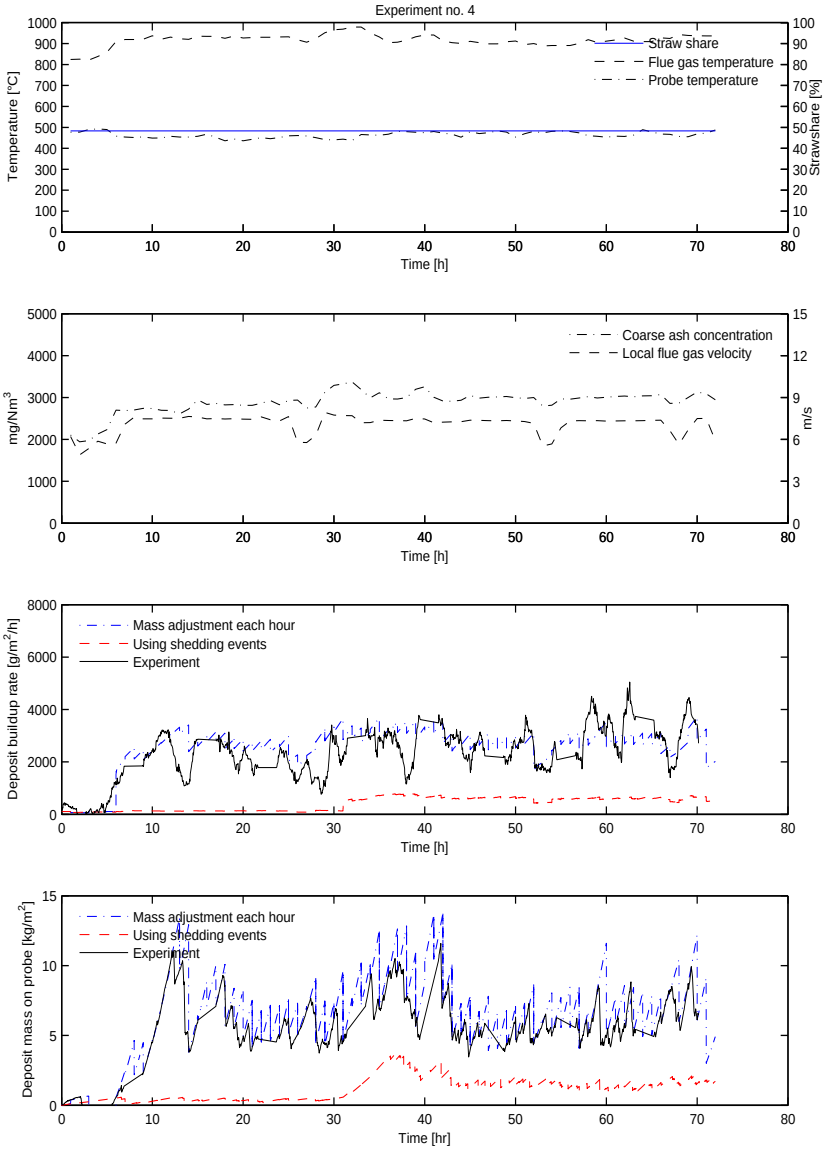

Figure E.3: Results of full scale test 4. From the top, the figures show: (1) temperatures and estimated straw share (2) predicted coarse ash concentration and flue gas velocity (3) predicted and measured deposit formation rates and (4) predicted and measured deposit mass on the probe.

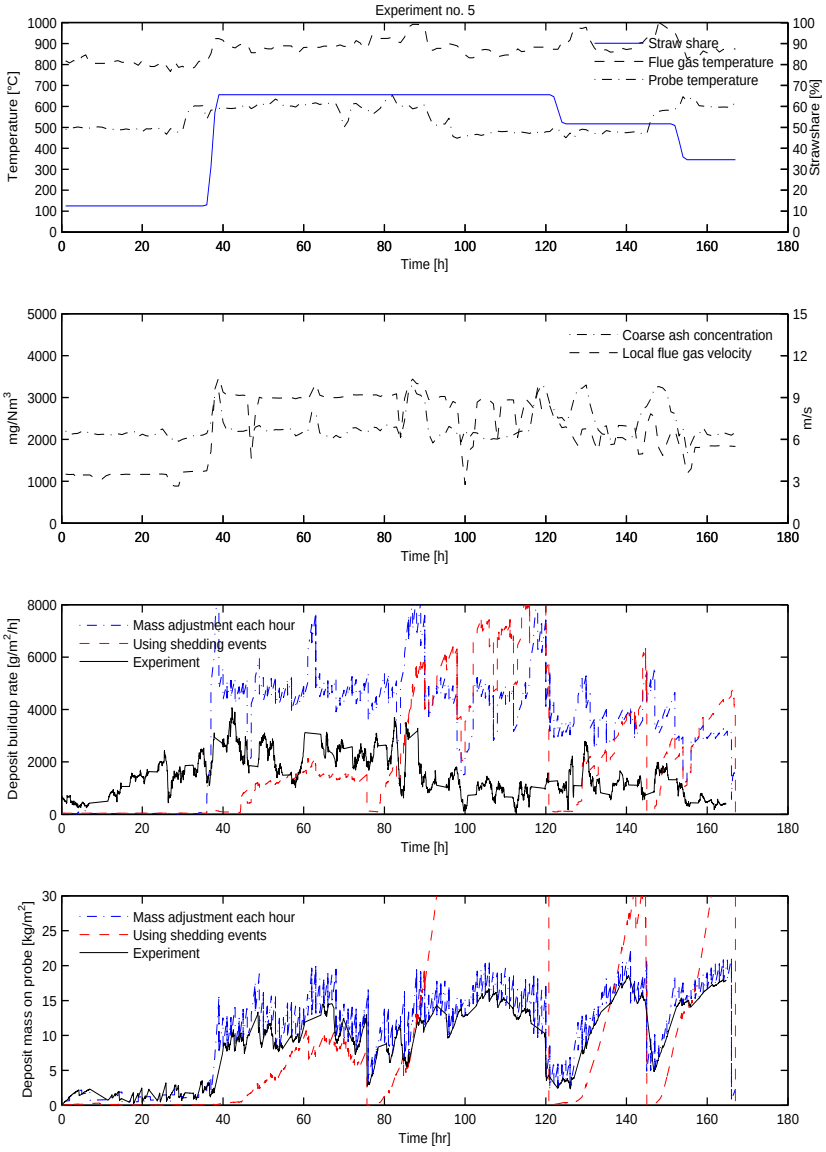

Figure E.4: Results of full scale test 5. From the top, the figures show: (1) temperatures and estimated straw share (2) predicted coarse ash concentration and flue gas velocity (3) predicted and measured deposit formation rates and (4) predicted and measured deposit mass on the probe.

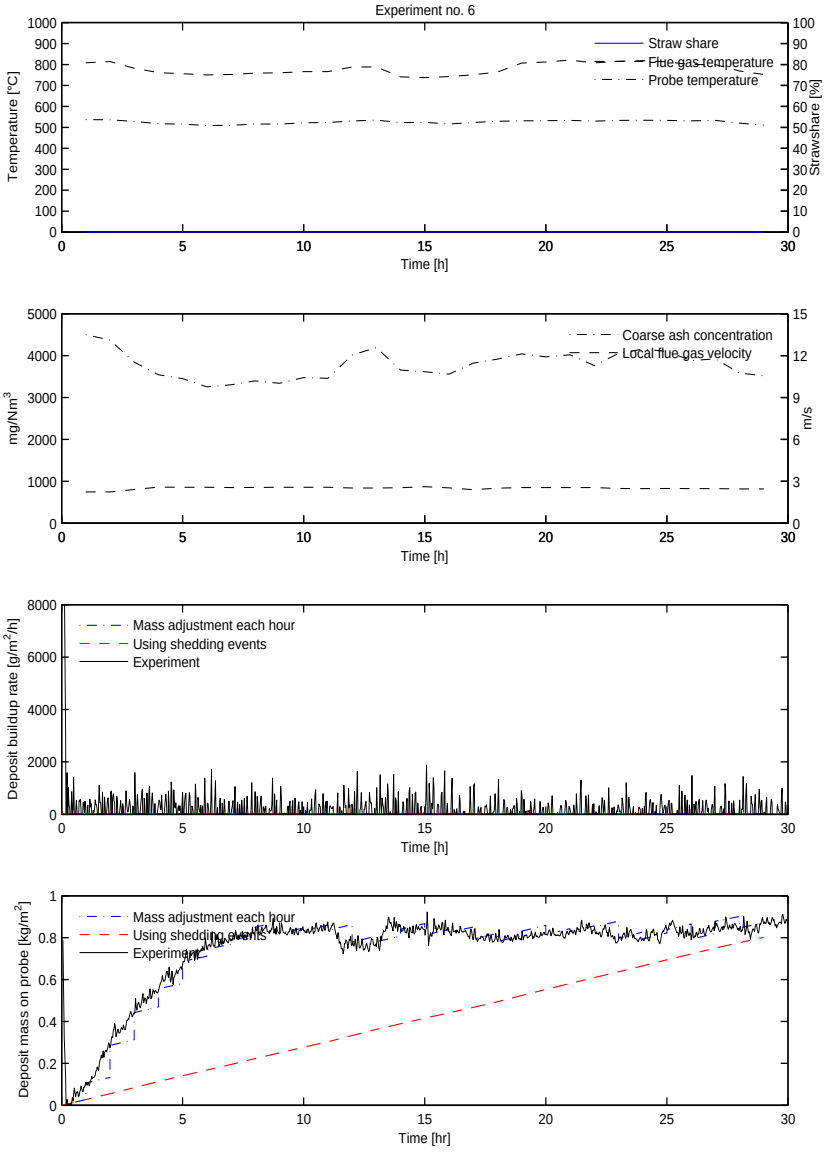

Figure E.5: Results of full scale test 6. From the top, the figures show: (1) temperatures and estimated straw share (2) predicted coarse ash concentration and flue gas velocity (3) predicted and measured deposit formation rates and (4) predicted and measured deposit mass on the probe.

Department of Chemical and Biochemical Engineering
Technical University of Denmark
Søltofts Plads, Building 229
2800 Kgs. Lyngby
Denmark

Phone: +45 45 25 28 00
Web: www.kt.dtu.dk/